



**HAL**  
open science

# New insights in understanding the interaction between recrystallization and phase transformation during intercritical annealing in DP steels

Clélia Couchet

► **To cite this version:**

Clélia Couchet. New insights in understanding the interaction between recrystallization and phase transformation during intercritical annealing in DP steels. Materials. Université de Lorraine, 2024. English. NNT: 2024LORR0019 . tel-04585607

**HAL Id: tel-04585607**

**<https://hal.univ-lorraine.fr/tel-04585607>**

Submitted on 23 May 2024

**HAL** is a multi-disciplinary open access archive for the deposit and dissemination of scientific research documents, whether they are published or not. The documents may come from teaching and research institutions in France or abroad, or from public or private research centers.

L'archive ouverte pluridisciplinaire **HAL**, est destinée au dépôt et à la diffusion de documents scientifiques de niveau recherche, publiés ou non, émanant des établissements d'enseignement et de recherche français ou étrangers, des laboratoires publics ou privés.



**UNIVERSITÉ  
DE LORRAINE**

**BIBLIOTHÈQUES  
UNIVERSITAIRES**

## AVERTISSEMENT

Ce document est le fruit d'un long travail approuvé par le jury de soutenance et mis à disposition de l'ensemble de la communauté universitaire élargie.

Il est soumis à la propriété intellectuelle de l'auteur. Ceci implique une obligation de citation et de référencement lors de l'utilisation de ce document.

D'autre part, toute contrefaçon, plagiat, reproduction illicite encourt une poursuite pénale.

Contact bibliothèque : [ddoc-theses-contact@univ-lorraine.fr](mailto:ddoc-theses-contact@univ-lorraine.fr)  
*(Cette adresse ne permet pas de contacter les auteurs)*

## LIENS

Code de la Propriété Intellectuelle. articles L 122. 4

Code de la Propriété Intellectuelle. articles L 335.2- L 335.10

[http://www.cfcopies.com/V2/leg/leg\\_droi.php](http://www.cfcopies.com/V2/leg/leg_droi.php)

<http://www.culture.gouv.fr/culture/infos-pratiques/droits/protection.htm>



# New insights in understanding the interaction between recrystallization and phase transformation during intercritical annealing in DP steels

## THÈSE

soutenue le 4 Mars 2024

pour l'obtention du

**Doctorat de l'Université de Lorraine**

(spécialité Sciences des Matériaux)

par

Clélia Couchet

### Composition du jury

<i>Président :</i>	Julien Zollinger	IJL, Nancy France
<i>Rapporteurs :</i>	Helena Zapolsky Hatem Zurob	GPM, Rouen France McMaster, Hamilton Canada
<i>Examineurs :</i>	Sophie Cazottes Hugo Van Landeghem	MATEIS, Lyon France SIMAP, Grenoble France
<i>Invités :</i>	Frédéric Bonnet Guillaume Geandier	ArcelorMittal, Maizières-lès-Metz France IJL, Nancy France
<i>Directeur :</i>	Sébastien Allain	IJL, Nancy France
<i>Co-directeur :</i>	Julien Teixeira	IJL, Nancy France



You don't have to be afraid  
You don't even have to be brave  
Living in a gilded cage,  
The only risk is that you'll go...  
Go, Go  
Insane

---

*Insane*  
*Flume*



---

# Acknowledgments

---

D'abord, je souhaiterais remercier Hatem Zurob et Helena Zapolsky, qui ont accepté le rôle de rapporteur-se, ainsi que Sophie Cazottes, Hugo Van Landeghem, examinateur-ice-s, et Julien Zollinger, président de ce Jury. Merci de vous être intéressé-e-s à mon travail et merci pour les discussions scientifiques enrichissantes.

Je remercie également Sébastien Allain, Julien Teixeira, Guillaume Geandier et Frédéric Bonnet. Merci à vous de m'avoir proposé ce sujet de thèse et d'avoir cru en moi pendant toutes ces années. Cette thèse a su répondre à beaucoup de mes attentes. Elle a demandé la connaissance de multiples mécanismes métallurgiques tous intéressants séparément. Le défi de comprendre leurs interactions a été très stimulant intellectuellement. J'ai pu utiliser de nombreuses méthodes expérimentales et numériques. Apprendre, comprendre et découvrir ont été un réel plaisir.

De fait, cette thèse a nécessité de nombreuses expériences utilisant une grande variété de techniques. Je tiens donc à remercier Carla Oberbillig, Guisepe Sollazzo, Patrick Barges et Daniela Obriot, d'ArcelorMittal Maizières Research. Nous n'aurions pas pu proposer un travail d'une telle envergure et si complet sans leur expertise. Merci à elle-eux d'avoir partagé leurs connaissances.

La thèse est une aventure scientifique, certes, mais également humaine. Au cours de ces années de thèse, j'ai créé de nombreux liens qui m'ont aussi fait grandir en tant que personne.

À mes collègues d'ArcelorMittal. Un grand merci pour votre accueil. Je me suis sentie intégrée au groupe malgré mon arrivée en période de confinement et mes présences rares.

À Lucile. Tu as d'abord été pour moi une enseignante aux Mines de Nancy. Je t'ai ensuite retrouvée en tant que collègue au labo. Je voulais te remercier pour l'accueil que tu m'as fait au labo. Merci pour les nombreuses discussions et lectures qui m'ont fait réfléchir sur notre monde et notre société.

À Guillaume et Benoit. Merci pour votre bonne humeur. J'ai apprécié partager avec vous, voisins de bureau, une ambiance de travail pour le moins musicale. Un grand merci également pour toutes nos aventures synchrotronesques, qui resteront toutes gravées dans ma mémoire.

On m'avait prévenue. Écrire a été intense. Les rares moments d'*eurêka* ont certes été agréables, mais si succincts face aux semaines d'errance. J'ai été paralysée par la peur au début. Puis j'ai avancé, sans repère. À des croisements, il a fallu choisir une direction. J'ai vu au loin des routes intéressantes, mais inaccessibles. J'ai aussi dû faire face à des voies sans issue, où il a fallu savoir faire demi-tour. Je me suis perdue souvent, j'ai tourné en rond parfois, j'ai fait quelques pauses pour reprendre mon souffle. Un jour, j'ai cru devoir arrêter, vaincue par l'épuisement.

Mais, bien heureusement, je n'étais pas seule et j'aimerais remercier, du plus profond de mon cœur, mes compagnons de route.

À Cécile, Imed, Steve, Hélène, Mathias, Guillaume, Corentin, Asize et Olha. Pour certain-e-s, je vous ai vu sur ces mêmes chemins avant moi et je vous ai vu réussir, toujours avec beaucoup d'émotions. Tou-te-s, vous m'avez montré que c'était possible, qu'on s'en sort et qu'il y a une vie après.

À Killian, Nathan, Clovis, Mauricio, Mariam, Maxence, Sébastien, Miguel, Gatien, Corentin, Loris. Un grand merci pour votre accueil et votre bienveillance. Un merci tout particulier à ma team salvatrice, qui m'a soutenue et m'a permise de me relever après ma chute au plus bas. Et à celle-eux qui sont en rédaction où qui le seront bientôt, je crois en vous et vous souhaite bon courage. J'ai hâte de vous voir, vous aussi, découvrir le soulagement du dépôt et l'euphorie de la soutenance.

À Juan. Tu as été un co-bureau de rêve. Travailler en ta présence m'a beaucoup apporté scientifiquement et j'espère que nous aurons de nouveau l'occasion de retravailler ensemble. L'ambiance de travail que nous avons construite, à grand renfort de luminaires de Noël et de musiques en tout genre, a été une véritable source d'épanouissement au sein du laboratoire. Comme le dit si bien notre fabulous Bonnie Tyler, "Every now and then, I know there's no one in the universe As magical and wondrous as you". Alt+3

À Lucie. Tu es de loin ma plus belle découverte faite au sein du laboratoire. Tu es une personne exceptionnelle et je suis très heureuse d'avoir eu la chance d'être ton amie. Tu sais m'apprécier pour qui je suis, au naturel. Je te remercie pour tous ces moments passés ensemble, merci pour toutes les discussions féministes, merci pour tous les brunchs à Big Sister, merci pour le partage de nombreuses astuces de vie quotidienne, merci de m'avoir emmenée si souvent à la librairie. Merci pour tout le soutien émotionnel. Un grand merci pour la joie de vivre que tu dégages. Te voir sourire, rire, faire des roulades et autres danses illuminent toujours mes journées. Pour finir, quelle que soit la voie que tu choisis pour la suite, je crois en toi et j'espère ne jamais être très loin. Et si tu viens à ouvrir une librairie ou une pâtisserie, je serai ta première cliente.

À Marco. On s'est rencontré dans l'adversité de la prépa. On s'est retrouvé dans l'adversité de la thèse. On s'est entre-aidé pour faire face à l'isolement lié aux confinements à répétition. On a parlé de longues heures, sur tant de sujets. Je pense que tu es la seule personne qui m'aie jamais vraiment comprise, dans toute mon étrangeté, dans toute mon agitation, dans toute ma sonorité. Ton soutien inconditionnel et sans faille m'a permis de traverser les moments les plus difficiles de ces dernières années. Malgré tous mes efforts, tous les mots que je pourrais utiliser me paraissent trop faibles pour ce que je ressens et tous les merci du monde ne feraient pas honneur à tout ce que tu fais pour moi.

---

# Contents

---

<b>Acknowledgments</b>	<b>i</b>
<b>Contents</b>	<b>iii</b>
<b>Glossary</b>	<b>v</b>
<b>List of Figures</b>	<b>vii</b>
<b>List of Tables</b>	<b>xviii</b>
<b>Résumé étendu en français</b>	<b>xix</b>
<b>Introduction</b>	<b>1</b>
<b>Chapter I Literature review</b>	<b>7</b>
I.1 Recovery and recrystallization . . . . .	9
I.2 Austenite formation during intercritical annealing . . . . .	22
I.3 Interactions between ferrite recrystallization and phase transformation . . . . .	39
I.4 Modeling the austenite formation . . . . .	47
I.5 Summary . . . . .	54
<b>Chapter II Experimental and simulation methods</b>	<b>57</b>
II.1 Studied materials . . . . .	59
II.2 Thermal treatments . . . . .	61
II.3 Optical microscopy . . . . .	62
II.4 Scanning Electron Microscopy . . . . .	63
II.5 Transmission Electron Microscopy . . . . .	67
II.6 Wavelength-Dispersive Spectrometry . . . . .	69
II.7 Inductively Coupled Plasma Optical Emission Spectroscopy . . . . .	70
II.8 Vickers Micro-Hardness . . . . .	70
II.9 High Energy X-Ray Diffraction . . . . .	72
II.10 Phase transformation modelling: approach and tools . . . . .	83

<b>Chapter III Interaction between recrystallization and austenite formation investigated by in situ HEXRD experiments</b>	<b>85</b>
III.1 Effect of the heating rate on the austenite transformation . . . . .	88
III.2 Effect of the micro-alloying and cold-rolling ratio on the austenite transformation	111
III.3 Conclusions on the interaction between ferrite recrystallization and austenite formation . . . . .	132
<b>Chapter IV Thermo-kinetics investigation of austenite formation during inter-critical annealing</b>	<b>135</b>
IV.1 Thermo-kinetic analysis of austenite growth in the quinary Fe-0.1C-1.9Mn-0.2Si-0.2Cr system . . . . .	136
IV.2 Predictive physically-based model of austenite formation during the holding stage	145
IV.3 Conclusions on the thermo-kinetics investigation of austenite formation during intercritical annealing . . . . .	156
<b>Conclusion</b>	<b>159</b>
<b>References</b>	<b>165</b>
<b>A Ferrite recrystallization followed by SEM/EBSD</b>	<b>179</b>
<b>B Repeatability of HEXRD experiments</b>	<b>183</b>
<b>C Physically-based prediction of the austenite fraction during heating stage</b>	<b>185</b>
C.1 Austenite fraction from cementite particles isolated in the ferrite matrix (CP&M subsystem) . . . . .	186
C.2 Austenite fraction from the pearlite (P subsystem) . . . . .	190
C.3 Global kinetics . . . . .	192
C.4 Conclusions on the prediction of austenite fraction along the heating stage . . . .	194
<b>Summary</b>	<b>197</b>
<b>Résumé</b>	<b>198</b>

---

# Glossary

---

**CA** Cellular Automaton. 52

**EBSD** Electron BackScattering Diffraction. xxii, 15, 16, 17, 21, 22, 59, 64, 65, 66, 72, 78, 81, 82, 83, 160

**EDXS** Energy-Dispersive X-ray Spectroscopy. xxii, 59, 68, 87, 89, 106, 110, 132, 160

**GOS** Grain Orientation Spread. 15, 16, 64, 65, 66, 71

**GWM** Generalized Wycliffe Model. xxix, 136, 150, 151, 152, 153, 155, 156, 160, 162

**HAGBs** High Angle Grain Bondaries. 10, 11, 13, 14, 15

**HEXRD** High Energy X-Ray Diffraction. 5, 6, 10, 17, 18, 20, 21, 22, 36, 46, 54, 59, 64, 67, 72, 75, 76, 87, 88, 89, 96, 100, 101, 103, 105, 106, 109, 110, 112, 117, 118, 122, 123, 128, 129, 132, 142, 143, 155, 159, 161, 162

**ICP-OES** Inductively Coupled Plasma Optical Emission Spectroscopy. 70, 114

**IDST** Isolated Diffraction Spot Tracking. xxiii, 76, 81, 82, 83, 87, 89, 99, 110, 112, 116, 122, 130, 132, 159, 160, 162

**IPF** Inverse Pole Figure. 64, 65

**LAGBs** Low Angle Grain Bondaries. 10, 14

**LE** Local Equilibrium. 26, 27, 28, 84

**LENP** Local Equilibrium with Negligible Partitioning. xxiii, xxiv, xxv, xxvii, xxviii, 27, 31, 32, 33, 35, 36, 39, 49, 51, 52, 53, 93, 94, 100, 102, 106, 108, 109, 111, 112, 113, 114, 117, 118, 119, 123, 129, 131, 133, 136, 137, 138, 139, 140, 142, 143, 145, 146, 153, 155, 156, 161

**LEP** Local Equilibrium with Partitioning. xxv, xxvii, xxviii, xxix, 27, 29, 30, 31, 32, 33, 35, 36, 39, 49, 52, 109, 110, 111, 129, 132, 133, 137, 143, 145, 146, 147, 151, 155, 156, 157, 161

**mWH** modified Williamson-Hall. 18

**OE** Ortho-Equilibrium. xxii, xxiii, xxv, xxviii, 25, 26, 27, 28, 29, 34, 36, 39, 55, 84, 87, 92, 100, 102, 109, 110, 112, 113, 114, 118, 119, 124, 129, 137, 139, 140, 153, 154, 155

**PE** Para-Equilibrium. 84

**PF** Phase Field. 52, 53, 54

**PNTT** Partition to Non-partition Transition Temperature. xxiv, 31, 32, 33, 35, 36, 106, 107, 108, 111, 129, 133, 145, 161, 162

**RPC** Recrystallization Peak Counting. 20, 22, 83, 159

**SEM** Scanning Electron Microscopy. 15, 16, 17, 21, 22, 59, 63, 64, 65, 66, 67, 69, 70, 72, 74, 78, 81, 82, 83, 87, 89, 104, 110, 112, 114, 119, 124, 130, 132, 160

**SIBM** Strain Induced Boundary Migration. 14, 22, 54

**TEM** Transmission Electron Microscopy. 16, 67, 87, 89, 90, 110, 130, 132, 160

**WDS** Wavelength-Dispersive Spectrometry. xxii, 59, 69, 87, 89, 95, 104, 110, 111, 132, 160

**XRD** X-Ray Diffraction. 18, 19

---

# List of Figures

---

1	Représentation schématique d'un diagramme de phase binaire Fe-C (a) et du cycle thermo-mécanique industriel de production d'acier DP (b). La succession des étapes est décrite en (c). L'évolution de la microstructure est schématisée en (b) de (1) à (6). . . . .	xx
2	Cinétique de recristallisation (a) et de formation d'austénite (b et c) pendant le recuit intercritique du DP600 CR65 à 3 °C/s (bleu) et 30 °C/s (vert) suivi par DRXHE (méthode IDST et analyse Rietveld respectivement). Les fractions sont représentées pendant les étapes de chauffe (a et b) et de maintien isotherme (c). . . . .	xxiv
3	Écart entre la fraction d'austénite estimée à partir des expériences de DRXHE et l'OE pendant le maintien isotherme du DP600 CR65 (diamants), du DP600Nb15 CR65 (triangles) et du DP600Nb30 CR65 (triangles inversés). . . . .	xxvi
4	Cinétique de recristallisation (a) et de formation d'austénite (b et c) pendant le recuit intercritique du DP600 CR30 (carrés bleus vides), du DP600 CR45 (diamants bleus vides), du DP600 CR60 (carrés bleus remplis) et du DP600 CR65 (diamants bleus remplis) suivi par HEXRD. Les fractions sont représentées pendant l'étape de chauffe à 3 °C/s (a et b) et l'étape de maintien isotherme (c). . . . .	xxvii
5	Fractions d'austénite lors d'une chauffe lente (3 °C/s) (a) et d'un maintien isotherme à 800 °C (b) dans le ternaire Fe-0.1C-1.9Mn (noir) et le quinaire Fe-0.1C-1.9Mn-0.2Si-0.2Cr (rouge). . . . .	xxix
6	Fraction d'austénite pendant le maintien isotherme à 800 °C après une chauffe lente (3 °C/s en bleu) ou rapide (30 °C/s en vert) de notre DP600 calculé avec notre GWM (lignes continues) comparée aux données expérimentales (diamants) obtenues à partir d'expériences DRXHE (Figure 2). . . . .	xxx
7	(a) Classification of steel families as a function of their total elongation and their UTS [Kwo+10; Mat+12; Nan+19] and (b) DP steels in a car BIW [Arc] . . . . .	2
8	(a) Optical observation of the typical microstructure of a DP steel after etching. Martensite ( $\alpha'$ ) appears in brown and ferrite ( $\alpha$ ) in white (from this work). (b) Map of simulated Ultimate Tensile Strength (UTS in MPa) of DP steels as a function of the martensite fraction and nominal carbon content [All+15]. . . . .	2
9	Schematic representation of a binary phase diagram Fe-C (a) and of the industrial schedule for DP steel production (b). The succession of steps is described in (c). The evolution of the microstructure is schematized in (b) from (1) to (6). . . . .	3

10	Effect of the heating rate on the austenite formation kinetics along the soaking stage at 750 °C (a) and on the austenite morphology (b and c) at the end of the soaking stage (10 min) of a cold-rolled Fe-C-Mn-Mo steel. Martensite (austenite before quenching) is in dark grey and ferrite in light grey. A typical "necklace" morphology is observed after slow heating at 1 °C/s (c), while a more "banded" morphology is obtained after fast heating at 100 °C/s (b). The red zones show austenite rich zones and their morphology (adapted from [HPM04]). . . . .	4
I.1	Dislocation densities estimated from High Energy X-Ray Diffraction (HEXRD) during isothermal annealing at 450 °C (blue), 500 °C (green), 550 °C (orange) and 650 °C (red) after fast heating (100 °C/s). Dislocation densities deduced from Vickers hardness tests during annealing at 550 °C are represented by black triangles. (from [Cou+21]) . . . . .	10
I.2	Successive rearrangements of dislocation structures during static recovery [HH95]. . .	11
I.3	Schematic representation of the microstructure evolution along recrystallization. a) deformed state. b) recrystallized grain nuclei. c) recrystallized grain growth. d) abnormal growth in the fully recrystallized material. . . . .	12
I.4	Recrystallization kinetics of (a) aluminum at 350 °C after three deformation levels and (b) a Fe-3.5Si (wt%) cold-rolled at 60 % annealed at several temperatures. Higher deformation or annealing temperature accelerates recrystallization kinetics. (adapted from [HH95]) . . . . .	13
I.5	Softening fractions determined from double-hit compression tests monitoring austenite recrystallization in a Fe-0.2C-1.5Mn (a) and a Fe-0.2C-1.5Mn-0.02Nb (b) steels during isothermal treatments at different temperatures (adapted from [Ver+09]). . .	13
I.6	Nucleation of a recrystallized grain from a dislocation cell (a) or a sub-grain (b) in the Strain Induced Boundary Migration Theory adapted from [ZBD06]. Grain II contains more dislocations and stores a higher energy $E_{II}$ than grain I, storing a lower energy $E_I$ . . . . .	14
I.7	Optical micrograph of the microstructure after etching (Nital 2 %) of a low-carbon steel after 11 s at 600 °C. A recrystallized grain is indicated by a black arrow. A non-recrystallized grain is indicated by a red arrow. (adapted from [MAG04]) . . . .	15
I.8	SEM/EBSD map post-processed to reveal the Grain Orientation Spread (GOS) in a DP600 steel after a heating sequence at 3 °C/s interrupted at 700 °C (He gas quenched). (adapted from [Mor+18]) . . . . .	16
I.9	TEM micrograph ( $\vec{g} = \{111\}$ ) of a low-carbon steel cold-rolled at 84 %. A dislocation cell, indicated by a black arrow, is delimited by dislocation walls, indicated by red arrows. (adapted from [MAG04]). . . . .	17
I.10	3DXRD experimental setup (adapted from [Lau01]) for growth tracking of individual recrystallized grains. . . . .	19
I.11	Diffraction pattern of a fully recrystallized 90 % cold-rolled aluminum alloy AA1050 annealed at 270 °C. (adapted from [Lau+03]) . . . . .	19
I.12	(a) Four examples of intensities of diffraction spots as a function of time during annealing at 315 °C of an aluminum alloy AA5182 hot deformed at 400 °C to a strain of 2.0 (adapted from [Lau01]). (b) Six examples of grain volume evolution in a 90 % cold-rolled aluminum alloy AA1050 during annealing at 270 °C deduced from the intensity of several tracked grains using equation I.3 (adapted from [Lau+03]) . . . .	20

I.13	Ferrite recrystallization of a DP600 steel cold-rolled at 60 % followed using the RPC method developed in [Mor+18]. (a) Azimuthal investigation of the 200 ferrite diffraction ring. (b) 1D diffractogram of the 200 ferrite ring at room temperature (in black) and at 700 °C (in red) along heating at 3 °C/s. (c) Number of recrystallization peaks counted along the heating at 3 °C/s (in blue) and 30 °C/s (in black). (d) Recrystallized volume fraction estimated from the RPC method (with crosses) and from SEM/EBSD observations (with dots) (Figure I.8). . . . .	21
I.14	Schematic representation of a pseudo-binary phase diagram Fe-C-Mn (a) and of the formation of the microstructure before intercritical annealing along an industrial thermo-mechanical schedule (b). The succession of industrial steps is described in (c). The evolution of the microstructures is schematized in (b) from (1) to (5). . . . .	23
I.15	Microstructures before intercritical annealing of (a) a Fe-0.178C-1.55Mn-1.7Si cold-rolled at 50 % studied in [HPM04] and (b) a DP590 grade cold-rolled at 70 % studied in [Li+13]. Both microstructures show deformed ferrite, indicated by white arrows, and pearlite, indicated by red arrows. The DP590 grade also shows cementite particles at ferrite grain boundaries, indicated by black arrows. A schematic representation of the microstructure before intercritical annealing (c) highlights the main microstructural features. . . . .	25
I.16	3D representation of the OE from [Gou+15]. The blue and red surfaces represent the Gibbs free energy surfaces of ferrite ( $\alpha$ ) and austenite ( $\gamma$ ) respectively as a function of the ternary composition at a given temperature. The tangent plane defines the OE where the chemical potential of each of the three elements is equal between the phases. The projection of the intersections between the tangent plane and the Gibbs free energy surfaces defines a tie-line in the two-phase domain. . . . .	26
I.17	Schematized phase diagram and profile of the substitutional element X at the interface at a given temperature in a Fe-C-X steel where X is either a $\gamma$ stabilizer (a) or an $\alpha$ stabilizer (b). The operative tie-line considering OE is drawn with a dotted line. . . . .	28
I.18	Schematized phase diagram and profile of the substitutional element X at the interface at a given temperature in a Fe-C-X steel where X is either a $\gamma$ stabilizer (a and c) or an $\alpha$ stabilizer (b and d). The operative tie-line considering Local Equilibrium with Partitioning (a and b) and LENP (c and d) are drawn with a dotted line. . . . .	29
I.19	Thermo-kinetic stages of austenite formation from an initial ferrite-pearlite microstructure to OE completion (from [SDM81]) (phases and their local C and Mn composition fields). . . . .	30
I.20	Austenite formation kinetics during annealing at various temperatures of a medium manganese steel simulated with the DICTRA module of the Thermo-Calc software. (adapted from [Kam+15]) . . . . .	30
I.21	Schematic representation of the simulation cell used to study the dissolution of a cementite particle $\theta$ in a ferrite matrix (a) and the schematic Fe-C-Mn phase diagram at the annealing temperature (b). The initial manganese composition of ferrite and cementite are written $U_{Mn}^{\alpha}$ and $U_{Mn}^{\theta}$ respectively. The squares represent the austenite composition at the interfaces, written $U_{Mn}^{\gamma/\theta}$ at interface 1 and $U_{Mn}^{\gamma/\alpha}$ at interface 2. The austenite compositions at interfaces are indicated considering LENP mode, i.e. considering no manganese partition ( $U_{Mn}^{\theta} = U_{Mn}^{\gamma/\theta}$ and $U_{Mn}^{\alpha} = U_{Mn}^{\gamma/\alpha}$ ). (adapted from [Miy+10]) . . . . .	31

I.22	Map of the cementite dissolution modes as a function of cementite composition in manganese and annealing temperature (adapted from [GMD12])). The black horizontal dashed lines indicate the cementite compositions considered in Figure I.23. The red vertical dashed line indicates the annealing temperature considered in Figure I.23. This map predicts a dissolution under LENP mode for the particle with 7 wt% Mn and a dissolution under LEP mode for the particle with 25 wt% Mn. . . .	32
I.23	Austenite formation kinetics during an isothermal treatment at 740 °C. The composition in manganese of the cementite particles is set at 7 wt% in (a) and 25 wt% in (b). (adapted from [Lai+16]) . . . . .	33
I.24	Operative tie-lines at the interface $\gamma/\alpha$ at 730 °C (dark-blue), 740 °C (blue), and 760 °C (green) during heating at 3 °C/s simulated with DICTRA. The initial manganese u-fraction in ferrite is indicated by a black dotted line (from [Cou+23]). . . . .	33
I.25	Schematic representation (a, adapted from [Miy+10]) and austenite formation kinetics (b, adapted from [Wu+20]) during the dissolution of cementite particles. Cementite particles can be nucleation sites (Configuration A) or not (Configuration B). In configuration B, carbon diffuses through ferrite from the dissolving cementite particle to the growing austenite. In (b), the proportion of nucleation sites among cementite particles is indicated by $\Phi$ . When $\Phi = 1$ , all cementite particles are nucleation sites. When $\Phi = 0$ , no cementite particle is a nucleation site. . . . .	34
I.26	Growth competition between austenite islands with LENP and LEP interface conditions. (a) schematic representation of the simulation cell. At the interface set with LEP conditions ( $\gamma_{LEP}/\alpha$ on the right), a manganese depletion is imitated (Figure I.18 a). The simulated fraction of the austenite starting with LENP (dotted-dashed line) and the austenite starting with LEP (double dotted-dashed line), as well as the total austenite fractions (solid line) are plotted during the heating stage (b) and the isothermal holding stage (c) [Cou+23] . . . . .	37
I.27	Austenite formation kinetics in a 60 % cold-rolled DP600 held 10 min at 800 °C after heating at 3 °C/s (red), 30 °C/s (blue) and 100 °C/s (black). The higher the heating rate, the faster the kinetics and the higher the overshoot of the OE fraction at the end of the isothermal holding. (adapted from [Tei+21]) . . . . .	38
I.28	Microstructures of a cold-rolled Fe-C-Mn-Mo steel heated at 1 °C/s (a) or 100 °C/s (b) and annealed at 750 °C for 10 min. Martensite (austenite before quenching) is in dark grey and ferrite in light grey. A typical "necklace" morphology is observed after slow heating (a), while a more "banded" morphology is obtained after fast heating (b). The red zones show austenite rich zones and their morphology. (adapted from [HPM04]) . . . . .	38
I.29	Schematic representation of the microstructure at Ac1 during slow heating. . . . .	41
I.30	Schematic representation of the genesis of a necklace microstructure above Ac1 during slow heating. Austenite is represented in red, ferrite in white and cementite in black. . . . .	41
I.31	2D Phase-Field simulations of the microstructures of a DP600 grade steel annealed at 770 °C for 300 s after heating at 1 °C/s (a) and 100 °C/s (b). Austenite grains are in red (A) and ferrite grains in white (F). (adapted from [ZM15]) . . . . .	42
I.32	Schematic representation of the microstructure at Ac1 during annealing using an intermediate heating rate. . . . .	43
I.33	Schematic representation of the genesis of a banded microstructure above Ac1 during fast heating ( $> 10$ °C/s). . . . .	43

I.34	Austenite transformation kinetics of an industrial DP600 steel cold rolled at 60 % annealed at 800 °C using a low (a) and a fast (b) heating rate. Austenite fractions simulated for the simplified ternary nominal composition with the DICTRA module of the Thermo-Calc software considering two separated subsystems (in color) are compared to austenite fractions obtained from HEXRD experiments (in black). (adapted from [Mor19]) . . . . .	46
I.35	Austenite formation kinetics predicted by a differential JMAK model (dashed lines), compared to experimental data (dilatometry, in solid line), during continuous heating using various heating rates of a recrystallized DP1000 grade steel. The initial microstructure contains equiaxed ferrite grains and aggregates of spheroidized cementite particles. (from [Oll+17]) . . . . .	49
I.36	Evolution of the simplified composition profile of carbon (a, c, e) and manganese (e, d, f) during the austenite growth in the surrounding ferrite in a Fe-C-Mn steel during isothermal holding proposed by Wycliffe et al. [WPE81]. From the initial state (a and b), the austenite growth is modelled considering the LENP mode (c and d), until carbon is homogeneous in austenite. Then, the austenite growth is modeled with the LEP mode (e and f) with partition of manganese in austenite. . . . .	50
I.37	Austenite formation kinetics predicted by a mixed-mode model (dashed lines), compared to experimental data (dilatometry, in solid line), during continuous heating using various heating rates of a recrystallized DP1000 grade steel. The initial microstructure contains equiaxed ferrite grains and aggregates of spheroidized cementite particles. (from [Oll+18]) . . . . .	52
II.1	Schema of samples cut down from the cold-rolled sheets (a) and dimensions of the samples (b) . . . . .	60
II.2	Bähr dilatometer available at DESY facilities (a) and position of the welded thermocouple and analyzed zone on a sample studied by HEXRD (b). A dashed red line represents the beam path. . . . .	61
II.3	The dilatometer samples are cut in the transverse direction for microscopy (a). The observed surface is colored in red. Microscopical observations are performed at sheet quarter thickness (b). . . . .	62
II.4	Optical micrograph of the DP600Nb15 CR65 in the cold-rolled state (a) and segmentation of pearlite in red (b). Isolated cementite particles, seen in (b) in dark grey, are erased from the segmentation on morphological base. . . . .	63
II.5	SEM/EBSD map (magnification x 300) of the Grain Orientation Spread (GOS) in the Mn20 CR65 steel after 100 s at 650 °C. . . . .	65
II.6	IPF map (a) and GOS maps (b,c) (magnification x 300) of the Mn20 CR65 steel after 200 s at 650 °C. (b) highlights grains with a GOS lower than 3 °. (c) highlights grains with a GOS lower than 5.5 °. White arrows show recrystallized grains with subgrains. . . . .	66
II.7	IPF map (a) and GOS maps (b,c) (magnification x 300) of the Mn05 CR65 steel after 20 s at 650 °C. (b) highlights grains with a GOS lower than 3 °. (c) highlights grains with a GOS lower than 10°. . . . .	67
II.8	SEM/EBSD map (magnification x 300) of the Grain Orientation Spread (GOS) in the Mn05 CR65 steel after 10 s at 650 °C. . . . .	68

II.9 SEM/EBSD maps (magnification x 300) of the Grain Orientation Spread (GOS) in the Mn05 CR65 steel after 5 s at 650 °C. The recrystallized fractions are estimated at 4 % in (a) and 9 % in (b). . . . .	68
II.10 Recrystallized fraction obtained from SEM/EBSD maps during annealing at 650 °C of the studied Mn05 CR65 (a) and Mn20 CR65 (b) as a function of the annealing time. We consider as grain boundaries, boundaries with a misorientation higher than 10 °. We consider as recrystallized, grains with a GOS lower than 3 ° (in blue (a) or red (b)). Samples with poor surface state are post treated twice. The second post treatment considers GOS up to 10 °. The obtained recrystallized fraction is then plotted in black. Trends curves are plotted in dotted lines. . . . .	69
II.11 Vickers micro-hardness during annealing at 650 °C of the studied Mn05 CR65 (a) and Mn20 CR65 (b) . . . . .	70
II.12 GOS maps (magnification x 300) in the Mn05 CR65 (a) and Mn20 CR65 (b) steels heated up to 650 °C and gas quenched (0 s holding). . . . .	71
II.13 Recrystallized fraction obtained from Vickers micro-hardness measurements during annealing at 650 °C of the studied Mn05 CR65 (a) and Mn20 CR65 (b). Trend curves are plotted in dashed lines. The trend curves of the SEM/EBSD measurements (dotted lines) are plotted as reference. . . . .	72
II.14 Schema (a) and pictures (b,c) of the in situ High Energy X-Ray Diffraction (HEXRD) experiment setup used on the PETRA III - P07 beamline at the DESY facilities. . .	73
II.15 Debye-Scherrer rings (a) and 1D diffraction patterns (b, c) during the annealing of the DP600 CR65 at 800 °C. The experimental 1D diffraction pattern is plotted with black circles and the fitted theoretical diffraction pattern is plotted with a red line. The temperature and the axis scales are chosen to show the diffracting planes of ferrite and austenite. . . . .	75
II.16 Diffraction patterns of the Mn20 CR65 steel (a) at room temperature, (b) after 550 s at 650 °C. . . . .	77
II.17 1D example of the detection step in the IDST method. The simple threshold (in red) erases the background noise. The local threshold (in green) is calculated based on the local mean intensity (in blue) and separates nearby local maxima. . . . .	78
II.18 Build of a track. An object (black spot) is detected at on the frame n and a ROI is defined (limited by a dashed circle) (a). On the next frame n + 1, an object detected in the searching region (green spot) is identified as the same object (b). The resulting track contains the information (position, intensity, size, . . .) of the object over time (c). . . . .	79
II.19 Detected spots (circled in blue) on the diffraction pattern of the Mn20 CR65 after 100 s at 650 °C. . . . .	79
II.20 Number of detected (black line) and tracked spots (green line) during the holding stage at 650 °C of the Mn05 CR65 (a) and Mn20 CR65 (b). . . . .	80
II.21 Recrystallized fractions obtained by the IDST method (in solid line), by SEM/EBSD maps (in circles) and by Vickers micro-hardness measurements (in diamonds) during annealing at 650 °C of the Mn05 CR65 (a) and Mn20 CR65 (b). . . . .	82

III.1 Schematic representation of the experimental strategy developed in this thesis. The different annealing conditions are compared in terms of ferrite recrystallization and austenite formation. In Section III.1, the mechanisms are controlled by the heating rate and, in Section III.2, by niobium micro-alloying and cold-rolling ratio. The parameters of the reference experiment are highlighted in bold font (non-micro-alloyed DP600 steel composition annealed at 3 °C/s up to 800 °C during 10 min, after 65 % cold-rolling). . . . .	88
III.2 SEM/SE micrograph of the microstructure of the DP600 CR65 steel in the cold-rolled state (Picral and Nital etching). Cementite particles (either in pearlite or in the matrix) are in white contrast and ferrite in dark contrast. . . . .	90
III.3 TEM images of cementite particles extracted by replica in a DP600 CR65 sample heated at 3 °C/s up to 710 °C and gas quenched (He). The extracted particles (a) were identified either as cementite particles from pearlite islands (c) or cementite particles isolated in the matrix (b). . . . .	91
III.4 Manganese and chromium composition of 22 isolated carbides analyzed in the initial state sample (non-enriched particles in green) and 9 isolated carbides in the sample heated up to 710 °C at 3 °C/s (enriched particles in blue). OE (in red) stands for Ortho-Equilibrium. . . . .	92
III.5 Optical micrographs (Metabi etching) of DP600 CR65 samples heated at 3 °C/s up to 750 °C (a), 760 °C (b), 780 °C (c) and 800 °C (d) and quenched. The ferrite appears in white and austenite (martensite after quenching) is colored in brown. Examples of thin austenite grains, attributed to austenite forming from the dissolution of intergranular cementite particles, are identified by black arrows. Examples of elongated austenite grains, identified as previous pearlite islands, are indicated by red arrows. . . . .	94
III.6 Austenite fraction during heating at 3 °C/s of a DP600 CR65 sample. The fraction of austenite in elongated bands ( $f_{\gamma}^P$ ) is plotted with red filled diamonds. The fraction of austenite in thin inter-granular films ( $f_{\gamma}^{CP}$ ) is plotted with black open diamonds. The total austenite fraction evaluated from optical micrographs by image analysis is plotted with blue open diamonds. . . . .	95
III.7 Carbon content maps obtained by WDS on DP600 CR65 samples heated at 3 °C/s up to 760 °C (a) and 780 °C (b) and gas quenched (He). . . . .	96
III.8 Mean carbon contents obtained from WDS measurements in austenite in elongated bands (red filled diamonds) or in thin intergranular films (black open diamonds) on DP600 CR65 samples heated at 3 °C/s up to 760 °C and 780 °C and gas quenched (He). . . . .	97
III.9 Partial diffraction patterns at 625 °C (a, b), 700 °C (c, d), 750 °C (e, f), 775 °C (g, h) and 800 °C (i, j) during the heating stage at 3 °C/s (a, c, e, g, i) and 30 °C/s (b, d, f, h, j) of the DP600 CR65. The diffracting phase and planes are indicated on the corresponding diffraction ring. Arrows indicate diffraction spots on diffraction rings. . . . .	98
III.10 1D diffractogram at 625 °C (blue) and 780 °C (red) during the annealing of a DP600 CR65 sample at low heating rate (3 °C/s). Arrows indicate cementite diffraction peaks. No cementite diffraction peak is observed at 780 °C. . . . .	99
III.11 Number of diffraction spots tracked during the heating stage of the intercritical annealing of the DP600 CR65 at 3 °C/s (blue) and 30 °C/s (green). . . . .	100
III.12 Recrystallization (a) and austenite formation (b and c) kinetics during the intercritical annealing of the DP600 CR65 at 3 °C/s (blue) and 30 °C/s (green) followed by HEXRD (IDST and Rietveld post-processes respectively). Fractions are plotted during the heating (a and b) and isothermal holding (c) stages. . . . .	101

III.13	Optical micrographs of the microstructure of a DP600 CR65 at 800 °C at the end of heating stage after slow (a) and fast heating (b). . . . .	102
III.14	Schematic representation of austenite formation mechanisms during slow heating (3 °C/s, reference scenario) . . . . .	104
III.15	Distribution of PNTT associated with the distribution of manganese and chromium composition of isolated carbides presented in Figure III.4. The distribution in green corresponds to the non-enriched particles in the as-cold-rolled sample. The distribution in blue corresponds to the enriched particles in the sample heated up to 710 °C at 3 °C/s. . . . .	107
III.16	Austenite fractions at Ortho-Equilibrium (OE), in dotted lines, and theoretical Local Equilibrium with Negligible Partitioning (LENP), in dashed lines, considering the measured nominal composition of the DP600 (blue diamonds), the DP600Nb15 (blue triangles) and the DP600Nb30 (inverted blue triangles). . . . .	113
III.17	SEM micrographs of the microstructures of the DP600Nb15 CR65 (a) and the DP600Nb30 CR65 (b) in the cold-rolled state. Cementite particles (either in pearlite or in the matrix) are in white contrast and ferrite in dark contrast. . . . .	115
III.18	Optical micrographs of the microstructures of the DP600Nb15 CR65 (a) and the DP600Nb30 CR65 (b) at 800 °C. Martensite (austenite before quenching) in colored in brown by the etchant and ferrite stays in white. . . . .	117
III.19	Recrystallization and austenite formation during the intercritical annealing of the DP600 CR65 (diamonds), the DP600Nb15 CR65 (triangles) and the DP600Nb30 CR65 (inverted triangles) followed by HEXRD. Number of diffraction spots tracked during the heating stage (a). Austenite weight fraction during the heating (b) and isothermal holding (c) stages. . . . .	118
III.20	Gap between the austenite fraction estimated from HEXRD experiment and the OE during the isothermal holding of the DP600 CR65 (diamonds), the DP600Nb15 CR65 (triangles) and the DP600Nb30 CR65 (inverted triangles). . . . .	119
III.21	SEM micrographs of the microstructures of the DP600 CR45 (a), the DP600 CR60 (b) and the DP600 CR65 (c) in the cold-rolled state. Cementite particles (either in pearlite or in the matrix) are in white contrast and ferrite in dark contrast. . . . .	120
III.22	Optical micrographs of the microstructures of the DP600 CR30 (a) and the DP600 CR60 (b) at 800 °C. Martensite (austenite before quenching) in colored in brown by the etchant and ferrite stays in white. Martensite is either in large islands, indicated by red arrows, or in thin films at ferrite grain boundaries, indicated by black arrows. . . . .	121
III.23	Partial diffraction patterns at 760 °C of the DP600 CR30 (a), the DP600 CR45 (b), the DP600 CR60 (c) and the DP600 CR65 (d) during the heating stage (3 °C/s). The diffracting phase and planes are indicated on the corresponding diffraction rings. Arrows highlight few diffraction spots on diffraction rings. . . . .	123
III.24	Number of diffraction spots tracked during the heating stage (3 °C/s) of the intercritical annealing of the DP600 CR30 (opened blue squares), the DP600 CR45 (open blue diamonds), the DP600 CR60 (filled blue squares) and the DP600 CR65 (filled blue diamonds). . . . .	124
III.25	Recrystallization (a) and austenite formation (b and c) kinetics during the intercritical annealing of the DP600 CR30 (opened blue squares), the DP600 CR45 (open blue diamonds), the DP600 CR60 (filled blue squares) and the DP600 CR65 (filled blue diamonds) followed by HEXRD. Fractions are plotted during the heating stage at 3 °C/s (a and b) and isothermal holding stage (c). . . . .	125

III.26	Schema of the temperature domain overlap between ferrite recrystallization and austenite formation during the heating stage at 3 °C/s. . . . .	126
III.27	Mechanisms driving the austenite formation kinetics during the intercritical annealing. (a) During the heating stage, the austenite formation kinetics is mainly driven by thermodynamics. (b) During the isothermal holding stage, the austenite formation kinetics is also driven by thermodynamics but is sensitive in first order by the diffusion distances in the microstructure. These distances depend on the previous heating stage, the nominal composition and the cold-rolling ratio. . . . .	131
IV.1	Simulation cell for austenite ( $\gamma$ ) planar growth in ferrite ( $\alpha$ ) during annealing at 800 °C for 10 min using a low heating rate (3 °C/s). . . . .	138
IV.2	Austenite fractions during the slow (3 °C/s) heating stage (a) and the isothermal holding at 800 °C (b) in the ternary Fe-0.1C-1.9Mn (black) and the quinary Fe-0.1C-1.9Mn-0.2Si-0.2Cr (red). . . . .	139
IV.3	Operative tie-lines in pseudo-ternary phase diagram Fe-C-Mn (a), Fe-C-Si (b) and Fe-C-Cr (c) and carbon profiles (d) during the heating stage at 760 °C (green), 780 °C (yellow) and 800 °C (orange) computed in the quinary Fe-0.1C-1.9Mn-0.2Si-0.2Cr. In (a, b and c), the phase diagram boundaries are plotted with dashed lines. The nominal substitutional composition is indicated by a black dotted line. In (d), the position of the interface is indicated by dashed lines. . . . .	140
IV.4	Operative tie-lines in pseudo-ternary phase diagram Fe-C-Mn (a), Fe-C-Si (b) and Fe-C-Cr (c) and carbon profiles (d) during the heating stage at 760 °C/s (green), 780 °C (yellow) and 800 °C (orange) computed in the quinary Fe-0.1C-1.9Mn-0.2Si-0.2Cr. In (a, b and c), the phase diagram boundaries are plotted with dashed lines. The nominal substitutional composition is indicated by a black dotted line. In (d), the position of the interface is indicated by dashed lines. . . . .	141
IV.5	Austenite fractions during the heating stage at 3 °C/s (a) and the isothermal holding at 800 °C (b). The austenite fractions predicted in this work, using the quinary system Fe-0.1C-1.9Mn-0.2Si-0.2Cr (in red solid line), is compared with the fraction predicted in the previous numerical work from Moreno et al. [Mor19; Tei+21] (in blue solid line), using the simplified ternary Fe-0.1C-1.9Mn, and the experimental data (in blue diamonds), from the HEXRD experiments from Chapter III (Figure III.12). The LENP and OE fractions of the simplified ternary (in black) and the quinary system Fe-0.1C-1.9Mn-0.2Si-0.2Cr (in red) are indicated by dashed and dotted lines respectively. . . . .	144
IV.6	Schema of a typical simulation cell in our generalized Wycliffe's model. . . . .	146
IV.7	Profile of $\gamma$ -stabilizers (a, c) (manganese and chromium) and the $\alpha$ -stabilizer (b, d) (silicon) before (a, b) and after (c, d) soft-impingement. . . . .	147
IV.8	Austenite fraction during isothermal holding. The fractions computed with the Generalized Wycliffe's Model (GWM in solid lines) are compared to the ones computed with DICTRA simulations (in dotted lines). The reliability of the GWM regarding the increment time (a), the cell size (b), the holding temperature (c) and the nominal composition of the steel (d) is tested. . . . .	150
IV.9	Carbon (a), manganese (b), silicon (c) and chromium (d) profiles after 100 s at 800 °C, computed with our model (red) and with DICTRA (black). . . . .	152

IV.10	Austenite fraction during an isothermal holding at 800 °C in the studied DP600 computed with our GWM using cell sizes $D$ between 0.5 $\mu\text{m}$ and 25 $\mu\text{m}$ with a step of 0.5 $\mu\text{m}$ . The OE fraction is indicated by a black dotted line. . . . .	154
IV.11	Austenite fraction during the isothermal holding at 800 °C after slow (3 °C/s in blue) or fast (30 °C/s in green) heating of our DP600 computed with our GWM (solid lines) compared with experimental data (filled diamonds) obtained from HEXRD experiments (Figure III.12). . . . .	155
A.1	IPF maps (a, c, e) and GOS maps (b, d, f) (magnification $\times 300$ ) of the Mn05 CR65 steel after 0 s (a and b), 15 s (c and d) and 50 s (e and f) at 650 °C. (b), (d) and (f) highlight grains with a GOS lower than 3 °. . . . .	180
A.2	IPF maps (a, c, e, g) and GOS maps (b, d, f, h) (magnification $\times 300$ ) of the Mn20 CR65 steel after 0 s (a and b), 25 s (c and d), 300 s (e and f) and 400 s (g and h) at 650 °C. (b), (d), (f) and (h) highlight grains with a GOS lower than 3 °. . . . .	181
B.1	Austenite formation kinetics during the intercritical annealing of the DP600 CR65 at 3 °C/s (blue) and 30 °C/s (green), during the heating (a) and isothermal holding (b) stages, followed by HEXRD (Rietveld post-treatments respectively). The experiments were performed in 2016 (in squares) and in 2022 (in diamonds) on the PETRA III – P07 synchrotron beamline at DESY facilities. . . . .	183
C.1	Diagram of the approach to predict the austenite formation kinetics along the heating stage. . . . .	185
C.2	Austenite fractions computed with the approach proposed in the present work (in red) and with DICTRA during slow heating at 3 °C/s (in black). The theoretical LENP and OE fractions are plotted with a dashed line and a dotted line respectively considering the simplified ternary composition Fe-0.045C-1.9Mn (%wt) of the subsystem CP&M. . . . .	188
C.3	Austenite fractions predicted with our approach accounting for the distribution of compositions of the isolated cementite particles, enriched (blue) along slow heating or not (green), presented in Chapter III (III.1.2.2). The predicted fractions are compared to the austenite fraction obtained by optical micrography (black open diamonds). The theoretical LENP (in black dashed line) and OE (in black dotted line) fraction of the subsystem (CP&M) Fe-0.045C-1.9Mn-0.2Si-0.2Cr (wt%) are plotted as references. . . . .	189
C.4	Austenite fraction computed with the differential JMAK (in black line) formed from pearlite in the full system during the heating stage (3 °C/s). The computed fractions are compared with the experimental fractions presented in Chapter III (in red filled diamonds). . . . .	191

- C.5 Global austenite fraction during the heating stage (3 °C/s). Our prediction of the austenite fraction under 780 °C uses the approach with the subsystems (CP&M) and (P). The prediction accounts for the distribution of compositions of the isolated cementite particles, enriched (blue) during slow heating or not (green), as presented in Chapter III (Figure III.4). Above 780 °C, the global austenite fraction (in black) is supposed to follow the theoretical LENP fraction considering the full quinary composition of the studied DP600. The predicted fractions are compared to the fraction predicted by Moreno et al. [Mor19] using their DICTRA simulations and the experimental fraction obtained from the HEXRD experiments (in blue filled diamonds – Figure III.12) and from optical observations (in blue open diamonds – Figure III.6). The theoretical LENP (in black dashed line) and OE (in black dotted line) fraction of the DP600 (measured nominal composition – Table III.1) are plotted as references. 193

---

# List of Tables

---

II.1	Chemical composition of the five studied steels in weight percent (wt%) . . . . .	60
III.1	Aimed and measured nominal composition (wt%) of the studied DP600 steel. . . . .	89
III.2	Typical mean sizes in the microstructure at the end of the heating stage of the studied DP600 depending on the heating rate. . . . .	103
III.3	Aimed and measured nominal composition (wt%) of the studied steels. Values for the DP600 have already been disclosed in Table III.1. . . . .	113
III.4	Typical mean sizes in the initial microstructures of the studied steels. . . . .	116
III.5	Typical mean sizes in the microstructures of the studied steels at the end of a heating stage at 3 °C/s. . . . .	116
III.6	Typical mean sizes in the initial microstructures of the studied DP600 depending of the cold-rolling ratio. . . . .	121
III.7	Typical mean sizes in the microstructures of the studied DP600 at the end of a heating stage at 3 °C/s depending on the cold-rolling ratio. . . . .	122
IV.1	Austenite fraction at OE at 800 °C of the studied DP600 (Fe-0.1C-1.9Mn-0.2Si-0.2Cr) using the simplified ternary Fe-0.1C-1.9Mn, the quaternary Fe-0.1C-1.9Mn-0.2Si, the quaternary Fe-0.1C-1.9Mn-0.2Cr and the full quinary Fe-0.1C-1.9Mn-0.2Si-0.2Cr . . . . .	137
IV.2	Simulation parameters for each system (compositions in (at%)) . . . . .	139
IV.3	Theoretical LEMP fraction and carbon content in austenite and ferrite, computed with Thermo-Calc at 800 °C . . . . .	153
IV.4	Cell size and initial position of the interface for simulation of austenite growth after slow (3 °C/s) and fast (30 °C/s) heating. . . . .	154

---

# Résumé étendu en français

---

## Introduction

Les aciers Dual-Phase (DP) sont des aciers AHSS (Advanced High Strength Steels) de première génération, industrialisés depuis les années 90 et largement utilisés dans l'industrie automobile. Leur résistance mécanique en traction est entre 600 et 1000 MPa. Leur formabilité les rend idéaux pour les opérations de mise en forme (emboutissage, étirage, cintrage) des pièces de structure (Body-In-White), même si leur ductilité peut parfois être limitée.

Grâce au compromis entre résistance et formabilité, la fabrication de pièces de sécurité automobile de forme complexe est relativement peu coûteuse. En outre, l'épaisseur des tôles peut être réduite tout en conservant des propriétés mécaniques intéressantes. Cela permet de fabriquer des pièces de sécurité automobile plus légères, ce qui contribue à répondre aux exigences en matière de consommation d'énergie et de réduction des émissions CO<sub>2</sub> [Age+19]. Pour ces raisons, les aciers DP sont aujourd'hui des aciers standard et restent extrêmement importants pour les sidérurgistes et les constructeurs automobiles, malgré le développement des AHSS de deuxième et de troisième génération. Les aciers DP représentent une grande partie de la production mondiale d'acier et sont produits dans différentes usines. La modélisation est essentielle pour obtenir des propriétés mécaniques cohérentes dans tous ces sites de production.

Une microstructure d'acier DP contient typiquement une matrice ferritique ductile ( $\alpha$ ) avec des grains polygonaux durcis par des îlots martensitiques dispersés ( $\alpha'$ ). Elle contient éventuellement de la bainite. Les propriétés mécaniques des aciers DP sont déterminées par la fraction des phases (de 5 % à 100 % de martensite) et leur morphologie [All+15; Pus+15; Sco+17].

Cette microstructure est obtenue par un procédé de fabrication conventionnel pour les produits plats, représenté dans la Figure 1. Après la coulée continue, les brames sont réchauffées pour atteindre le domaine austénitique, au-dessus de Ac3 (généralement au-dessus de 900 °C) et maintenues pour une austénitisation complète de la brame. Le laminage à chaud réduit leur épaisseur, généralement jusqu'à 3 mm. Après cette opération, la microstructure contient des grains d'austénite équiaxes grâce à la recristallisation dynamique (Figure 1 b 1). Sous Ar3, la ferrite germe et croît, conduisant à un mélange d'austénite et de ferrite (Figure 1 b 2). En utilisant une vitesse de refroidissement lente (généralement inférieure à 100 °C/s), un mélange ferrite-perlite se forme (Figure 1 b 3). Vers 550 °C, la tôle d'acier est bobinée et refroidie à l'air jusqu'à la température ambiante. Les tôles d'acier sont ensuite laminées à froid jusqu'à l'épaisseur finale. Ce processus de déformation plastique sévère déforme fortement la microstructure, ce qui donne des formes allongées, alignées sur la direction du laminage à froid [BVS22;

Bel+19; Chb+14; HPM04; Li+13; MGF11; Tei+21; TM18] (Figure 1 b 4). Ensuite, les tôles d'acier subissent un recuit intercritique. Cette étape consiste à réchauffer et à maintenir les tôles d'acier dans la plage de température intercritique (dans le domaine  $\gamma + \alpha$  du diagramme de phase dans Figure 1 a). La tôle d'acier subit une austénitisation partielle (Figure 1 b 5). Au cours de la phase de refroidissement suivante, la ferrite croît mais la formation de perlite est empêchée et l'austénite se transforme en phase de trempe comme la bainite ou la martensite par des transformations displacives (Figure 1 b 6).

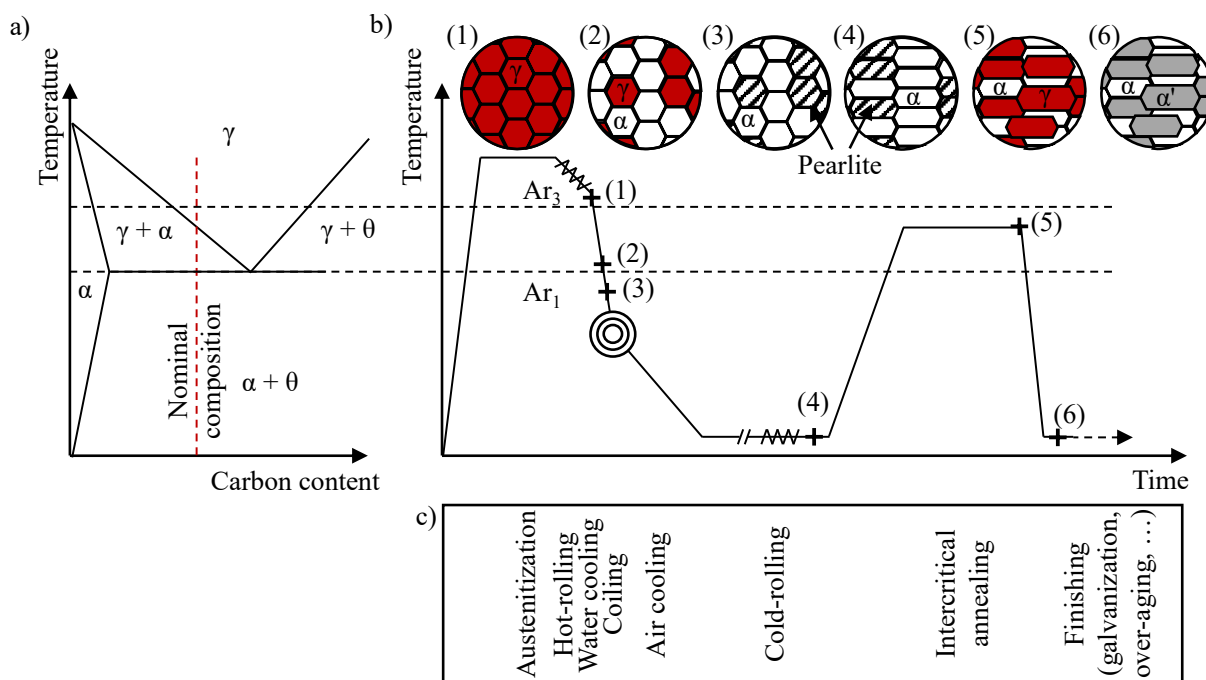


Figure 1: Représentation schématique d'un diagramme de phase binaire Fe-C (a) et du cycle thermo-mécanique industriel de production d'acier DP (b). La succession des étapes est décrite en (c). L'évolution de la microstructure est schématisée en (b) de (1) à (6).

La fraction finale des phases et leur morphologie, et par suite les propriétés mécaniques finales, sont héritées de la microstructure intermédiaire austénite-ferrite formée lors du recuit intercritique [All+15; Pus+15; Sco+17]. La fraction et la morphologie de l'austénite à la fin du maintien sont très sensibles aux paramètres de recuit, tels que la température de maintien ou la vitesse de chauffe. Les faibles vitesses de chauffe ( $\approx 1 \text{ }^\circ\text{C/s}$ ) produisent des microstructures en "collier". Au contraire, les microstructures en "bandes" sont obtenues en utilisant des vitesses de chauffe élevées ( $> 50 \text{ }^\circ\text{C/s}$ ). La vitesse de chauffe n'affecte pas seulement la morphologie mais aussi la cinétique de formation de l'austénite et la fraction finale d'austénite. Une vitesse de chauffe plus élevée entraîne une cinétique de formation d'austénite plus rapide et une fraction d'austénite finale plus élevée. Ce dernier fait expérimental est difficilement expliqué dans la littérature, comme montré dans le Chapitre I. L'objectif principal de ce travail est d'apporter de nouveaux éléments pour le comprendre.

Pendant le recuit intercritique, de nombreux phénomènes métallurgiques se produisent et peuvent interagir entre eux. La matrice ferritique déformée subit une restauration [Cou+21; HH95; Nes95] et une recristallisation [Chb+14; HH95; Li+13] au cours de la chauffe. Les lamelles

de cémentite de la perlite, fragmentées par le laminage à froid, se sphéroïdisent [Lai+16; Mor19; TK87]. La cémentite peut s'enrichir en éléments d'alliage [Mor19]. À plus haute température, la cémentite se dissout et l'austénite germe et croît. Au cours de ces transformations de phase, les éléments d'alliage peuvent se redistribuer dans les différentes phases [Cou+23; Lai+16; Mor19; SDM81; Tei+21].

La présente thèse s'inscrit dans le cadre d'un partenariat à long terme entre l'Institut Jean Lamour (équipe Microstructures et Contraintes) et ArcelorMittal Maizières Research. Elle fait suite à la thèse de Moreno [Mor19] et est financée par ArcelorMittal Maizières Research et l'ANRT (Agence Nationale de la Recherche et de la Technologie) dans le cadre de la convention CIFRE (2020/1022). Elle se concentre principalement sur la formation d'austénite pendant le recuit intercritique et ses interactions possibles avec la recristallisation de la matrice de ferrite. Une nouvelle méthode utilisant la Diffraction des Rayons X de Haute Energie (DRXHE) est développée pour étudier la recristallisation. Grâce à cette méthode, la recristallisation de la ferrite et la formation de l'austénite peuvent être suivies simultanément lors d'une même expérience avec une haute résolution temporelle pendant un traitement de recuit intercritique. Cette méthode et d'autres méthodes de caractérisation plus conventionnelles sont utilisées pour étudier la formation de l'austénite et ses interactions avec la recristallisation de la ferrite. Les conclusions de l'état de l'art sur l'effet de la vitesse de chauffe et la manière dont elle contrôle la cinétique de formation et la morphogenèse de l'austénite sont revisitées d'un point de vue expérimental. L'objectif final de cette thèse est de proposer un modèle pour la cinétique de formation de l'austénite dans des systèmes quinaires pendant le recuit intercritique des aciers DP.

## Chapitre I

Le Chapitre I propose une revue de la littérature sur les mécanismes métallurgiques survenant pendant le recuit intercritique pour la production d'aciers DP. Elle se concentre principalement sur la restauration et la recristallisation de la ferrite, ainsi que sur la formation d'austénite. Leurs mécanismes et interactions sont détaillés. Elle fournit également des notions utiles d'analyse thermodynamique et thermocinétique de la formation de l'austénite. L'état actuel des connaissances sur l'effet de la vitesse de chauffe sur la cinétique de formation et la morphologie de l'austénite est présenté et discuté. Ce chapitre aborde enfin les options de modélisation de la formation de l'austénite pendant le recuit intercritique. Voici les principales conclusions de cette revue de la littérature.

La restauration et la recristallisation sont des phénomènes étroitement liés puisqu'ils sont en concurrence pour la même force motrice. De plus, la théorie SIBM (Strain Induced Boundary Migration) attribue la "germination" de la recristallisation à la restauration. La caractérisation expérimentale de la restauration et de la recristallisation utilise souvent les mêmes méthodes et il peut être difficile de décorrélérer leurs effets. Cette thèse vise à améliorer et à valider la nouvelle technique, résolue en temps, de suivi de la recristallisation proposée dans les travaux récents de Moreno et al. [Mor+18]. La méthode développée, détaillée dans le Chapitre II, utilise des expériences DRXHE in situ et ne nécessite pas d'expériences post-mortem interrompues.

Pendant l'étape de chauffe du recuit intercritique, la recristallisation de la ferrite interagit avec la formation d'austénite. L'étude de ces interactions est complexe, car elle implique la diffusion du carbone, la distribution spatiale des sources de carbone et la germination de l'austénite, qui s'influencent mutuellement. La littérature montre largement que la concomitance de la re-

cristallisation de la ferrite et de la formation de l'austénite affecte fortement la morphologie finale de la microstructure. La recristallisation affecte la distribution spatiale des sites de germination de l'austénite, tels que les particules de cémentite inter-granulaires.

D'un point de vue cinétique, une vitesse de chauffe plus élevée conduit à une fraction finale d'austénite plus importante et aucun consensus clair n'explique cette observation. Les discussions dans la littérature concernent principalement la diffusion du carbone et la manière dont la recristallisation peut affecter son efficacité. Cependant, certains auteurs affirment que la formation de l'austénite est contrôlée par la diffusion d'éléments substitutionnels, comme le manganèse, plutôt que par celle du carbone. Moreno et al. [Mor19; Tei+21] affirment que la cinétique de dissolution des particules de cémentite inter-granulaires est responsable de l'effet observé.

Les simulations DICTRA sont identifiées comme des outils numériques pertinents pour mieux comprendre la thermocinétique de la formation de l'austénite et l'interaction entre les éléments substitutionnels. Le Chapitre I présente plusieurs conclusions de l'analyse thermocinétique de la formation de l'austénite. En particulier, il détaille l'analyse thermocinétique de Moreno et al. [Mor19], considérant deux sous-systèmes fermés, l'un contenant les îlots de perlite, l'autre les particules de cémentite. Cette approche intéressante reproduit le dépassement de la fraction Ortho-Equilibrium (OE) observé expérimentalement, mais elle souffre de plusieurs limitations. En particulier, l'hypothèse de sous-systèmes fermés est probablement trop forte, car notre récente étude numérique [Cou+23] montre des interactions entre les îlots d'austénite par diffusion du carbone dans la matrice de ferrite.

Enfin, le modèle proposé par Wycliffe et al. [WPE81] s'est avéré être un modèle efficace pour la cinétique de formation de l'austénite, en termes de temps de calcul, grâce aux profils de composition simplifiés. Ce modèle est étendu aux systèmes quinaires dans le Chapitre IV.

## Chapitre II

Le Chapitre II présente les aciers étudiés ainsi que les méthodes expérimentales et de simulation mises en œuvre pour étudier les mécanismes métallurgiques (recristallisation, dissolution de la cémentite et formation d'austénite) se produisant pendant le recuit intercritique.

Nos expériences consistent principalement en des simulations de recuit industriel dans un dilatomètre. La formation de l'austénite est étudiée au cours de traitements thermiques à partir de différents états initiaux, soit *in situ*, soit *post mortem* (après des traitements interrompus).

Pendant les simulations de recuit, les traitements sont interrompus à des températures stratégiques pour observer la microstructure, en utilisant la microscopie optique et la microscopie électronique à balayage (MEB) en mode imagerie en électrons secondaires. La recristallisation est suivie par diffraction d'électrons rétrodiffusés (EBSD) et par des mesures de microdureté Vickers. Des techniques avancées d'analyse chimique locale ont été utilisées pour étayer les discussions dans le Chapitre IV. La teneur en carbone des îlots d'austénite est cartographiée par spectrométrie de rayons X à dispersion de longueur d'onde (WDS) et la composition chimique des particules de cémentite est mesurée par spectroscopie à rayons X à dispersion d'énergie (EDXS).

Des expériences de DRXHE *in situ* ont été réalisées sur la ligne synchrotron P07 sur PETRA III à DESY à Hambourg. Ces expériences *in situ* visaient tout d'abord à obtenir la cinétique de formation de l'austénite pendant le traitement de recuit. Une analyse minutieuse des données recueillies nous a permis de développer une nouvelle méthode utilisant la DRXHE pour étudier

la recristallisation. La méthode est détaillée et discutée. Grâce à cette méthode, nous suivons simultanément la recristallisation de la ferrite et la formation de l'austénite in situ lors d'une même expérience avec une haute résolution temporelle. Notre méthode permet d'étudier leurs interactions éventuelles pendant le recuit dans le Chapitre III.

Ce chapitre détaille également les outils de calcul commerciaux pour la simulation de la transformation de phase et les bases de données thermodynamiques utilisées pour modéliser la dissolution de la cémentite et la formation de l'austénite pendant les traitements thermiques. Le logiciel Thermo-Calc et son module DICTRA sont brièvement présentés, tandis que les configurations complètes des simulations effectuées sont détaillées dans le Chapitre IV.

## Chapitre III

Le Chapitre III remet en question les conclusions du Chapitre I sur les interactions entre la recristallisation de la ferrite et la formation de l'austénite sur une base expérimentale.

### Effet de la vitesse de chauffe sur la transformation de l'austénite

La cinétique de recristallisation primaire est estimée à l'aide de la méthode IDST (Isolated Diffraction Spot Tracking), présentée dans le Chapitre II. Les cinétiques de recristallisation de la ferrite lors des chauffes à 3 °C/s (bleu) et à 30 °C/s (vert) sont représentées dans la Figure 2 (a). Le début de la recristallisation de la ferrite est retardé de 65 °C en raison de la chauffe rapide. Lors d'une chauffe lente, la recristallisation de la ferrite est terminée lorsque la formation de l'austénite commence à 725 °C (Figure 2 a et b). Au contraire, la recristallisation de la ferrite et la formation de l'austénite se chevauchent lors de la chauffe rapide.

Les Figures 2 (b) et (c) montrent la fraction massique d'austénite estimée par affinement Rietveld à partir d'expériences DRXHE in situ pendant les étapes de chauffe et de maintien isotherme respectivement. Les fractions d'austénite sont comparées aux fractions Local Equilibrium with Negligible Partitioning (LENP) et OE théoriques attendues, calculées avec Thermo-Calc en utilisant la composition nominale complète des aciers étudiés. Nous observons l'influence attendue de la vitesse de chauffe sur le début de la formation de l'austénite. La transformation est retardée de 720 °C, lors d'une chauffe lente (3 °C/s en bleu), à 740 °C, lors d'une chauffe rapide (30 °C/s en vert), comme déjà observé dans [Mor19; Tei+21]. Jusqu'à 750 °C, la cinétique de formation de l'austénite dépend de la vitesse de chauffe. La Figure 2 (b) montre qu'au delà de 750 °C, les fractions d'austénite suivent les fractions LENP théoriques, quelle que soit la vitesse de chauffe. Cette observation nous amène à penser que l'austénite croît en mode LENP après un transfert de carbone, comme cela a déjà été proposé dans [Chb+14; Mor19; Tei+21].

Ce travail expérimental conduit aux conclusions suivantes :

- L'austénite croît à partir de deux sources principales de carbone : les îlots de perlite et les particules de cémentite isolées. Lors d'une chauffe lente (3 °C/s), sous 760 °C, la croissance de l'austénite peut être étudiée en considérant deux sous-systèmes fermés, l'un contenant la perlite et l'autre la matrice de ferrite avec les particules de cémentite isolées, comme proposé dans [Mor19; Tei+21]. Entre 760 °C et 780 °C, nos expériences ont révélé un transfert de carbone entre lesdits sous-systèmes. De fait, leur étude séparée n'est plus pertinente. Contrairement à [Mor19; Tei+21], la croissance de l'austénite après 780 °C est étudiée dans un système thermodynamique unique. Au cours de la chauffe, au-dessus

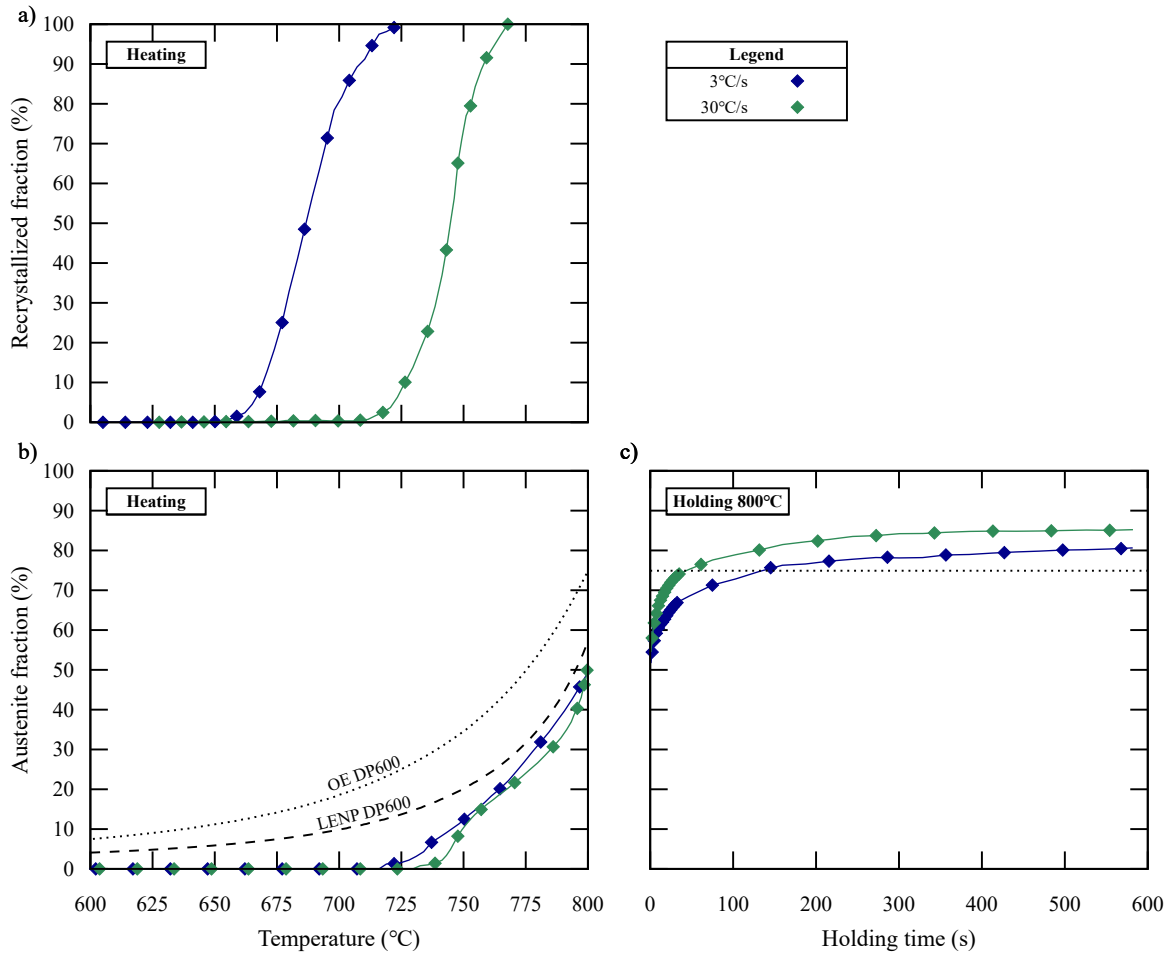


Figure 2: Cinétique de recrystallisation (a) et de formation d'austénite (b et c) pendant le recuit intercritique du DP600 CR65 à 3 °C/s (bleu) et 30 °C/s (vert) suivi par DRXHE (méthode IDST et analyse Rietveld respectivement). Les fractions sont représentées pendant les étapes de chauffe (a et b) et de maintien isotherme (c).

de 750 °C, nos données expérimentales soutiennent une croissance de l'austénite en mode LENP, quelle que soit la vitesse de chauffe.

- Les particules de cémentite isolées subissent un enrichissement en manganèse et en chrome au cours d'un chauffage lent (3 °C/s). Plus la teneur en manganèse ou en chrome est élevée, plus la température de transition partition-non partition (Partition to Non-partition Transition Temperature (PNTT)) associée est élevée. En particulier, le chrome augmente fortement la PNTT malgré sa faible teneur dans l'acier étudié. Une distribution de composition chimique des particules de cémentite donne une distribution de PNTT. Cependant, notre discussion montre que les faibles vitesses de chauffe favorisent l'enrichissement des particules et augmente leur PNTT, ce qui est en contradiction avec le retard du début de transformation de l'austénite avec des vitesses de chauffe plus élevées, observé expérimentalement.

- Nos expériences ont reproduit l'effet de la vitesse de chauffe sur la morphologie de l'austénite. La faible vitesse de chauffe a produit une morphologie en "collier", tandis que la vitesse de chauffe élevée a produit une morphologie en "bandes". à ce stade, aucune de nos observations ne contredit ou ne valide les mécanismes exposés dans le Chapitre I.
- Pendant le maintien, nos expériences vont dans le sens des analyses thermocinétiques précédentes, suggérant que l'austénite croît en mode Local Equilibrium with Partitioning (LEP). Nous avons montré que plus la vitesse de chauffe est élevée, plus la fraction finale d'austénite est importante. L'explication de [Mor19; Tei+21] pour cette tendance, basée sur l'étude en sous-systèmes, est contredite par nos expériences, montrant un transfert de carbone dans l'austénite. Nous montrons également que plus la vitesse de chauffe est élevée, plus la cinétique de formation de l'austénite est rapide pendant le maintien isotherme, comme montré par la littérature. En considérant un état similaire, hérité de la croissance en mode LENP pendant l'étape de chauffe, la microstructure plus fine dans l'échantillon chauffé rapidement peut expliquer les deux tendances majeures observées pendant le maintien isotherme. Cette hypothèse est discutée plus en détail sur la base de simulations dans le Chapitre IV.

### Effet du micro-alliage et du taux de laminage à froid sur la transformation de l'austénite

Nous proposons des expériences supplémentaires pour discuter l'hypothèse soulevée dans la littérature qui explique les effets de la vitesse de chauffe par les interactions entre la recristallisation de la ferrite et la formation de l'austénite.

Dans la littérature et dans la section précédente, la concomitance de la recristallisation de la ferrite et de la formation d'austénite est due à la vitesse de chauffe. Cette section vise à aller plus loin en décorrélant la vitesse de chauffe et la concomitance de la recristallisation de la ferrite et de la formation d'austénite. En particulier, tous les traitements thermiques sont réalisés avec une vitesse de chauffe unique (3 °C/s) pour éviter un impact sur les mécanismes thermiquement activés. Le micro-alliage au niobium et des taux de laminage à froid plus faibles sont utilisés pour retarder la recristallisation de la ferrite et pour provoquer sa concomitance avec la formation d'austénite.

Comme prévu [All+20; Son+14; Ver+09], le micro-alliage au niobium inhibe complètement la recristallisation de la ferrite dans nos aciers, bien que notre vitesse de chauffe soit suffisamment lente pour permettre la recristallisation de la ferrite dans le DP600 CR65. La Figure 3 (a) représente l'écart entre la fraction d'austénite estimée à partir des expériences DRXHE et la fraction d'austénite théorique LENP pendant l'étape de chauffe du recuit intercritique des DP600 micro-alliés au niobium (0,015 wt% Nb avec des triangles et 0,030 wt% Nb avec des triangles inversés). La Figure 3 (b) représente la fraction d'austénite estimée à partir des expériences DRXHE et l'OE pendant le maintien isotherme. Celui-ci souligne que plus la teneur en niobium est élevée, plus la cinétique est rapide et plus la fraction finale dépasse la fraction OE.

Les cinétiques de recristallisation de la ferrite pendant l'étape de chauffe (3 °C/s) du DP600 CR30 (carrés bleus vides), du DP600 CR45 (diamants bleus vides), du DP600 CR60 (carrés bleus remplis) et du DP600 CR65 (diamants) sont représentées dans la Figure 4 a). Comme prévu [HH95; Rei52], des taux de laminage à froid plus faibles retardent la recristallisation de la ferrite dans notre DP600 étudié. Les Figures 4 (b) et (c) montrent la fraction massique d'austénite pendant la chauffe (3 °C/s) et le maintien isotherme (800 °C) estimée par affinement Rietveld

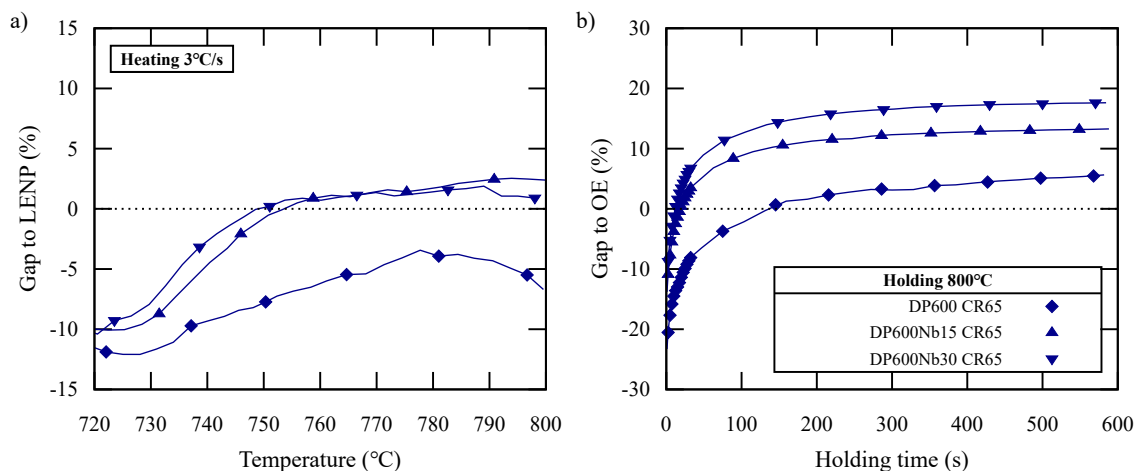


Figure 3: Écart entre la fraction d'austénite estimée à partir des expériences de DRXHE et l'OE pendant le maintien isotherme du DP600 CR65 (diamants), du DP600Nb15 CR65 (triangles) et du DP600Nb30 CR65 (triangles inversés).

à partir des expériences DRXHE in situ. En particulier, plus le taux de laminage à froid est faible, plus la cinétique de croissance de l'austénite est lente pendant le maintien.

À première vue, nous observons des effets contradictoires. L'étude utilisant des aciers micro-alliés au niobium semble lier l'absence de recristallisation de la ferrite et la cinétique de formation plus rapide de l'austénite pendant la phase de maintien. Au contraire, l'étude utilisant des taux de laminage à froid plus faibles semble lier l'interaction entre la recristallisation de la ferrite et la formation de l'austénite à une cinétique de formation de l'austénite plus lente pendant le maintien. Au-delà de la contradiction apparente, nous proposons d'expliquer ces tendances par les distances de diffusion dans les microstructures, qui dépendent de la distribution des germes d'austénite lors de la chauffe. La recristallisation elle-même n'affecte pas directement le processus (puisque'elle est souvent terminée avant le maintien).

Ces nouvelles expériences répondent à plusieurs questions. Voici nos principales conclusions :

- L'interaction entre la recristallisation de la ferrite et la formation d'austénite affecte fortement la microstructure et la morphologie de l'austénite. Dans les aciers micro-alliés au niobium, une coopération entre les particules de cémentite isolées et l'inhibition de la recristallisation de la ferrite a conduit à une microstructure allongée à la fin de la chauffe, ressemblant à des microstructures en bandes, confirmant les travaux de Teixeira et al. ([Tei+21]). Dans les aciers faiblement laminés à froid, la microstructure en fin de chauffe présentait des formes allongées attendues des morphologies en bandes. Ceci confirme que plus la recristallisation de la ferrite est tardive, plus la morphologie de l'austénite est en bandes à la fin de la chauffe. Cependant, dans ce travail, la microstructure initiale a fortement déterminé la taille de grain de la ferrite à 800°C, malgré sa recristallisation.
- La température de départ de la formation de l'austénite est insensible à l'état courant de recristallisation de la matrice de ferrite ou à la proportion d'îlots de perlite et de

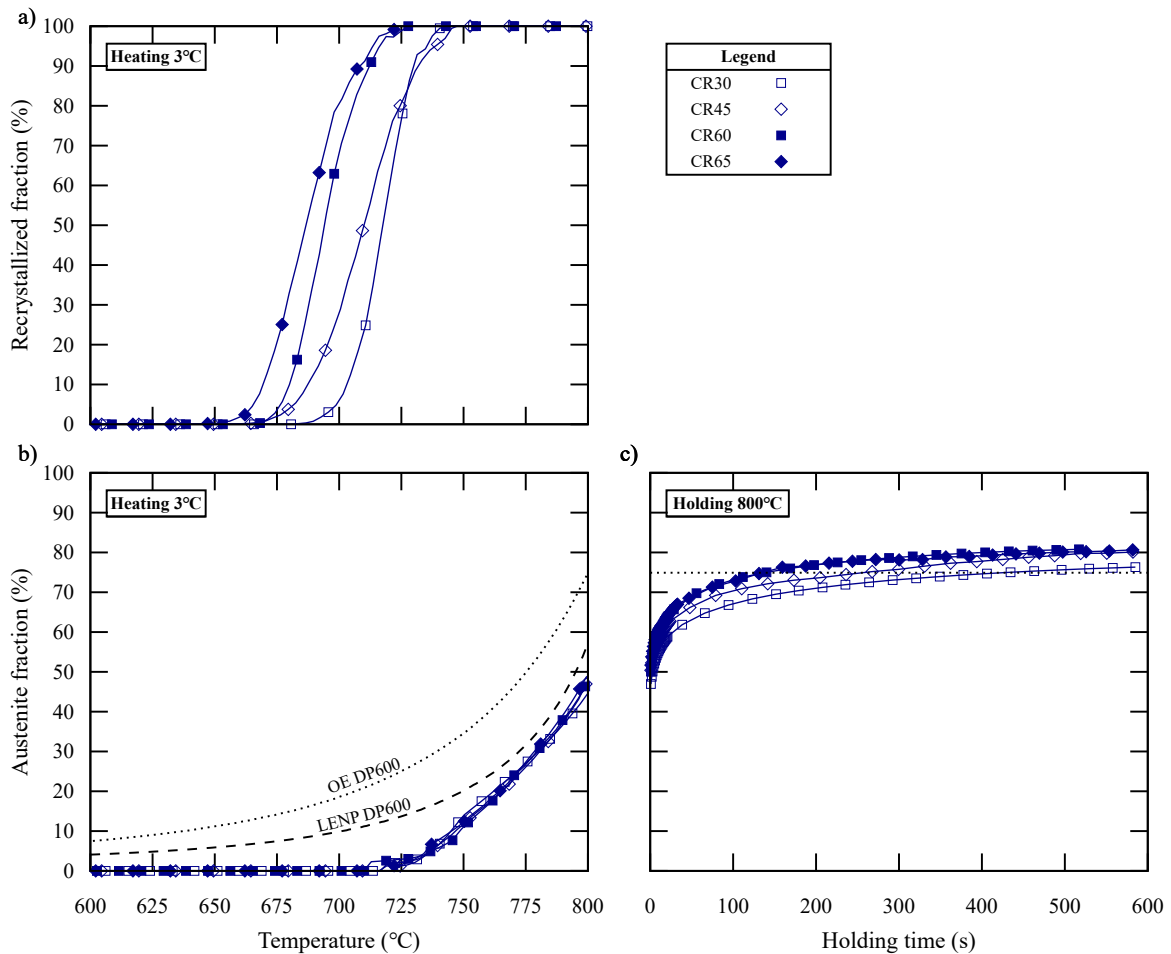


Figure 4: Cinétique de recrystallisation (a) et de formation d'austénite (b et c) pendant le recuit intercritique du DP600 CR30 (carrés bleus vides), du DP600 CR45 (diamants bleus vides), du DP600 CR60 (carrés bleus remplis) et du DP600 CR65 (diamants bleus remplis) suivi par HEXRD. Les fractions sont représentées pendant l'étape de chauffe à 3 °C/s (a et b) et l'étape de maintien isotherme (c).

particules de cémentite isolées dans la microstructure initiale. Nous attribuons le retard de germination de l'austénite lors de la chauffe rapide à l'activation thermique affectée par la vitesse de chauffe.

- Ce travail confirme que la cinétique de formation de l'austénite est contrôlée par les conditions de l'interface LEP, c'est-à-dire par la diffusion du carbone, pendant la chauffe, après le transfert de carbone. La ferrite non recrystallisée, le niobium en solution solide ou la taille de la microstructure n'ont pas d'effet significatif sur la cinétique de formation de l'austénite.
- Pendant le maintien, toutes les cinétiques de formation d'austénite obtenues ont montré des caractéristiques en faveur de la croissance de l'austénite en mode LEP, c'est-à-dire avec

une redistribution d'éléments substitutionnels. Pour les aciers micro-alliés au niobium, dans lesquels la recristallisation de la ferrite est inhibée, la cinétique de formation de l'austénite est plus rapide que dans le DP600 CR65 de référence. Au contraire, les aciers faiblement laminés à froid, dans lesquels la recristallisation de la ferrite est retardée, la cinétique de formation de l'austénite est plus lente que dans le DP600 CR65 de référence. Cette tendance surprenante s'explique par la taille de la microstructure à la fin de la chauffe. Une microstructure plus fine offre des chemins de diffusion courts pour les éléments substitutionnels, ce qui accélère la formation d'austénite en mode LEP pendant le maintien isotherme [BVS22; Bel+19; Chb+14; MGF11; Oll+17; TM18]. Nous attribuons finalement la cinétique de formation plus rapide de l'austénite pendant le maintien isotherme à la microstructure plus fine observée en fin de chauffe rapide.

## Chapitre IV

Le Chapitre IV étudie l'effet des éléments d'alliage mineurs (chrome et silicium) dans notre acier DP600, en considérant la composition nominale quinaire, sur la cinétique de croissance de l'austénite. Il complète l'analyse thermocinétique de la formation de l'austénite pendant le recuit intercritique en utilisant des simulations DICTRA. Nos nouveaux résultats du Chapitre III sont combinés à notre discussion du Chapitre I pour proposer un modèle prédisant la cinétique de formation de l'austénite et les profils de composition dans les systèmes quinaires au cours d'un maintien isotherme intercritique. Ce Chapitre apporte finalement de nouveaux résultats pour appuyer l'analyse du Chapitre III concernant l'influence des distances de diffusion sur les cinétiques au cours du maintien.

### Analyse thermo-cinétique de la croissance d'austénite dans le système quinaire Fe-0.1C-1.9Mn-0.2Si-0.2Cr

Les fractions d'austénite calculées avec DICTRA dans le quinaire Fe-0.1C-1.9Mn-0.2Si-0.2Cr (en rouge) sont représentées dans la Figure 5 lors d'une chauffe à 3 °C/s (a) et d'un maintien isotherme à 800 °C (b). Les fractions d'austénite calculées avec DICTRA dans le ternaire Fe-0.1C-1.9Mn de notre étude précédente [Cou+23] sont représentées en noir. Les fractions LENP et OE théoriques attendues sont indiquées comme références. La prise en compte des éléments substitutionnels mineurs ralentit considérablement la cinétique de formation de l'austénite.

Cette section montre également que les éléments substitutionnels, même mineurs, affectent les compositions d'équilibre local et les régimes de redistribution. Lors de la chauffe, la croissance de l'austénite se produit en mode LENP. Aucun élément substitutionnel ne se redistribue et la croissance de l'austénite est contrôlée par la diffusion du carbone dans l'austénite. Un écart entre la fraction LENP théorique (conditions d'interface LENP et absence de gradient de composition) est observé car la vitesse de chauffe est trop élevée pour que le carbone s'homogénéise dans l'austénite. Ce gradient résiduel peut expliquer l'écart entre les données expérimentales et la fraction LENP théorique observée expérimentalement dans le Chapitre III. Ce travail confirme également que l'austénite croît avec une redistribution de tous les éléments substitutionnels (mode LEP) au cours du maintien. Les temps de maintien utilisés dans ce travail sont trop courts pour observer une diffusion significative des éléments substitutionnels dans l'austénite.

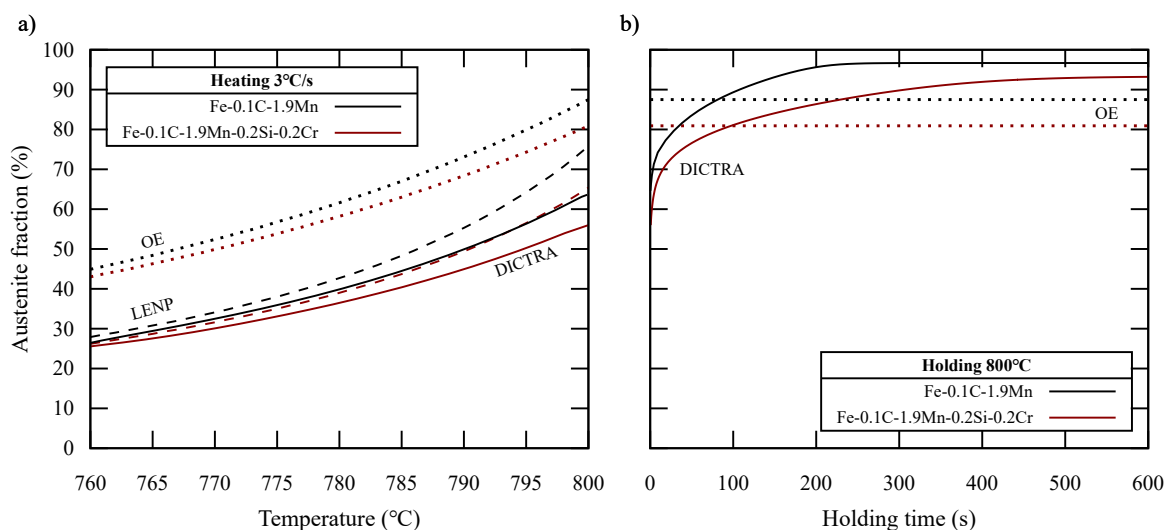


Figure 5: Fractions d'austénite lors d'une chauffe lente (3 °C/s) (a) et d'un maintien isotherme à 800 °C (b) dans le ternaire Fe-0.1C-1.9Mn (noir) et le quinaire Fe-0.1C-1.9Mn-0.2Si-0.2Cr (rouge).

### Modèle prédictif à base physique de la formation d'austénite au cours du maintien

Cette section propose un modèle, inspiré des travaux de Wycliffe [WPE81], pour la croissance de l'austénite lors du maintien isotherme, sur la base des conclusions du Chapitre III et de la section précédente. Ce modèle doit prédire la cinétique de transformation pendant le maintien ainsi que la redistribution des éléments substitutionnels (mode LEP) dans un système quinaire avec une grande stabilité numérique.

La Figure 6 montre la fraction d'austénite pendant un maintien isotherme à 800 °C après une chauffe lente (3 °C/s en bleu) ou rapide (30 °C/s en vert) dans notre DP600, calculée avec notre modèle de Wycliffe généralisé (GWM en ligne continues). Les fractions simulées sont comparées aux données expérimentales (diamants) obtenues à partir des expériences DRXHE (Figure 2). Contrairement aux travaux de Moreno et al. [Mor19; Tei+21], nos simulations reproduisent non seulement l'écart de la fraction d'austénite finale en fin de maintien en fonction de la vitesse de chauffe, mais reproduisent également la cinétique complète et les valeurs absolues des fractions avec une assez bonne précision.

Ces résultats plaident en faveur de notre hypothèse proposée dans le Chapitre III. Selon notre étude expérimentale, soutenue par la présente étude numérique, la cinétique de formation de l'austénite pendant la phase de maintien est entièrement pilotée par le mode LEP, contrôlé par la diffusion des éléments substitutionnels dans la ferrite, et l'effet de la vitesse de chauffe pendant le maintien isotherme provient de la microstructure plus fine à la fin de la phase de chauffe en utilisant une vitesse de chauffe plus rapide.

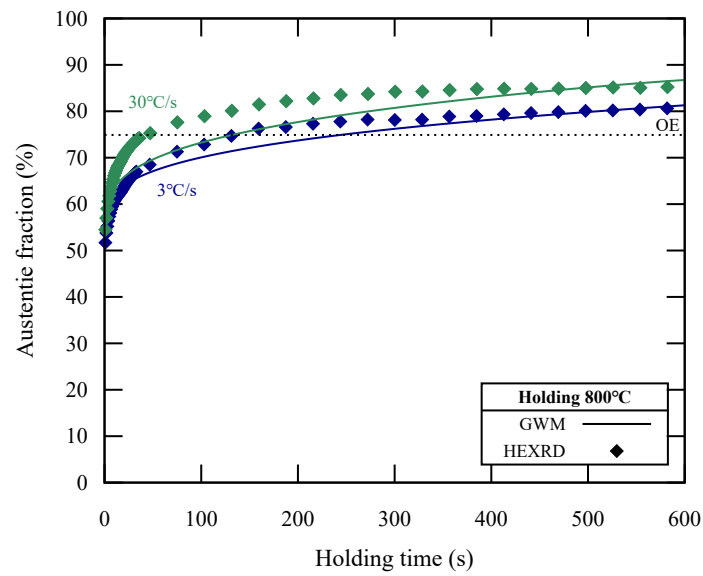


Figure 6: Fraction d'austénite pendant le maintien isotherme à 800 °C après une chauffe lente (3 °C/s en bleu) ou rapide (30 °C/s en vert) de notre DP600 calculé avec notre GWM (lignes continues) comparée aux données expérimentales (diamants) obtenues à partir d'expériences DRXHE (Figure 2).

---

# Introduction

---

Aux premières heures du jour  
tout est possible  
Si l'on veut reprendre dès le  
début, redéfinir la règle du jeu  
Briser les chaînes, fissurer la dalle  
Inventer la lune, que tous la  
voient

---

*Tôt le matin*  
*Gaël Faye*

## Dual Phase steels

Dual-Phase (DP) steels are first generation Advanced High Strength Steels (AHSS) (Figure 7 a), industrialized since the 90's and widely used in the automotive industry. The Ultimate Tensile Strength (UTS) of DP steels can be tuned between 600 and 1000 MPa. Their formability (in the sense of the forming limit diagram) makes them ideal for forming operations (stamping, drawing, bending, ...) of the Body-In-White (BIW) parts (Figure 7 b), even if their ductility (hole expansion performance) can sometimes be limited.

Thanks to their balance between strength and formability, manufacturing complex shaped automotive security parts is relatively low-cost. Additionally, the thickness of the sheets can be reduced, while keeping interesting mechanical properties. This allows the fabrication of lighter automotive BIW, helping meet the energy consumption and CO<sub>2</sub> emission reduction requirements [Age+19]. For these reasons, DP steels are standard steels nowadays and still extremely relevant for steel- and car-makers, despite the development of second (austenitic Twinning Induced Plasticity steels) and third generation AHSS. These steels represent a large part of global steel production and are produced in different factories. Modeling is key to achieving consistent mechanical properties across these production sites.

A typical microstructure of DP steels (Figure 8 a) mainly consists of a ductile ferritic ( $\alpha$ ) matrix with polygonal grains hardened by dispersed martensitic islands ( $\alpha'$ ) and possibly bainite to adjust the compromise between formability and ductility. The mechanical properties of DP steels are determined by the fraction of the phase and the morphology of their final heterogeneous microstructures [All+15; Pus+15; Sco+17]. Figure 8 (b) maps the Ultimate Tensile Strength

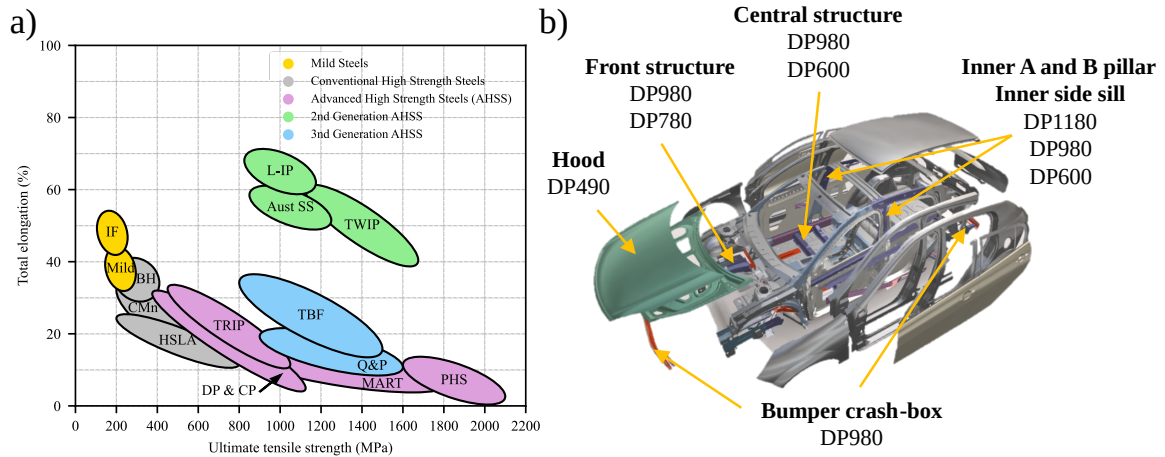


Figure 7: (a) Classification of steel families as a function of their total elongation and their UTS [Kwo+10; Mat+12; Nan+19] and (b) DP steels in a car BIW [Arc]

(UTS in MPa) of DP steels as a function of the martensite fraction and nominal carbon content simulated in [All+15]. The higher the carbon content and the fraction of martensite, the higher the UTS. In the E domain of the Figure, the sensitivity is about +10 MPa for each increase of 1% of martensite.

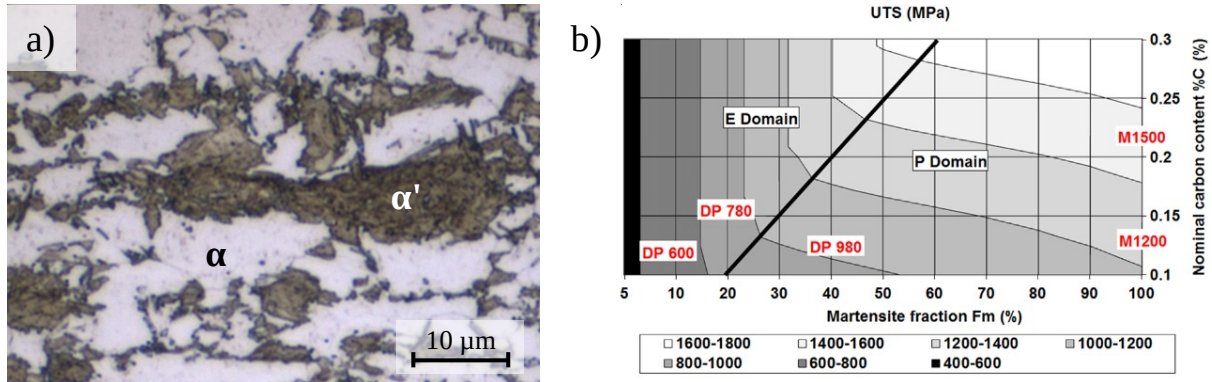


Figure 8: (a) Optical observation of the typical microstructure of a DP steel after etching. Martensite ( $\alpha'$ ) appears in brown and ferrite ( $\alpha$ ) in white (from this work). (b) Map of simulated Ultimate Tensile Strength (UTS in MPa) of DP steels as a function of the martensite fraction and nominal carbon content [All+15].

This typical microstructure is obtained by a conventional manufacturing route for flat products represented in Figure 9. After continuous casting, the slabs are reheated to reach the austenitic domain, above  $A_{c3}$  (usually above 900  $^{\circ}\text{C}$ ) and maintained for complete austenitization of the slab. Hot-rolling reduces their thickness, typically down to 3 mm. After this operation, the microstructure contains equiaxed austenite grains thanks to dynamic recrystallization (Figure 9 b 1). Under  $A_{r3}$ , ferrite nucleates and grows, leading to an austenite-ferrite

mixture in (2) in (Figure 9 b). Using slower cooling rate (usually lower than  $100\text{ }^{\circ}\text{C/s}$ ), a typical ferrite-pearlite mixture is formed (Figure 9 b 3). Around  $550\text{ }^{\circ}\text{C}$ , the steel sheet is coiled and air-cooled down to room temperature. The steel sheets are then cold-rolled down to the final thickness. This Severe Plastic Deformation (SPD) process strongly deforms the microstructure leading to elongated shapes aligned with the cold-rolling direction [BVS22; Bel+19; Chb+14; HPM04; Li+13; MGF11; Tei+21; TM18] (Figure 9 b 4). Then, the steel sheets undergo intercritical annealing. This stage consists of reheating and maintaining (soaking stage) the steel sheets in the intercritical temperature range (in the  $\gamma + \alpha$  domain of the phase diagram in Figure 9 a). The steel sheet undergoes partial austenitization (Figure 9 b 5). During the following cooling stage, ferrite can grow but pearlite formation is prevented and austenite transforms into quench components as bainite or martensite by displacive transformations (Figure 9 b 6). During this cooling stage, the sheet can be hot-dip galvanized (HDG). Finally, the steel sheets go through finishing steps, such as electro-galvanizing (if not done by HDG), skin-passing, phosphating, ...

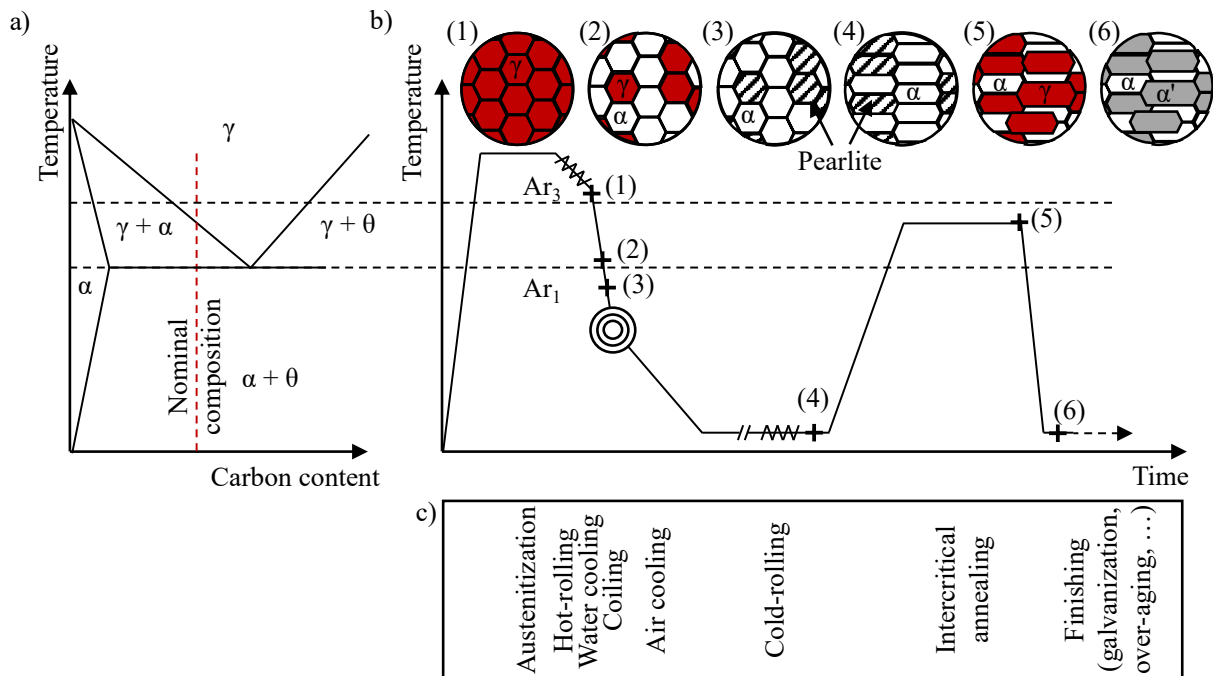


Figure 9: Schematic representation of a binary phase diagram Fe-C (a) and of the industrial schedule for DP steel production (b). The succession of steps is described in (c). The evolution of the microstructure is schematized in (b) from (1) to (6).

The final fraction of phases and their morphology, and thus the final mechanical properties, are inherited from the intermediate austenite-ferrite microstructure formed during intercritical annealing [All+15; Pus+15; Sco+17]. The fraction and morphology of austenite at the end of the soaking stage is very sensitive to the annealing parameters, such as the soaking temperature or the heating rate. The effect of the latter is well illustrated in the work of Huang et al. [HPM04]. Low heating rates ( $\approx 1\text{ }^{\circ}\text{C/s}$ ) are known to produce typical "necklace" microstructures, as shown in Figure 10 c). Equiaxed ferrite grains (in white) are surrounded by thin austenite films, localized at ferrite grain boundaries. On the contrary, typical "banded" microstructures (Figure 10 b) are obtained using high ( $> 50\text{ }^{\circ}\text{C/s}$ ) heating rates. Such microstructures show large

elongated austenite bands alternated with large ferrite-rich bands. The heating rate not only affects the morphology but also the austenite formation kinetics (the evolution of the austenite fraction) and the final austenite fraction, as illustrated in Figure 10 a). A higher heating rate leads to faster austenite formation kinetics and a higher final austenite fraction. This last experimental fact is hardly explained in literature, as it will be shown in Chapter I. The core of the present PhD work is to provide new insights to understand this experimental fact.

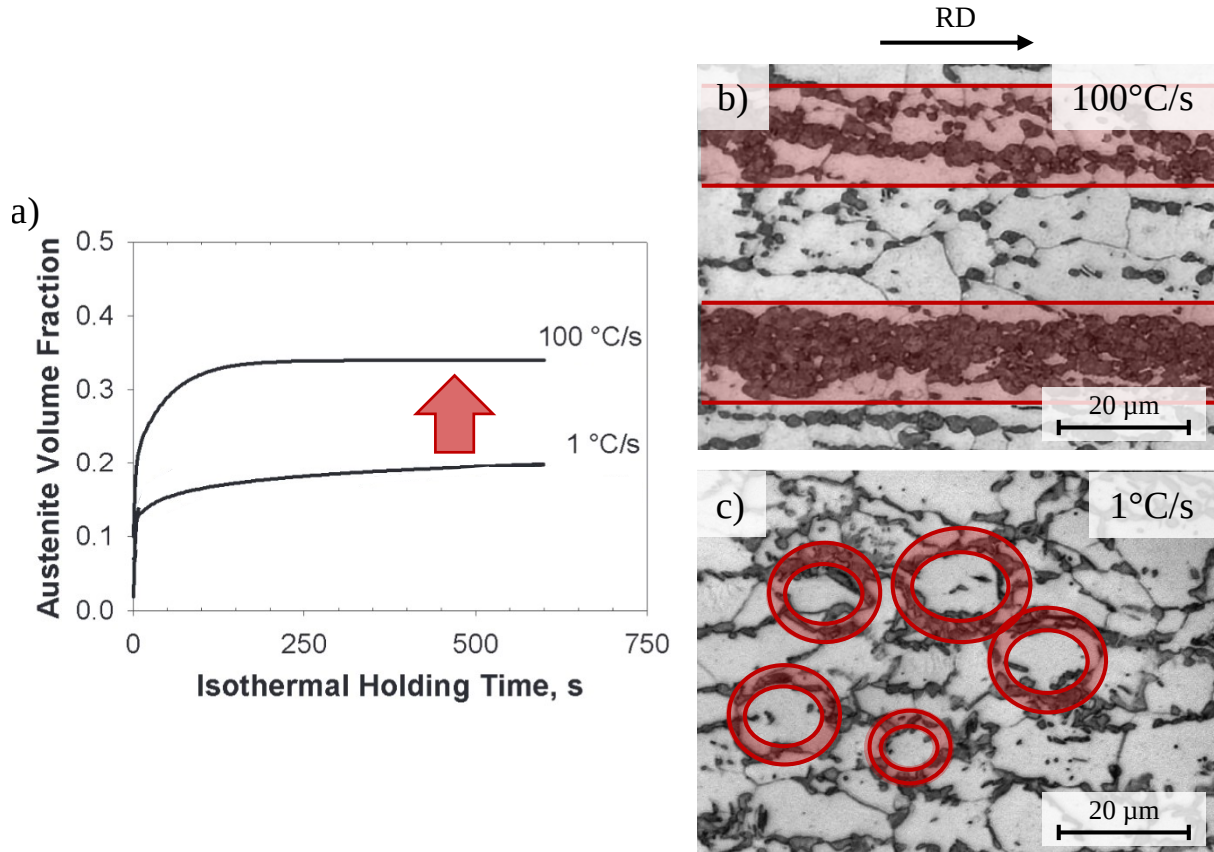


Figure 10: Effect of the heating rate on the austenite formation kinetics along the soaking stage at 750 °C (a) and on the austenite morphology (b and c) at the end of the soaking stage (10 min) of a cold-rolled Fe-C-Mn-Mo steel. Martensite (austenite before quenching) is in dark grey and ferrite in light grey. A typical "necklace" morphology is observed after slow heating at 1 °C/s (c), while a more "banded" morphology is obtained after fast heating at 100 °C/s (b). The red zones show austenite rich zones and their morphology (adapted from [HPM04]).

Understanding the austenite formation during the intercritical annealing stage is essential for steel-makers as it is crucial in determining the final mechanical properties. This task requires handling many metallurgical phenomena, possibly interacting with each other, taking place during intercritical annealing. Here is a non-exhaustive list of examples. The ferrite matrix, severely deformed by the cold-rolling process, undergoes recovery [Cou+21; HH95; Nes95] and recrystallization [Chb+14; HH95; Li+13] during the heating stage. The cementite lamellas in pearlite, fragmented by cold-rolling, spheroidize [Lai+16; Mor19; TK87]. Cementite may experience enrichment in alloying elements [Mor19]. At higher temperature, cementite dissolves

and austenite nucleates and grows. During these phase transformations, alloying elements may redistribute in the different phases [Cou+23; Lai+16; Mor19; SDM81; Tei+21].

## Objectives of this PhD thesis

The present PhD work is part of a long-term partnership between the Jean Lamour Institute (Microstructures and Stresses team) and ArcelorMittal Maizières Research. This work continues the previous PhD work of Moreno [Mor19] and is funded by ArcelorMittal Maizières Research and the French ANRT (Agence Nationale de la Recherche et de la Technologie) under the CIFRE convention (2020/1022).

Within the scope of the digital transition to Industry 4.0, steel-makers develop new real-time monitoring methods and modeling tools to drive their product lines [AB08; All+20; Pus+15]. Contrary to purely statistical approaches (including new machine learning methods), physics-based models offer additional advantages in terms of prediction capabilities (even outside their calibration range), modularity or possible extensions to other production steps or sites. However, such models require being able to understand, quantify and predict all the metallurgical mechanisms as well as their interaction along the production line.

The present PhD work aims to contribute to the numerical transition of production lines of conventional Dual-Phase steels. It mainly focuses on the austenite formation during intercritical annealing and its possible interactions with the recrystallization of the ferrite matrix.

First, we develop a new method using High Energy X-Ray Diffraction (HEXRD) to investigate recrystallization. Thanks to this method, the ferrite recrystallization and the austenite formation can be monitored simultaneously but separately in a single experiment with a high time-resolution during an intercritical annealing treatment.

We use this method and other, more conventional characterization methods to investigate austenite formation and its interactions with ferrite recrystallization. We challenge the state-of-the-art conclusions on the effect of the heating rate and how it controls the formation kinetics and the morphogenesis of austenite from an experimental point of view.

The final objective of this PhD work required by the industrial partner was to propose a CPU-efficient model for the austenite formation kinetics during the intercritical annealing of DP grade steels, accounting for multi-constituent systems (quinary systems in the present work).

## Outline of this manuscript

The present manuscript is divided into four chapters.

Chapter I proposes a literature review on the metallurgical mechanisms occurring during intercritical annealing for Dual Phase steels production. It focuses mainly on ferrite recovery and recrystallization, as well as austenite formation. The basic underlying mechanisms of these complex phenomena are detailed, as well as their possible interactions. It also provides useful notions of thermodynamic and thermo-kinetic analysis of the austenite formation. The current state of the art on the effect of the heating rate on the formation kinetics and the morphology of austenite is presented and discussed. This chapter finally discusses the modeling options for austenite formation during intercritical annealing.

Chapter II presents the studied steels, the experimental methods used and the modeling tools implemented in the present work. We detail the fabrication of the studied steels and the preparation of the samples for optical and electronic microscopy. Our HEXRD setup on a syn-

chrotron beamline and the post-process of the collected data is then presented. In particular, we present in detail our new method to monitor recrystallization. Our method is used on model steels and validated using reference methods (micro-Vickers Hardness and Electron BackScattering Diffraction). The chapter finally presents the commercial computational tools for phase transformation (Thermo-Calc and its DICTRA module) and thermodynamic databases used in this work.

Chapter III first reproduces the effect of the heating rate on the studied steel during simulated intercritical annealing treatments. We combine post-mortem microstructure investigations after interrupted thermal treatments, performed at ArcelorMittal Maizières Research, and in situ HEXRD experiments, performed on the PETRA III - P07 (DESY) synchrotron beamline, to investigate the nucleation and growth of austenite from the two identified cementite aggregates (inter-granular cementite particles and pearlite islands). We propose additional original experiments to challenge the hypothesis raised in the literature that explains the effects of the heating rate through the interactions between ferrite recrystallization and austenite formation. From our new conclusions, we attribute the effect of the heating rate on the austenite formation kinetics to interactions between microstructural parameters and thermo-kinetics mechanisms, in which ferrite recrystallization has no direct influence.

Chapter IV studies the effect of minor alloying elements (chromium and silicon) in the considered quinary systems on austenite growth kinetics and completes the thermo-kinetic analysis of austenite formation during intercritical annealing using DICTRA simulations. Our new findings from Chapter III are combined to our discussion in Chapter I to propose a CPU-efficient model to predict the austenite formation kinetics and the composition profiles in multi-component systems during an isothermal holding in the intercritical temperature range. This model is finally used to further discuss our explanations proposed in Chapter III for the effect of the heating rate on the austenite formation kinetics.

The present manuscript ends with the summary of the main scientific conclusions of this PhD work and the proposed future work.

---

# Chapter I

## Literature review

---

Mais c'est tout ce que je sais  
C'est tout ce que je dirai  
C'est tout ce que je connais (×2)  
Et dans tout ce que je fais  
J'essaie de taffer le sujet  
Y'a rien qui me plaît moins  
Que celui qui se permet  
De parler de ce qu'il a sur-survolé  
Qui montre du doigt  
Qui condamne et qui sait

---

*La cause*  
*Grand Corps Malade, Ben Mazué*  
*Gaël Faye*

I.1	Recovery and recrystallization . . . . .	9
I.1.1	Recovery . . . . .	9
I.1.2	Recrystallization . . . . .	11
I.1.3	Recovery for recrystallized grain nucleation . . . . .	12
I.1.4	Experimental characterization . . . . .	15
I.1.5	Summary on recovery and recrystallization . . . . .	22
I.2	Austenite formation during intercritical annealing . . . . .	22
I.2.1	Formation of the cold-rolled ferrite-pearlite microstructure . . . . .	23
I.2.2	Austenite nucleation . . . . .	24
I.2.3	Interface conditions governing austenite growth . . . . .	25
I.2.3.1	Thermodynamics of Fe-C-X ternary systems . . . . .	25
I.2.3.2	Austenite nucleation and growth from pearlite islands . . . . .	28
I.2.3.3	Austenite nucleation and growth from spheroidized cementite particles . . . . .	30
I.2.3.4	Competitions during austenite growth . . . . .	35
I.2.4	Effect of the heating rate . . . . .	36

I.2.5	Summary on the thermo-kinetics of austenite formation during the inter-critical annealing . . . . .	38
I.3	Interactions between ferrite recrystallization and phase transformation . . . . .	39
I.3.1	The necklace morphology . . . . .	40
I.3.2	The banded morphology . . . . .	42
I.3.3	Effect on the austenite formations kinetics . . . . .	45
I.3.4	Conclusions on the interactions between ferrite recrystallization and phase transformation . . . . .	47
I.4	Modeling the austenite formation . . . . .	47
I.4.1	Empirical laws . . . . .	48
I.4.2	Full-field sharp interface models . . . . .	48
I.4.2.1	Diffusion-controlled models . . . . .	49
I.4.2.2	Interface-controlled models . . . . .	50
I.4.2.3	Mixed-mode models . . . . .	51
I.4.2.4	Cellular Automaton (CA) . . . . .	52
I.4.3	Phase Field (PF) models . . . . .	52
I.4.4	Machine learning . . . . .	53
I.4.5	Conclusions on phase transformations modeling . . . . .	54
I.5	Summary . . . . .	54

This first chapter proposes a literature review on the metallurgical mechanisms occurring during the intercritical annealing for Dual Phase steels production. It focuses mainly on ferrite recovery and recrystallization, as well as austenite formation, in industrial cold-rolled steels during intercritical annealing.

First section deals with recovery and recrystallization. The section reviews the basic underlying mechanisms of these complex phenomena as well as their possible interactions. The experimental techniques generally used to characterize them are discussed in detail. An overview on the formation during the intercritical annealing is proposed in second section. In particular, it provides useful notions of thermodynamic and thermo-kinetic analysis, before presenting the current state of the art on the thermo-kinetics analysis of the austenite formation. Then, third section is dedicated to the interactions between ferrite recrystallization and austenite transformation. The impact of these interactions on the morphology of the DP microstructure, as well as on the austenite formation kinetics, is discussed.

As exposed in the introduction, one objective of the present PhD work is to propose a model for the austenite formation kinetics. The proposed model should be very efficient in term of computation time, as the model is supposed to drive an industrial production line. In addition, the model should account for quinary systems (Fe-C-Mn-Si-Cr). The fourth and last section discusses the modeling options available in the literature for austenite formation during the intercritical annealing.

## I.1 Recovery and recrystallization

Recovery and recrystallization are metallurgical mechanisms taking place in deformed crystalline materials. Both are thermally activated mechanisms and find their driving force in the same stored elastic energy resulting from the deformation process, leading to an expected competition. They both occur in the deformed ferrite matrix during the intercritical annealing of cold-rolled ferrite-pearlite microstructures for DP steel production. They affect the morphology of the phases, presumably the further phase transformation kinetics and, consequently, final mechanical properties of the products. Hence, the understanding and characterization of these mechanisms are of great importance for steelmakers. The literature already offers extensive reviews on recovery and recrystallization [Doh+97; Hum99; HH95]. This section is not exhaustive and mainly focuses on cold rolled steels.

### I.1.1 Recovery

At room temperature, plastic deformation of conventional metallic alloys is achieved mainly by dislocation gliding. These linear defects of the crystalline structure store an elastic distortion energy, roughly proportional to  $\rho\mu b^2$  with  $\rho$  the density of dislocations ( $\text{m}^{-2}$ ),  $\mu$  the shear modulus (GPa) and  $b$  the Burgers' vector (m), characterizing the defects. When the deformation is sufficiently large (beyond stage III of work-hardening), as produced by cold-rolling, the density of dislocations in the metals increases drastically, so that the energy stored could become significant. About 10 % of the work provided for plastic deformation is stored [HH95; Mar+04; OMG08; ZR13]. In this section, the case of Severe Plastic Deformation (SPD) processes and their consequences on the deformed microstructures will not be discussed.

Recovery is a general term encompassing thermally-activated mechanisms, such as dislocation annihilation by recombination, leading to a decrease in dislocation density and, thus, to a

rearrangement of the dislocation structure. Recovery is often studied by performing heat treatments on deformed materials. In one of our previous works [Cou+21], we studied recovery in severely deformed model ultra-low carbon (0.001 wt%) steels. Figure I.1 plots the dislocation density, estimated from High Energy X-Ray Diffraction (HEXRD) experiments (with crosses), whose method is explained later in this section, and Vickers micro-hardness (with inverted triangles), during annealing at 450 °C (blue), 500 °C (green), 550 °C (orange) and 650 °C (red). It shows the decrease in dislocation density during the studied isothermal treatments.

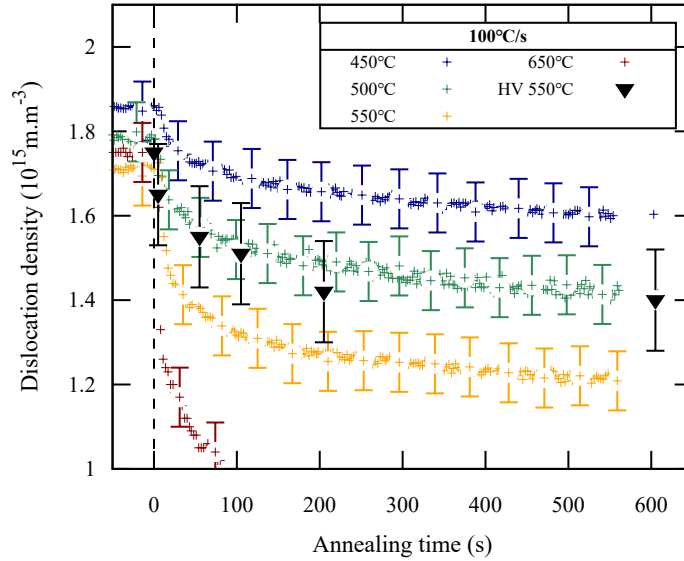


Figure I.1: Dislocation densities estimated from High Energy X-Ray Diffraction (HEXRD) during isothermal annealing at 450 °C (blue), 500 °C (green), 550 °C (orange) and 650 °C (red) after fast heating (100 °C/s). Dislocation densities deduced from Vickers hardness tests during annealing at 550 °C are represented by black triangles. (from [Cou+21])

During such heat treatments, the dislocation density decreases but a reorganization of the dislocation layout is also reported. Figure I.2 shows schematically the evolution of the dislocation structures during an annealing. Diagrams a) to e) represent the succession of states leading to a progressive decrease of the stored elastic energy. From the initial entanglement (Figure I.2 a), dislocations migrate and form cell walls (Figure I.2 b). Inside dislocation cells, dislocations annihilate (Figure I.2 c) as recovery continues. The dislocations entangled in the cell walls are ordered and the walls become Low Angle Grain Boundaries (LAGBs), with a misorientation lower than 10° to 15°, delimiting defect-free sub-grains (Figure I.2 d). Over time, sub-grain growth is observed, leading to coarser microstructures (Figure I.2 e) [HH95; Nes95]. Usually, dislocation cells are already present in steels after cold deformation, as in Figure I.2 b).

Recovery finds its driving force in the energy of dislocations [Doh+97; Hum97; HH95; VBG98]. It differs from recrystallization in the absence of the creation or migration of grain boundaries with high misorientation (higher than 10° to 15°) called High Angle Grain Boundaryies (HAGBs) [Doh+97; HH95]. Recovery occurs along annealing at moderate temperatures (static recovery) [Cou+21; Doh+97; HH95; Mar+04; VBG98] or during the deformation itself (dynamic recovery). This mechanism is a thermally activated process related to the out-of-plane mobility

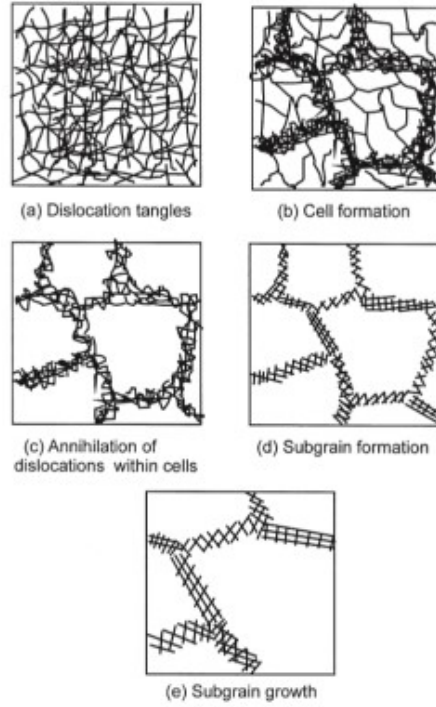


Figure I.2: Successive rearrangements of dislocation structures during static recovery [HH95].

of dislocations (contrary to dislocation gliding). Figure I.1 shows the effect of the annealing temperature on the recovery kinetics. The higher the annealing temperature, the faster the recovery kinetics. A temperature dependent saturation of recovery is also observed in that case.

During recovery, the decrease in dislocations densities combined with the increase in the mean subgrain size leads to a decrease in both strength and hardness of the studied material.

### I.1.2 Recrystallization

Like recovery, recrystallization is a metallurgical mechanism taking place in deformed materials and is driven by the excess energy carried by dislocations introduced during plastic deformation. Recrystallization is a reconstructive process by which new grains almost free of crystalline defects are formed [Doh+97; HH95; Mor+18; Pou+11; Rei52], leading to a drastic decrease in the stored elastic energy. Contrary to recovery, HAGBs form and migrate during recrystallization [Doh+97; HH95]. This process is often rationalized as a heterogeneous diffusive phase transformation. The main steps of recrystallization are schematized in Figure I.3. From a deformed state (Figure I.3 a), primary recrystallization is described by the nucleation (Figure I.3 b) and growth of new grains, which replace the deformed grains (Figure I.3 c) [HH95; Lau+03; Lau+06; OMG08; Pou+11]. Then, secondary recrystallization consists of abnormal grain growth in the fully recrystallized material (Figure I.3 d). This last stage is governed by the decrease in the energy related to grain boundaries.

When studying recrystallization during isothermal treatments, recrystallization kinetics, i.e. the evolution of the recrystallized fraction as a function of time, generally follows a typical sigmoidal function [HH95; Mor+18; OMG08; Rei52]. Figure I.4 (a) plots for instance the recrystallization kinetics of aluminum deformed at three different levels during an annealing at

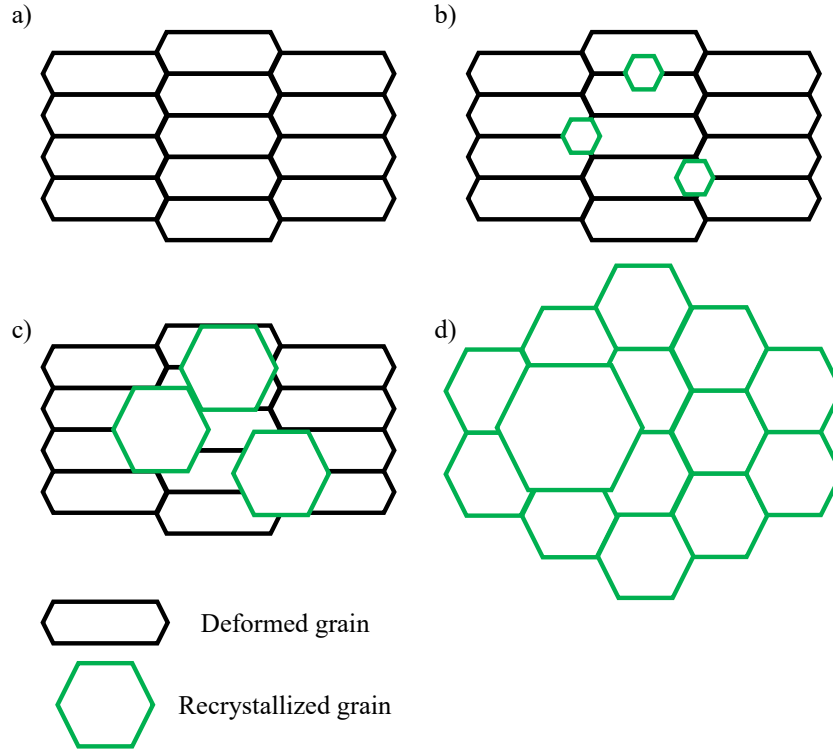


Figure I.3: Schematic representation of the microstructure evolution along recrystallization. a) deformed state. b) recrystallized grain nuclei. c) recrystallized grain growth. d) abnormal growth in the fully recrystallized material.

350 °C. As recrystallization finds its driving force in crystalline defects, it is promoted by higher deformation. This will be used in Chapter III, to vary the recrystallization kinetics by changing the cold-rolling ratio.

Figure I.4 (b) plots the recrystallization kinetics of a Fe-3.5Si (wt%) cold-rolled at 60 % annealed at different temperatures. The recrystallization kinetics is accelerated by higher temperature. Like recovery, recrystallization is a thermally-activated phenomenon.

The addition of solutes in alloys, and especially in steels, usually hinders recrystallization [HH95]. Solute may affect both the nucleation and growth steps but mainly decreases the grain boundary mobility. Figure I.5 shows the softening fraction of a Fe-0.2C-1.5Mn (a) and a Fe-0.2C-1.5Mn-0.02Nb (b) during austenite recrystallization, studied by Vervynckt et al. [Ver+09]. The softening fraction is a normalization of mechanical properties between the initial and final state (see for instance Equation I.1). As explained later in I.1.4, the softening fraction is here interpreted as the recrystallized fraction. The recrystallization kinetics is strongly delayed by the addition of niobium [All+20; Son+14; Ver+09]. This solute addition will be part of our strategy in Chapter III to inhibit recrystallization in the studied steel.

### I.1.3 Recovery for recrystallized grain nucleation

Primary recrystallization is described by the nucleation and the growth of new grains defect-free [HH95; Lau+06; Lau+03; OMG08; Pou+11]. Nucleation of newly recrystallized grains was first described using Classical Nucleation Theory (CNT), applied by Burke and Turnbull in 1952.

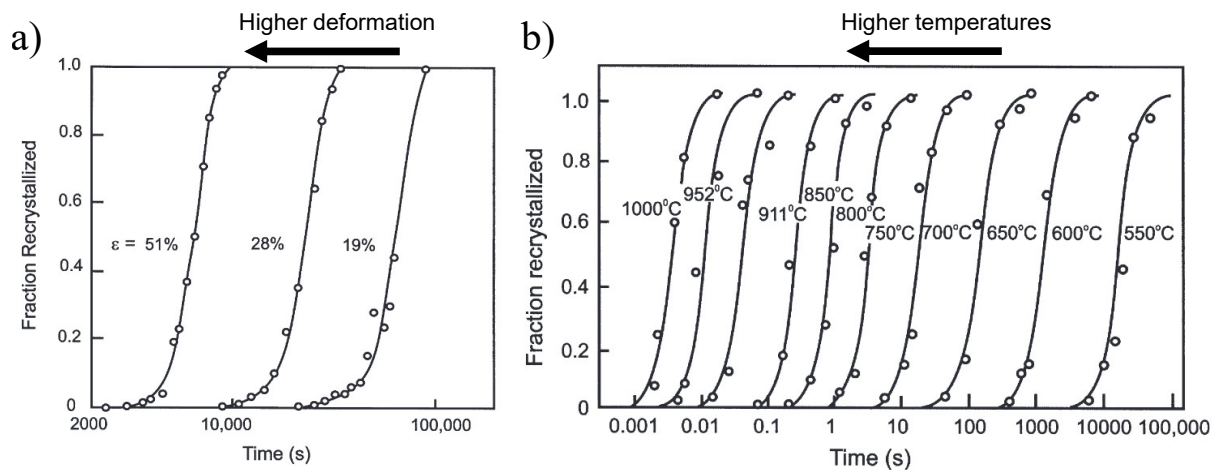


Figure I.4: Recrystallization kinetics of (a) aluminum at 350 °C after three deformation levels and (b) a Fe-3.5Si (wt%) cold-rolled at 60 % annealed at several temperatures. Higher deformation or annealing temperature accelerates recrystallization kinetics. (adapted from [HH95])

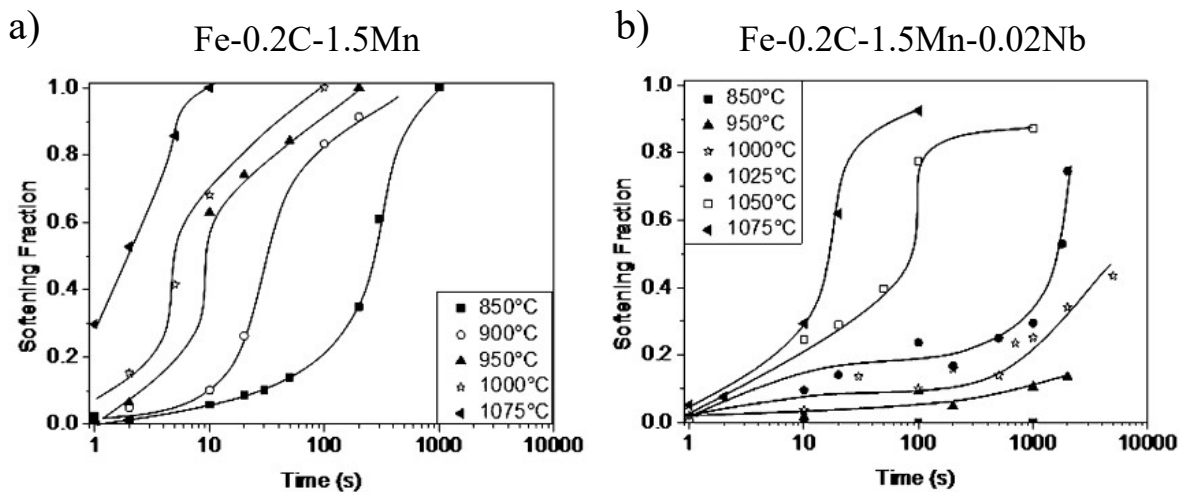


Figure I.5: Softening fractions determined from double-hit compression tests monitoring austenite recrystallization in a Fe-0.2C-1.5Mn (a) and a Fe-0.2C-1.5Mn-0.02Nb (b) steels during isothermal treatments at different temperatures (adapted from [Ver+09]).

Although the incubation times and preferential nucleation sites determined using this theory agree with experiments, this is not the case for the kinetics. Given the high interface energy carried by HAGBs and the low driving force, the critical radius is far too large, leading to a nucleation flux far lower than that determined experimentally. It was quickly concluded that the formation of new recrystallized grains is not a thermodynamic-controlled nucleation process, i.e. generated by random atomic fluctuation leading to defect-free crystallites and HAGBs.

A second theory puts forward the idea that nuclei are formed by the rearrangement of dislocations during recovery. Cells and sub-grains formed during recovery can reach a critical size

by migration of LAGBs and become nuclei for recrystallized grains [Hum97; HH95]. HAGBs can be created by recovery from strong orientation gradients. The propagation of certain orientations by migration of LAGBs leads to the formation of HAGBs when sufficiently different orientations meet [HH95]. In absence of strong orientation gradients, the proximity of already formed HAGBs is necessary. Only cells or sub-grains bordering deformed grains are likely to become recrystallization nuclei [Doh+97]. The Strain Induced Boundary Migration (SIBM) directly results from this latter idea [Hum97; HH95; Vat+96; ZBD06]. Figure I.6 illustrates the nucleation process from either a dislocation cell (a) or a sub-grain (b), both formed during recovery. In both cases, grain II is less recovered and stores a higher dislocation density, i.e. has a higher energy  $E_{II}$ . On the contrary, grain I is recovered by the creation of dislocation cell or sub-grain and stores a lower energy  $E_I$ . The migration of HAGBs is assumed to be driven by a difference in stored energy across the boundary. HAGBs migration start when the driving force  $\Delta E = E_{II} - E_I$  exceeds the boundary curvature, i.e. when  $\Delta E > 2\gamma/R$ , where  $\gamma$  is the interface energy ( $\text{J}\cdot\text{m}^{-2}$ ) and  $R$  the radius of curvature of the boundary (m) [HH95; ZBD06]. When the radius becomes higher than the critical radius  $R_{\text{crit}} = 2\gamma/\Delta E$ , the cell or sub-grain becomes a stable nucleus of a recrystallized grain.

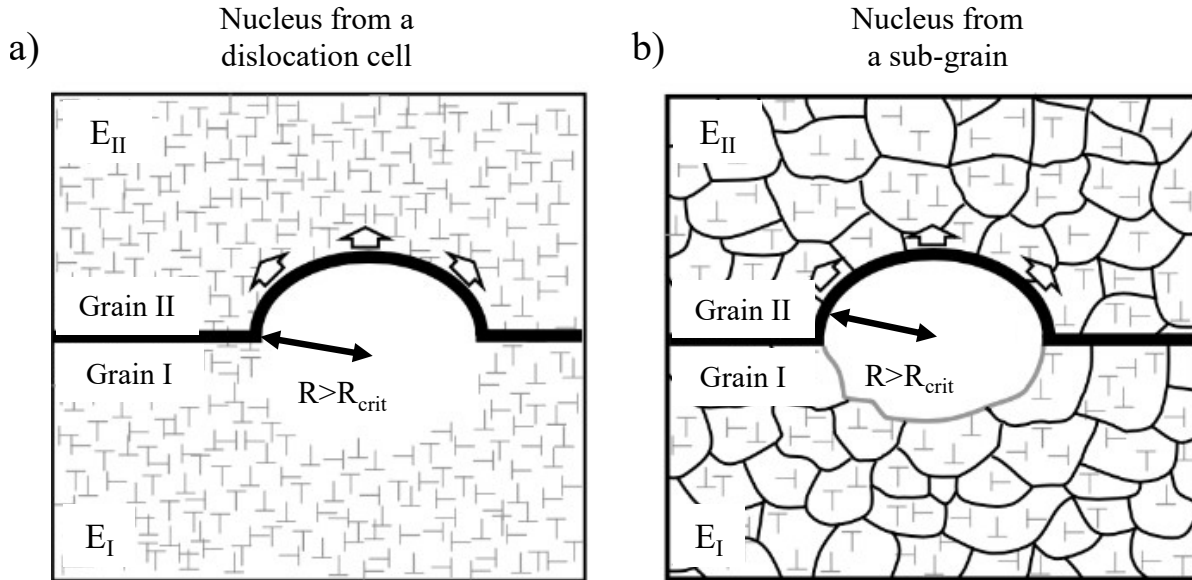


Figure I.6: Nucleation of a recrystallized grain from a dislocation cell (a) or a sub-grain (b) in the Strain Induced Boundary Migration Theory adapted from [ZBD06]. Grain II contains more dislocations and stores a higher energy  $E_{II}$  than grain I, storing a lower energy  $E_I$ .

In this theory, recovery and recrystallization both cooperate together and compete against each other. Recovery helps creating nuclei of recrystallized grains but recovery and recrystallization consume the same driving force [Doh+97; Rei52; VR90]. Consequently, if recovery is in its early stage, the substructure is dense with a still high dislocation density, providing to recrystallization a high density of nucleation sites and a large driving force. On the contrary, if recovery is more advanced, coarser sub-grains limit the number of nucleation sites, and the lower dislocation density strongly diminishes the driving force available for recrystallization.

Grain orientation and size also influence recrystallization, through the migration rate of HAGBs. Interface mobility depends on the orientation on each side of the interface [Doh+97; Hum97; HH95]. This affects not only recovery, which can slow down recrystallization if impaired by the orientation distribution; but also recrystallization itself, especially during the growth stage.

#### I.1.4 Experimental characterization

As recovery and recrystallization have the same driving force (the decrease in the total dislocation density), both affect the same mechanical and physical properties. Consequently, experimental characterization of recovery and recrystallization is carried out using similar methods and it is usual that one of these mechanisms interfere with the characterization of the other I.7 [Cou+21; MAG04]. The experimental characterization of recovery or recrystallization often requires the use of several techniques and the discussion of the impact of both mechanisms on the results.

Recovery and recrystallization can be characterized using different microscopy techniques. After etching, optical microscopy can reveal the dislocations cells formed by recovery [HH95; Mar+04] and the recrystallized grains [OMG08]. Figure I.7 shows an optical micrograph of the microstructure after etching (Nital 2 %) of a low-carbon steel after 11 s at 600 °C, from the work of Martínez-de-Guerenu et al. [MAG04]. Recrystallized grains, indicated by a black arrow in Figure I.7, present a different morphology than still deformed grains, indicated by a red arrow in Figure I.7, and are often characterized by the absence of substructure after etching.

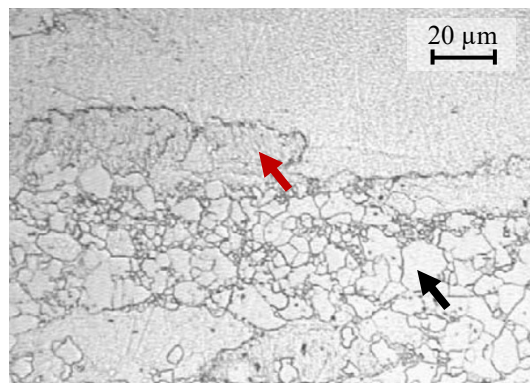


Figure I.7: Optical micrograph of the microstructure after etching (Nital 2 %) of a low-carbon steel after 11 s at 600 °C. A recrystallized grain is indicated by a black arrow. A non-recrystallized grain is indicated by a red arrow. (adapted from [MAG04])

The resolution of optical microscopy is too low to observe the dislocations or the nucleation of recrystallization. But the progress of recovery or recrystallization can be estimated with a higher resolution using Scanning Electron Microscopy (SEM). The evolution of the microstructure and, in particular, the orientation distribution are often analyzed using Electron BackScattering Diffraction (EBSD) maps [Doh+97; HH95; Liu+16; Mar+04; OMG08; Sla18]. The spatial resolution needed for such analysis requires Electron BackScattering Diffraction (EBSD) setup with high angular resolution, which became the reference technique [HH95; Rad15; Sla18] in the last 20 years. The acquired orientation maps are necessarily post-processed with different mathematical methods such as Grain Orientation Spread (GOS) representation, Kernel Average Misorientation (KAM) or Grain Average Misorientation (GAM) to identify the recrystallized

grains [Aya+12; Zha+14]. These techniques rely on the calculation of a scalar value representing the local misorientation angle with respect to a mean value inside each studied grain. For instance, GOS corresponds to the standard deviation of crystallographic misorientation inside the studied grain knowing its mean orientation. The higher the GOS, the higher the density of defects in the grain [Mor+18; Rad15]. Figure I.8 shows a Scanning Electron Microscopy (SEM)/EBSD map of a DP600 steel after a heating sequence at 3 °C/s interrupted at 700 °C (He gas quenched), post treated to show the GOS, from the work of Moreno et al. [Mor+18]. By defining a threshold, typically 1.5°, recrystallized grains, whose GOS is lower and colored in blue in Figure I.8, are distinguished from deformed grains, whose GOS is higher and colored from green to red in Figure I.8. The recrystallized volume fraction can be estimated from such analysis, as reported in Figure I.13, but strongly depends on the threshold and the original quality of the EBSD map. This method will be used as the reference technique in Chapter II to evaluate the recrystallized volume fraction in our samples.

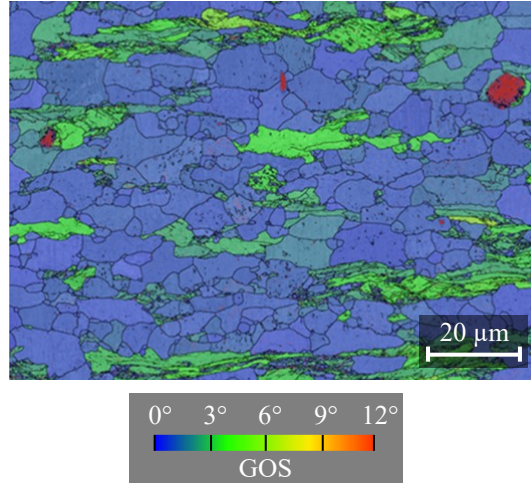


Figure I.8: SEM/EBSD map post-processed to reveal the Grain Orientation Spread (GOS) in a DP600 steel after a heating sequence at 3 °C/s interrupted at 700 °C (He gas quenched). (adapted from [Mor+18])

Transmission Electron Microscopy (TEM) is the reference technique to study dislocations in crystalline material [FKM04; Hum99; MAG04]. However, the dislocation density in cold-rolled steels can be too high to be revealed individually using TEM, and only the dislocation substructure can be studied [VBG98]. Figure I.9 shows a TEM micrograph with a {111} orientation of a low-carbon steel cold-rolled at 84 %, studied by Martínez-de-Guerenu et al. [MAG04]. A dislocation cell (dislocation-depleted volume), indicated by a black arrow, is delimited by dislocation walls (planar structure extremely dense in dislocations), indicated by a red arrow.

Mechanical testing is also widely used to characterize the progress of recovery or recrystallization.

The forest-hardening law given by Taylor,  $\sigma = \sigma_0 + \alpha M \mu b \sqrt{\rho}$ , where  $\sigma_0$  is the lattice friction,  $M$  is the Taylor coefficient,  $\mu$  the shear modulus and  $b$  the norm of the Burgers' vector, shows that the flow stress of a metals is directly a function of its dislocation density  $\rho$  [HH95; Smi+04; VBG98]. Thus, mechanical tests can be used to measure the evolution of the flow stress, and, in turn, the evolution of the dislocation density. For instance, the strain-hardening rate was studied and modeled in the work of Verdier et al. [VBG98] to follow recovery in AlMg alloys

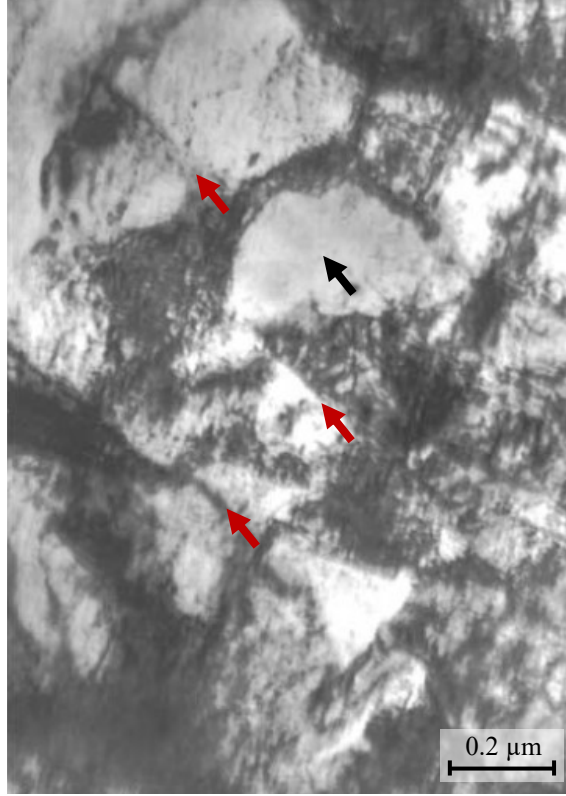


Figure I.9: TEM micrograph ( $\vec{g} = \{111\}$ ) of a low-carbon steel cold-rolled at 84 %. A dislocation cell, indicated by a black arrow, is delimited by dislocation walls, indicated by red arrows. (adapted from [MAG04]).

using this strategy. Double-hit compression tests were used by Vervynckt et al. [Ver+09] to follow the austenite recrystallization in Fe-0.2C-1.5Mn and, finally to highlight the effect of niobium micro-alloying on the recrystallization kinetics, as shown in Figure I.5.

Hardness tests are easy to systematically carry out and often used to highlight the decrease in dislocation density due to both recovery [HH95] and recrystallization [MAG04], as the hardness can be related easily to the material strength through empirical relationships, such as  $\sigma \approx 3 \times HV$  [ST94].

For instance, in our previous work [Cou+21], we used hardness measurements to follow recovery in severely deformed ferrite. The deduced dislocation densities, plotted with inverted triangles in Figure I.1, were used to compare against the recovery kinetics obtained from HEXRD experiments, plotted with crosses in Figure I.1 (method detailed later in this section). Hardness tests will be used in Chapter II in addition to SEM/EBSD to follow the recrystallization kinetics in our experiments. The recrystallized fraction,  $f_{Rec}$ , is obtained from the softening fraction as follows:

$$f_{Rec} = \frac{HV - HV_0}{HV_{full\ rec} - HV_0} \quad (I.1)$$

With  $HV$ , the current hardness,  $HV_0$ , the reference hardness before treatment, and  $HV_{full\ rec}$ , the hardness measured on the fully recrystallized material. The method is further discussed in

## Chapter II.

Both microscopy and mechanical testing are *ex situ* and *post-mortem* manipulations. The observations and measurements are carried out on different samples after interrupted treatments, making these techniques very time-consuming. Physical properties also tend to change during recovery or recrystallization and are easier to characterize using non-destructive methods.

Electrical resistivity increases in the presence of lattice defects. Dislocations disrupt the flow of electrons through the metal. This is the reason why Clareborough et al. [HH95], Verdier et al [VBG98] and Swanson et al [Swa64] used *in situ* measurements of the electric resistivity to monitor recovery in aluminum alloys. Clareborough et al. [HH95] also measured the variation in stored energy by calorimetry. Calorimetry can only be used in the absence of phase transformation or precipitation [HH95], as the energy stored during deformation is very small compared to the ones involved in the other processes.

Martínez-de-Guerenu et al [MAG04] and Oyarzábal et al [OMG08] used the coercive field variation to monitor recovery in a low-carbon steel, while other methods, such as hardness measurements, were mainly impacted by recrystallization and show low sensitivity to recovery.

Finally, X-Ray Diffraction (XRD) is one of the most popular characterization method to determine the dislocation density [Kho+11; Peš+03; RGU04; RU10; Sal+15; Ung+14; WH53] in a crystalline material. The measurement is based on the distortions of the crystal lattice induced by dislocations that broaden the diffraction peaks of the considered structure.

The pioneers in this field were Scherrer, followed by Williamson and Hall [Kho+11; MH96; WH53]. Their work demonstrated that the Full Width at Half Maximum (FWHM) of the diffraction peaks were a function of a crystallite size  $D$  (m), defined as a defect-free zone, and a deformation  $\epsilon$  (n.d.) of the crystal.

In a previous work [Cou+21], we determined the dislocation density during the annealing of severely deformed ferrite from *in situ* HEXRD experiments using the modified Williamson-Hall (mWH) elaborated by Ungar et al. [Ung04; Ung+99; UB96]. In this approach, the magnitude of the diffraction vector  $K = \frac{2\sin(\theta_0)}{\lambda}$  is related to its variation  $\Delta K = \frac{\cos(\theta_0)}{\lambda} \times FWHM$  [Sal+15; Ung+99] as follows:

$$\Delta K = \frac{k}{D} + \frac{\pi}{2} R_e^2 b^2 \rho^{3/2} (K \sqrt{\bar{C}})^2 \quad (\text{I.2})$$

With  $\rho$  the dislocation density ( $\text{m}\cdot\text{m}^{-3}$ ),  $D$  the crystallite size (m),  $k$  a constant taken equal to 0.94,  $R_e$  the cut-off radius (m), defining the area of influence of a dislocation,  $\bar{C}$  the average contrast factor and  $b = 2.5 \times 10^{-10}$  m the magnitude of the Burgers vector (m). The dislocation densities obtained with this method are plotted with crosses in Figure I.1 during the thermal treatments of a model alloy.

Calibrating parameters associated with the Williamson-Hall method, such as the cut-off radius  $R_e$ , may be difficult to estimate unambiguously. Coupling the mWH method to the Warren-Averbach method [Sal+15; TMT19; TMT18] limits the use of fitting parameters [Sal+15]. The Warren-Averbach equation links the diffraction vector  $K$  to the Fourier's coefficients modelling the diffraction peaks [Sal+15].

Such measurements can be conducted advantageously on a synchrotron beamline using HEXRD experiments [Cou+21; Mor+18]. *In situ* investigations in bulk (as done in Figure I.1) are made possible by the high energy and brilliance of the beam offered by these large instruments, while laboratory set-ups are limited to the *ex situ* investigations of the sub-surface.

Techniques for determining dislocation densities to study recovery kinetics are now very operational. On the other hand, there are few diffraction techniques to follow the recrystallization

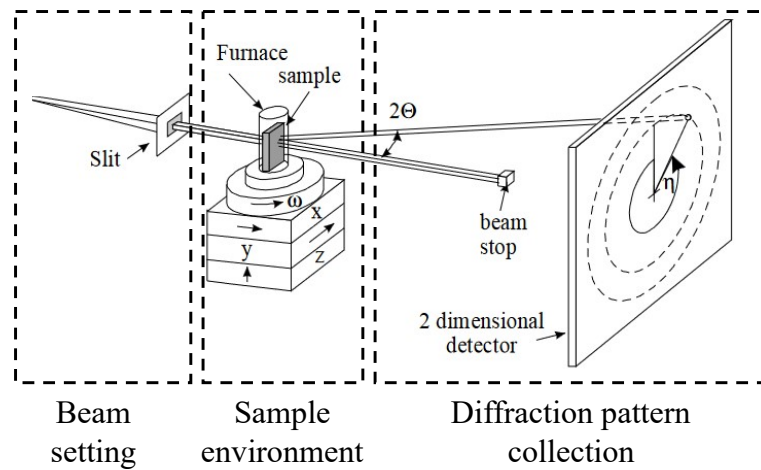


Figure I.10: 3DXRD experimental setup (adapted from [Lau01]) for growth tracking of individual recrystallized grains.

process in situ. 3DXRD tomography [Lau+06; Lau+03; Pou+11] enables the in situ measure of individual recrystallization kinetics of selected grains. Figure I.10 represents the experimental setup for 3DXRD tomography on the synchrotron beamline, described in [Lau01]. Upstream from the sample, the X-ray beam is made monochromatic and shaped by slits. The sample is placed in a furnace, controlling its environment. The sample is rotated around the z-axis during the treatment so that more grains fulfill the Bragg condition and diffract. Downstream, the diffraction patterns are collected on a 2D detector.

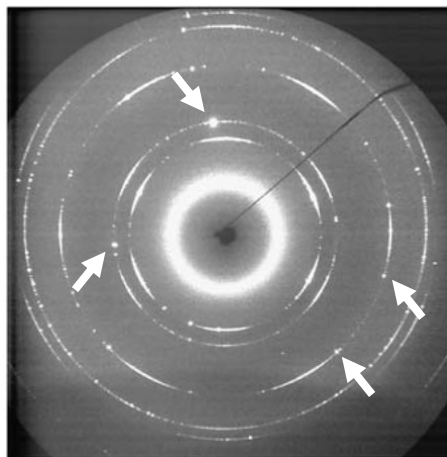


Figure I.11: Diffraction pattern of a fully recrystallized 90 % cold-rolled aluminum alloy AA1050 annealed at 270 °C. (adapted from [Lau+03])

During an annealing monitored in situ by XRD using the setup in Figure I.10, newly recrystallized grains in diffraction conditions also produce spots of high intensity on the 2D patterns. The gradient of misorientations inside a new recrystallized grain is supposed to be weak enough to concentrate the intensity of the spot. The observed spots can be deconvolved from the continuous background diffraction rings of the studied phase. White arrows in Figure I.11 show such

diffraction spots on the diffraction patterns of a fully recrystallized 90 % cold-rolled aluminum alloy AA1050 annealed at 270 °C, studied by Lauridsen et al. [Lau+03].

The intensity  $I$  of a given spot depends on its position on the diffraction pattern, given by the scattering angle  $2\theta$  and the azimuthal angle  $\eta$  (indicated in Figure I.10), the structure factor  $f(hkl)$  of the diffracting plane with Miller indices  $(hkl)$ ,  $\frac{1}{\sin(2\theta)|\sin(\eta)|}$  the Lorentz factor and the volume  $V$  of the diffracting grain as follows [Lau01]:

$$I = \text{const} \frac{f(hkl)^2}{\sin(2\theta)|\sin(\eta)|} V \quad (\text{I.3})$$

Consequently, the intensity of a diffraction spot is proportional to the volume of the diffracting grain. By tracking the intensity and position of the spots through time, growth kinetics of individual grains as well as precise nucleation conditions were determined from few in situ experiments by several authors [Lau01; Lau+06; Lau+03; Pou+11]. For instance, Figure I.12 a) plots the intensity of four diffraction spots collected during the annealing at 315 °C of an aluminum alloy AA5182 hot deformed at 400 °C to a strain of 2.0, studied in [Lau01]. Figure I.12 b) plots the grain volume deduced from the intensity using equation (see equation I.3) of several tracked grains in a 90 % cold-rolled aluminum alloy AA1050 annealed at 270 °C, studied in [Lau+03] (Figure I.11). The intensities and thus, grain volumes increase and follow several behaviors, showing a global grain growth but with different individual kinetics.

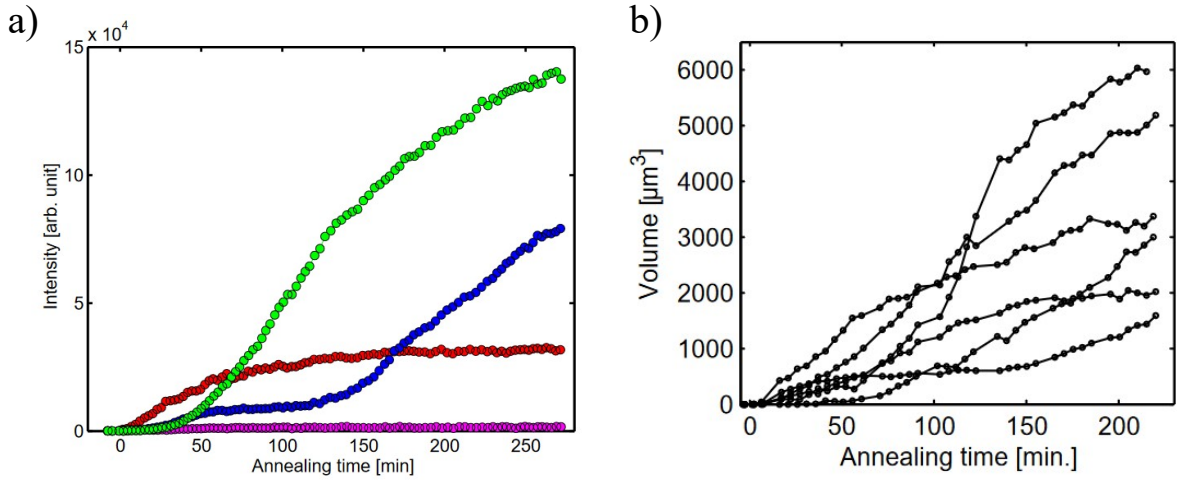


Figure I.12: (a) Four examples of intensities of diffraction spots as a function of time during annealing at 315 °C of an aluminum alloy AA5182 hot deformed at 400 °C to a strain of 2.0 (adapted from [Lau01]). (b) Six examples of grain volume evolution in a 90 % cold-rolled aluminum alloy AA1050 during annealing at 270 °C deduced from the intensity of several tracked grains using equation I.3 (adapted from [Lau+03])

Tracking grains is complex and 3DXRD was mainly performed on polycrystal with large grain size. This technique cannot be applied reasonably to materials with grains smaller than 5  $\mu\text{m}$ , such as industrial steels.

Inspired by these 3DXRD investigations, a new in situ method based on HEXRD experiments was proposed by Moreno et al. [Mor19; Mor+18]. The Recrystallization Peak Counting

(RPC) method consists in determining mean recrystallization kinetics in bulk, considering a large number of grains. It relies on the fact that new recrystallized grains produce spots on the 2D pattern as in 3DXRD, but their population is considered globally, without tracking individual grains.

Once collected, the HEXRD rings are integrated by sectors along the azimuth, as shown in Figure I.13 a). Figure I.13 b) represents the intensity along the (200) ring of ferrite of a DP600 steel cold-rolled at 60 % heated at 3 °C/s, studied in [Mor+18]. This 1D diffractogram is plotted when the sample is at room temperature (in black) and at 700 °C (in red). Spots of recrystallized grains appear as narrow peaks on the 1D diffractogram. The recrystallization peaks are extracted from mean textured diffraction signal using thresholds and counted all along the annealing treatment, as plotted in Figure I.13 c). In their study, Moreno et al. [Mor+18] correlate the evolution of the number of recrystallization peaks to the recrystallized fraction. The recrystallization kinetics is obtained by the normalization of the number of recrystallization spots, plotted with crosses in Figure I.13 d), and the correlation is validated by characterizing the recrystallization state using SEM/EBSD observations, plotted with dots Figure I.13 d), and with an empirical model.

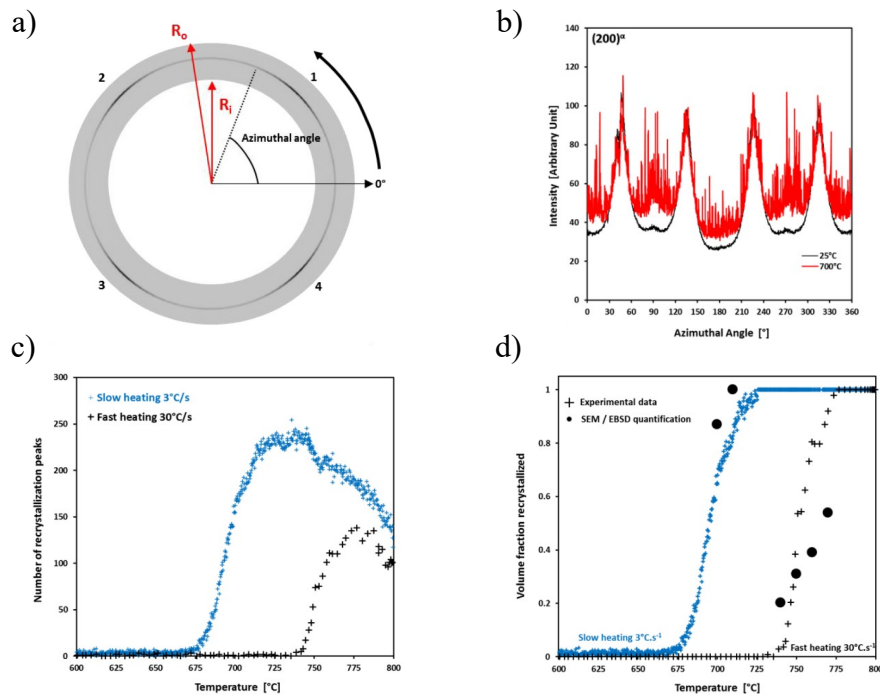


Figure I.13: Ferrite recrystallization of a DP600 steel cold-rolled at 60 % followed using the RPC method developed in [Mor+18]. (a) Azimuthal investigation of the 200 ferrite diffraction ring. (b) 1D diffractogram of the 200 ferrite ring at room temperature (in black) and at 700 °C (in red) along heating at 3 °C/s. (c) Number of recrystallization peaks counted along the heating at 3 °C/s (in blue) and 30 °C/s (in black). (d) Recrystallized volume fraction estimated from the RPC method (with crosses) and from SEM/EBSD observations (with dots) (Figure I.8).

As the sample is not rotated, only particular grain orientations are selected. Only recrystallized grain with orientation in diffraction conditions are detected, introducing a bias. Contrary

to fully ferritic steels or aluminum alloys, recrystallization texture is known to be limited in DP steels [KLH11; Per+10; Ray85]. After a systematic analysis on different rings leading to similar recrystallization kinetics, this source of uncertainty was neglected. The development of this method opens a time-resolved way to study of coupled metallurgical mechanisms as recovery, recrystallization, and phase transformation. However, this method needs an individual analysis of the rings. Even based on the 2D patterns, the method is a 1D method by construction, due to the azimuthal integration step, losing information in the process.

Among other challenges, this PhD work aims to improve and validate in depth the RPC method on model materials. This study is detailed in Chapter II. The new validated method is then used in Chapter III to study the intercritical annealing of DP steels.

### I.1.5 Summary on recovery and recrystallization

Recovery and recrystallization compete for the same driving force, the elastic energy stored during the deformation process in dislocations within crystalline materials. During recovery, the mechanisms of annihilation and rearrangement of dislocations reduce their density. Recrystallization, on the other hand, consists in the formation and growth of new defect-free grains.

These two phenomena are closely linked. In particular, the initiation of recrystallization nucleation is attributed to recovery, according to SIBM theory for instance. Therefore, the study of recovery and recrystallization must take into account their interactions.

The progress of recovery and recrystallization can be estimated by microscopy (optical, SEM and TEM). These mechanisms lead to changes in mechanical properties (decrease in hardness or flow stress), and physical properties (decrease in electrical resistivity). They can be monitored by following the evolution of these properties. In particular, SEM/EBSD observation and hardness measurements will be used in Chapter II to estimate post-mortem the recrystallized volume fraction in our annealed samples.

Finally, the recent work of Moreno et al. [Mor+18] offers a new time-resolved technique to follow in situ recovery and recrystallization at the same time. The developed methods use in situ HEXRD experiment and do not require interrupted treatments and time-consuming post-mortem experiments. However, the RPC method, which estimates the recrystallization kinetics, loses information from the 2D pattern due to the azimuthal integration step and was weakly validated using more conventional methods. One challenge addressed by the current thesis is improving and validating in depth the proposed method on model materials and then using it to study the intercritical annealing of DP steels.

## I.2 Austenite formation during intercritical annealing

The formation of austenite during intercritical annealing from a mixture of ferrite and cementite is a solid-state diffusive phase transformation usually described by a nucleation and growth process. This section offers an overview of this metallurgical process. First, we describe the formation of the microstructure before the intercritical annealing. Then, we present the austenite nucleation sites, before detailing the austenite growth during the annealing. A diffusion-controlled point of view is adopted in the present section. Other description of the physics controlling the austenite formation (interface-controlled and mixed-mode) are discussed in Section I.4. The thermodynamics of Fe-C-X systems is introduced, before detailing thermo-analyses of the austenite formation during the intercritical annealing. Finally, we present the impact of the heating rate on the austenite formation.

### I.2.1 Formation of the cold-rolled ferrite-pearlite microstructure

Figure I.14 schematizes the formation of the microstructure before the intercritical annealing during DP steel production. The microstructure elaborated by this upstream process will be considered as the "initial microstructure" in the following. The industrial thermo-mechanical schedule (temperature as a function of time), represented in (Figure I.14 b), is put aside a schematized pseudo-binary phase diagram for a Fe-C-Mn steel (a). The corresponding industrial operations of the schedule are indicated in (Figure I.14 c).

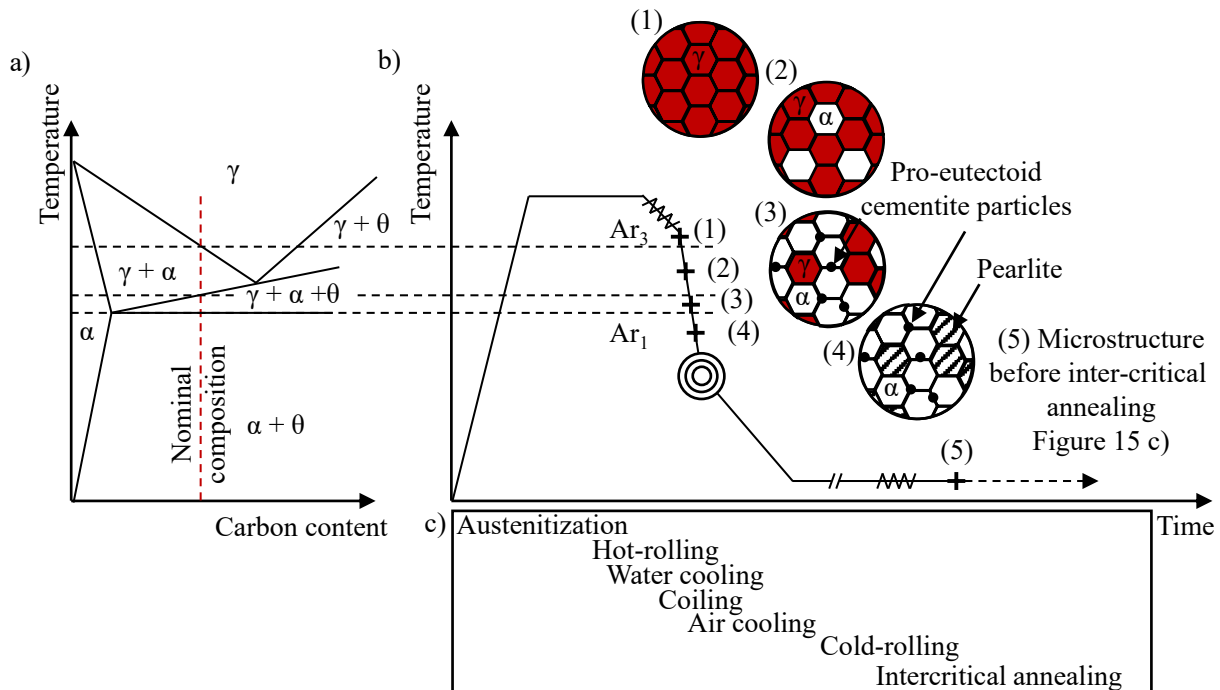


Figure I.14: Schematic representation of a pseudo-binary phase diagram Fe-C-Mn (a) and of the formation of the microstructure before intercritical annealing along an industrial thermo-mechanical schedule (b). The succession of industrial steps is described in (c). The evolution of the microstructures is schematized in (b) from (1) to (5).

The slabs are first reheated to reach the austenitic domain, above  $Ac_3$  (usually above 900 °C) and maintained for a complete austenitization. Then, slabs are hot-rolled to reach a typical thickness of 3 mm. After this operation, the microstructure contains equiaxed austenite grains thanks to dynamic recrystallization (Figure I.14 b 1).

From this state, different phases can form along the following cooling steps, depending on the cooling rate. Fast cooling rates produces bainite [MGF11] or possibly martensite [Bel+19; MGF11], if fast enough (usually higher than 300 °C/s). Using slower cooling rate (usually lower than 100 °C/s), a typical ferrite-pearlite mixture is formed. The present work mainly focuses on this mixture whose formation is schematized in Figure I.14 b).

Under  $Ar_3$ , ferrite nucleates and grows, leading to an austenite-ferrite mixture in (2) in (Figure I.14 b). The addition of alloying elements, such as manganese, opens a  $\gamma + \alpha + \theta$  domain in the pseudo-binary phase diagram in Figure I.14 a). Cementite particles can precipitate at the pro-eutectoid ferrite grain boundaries (Figure I.14 b 3) [Lee+93; LTH90]. Under  $Ar_1$ , the

remaining austenite, enriched during the ferrite formation, transforms into pearlite (Figure I.14 b 4). This transformation occurs when the Hultgren's criteria is fulfilled [Hul20], i.e. when the austenite composition and the temperature meet the extrapolation of the Ac<sub>m</sub> phase boundary.

The carbon-rich phases (here pearlite) are localized preferentially in the manganese segregation bands, as manganese decreases the carbon activity [BVS22; Chb+14; KPM13]. Around 550 °C, the steel sheet is coiled and air-cooled down to room temperature.

Finally, the steel sheets are cold-rolled. This deformation process not only reduces the thickness of the steel sheets, but introduces major changes in the microstructure. After cold-rolling, the studied steels show strongly deformed microstructures. The ferrite grains and the carbon-rich phases inherit an elongated shape aligned with the cold-rolling direction [BVS22; Bel+19; Chb+14; HPM04; Li+13; MGF11; Tei+21; TM18]. The ferrite grains contain a high density of crystalline defects (mainly dislocations) [HPM04]. In ferrite-pearlite steels, the deformed pearlite bands present deformed ferrite and fragmented cementite lamellas [BVS22; Chb+14; HPM04; Li+13; MGF11; Tei+21; TM18]. Figure I.15 (a) shows the microstructure before intercritical annealing of a Fe-0.178C-1.55Mn-1.7Si cold-rolled at 50 % studied in [HPM04]. The microstructure contains deformed ferrite, indicated by white arrows, and pearlite, indicated by red arrows, both elongated in the rolling direction (RD).

Some authors point out that the initial microstructure can contain, in addition to pearlite, clusters of cementite particles isolated in the ferrite matrix, located at the ferrite grain boundaries and aligned with the cold-rolling direction [Bel+19; Chb+14; Li+13; Tei+21; TM18]. Figure I.15 (b) shows the microstructure before intercritical annealing of a DP590 grade cold-rolled at 70 % studied in [Li+13]. This microstructure presents deformed ferrite and pearlite but also cementite particles at ferrite grain boundaries, indicated by black arrows.

This cold-rolled state defines the initial state before intercritical annealing. A schematic representation of a typical initial microstructure before intercritical annealing considered in the present review is proposed in Figure I.15 (c). The proposed representation defines the nomenclature of the objects studied in the present manuscript. The main carbon-rich phase is pearlite, as in the majority of the studies reported in the present review [BVS22; Chb+14; HPM04; Li+13; Tei+21; TM18]. The isolated carbides are on the contrary seldom reported and considered.

## I.2.2 Austenite nucleation

Now that we have defined the main characteristics of our initial microstructures, we will try to describe how the formation of austenite from them is described in the literature. Cementite particles are reported to be preferential nucleation sites for austenite [Bel+19; Chb+14; HPM04; MGF11; Tei+21; TM18]. Their high density in pearlite colonies makes these regions the first favorable nucleation site for austenite [BVS22; Chb+14; HPM04; Li+13; MGF11; Tei+21; TM18]. When observed, inter-granular cementite particles out of these cementite aggregates, such as previous inter-granular clusters, are expected to be the second preferential nucleation sites. Triple points of recrystallized ferrite were also identified as possible nucleation sites for austenite, but only after saturation of cementite particles (either in aggregates or in inter-granular clusters) [BVS22; Bel+19; HPM04; Li+13; MGF11].

Although rarely mentioned, intra-granular cementite particles are described as last-order nucleation sites [Bel+19; Chb+14]. They are most likely to act as carbon source for growing austenite, thanks to bulk diffusion in ferrite grains [GD81].

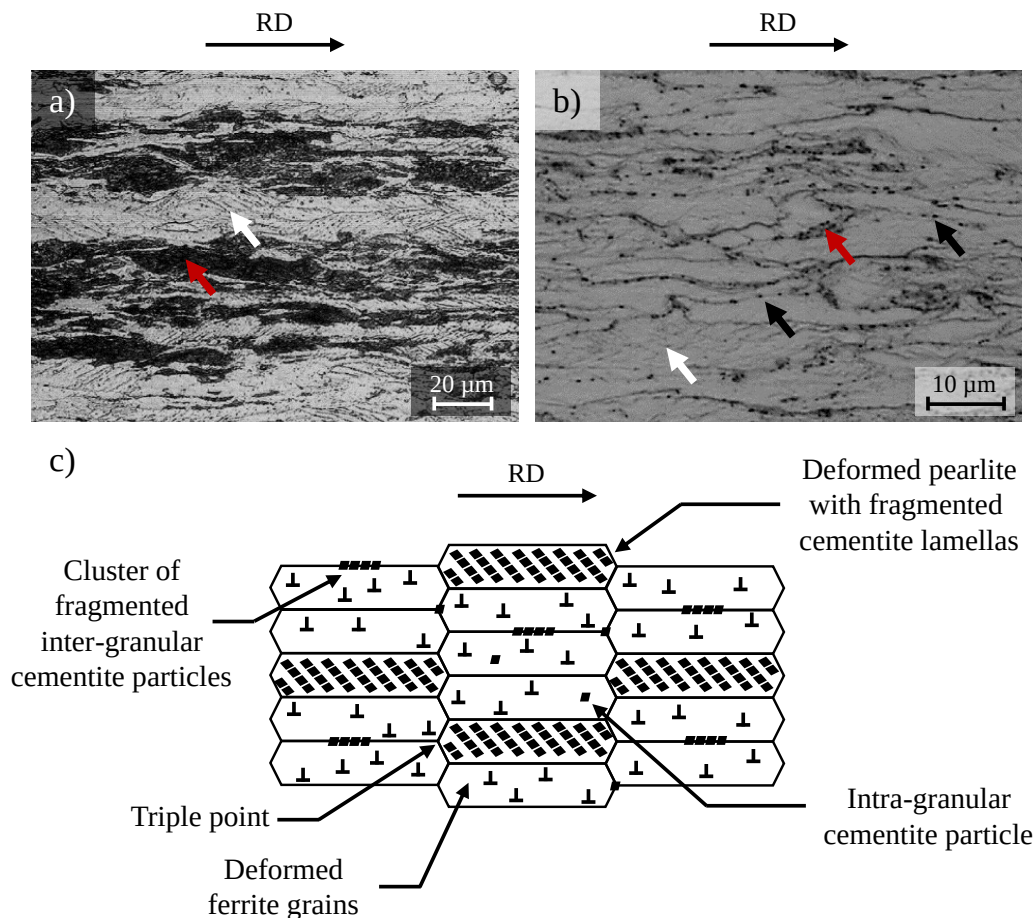


Figure I.15: Microstructures before intercritical annealing of (a) a Fe-0.178C-1.55Mn-1.7Si cold-rolled at 50 % studied in [HPM04] and (b) a DP590 grade cold-rolled at 70 % studied in [Li+13]. Both microstructures show deformed ferrite, indicated by white arrows, and pearlite, indicated by red arrows. The DP590 grade also shows cementite particles at ferrite grain boundaries, indicated by black arrows. A schematic representation of the microstructure before intercritical annealing (c) highlights the main microstructural features.

### I.2.3 Interface conditions governing austenite growth

The present subsection deals with Fe-C-X ternary systems, with carbon as interstitial element diffusing fast and X a substitutional element. It first gives general notions on the thermodynamics of Fe-C-X ternary systems, before detailing thermo-analyses of austenite growth from pearlite islands or from spheroidized cementite particles.

#### I.2.3.1 Thermodynamics of Fe-C-X ternary systems

Similarly to equilibrium in binary, the Ortho-Equilibrium (OE) assumption defines the global thermodynamic equilibrium in the ternary system by the equality of chemical potential of each component in all phases. The OE condition defines a tangent plane common to the Gibbs free energy surfaces of all present phases. Figure I.16 represents the OE in a ferrite-austenite mixture considering the ternary system Fe-C-X, with X a substitutional element. This representation

is often projected in 2D, in ternary phase diagrams, as shown on Figure I.16. The intersection points of the common plane and the Gibbs free energy surfaces give the composition of phases. Such a pair of compositions is named tie-line.

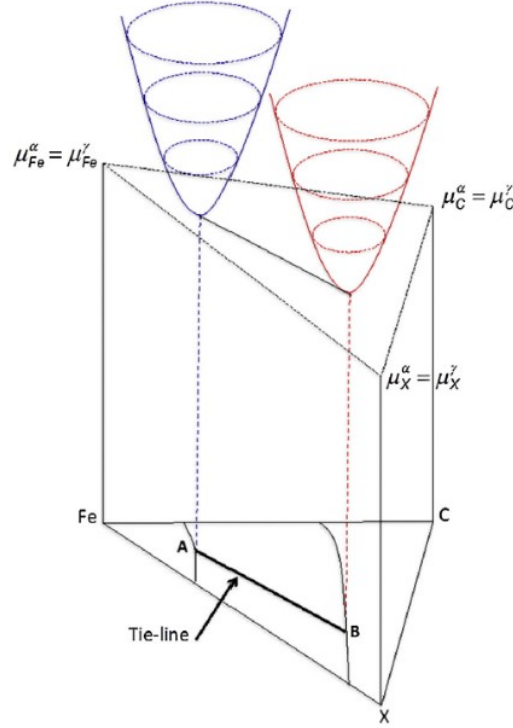


Figure I.16: 3D representation of the OE from [Gou+15]. The blue and red surfaces represent the Gibbs free energy surfaces of ferrite ( $\alpha$ ) and austenite ( $\gamma$ ) respectively as a function of the ternary composition at a given temperature. The tangent plane defines the OE where the chemical potential of each of the three elements is equal between the phases. The projection of the intersections between the tangent plane and the Gibbs free energy surfaces defines a tie-line in the two-phase domain.

The Local Equilibrium (LE) assumption defines a local thermodynamic equilibrium at the interface between phases. The LE approach was first designed and used for  $\gamma \rightarrow \alpha$  transformation [Coa72; Coa73b; Hul47; Hul53; PwK64] during the cooling of steels from the austenitic state. Still, the LE assumption was used to describe the reverse  $\alpha \rightarrow \gamma$  transformation [ECP; Oll+17; SDM81; Tei+21; Wei+13; WPE81] during heating in the intercritical or subcritical range. Considering the austenite ( $\gamma$ ) growth in ferrite ( $\alpha$ ), the LE imposes the equality of chemical potentials of each component in both phases, as follows:

$$\begin{cases} \mu_{Fe}^{\alpha} = \mu_{Fe}^{\gamma} \\ \mu_{C}^{\alpha} = \mu_{C}^{\gamma} \\ \mu_{X}^{\alpha} = \mu_{X}^{\gamma} \end{cases} \quad (\text{I.4})$$

Any tangent plane common to both Gibbs free energy surfaces of ferrite ( $\alpha$ ) and austenite ( $\gamma$ ) respects the LE conditions and, thus, describes a possible tie-line. The OE tie-line belongs to this set of tie-lines and is the one passing through the bulk alloy composition. Figure I.17

represents the phase diagram and the profile of the substitutional element X at the interface at a given temperature in a Fe-C-X steel where X is either a  $\gamma$  stabilizer, typically manganese, (a) or an  $\alpha$  stabilizer, such as silicon, (b). The tie-line at OE is drawn with a dotted line. There is no composition gradient in the phases in that last case.

The equilibrium description of ternary systems can be generalized to multi-component systems. In a system containing carbon and N substitutional elements, the equilibrium at the interface between ferrite ( $\alpha$ ) and austenite ( $\gamma$ ) by the equality of chemical potential of all component in both phases, as follows:

$$\begin{cases} \mu_{Fe}^{\alpha} = \mu_{Fe}^{\gamma} \\ \mu_C^{\alpha} = \mu_C^{\gamma} \\ \mu_{X_i}^{\alpha} = \mu_{X_i}^{\gamma}, \text{ for } 1 \leq i \leq N \end{cases} \quad (\text{I.5})$$

The LE condition defines a tangent hyperplane common to both Gibbs free energy surfaces of ferrite ( $\alpha$ ) and austenite ( $\gamma$ ).

Along a phase transformation under LE assumption, the interface conditions are given by a current tie-line, named operative tie-line. At a given time and temperature, the operative tie-line is chosen such that the LE conditions given by Equation I.4 are fulfilled and the velocity of the interface  $v$  is given by carbon or substitutional local mass balance [Gou+15]:

$$\begin{cases} J_C^{\gamma} - J_C^{\alpha} = \frac{v}{V_m} (x_C^{\gamma/\alpha} - x_C^{\alpha/\gamma}) \\ J_X^{\gamma} - J_X^{\alpha} = \frac{v}{V_m} (x_X^{\gamma/\alpha} - x_X^{\alpha/\gamma}) \end{cases} \quad (\text{I.6})$$

With  $J_C^{\gamma}$  and  $J_C^{\alpha}$  the molar carbon flux in austenite and ferrite,  $J_X^{\gamma}$  and  $J_X^{\alpha}$  the molar flux of the substitutional element X in austenite and ferrite,  $x_C^{\gamma/\alpha}$  and  $x_X^{\gamma/\alpha}$  the molar content of carbon and X in austenite at the interface and  $x_C^{\alpha/\gamma}$  and  $x_X^{\alpha/\gamma}$  the molar content of carbon and X in ferrite at the interface. The molar volume  $V_m$  is considered equal in all of the studied phases [Gou+15].

When carbon diffuses much faster than the substitutional element X, which is often the case in steels, two extreme scenarios are often considered: either the substitutional X undergoes significant partitioning, the so-called Local Equilibrium with Partitioning (LEP) mode, or not, named Local Equilibrium with Negligible Partitioning (LENP). Figure I.18 represents the phase diagram and the profile of the substitutional element X at the interface at a given temperature in a Fe-C-X steel where X is either a  $\gamma$  stabilizer (a and c) or an  $\alpha$  stabilizer (b and d). The operative tie-lines considering Local Equilibrium with Partitioning (a and b) and LENP (c and d) are drawn with a dotted line.

Under the LEP mode, the substitutional X is redistributed in the phase it stabilizes, as schematized in Figure I.18 when X is a  $\gamma$  stabilizer (a) or an  $\alpha$  stabilizer (b). Manganese, as a  $\gamma$  stabilizer, tends to partition in austenite, while silicon, an  $\alpha$  stabilizer, redistributes in ferrite. Under the LENP mode, schematized in Figure I.18 when X is a  $\gamma$  stabilizer (c) or an  $\alpha$  stabilizer (d), the growing phase inherits the u-fraction of the previous phase. The u-fraction of a phase  $\Phi$  in substitutional element X,  $u_X^{\Phi}$  is given by:

$$u_X^{\Phi} = \frac{x_X^{\Phi}}{1 - x_C^{\Phi}} \quad (\text{I.7})$$

With  $x_X^{\Phi}$  the molar fraction of  $\Phi$  in substitutional X and  $x_C^{\Phi}$  the molar fraction of  $\Phi$  in carbon. The composition profile of X presents a narrow spike at the interface to maintain the

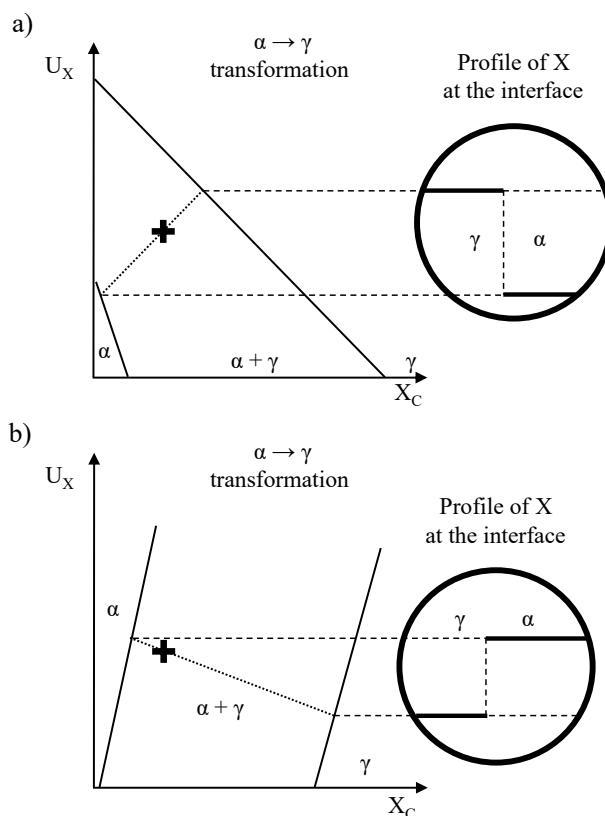


Figure I.17: Schematized phase diagram and profile of the substitutional element X at the interface at a given temperature in a Fe-C-X steel where X is either a  $\gamma$  stabilizer (a) or an  $\alpha$  stabilizer (b). The operative tie-line considering OE is drawn with a dotted line.

LE conditions. Using experimental evaluation of ferrite growth rate, the thickness of this spike was evaluated to be smaller than the interatomic distance [Coa73b], leading some authors to qualify this model as unrealistic [Bha16; Coa73a].

The Para-Equilibrium mode (PE mode), introduced by Hultgren [Hul47], describes a partial equilibrium where the fastest element (usually carbon in steels) respects a Local Equilibrium, whereas, the slowest element (usually the substitutional X) diffuses too slowly to redistribute, even in a narrow spike. It avoids the computation of an "unrealistic" spike.

### I.2.3.2 Austenite nucleation and growth from pearlite islands

The growth of austenite from a ferrite-pearlite microstructure was studied in the early 80's in Fe-C-Mn steels by Speich et al. [SDM81]. The austenite formation is studied during intercritical annealing at temperatures between 740 °C and 900 °C. This experimental and simulation work highlights that austenite formation from pearlite islands takes place in four steps, illustrated in Figure I.19.

First, austenite nucleates on the ferrite-pearlite grain boundaries. The pearlite islands dissolve rapidly, resulting in carbon-rich austenite islands, as pictured in Figure I.19 (a). Their carbon concentration is far higher than at OE. Then, the carbon-rich austenite islands grow fast in the surrounding ferrite matrix. This growth is first controlled by carbon diffusion (LENP

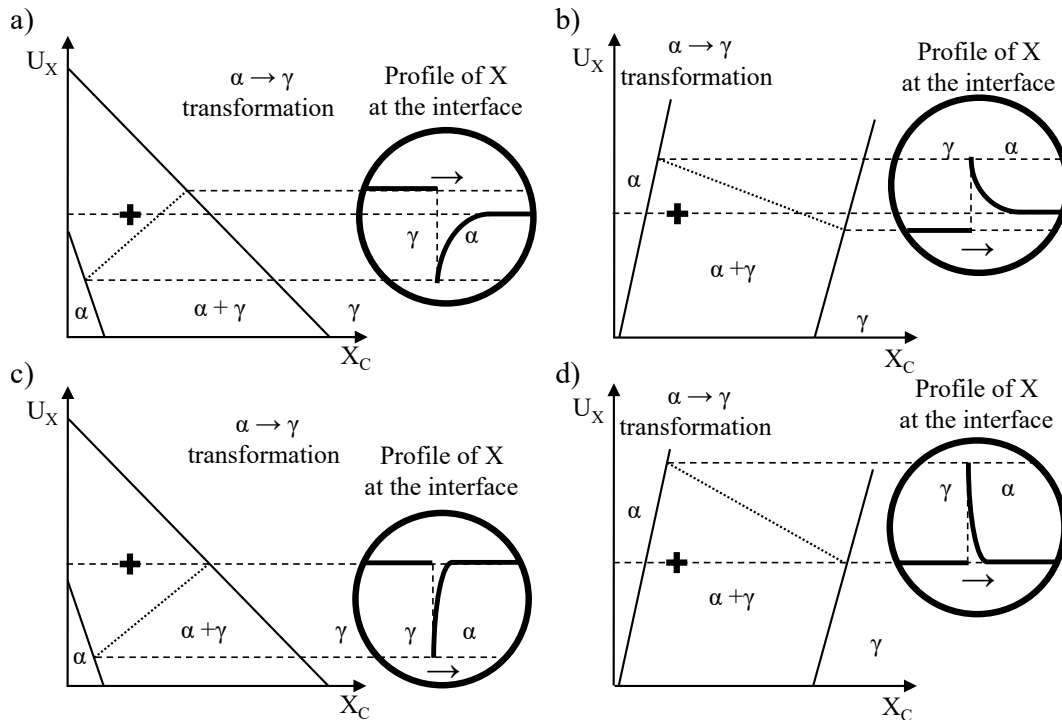


Figure I.18: Schematized phase diagram and profile of the substitutional element X at the interface at a given temperature in a Fe-C-X steel where X is either a  $\gamma$  stabilizer (a and c) or an  $\alpha$  stabilizer (b and d). The operative tie-line considering Local Equilibrium with Partitioning (a and b) and LENP (c and d) are drawn with a dotted line.

mode) in austenite and occurs with negligible manganese partition, as shown in Figure I.19 (b). Later, the growth becomes controlled by manganese diffusion in ferrite (LEP mode), as represented in Figure I.19 (c). Consequently, as manganese diffusion is significantly slower than carbon diffusion, the austenite growth rate decreases. The ultimate stage consists in reaching the OE by slow manganese homogenization in the austenite. The kinetics is controlled by manganese diffusion in austenite (LEP mode), which is two orders of magnitude slower than in ferrite. Manganese equilibration requires longer time than any of the previous stages. This interpretation claims that the interface conditions governing the kinetics, and consequently the growth rate, change during the transformation.

These austenite growth stages were observed in studies starting from different microstructures both experimentally and numerically [Kam+15; Tei+21; Wei+13]. Figure I.20 plots the austenite formation kinetics during isothermal holding at various intercritical temperatures of a medium manganese steel studied in [Kam+15]. These simulation results obtained using the DIC-TRA module of the Thermo-Calc software shows well the succession of growth modes towards the OE highlighted by Speich et al [SDM81], which are reported in Figure I.20.

In Figure I.20, the OE austenite fraction is reached at point D. During the austenite growth under LEP mode indicated c), the austenite fraction increases and exceeds the austenite fraction at OE. During the final step controlled by manganese diffusion in austenite, the interface usually goes backwards and the austenite fraction decreases down to the OE fraction. This fraction overshoot (i.e. the austenite fraction exceeding the OE) is due the manganese heterogeneity in

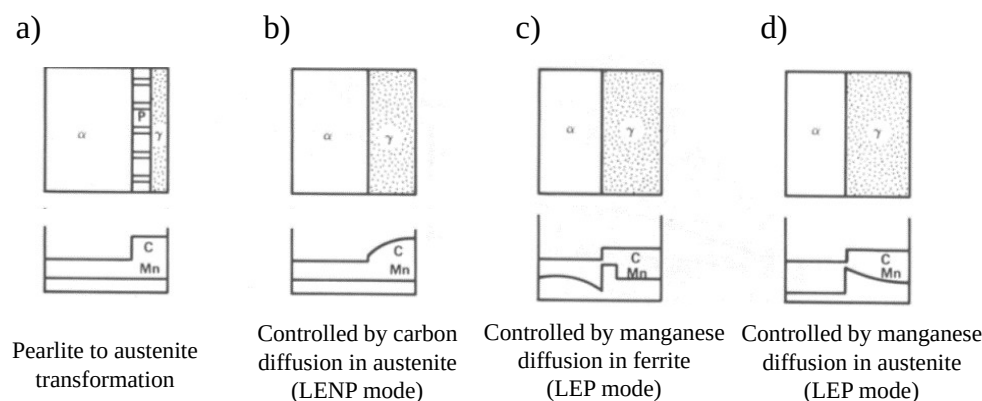


Figure I.19: Thermo-kinetic stages of austenite formation from an initial ferrite-pearlite microstructure to OE completion (from [SDM81]) (phases and their local C and Mn composition fields).

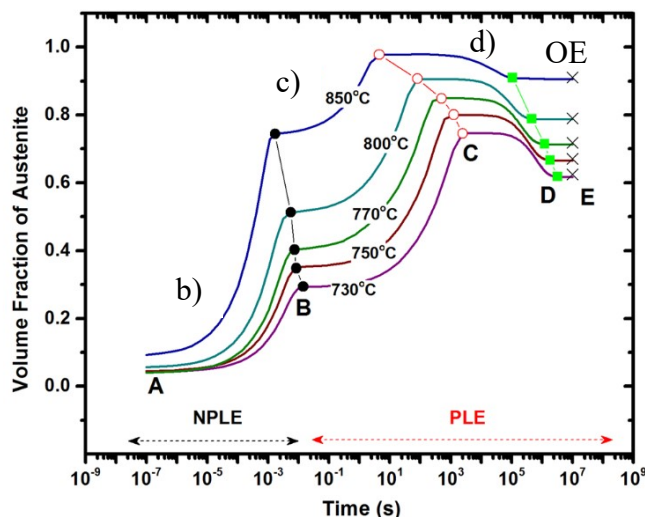


Figure I.20: Austenite formation kinetics during annealing at various temperatures of a medium manganese steel simulated with the DICTRA module of the Thermo-Calc software. (adapted from [Kam+15])

austenite, as explained by many authors in the literature [HPM04; Kam+15; Lai+16; Mor19; Oll+17; Wei+13]

### I.2.3.3 Austenite nucleation and growth from spheroidized cementite particles

As mentioned in the previous subsection, carbides isolated in the ferrite matrix are both nucleation sites and as sources of carbon for austenite. Austenite formation in Fe-C-X steels in a mixture of spheroidized carbides and ferrite is also documented [Eno+18; Lai+16; Liu+91; Mar+20; Miy+10; Oll+17; Tei+21; Wu+20], but more rarely than from pearlite. It is well known that austenite growth from spheroidized cementite particles may occur either under LEP mode

or LENP mode [Eno+18; GMD12; Lai+16; Miy+10; Oll+17; Tei+21]. Several thermodynamic criteria were given to determine the cementite dissolution mode.

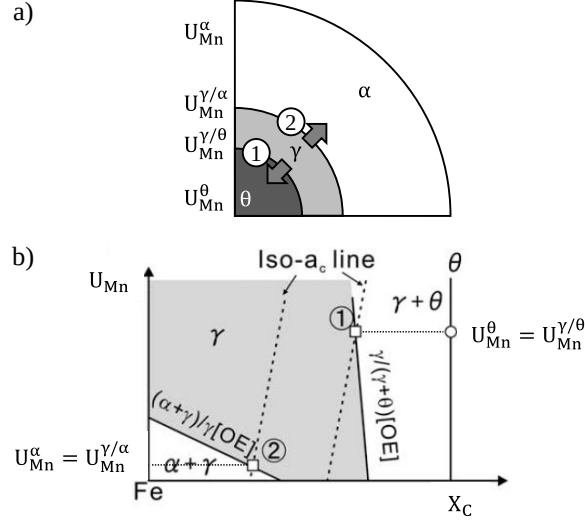


Figure I.21: Schematic representation of the simulation cell used to study the dissolution of a cementite particle  $\theta$  in a ferrite matrix (a) and the schematic Fe-C-Mn phase diagram at the annealing temperature (b). The initial manganese composition of ferrite and cementite are written  $U_{Mn}^{\alpha}$  and  $U_{Mn}^{\theta}$  respectively. The squares represent the austenite composition at the interfaces, written  $U_{Mn}^{\gamma/\theta}$  at interface 1 and  $U_{Mn}^{\gamma/\alpha}$  at interface 2. The austenite compositions at interfaces are indicated considering LENP mode, i.e. considering no manganese partition ( $U_{Mn}^{\theta} = U_{Mn}^{\gamma/\theta}$  and  $U_{Mn}^{\alpha} = U_{Mn}^{\gamma/\alpha}$ ). (adapted from [Miy+10])

One of these criteria is given by Miyamoto et al. [Miy+10]. Their criterion uses the activity, defined for an element X in a phase  $\Phi$  as  $a_X^{\Phi} = \exp\left(\frac{\mu_X^{\Phi} - \mu_X^{\Phi 0}}{RT}\right)$ , with  $\mu_X^{\Phi}$  the chemical potential of the element X in a phase  $\Phi$ ,  $\mu_X^{\Phi 0}$  the standard chemical potential, R the gas constant and T the temperature. Their numerical work investigates the dissolution of a cementite particle  $\theta$  in a ferrite matrix. The simulation cell used is represented in Figure I.21 (a). Figure I.21 (b) schematizes the Fe-C-Mn phase diagram at the annealing temperature. The initial manganese composition of ferrite and cementite are written  $U_{Mn}^{\alpha}$  and  $U_{Mn}^{\theta}$  respectively. The squares represent the austenite composition at the interfaces, written  $U_{Mn}^{\gamma/\theta}$  at interface 1 and  $U_{Mn}^{\gamma/\alpha}$  at interface 2. The austenite compositions at interfaces are indicated considering LENP mode, i.e. considering no manganese partition ( $U_{Mn}^{\theta} = U_{Mn}^{\gamma/\theta}$  and  $U_{Mn}^{\alpha} = U_{Mn}^{\gamma/\alpha}$ ). The dashed lines represent carbon iso-activity lines in austenite. As plotted in Figure I.21 (b) the carbon activity is different across interfaces in austenite. Consequently, a gradient of carbon activity exists across austenite. While the activity of carbon is not homogeneous in austenite, rapid carbon diffusion tends to equilibrate the carbon activity. The austenite grows under LENP mode. Once the carbon activity reaches its equilibrium value, i.e. the same iso-activity line crosses both the austenite composition at the  $\gamma/\theta$  interface (1) and at the  $\gamma/\alpha$  interface (2), the phase transformation continues, driven by manganese diffusion (LEP mode).

The equality of carbon activity in austenite at the interfaces, the criterion given by the work of Miyamoto et al. [Miy+10], defines a critical temperature, called Partition to Non-partition Transition Temperature (PNTT) [Eno+18; GMD12; Xia+13]. Under this critical temperature,

growth occurs under the LEP mode, while the LENP mode is active above.

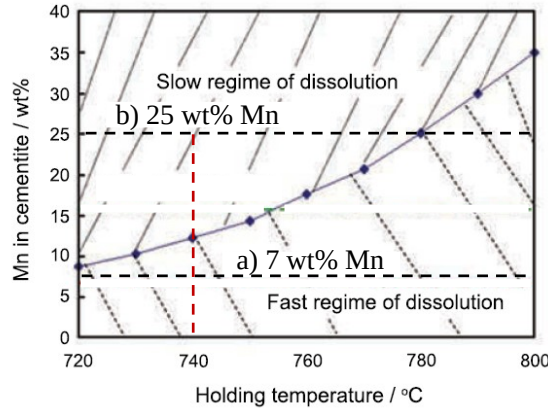


Figure I.22: Map of the cementite dissolution modes as a function of cementite composition in manganese and annealing temperature (adapted from [GMD12]). The black horizontal dashed lines indicate the cementite compositions considered in Figure I.23. The red vertical dashed line indicates the annealing temperature considered in Figure I.23. This map predicts a dissolution under LENP mode for the particle with 7 wt% Mn and a dissolution under LEP mode for the particle with 25 wt% Mn.

The PNTT depends on the cementite composition in substitutional elements [Eno+18; GMD12; Mor19]. Figure I.22 maps the cementite dissolution modes as a function of its composition in manganese and the annealing temperature. The PNTT is plotted with blue diamonds as a function of the composition of the dissolving cementite particle. For instance, the composition of the cementite particles studied in [Lai+16] are reported on Figure I.22 with black dashed lines.

Figure I.23 show the kinetics of austenite formation from cementite particles during annealing at 740 °C simulated using DICTRA software. The composition in manganese of the cementite particle is set at 7 wt% in (a) and 25 wt% in (b). At 740 °C (in red dashed line in Figure I.22), Figure I.22 predicts a fast dissolution under LENP mode for the particle with 7 wt% Mn (Figure I.23 a) and a slow dissolution under LEP mode for the particle with 25 wt% Mn (Figure I.23 b). Please note that the duration of the transformation increases by an order of magnitude.

A succession of stages is observed during the formation of austenite from isolated cementite particles during a isothermal holding. Considering a cementite particle with 7 wt% of manganese (Figure I.23 a), the austenite grows following the same stages as during austenite formation from pearlite (Figure I.19) and starts under LENP mode, as predicted by Figure I.22. Considering a cementite particle with 25 wt% of manganese Figure I.23 (b), the austenite formation no longer shows the carbon diffusion controlled stage and starts directly under LEP mode, as predicted by Figure I.22. Consequently, the austenite formation from cementite particles can be strongly affected by the manganese composition of the particles and slowed down by a growth under LEP mode.

Several phase transformation modes can occur in sequence during the austenite formation from spheroidized cementite particles in isothermal conditions. Figure I.23 (a) highlights the transition from LENP to LEP mode during the dissolution of a cementite particle with 7 wt% Mn.

During a continuous heating, the succession can be quite different as the PNTT can be exceeded during the heating stage itself. In a numerical investigation, published in [Cou+23]

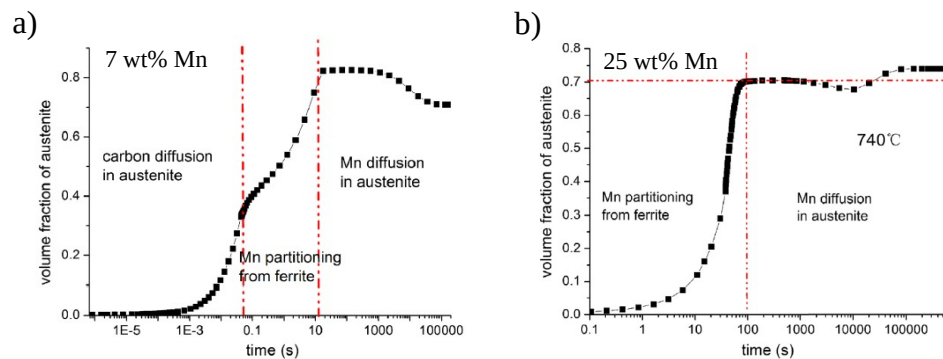


Figure I.23: Austenite formation kinetics during an isothermal treatment at 740 °C. The composition in manganese of the cementite particles is set at 7 wt% in (a) and 25 wt% in (b). (adapted from [Lai+16])

developed during this PhD work, we simulated the dissolution of cementite particles in an industrial DP600 during a continuous heating at 3 °C/s. The simulation cell was similar to the one represented in Figure I.21 (a). The cementite particle initially contains 8.8 wt% Mn. Figure I.24 plots the operative tie-line at the interface  $\gamma/\alpha$  at 730 °C (dark-blue), 740 °C (blue), and 760 °C (green). First, the particle dissolves slowly, under LEP mode, as shown by the operative tie-line at 730 °C (dark-blue). Then, the operative tie-line at 740 °C corresponds to a LENP mode as represented in Figure I.18 (c). Along the heating stage, the PNTT of the particle is overcome and the cementite particle dissolves fast under LENP mode. At 760 °C, the operative tie-line is once again of the LEP type as shown in Figure I.18 (a). At this temperature, the cementite particle is completely dissolved. The growth of the austenite continues, controlled by manganese diffusion.

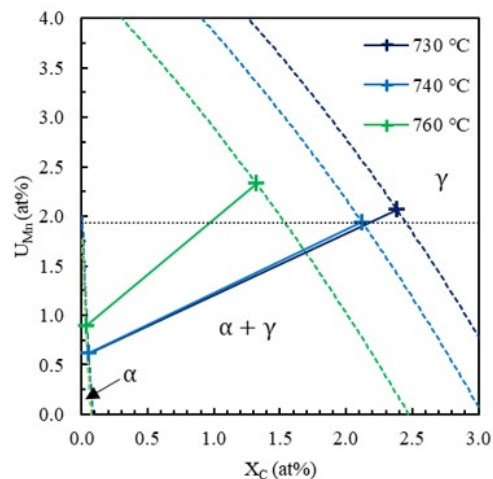


Figure I.24: Operative tie-lines at the interface  $\gamma/\alpha$  at 730 °C (dark-blue), 740 °C (blue), and 760 °C (green) during heating at 3 °C/s simulated with DICTRA. The initial manganese fraction in ferrite is indicated by a black dotted line (from [Cou+23]).

In such microstructures (spheroidized cementite particles in a ferrite matrix), not all cementite particles are austenite nucleation sites. As exposed in Subsection I.2.2, inter-granular particles are preferential nucleation sites due to the reduced nucleation energy barrier by heterogeneous nucleation. On the contrary, intra-granular particles are less favorable nucleation sites [Lai+16; Tei+21; Wu+20].

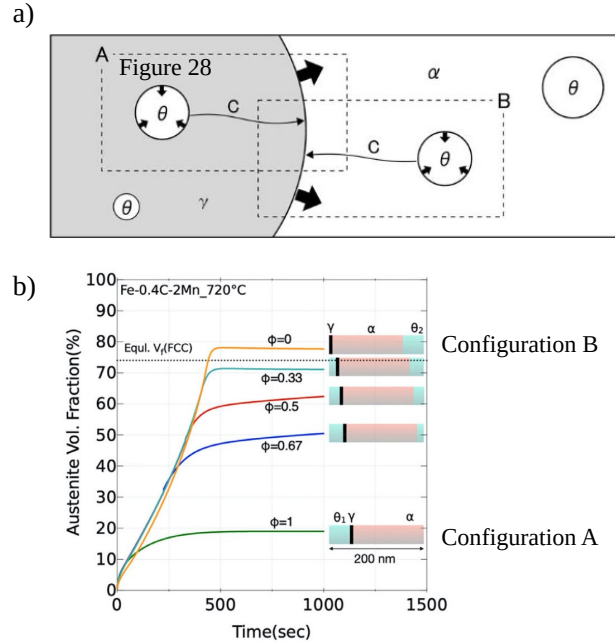


Figure I.25: Schematic representation (a, adapted from [Miy+10]) and austenite formation kinetics (b, adapted from [Wu+20]) during the dissolution of cementite particles. Cementite particles can be nucleation sites (Configuration A) or not (Configuration B). In configuration B, carbon diffuses through ferrite from the dissolving cementite particle to the growing austenite. In (b), the proportion of nucleation sites among cementite particles is indicated by  $\Phi$ . When  $\Phi = 1$ , all cementite particles are nucleation sites. When  $\Phi = 0$ , no cementite particle is a nucleation site.

Figure I.25 shows a schematic representation of the possible dissolution configurations of cementite particles. Configuration A represents cementite particles as nucleation sites. They dissolve by carbon diffusion in austenite, following the kinetic mechanisms described above. On the contrary, configuration B shows a cementite particle which is not a nucleation site. Such particles dissolve by carbon diffusion through ferrite from the dissolving cementite particle to the growing austenite [Eno+18; Hil71; Miy+10; Wu+20].

Wu et al. [Wu+20] numerically investigate the effect of the proportion of nucleation sites among the cementite particles on the austenite formation kinetics in a Fe-0.4C-2.0Mn during annealing at 720 °C. Figure I.25 (b) plots the austenite formation kinetics considering a proportion  $\Phi$  of nucleation sites among cementite particles. When  $\Phi = 1$ , all cementite particles are nucleation sites. When  $\Phi = 0$ , no cementite particle is a nucleation site. Their results show higher final austenite fractions when  $\Phi$  tends to 0. When  $\Phi = 0$ , the final austenite fraction can even surpass the OE fraction. As long as ferrite contains enough manganese, the austenite continues to grow with manganese partition. When a cementite particle dissolves without being

a nucleation site, its manganese is released in ferrite. This extends the LEP mode driven by manganese diffusion in ferrite and leads to higher final austenite fractions.

Finally, considering multi-component systems is important, as simulated kinetics using ternary systems are often significantly faster than experimental kinetics (Figure I.34). The enrichment of cementite in manganese or chromium stabilizes the carbide and slow down the austenite growth [Hil71; Lai+16; Mar+20; Oll+17; Wu+20; Zha+13]. The addition of silicon or aluminum helps manganese and chromium partitioning in cementite and slows down austenite growth [Wu+20].

#### I.2.3.4 Competitions during austenite growth

As mentioned in the overview on austenite formation, the microstructure of DP grade steels usually contains pearlite islands in a ferrite matrix [BVS22; Chb+14; HPM04; Li+13; Tei+21; TM18], as well as clusters of cementite particles isolated in the ferrite matrix [Bel+19; Chb+14; Li+13; Tei+21; TM18] (Figure I.15).

Moreno et al. [Mor19] proposed a thermo-kinetic analysis of the austenite formation in an industrial DP600 steel considering the austenite formation from both the pearlite islands and the isolated cementite particles. They study intercritical annealing at 800 °C, using three heating rates: 3 °C/s, 30 °C/s and 100 °C/s. They separate the studied system in two closed subsystems, each containing one of the two cementite aggregates (pearlite or isolated cementite particles), and study them separately.

Around 710 °C, austenite nucleates and grows on cementite particles isolated in the matrix (first cementite aggregate). These cementite particles are mainly inter-granular. Three steps were observed. The austenite grows slowly with manganese redistribution (under LEP mode) up to the PNTT [Miy+10]. Once the PNTT is reached, the austenite grows quickly without manganese redistribution (under LENP mode) up to complete dissolution of the cementite particle.

The PNTT of the cementite particles increases with their enrichment in manganese, as shown by their simulations and exposed in the previous subsection. Their study highlights manganese enrichment of the cementite particles during slow heating (3 °C/s), before austenite nucleation. Thus, the fast dissolution of the cementite particles under LENP mode occurs at higher temperatures during slow heating.

Around 760 °C, the austenite forms rapidly from the pearlite islands (second cementite aggregate) in a narrow temperature range. This transformation occurs with manganese redistribution (LEP mode), but with very short diffusion distances. The heating stage ends with austenite growth without manganese partitioning (LENP mode). During the isothermal holding, they showed that austenite grows with manganese redistribution (LEP mode) in both subsystems.

During the isothermal holding at 800 °C, the subsystem initially containing the pearlite is fully austenitized in less than 1 s, regardless of heating rate. On the contrary, the growth of austenite from the clusters of cementite particles is sensitive to heating rate due to the cementite enrichment during slow heating. As the PNTT is shifted to higher temperature, the dissolution of the cementite particle under LEP mode is extended. Low heating rates also favor manganese redistribution after complete dissolution of the cementite particle, as shown in [Cou+23]. Consequently, a larger amount of manganese is redistributed in austenite during the slow heating stage. Less manganese is available for the austenite growth under LEP mode during the isothermal holding and less austenite is formed.

The simulated austenite fraction, performed with Thermo-Calc/DICTRA and plotted in Figure I.34, reproduced experimentally observed characteristics of the transformation, such as

the austenite fraction at the end of the holding period exceeding the OE fraction.

However, the kinetics obtained are far too fast. The kinetics of austenite formation from the cementite particles is very steep at the PNTT and far from the smooth experimental kinetics. This is attributed to the consideration of mean compositions and sizes of cementite particles. Finally, considering the minor alloying elements, chromium and silicon, is expected to shift the simulated fractions closer to the experimental ones.

In addition, the simulation cell containing the pearlite comes to full austenitization but the final carbon content of the cell is higher than at OE. This result indicates that the hypothesis of closed subsystems may be too strong. Besides, in our recent numerical investigation on the same material [Cou+23], we highlight interactions between austenite islands through carbon diffusion in the ferrite matrix.

Inspired by the thermo-kinetic analysis on the austenite formation exposed above, our numerical study on austenite formation in a ferrite/pearlite microstructure with cementite particles isolated in the ferrite matrix show that different interface conditions, LENP or LEP, may coexist along the heating stage. Indeed, after dissolution of the cementite particles and transformation of the pearlite along slow heating (3 °C/s), the austenite formed from the cementite particles grows under LEP mode, while the austenite formed from the pearlite grows under LENP mode.

A simulation cell, represented in Figure I.26 (a), is designed to investigate the growth competition due to different interface conditions. The austenite island on the left is initialized with LENP interface conditions. At the interface set with LEP conditions ( $\gamma_{\text{LEP}}/\alpha$  on the right), a manganese depletion was imitated (Figure I.18 a). Figure I.26 also plots the simulated fraction of the austenite starting with LENP (dotted-dashed line) and the austenite starting with LEP (double dotted-dashed line), as well as the total austenite fractions (solid line) along the heating stage (b) and the isothermal holding stage (c). Only the austenite set with LENP interface conditions ( $\gamma_{\text{LENP}}$  in double dotted-dashed line) grows during the heating stage. The study reveals that the manganese depletion is responsible for a constant gradient of carbon chemical potential established in ferrite and at both interfaces. This gradient leads to a stable carbon flux from austenite set with LEP interface conditions ( $\gamma_{\text{LEP}}$  on the right), to  $\gamma_{\text{LENP}}$  (on the left) along the heating stage. This carbon flux hindered the  $\gamma_{\text{LEP}}$  growth and promoted the  $\gamma_{\text{LENP}}$  growth.

The coexistence of interfaces under LENP and LEP conditions promotes an interaction of austenite growth thanks to a carbon flux in the ferrite matrix from the LEP interface to the LENP interface. As a consequence, an austenite island with LENP interface conditions can exaggeratedly grow at the cost of the growth of an austenite island with LEP interface conditions. Such growth competition not only shows that the subsystems considered in [Mor19; Tei+21] may interact through the ferrite matrix, but it can also partially explain the impacts of heating parameters on the final microstructure in steels. Indeed, the heating rate can promote either LENP or LEP interface conditions during austenite formation from different carbon rich structures (pearlite islands, isolated cementite particles) [Mor19; Tei+21]. Then, the chosen heating rate may promote interface condition interactions, leading to strongly different austenite morphologies.

#### I.2.4 Effect of the heating rate

The austenite growth kinetics is also often shown to depend on the heating rate before the isothermal stage. Figure I.27 illustrates well the trend in a 60 % cold-rolled DP600 studied in [Tei+21] using HEXRD experiments. The austenite fraction during the holding stage at 800 °C

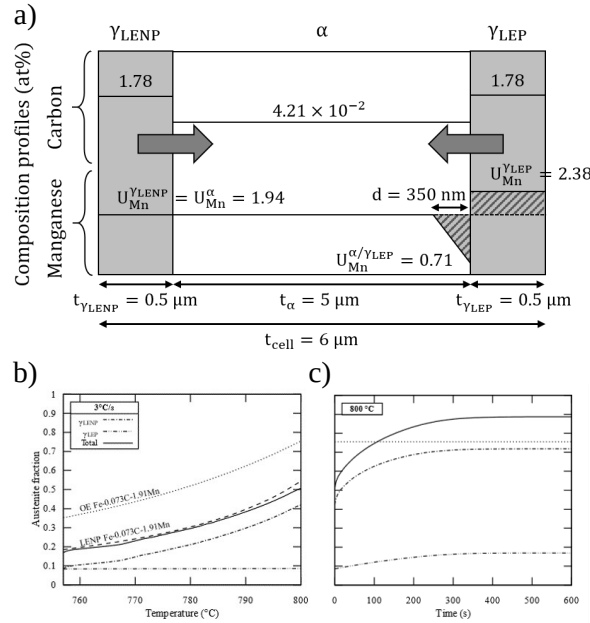


Figure I.26: Growth competition between austenite islands with LENP and LEP interface conditions. (a) schematic representation of the simulation cell. At the interface set with LEP conditions ( $\gamma_{LEP}/\alpha$  on the right), a manganese depletion is imitated (Figure I.18 a). The simulated fraction of the austenite starting with LENP (dotted-dashed line) and the austenite starting with LEP (double dotted-dashed line), as well as the total austenite fractions (solid line) are plotted during the heating stage (b) and the isothermal holding stage (c) [Cou+23]

for 10 min is plotted after heating at 3 °C/s (red), 30 °C/s (blue) and 100 °C/s (black). The higher the previous heating rate, the faster the austenite formation kinetics and the higher the austenite fractions at the end of the intercritical annealing [BVS22; Bel+19; Chb+14; HPM04; Li+13; MGF11; Mor19; Tei+21; TM18].

The heating rate not only affects the austenite formation kinetics, but also the morphology of the growing austenite. Figure I.28 shows microstructures of a cold-rolled Fe-C-Mn-Mo steel heated at 1 °C/s (a) or 100 °C/s (b) and annealed at 750 °C for 10 min. Martensite (austenite before quenching) is in dark grey and ferrite in light grey.

After slow heating (a), the microstructure is characterized by equiaxed ferrite grains, enlaced by austenite (martensite after quenching) at the ferrite grain boundaries, as highlighted by the red areas. This "necklace" morphology is typically obtained during intercritical annealing using a low heating rate (lower than 1 °C/s) [BVS22; Bel+19; Chb+14; HPM04; Li+13; MGF11; Mor19; Tei+21; TM18]. On the contrary, the microstructure after fast heating (b), presents a succession of elongated austenite-rich bands, indicated in red on Figure I.28 b, and ferrite-rich zones, with equiaxed recrystallized ferrite grains. The bands are aligned with the rolling direction. This "banded" morphology is obtained during intercritical annealing using a high heating rate (higher than 10 °C/s) [BVS22; Bel+19; Chb+14; HPM04; Li+13; MGF11; Mor19; Tei+21; TM18].

In both slow and fast heated samples, rare small austenite grains are found in recrystallized ferrite grains. Such grains are attributed to austenite nucleation on intra-granular cementite

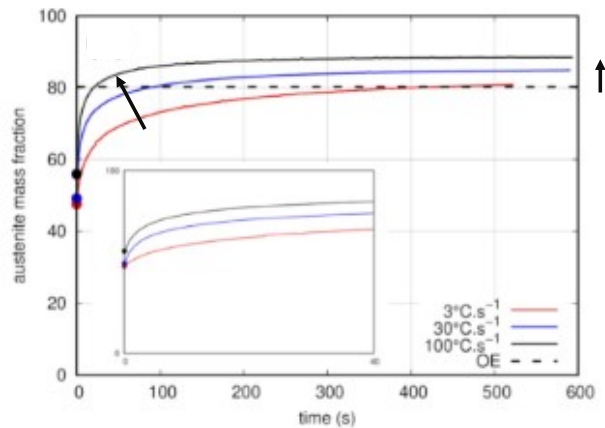


Figure I.27: Austenite formation kinetics in a 60 % cold-rolled DP600 held 10 min at 800 °C after heating at 3 °C/s (red), 30 °C/s (blue) and 100 °C/s (black). The higher the heating rate, the faster the kinetics and the higher the overshoot of the OE fraction at the end of the isothermal holding. (adapted from [Tei+21])

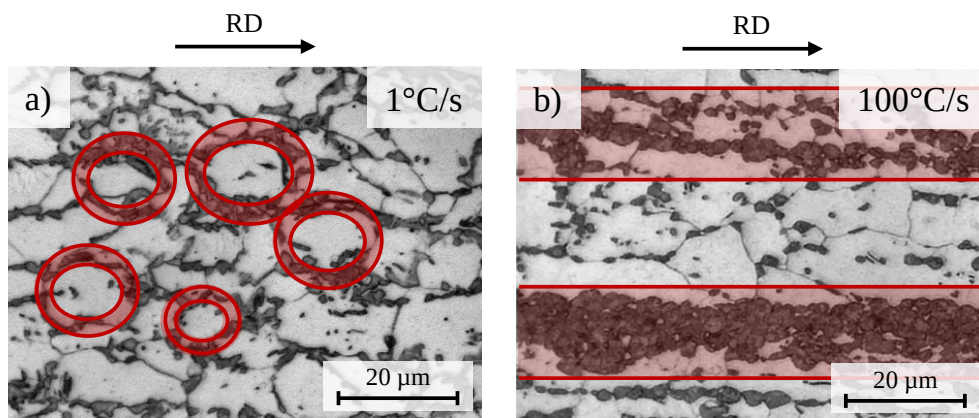


Figure I.28: Microstructures of a cold-rolled Fe-C-Mn-Mo steel heated at 1 °C/s (a) or 100 °C/s (b) and annealed at 750 °C for 10 min. Martensite (austenite before quenching) is in dark grey and ferrite in light grey. A typical "necklace" morphology is observed after slow heating (a), while a more "banded" morphology is obtained after fast heating (b). The red zones show austenite rich zones and their morphology. (adapted from [HPM04])

particles [Bel+19; Chb+14; Mor19; Tei+21].

### I.2.5 Summary on the thermo-kinetics of austenite formation during the intercritical annealing

This section introduced thermo-kinetic analyses of the austenite formation during the intercritical annealing. The more recent insights focus on the complex microstructures and deal with interactions between different carbon-rich structures and minor substitutional elements:

- The addition of chromium, silicon or aluminum slows down the austenite growth.

- Wu et al. [Wu+20] numerically investigate the interaction between cementite particles with and without austenite nucleated on. Their results show a major impact of the dissolution of a cementite particle in ferrite on the austenite formation kinetics.
- Moreno et al. [Mor19] proposed an interesting thermo-kinetic analysis of the austenite formation considering two closed subsystems, one containing the pearlite islands, the other the cementite particles. The simulated austenite fraction reproduced experimentally observed characteristics (the exceed of the OE fraction). But they highlighted also several limitations. In particular, their results suggest that the hypothesis of closed subsystems is too strong.
- Our recent numerical investigation [Cou+23] shows that the coexistence of interfaces under LENP and LEP conditions promotes an interaction of austenite growth thanks to a carbon flux in the ferrite matrix from the LEP interface to the LENP interface. New experiments are presented in Chapter III to discuss further the thermo-kinetic analyses of austenite formation. Our results are then used in Chapter IV to model the austenite formation kinetics and to try to overcome the limitations raised by Moreno et al. [Mor19].

### I.3 Interactions between ferrite recrystallization and phase transformation

As presented in the previous section, the heating rate affects the formation of austenite during intercritical annealing. Both the final morphology of the phase and the kinetics of the transformation depends on the heating rate. In literature, recrystallization is widely claimed to be responsible for these experimental observations.

As a thermally activated mechanisms, the recrystallization of the deformed ferrite matrix is delayed by increasing the heating rate, i.e. by decreasing the time spent at each temperature [Bel+19; HH95]. Consequently, fast heating rates (typically higher than 1 °C/s) generally induce a concomitance of the recrystallization of the ferrite matrix and the austenite formation. Thus, the austenite forms in a partially recrystallized ferrite matrix.

At first sight, no consensus unites the authors on the mechanisms behind austenite morphogenesis or its formation kinetics. Indeed, the following review gathers investigations on austenite formation during intercritical annealing starting from various initial microstructures, containing ferrite and a carbon-rich phase (pearlite [BVS22; Chb+14; HPM04; Li+13; Tei+21; TM18], martensite [Bel+19; MGF11] and/or bainite [MGF11]). Yet, it mainly focuses on initial ferrite/pearlite microstructures. Specifically, this review of the austenite morphogenesis concerns only initial ferrite/pearlite microstructure. The heating rates start from  $\approx 0.1$  °C/s [BVS22; TM18] and go higher than 500 °C/s [Li+13; TM18]. Authors usually call their studied heating rate "low" and "high", but this designation is very relative. In particular, heating rates ranging between 1 °C/s and 5 °C/s can be considered as "low" in [Chb+14; HPM04; Li+13; Mor19; Tei+21] but "intermediate" in [TM18]. In addition, the studied steels present various nominal compositions, with different alloying element contents and showing eventually niobium microalloying [BVS22; Bel+19; MGF11; TM18], known to affect both recrystallization and phase transformations [All+20; Son+14; Ver+09].

This review presents the identified mechanisms, to offer an overview on the current knowledge on the interaction between ferrite recrystallization and austenite transformation. First, we detail the mechanisms identified as leading to a typical necklace morphology during slow heating. Then,

we will describe the mechanisms presented as responsible for the typical banded morphology. We finally present the explanations given for the effects of the heating rate on the austenite formation kinetics.

### I.3.1 The necklace morphology

In literature, the heating rate is usually considered "low", when low enough to guarantee the full recrystallization of the ferrite matrix before the austenite nucleation [BVS22; Bel+19; Chb+14; HPM04; Li+13; MGF11; Mor19; Tei+21; TM18]. Low heating rates are typically lower than 5 °C/s.

During slow heating, an initial ferrite/pearlite microstructure undergoes several modifications before the austenite nucleation. The microstructure before austenite nucleation during slow heating is schematized in Figure I.29, starting from the model initial microstructure in Figure I.15 c).

The carbon-rich phases evolve by diffusion. In pearlite bands, the spheroidization of the fragmented cementite lamellas occurs [BVS22; Chb+14; HPM04; Li+13; MGF11; Tei+21; TM18]. The deformed ferrite recrystallizes, forming small equiaxed grains, due to pinning on the spheroidized cementite particles and manganese solute-drag [BVS22]. Starting from a ferrite-martensite microstructure, martensite tempering during heating leads to spheroidized cementite particles in recrystallized ferrite localized in the area of previous martensite [Bel+19].

Ferrite recrystallization is often reported responsible for a spatial redistribution of cementite particles [Bel+19; Chb+14; Li+13; Tei+21; TM18]. As the ferrite grain boundaries migrate, some particles are crossed by them, while others pin the migrating boundary. Consequently, the cementite particles are divided in "homogeneously" distributed inter-granular particles and eventual intra-granular particles.

Such cementite particles in the ferrite matrix are not systematically observed or studied in literature [HPM04; Yan+85]. Yet, when observed and studied, authors attribute a major role of cementite particles in the austenite morphogenesis [Bel+19; Chb+14; Li+13; Tei+21; TM18]. This is a crucial point for us, as the steels studied in the present work contains such cementite particles (III.1.2.2)

In the literature [BVS22; Bel+19; Chb+14; HPM04; Li+13; MGF11; Tei+21; TM18], the necklace microstructure is widely attributed to recrystallization, which redistributes the austenite nucleation sites evenly in the microstructure and affects their efficiency. Figure I.30 schematically represents the microstructure along austenite formation during slow heating from the model microstructure in Figure I.29.

Cementite particles at recrystallized ferrite grain boundaries become very efficient nucleation sites [Bel+19; Chb+14; HPM04; MGF11; Tei+21; TM18]. The austenite nuclei, now homogeneously distributed in the ferrite matrix, grow then along the ferrite grain boundaries, leading to the necklace microstructure. Two main points of view are given to explain the morphogenesis:

- Some authors [Li+13; MGF11] expose a competition between the growth of austenite nucleated in carbon-rich phases (from pearlite in Figure I.30) and austenite nucleated in the ferrite matrix (on inter-granular cementite particles when observed or ferrite triple junctions). As austenite nucleates and grows from secondary order sites as inter-granular particles or triple junctions in the matrix, less carbon is available for the growth of austenite nucleated in carbon-rich phases. The banded morphology of the carbon-rich phases, inherited from the cold-rolling process, weakens to the advantage of the austenite dispersed in the ferrite matrix.

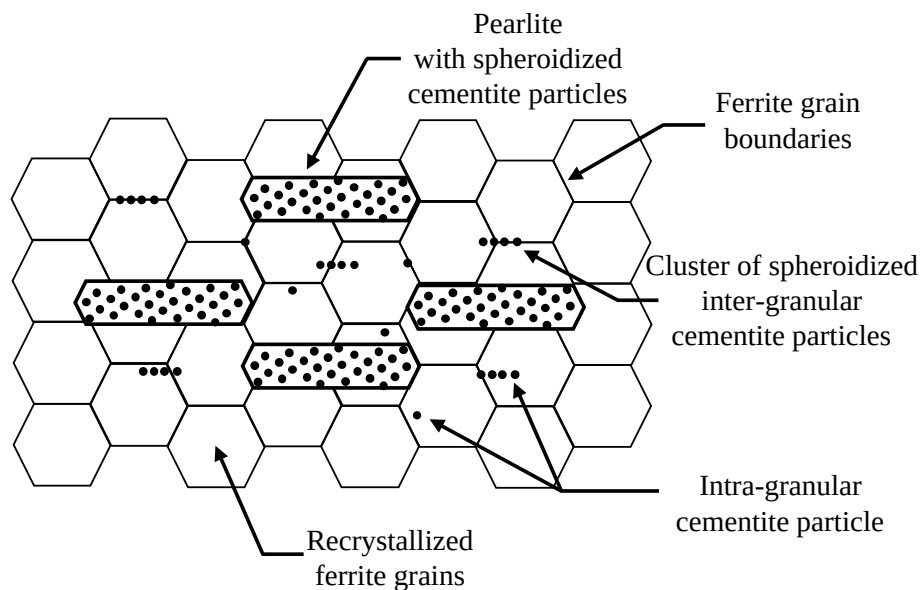


Figure I.29: Schematic representation of the microstructure at  $A_{c1}$  during slow heating.

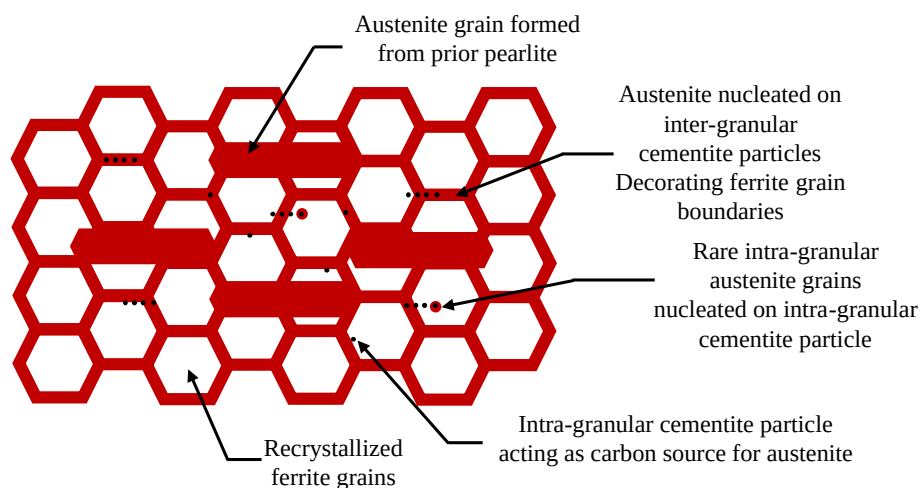


Figure I.30: Schematic representation of the genesis of a necklace microstructure above  $A_{c1}$  during slow heating. Austenite is represented in red, ferrite in white and cementite in black.

- More recently, Bandi et al. [BVS22] propose a "mutual-helping" outlook. In their work, the spheroidization of fragmented cementite particles by carbon diffusion in the recrystallized ferrite grain boundaries leads to the enrichment of the grain boundaries in carbon. The ferrite boundaries and triple points become more efficient nucleation sites. Besides, austenite, nucleated in carbon-rich phases (such as pearlite) or at the ferrite boundaries, grow more easily along the carbon-enriched boundaries. From this point of view, the austenite from carbon-rich phases participate actively to the necklace morphology.

Zhu et al. [ZM15] studied the austenite formation in a DP600 grade steel during annealing at 770 °C after slow heating at 1 °C/s, using a 2D Phase-Field model. The simulated microstructure

is shown in Figure I.31 (a). Austenite grains are red and ferrite grains are white. As explained above, the austenite from pearlite bands inherits their elongated shape. The necklace morphology, well reproduced by the 2D simulation, is mainly due to the inter-granular austenite. But contrary to the two approaches cited above, the heating rate affects weakly the morphology of the austenite forming from pearlite. It neither grows along the ferrite grain boundaries nor shrinks.

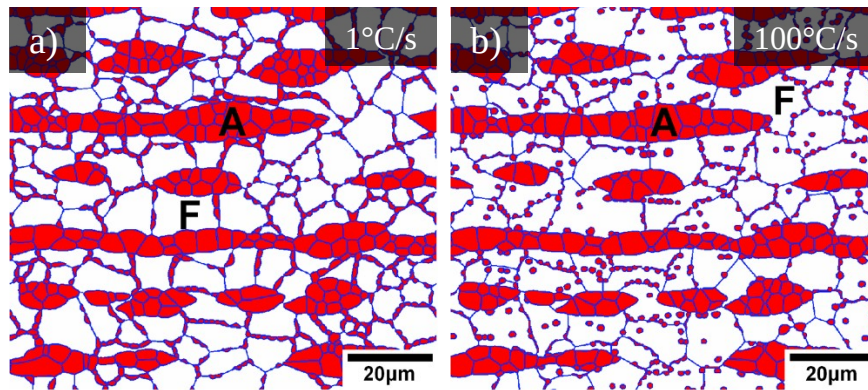


Figure I.31: 2D Phase-Field simulations of the microstructures of a DP600 grade steel annealed at 770 °C for 300 s after heating at 1 °C/s (a) and 100 °C/s (b). Austenite grains are in red (A) and ferrite grains in white (F). (adapted from [ZM15])

Finally, newly intra-granular cementite particles become inefficient nucleation sites. They are more likely to be a carbon source for austenite nucleated at ferrite grain boundaries by carbon diffusion through ferrite [Miy+10; Wu+20]. Yet, eventual austenite nucleation on rare intra-granular cementite particles leads to small austenite grains in recrystallized ferrite grains [Bel+19; Chb+14; Mor19; Tei+21].

### I.3.2 The banded morphology

Authors usually consider the heating rate as "high", when it is high enough (typically higher than 10 °C/s) to delay the recrystallization of the ferrite matrix up to the austenite nucleation [BVS22; Bel+19; Chb+14; HPM04; Li+13; MGF11; Mor19; Tei+21; TM18]. Using such a heating rate, the austenite formation starts and continues in a partially recrystallized ferrite matrix. Eventually, authors consider heating rates as "intermediate" when the ferrite recrystallization has started before the austenite nucleation but is not completed when austenite nucleates [Li+13; TM18]. Then, heating rates are considered "high" only if recrystallization has not started when austenite nucleates. Intermediate heating rates are usually between 1 °C/s and 100 °C/s, while fast heating rates are typically higher than 100 °C/s. The microstructure before austenite nucleation during annealing using an intermediate heating rate is schematized in Figure I.32, starting from the model initial microstructure in Figure I.15 c). The deformed ferrite recovers and partially recrystallizes. Fragmented cementite particles spheroidize. The faster the heating rate, the closer the microstructure before austenite nucleation is to the initial microstructure. Under fast heating (> 100 °C/s), no recrystallized ferrite grains are observed and deformed ferrite grains can be still present [Li+13; TM18]. Eventually, carbon diffusion is so restricted that no spheroidization of the fragmented cementite occurs.

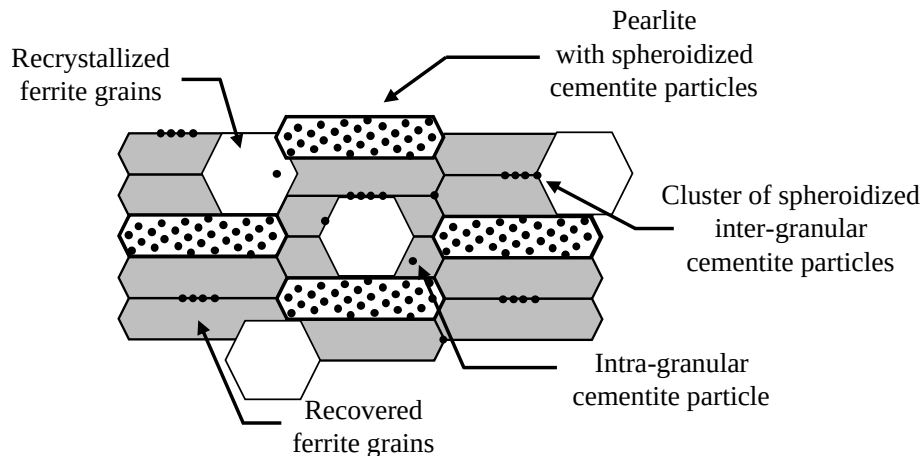


Figure I.32: Schematic representation of the microstructure at  $A_{c1}$  during annealing using an intermediate heating rate.

Figure I.33 represents of the genesis of a banded microstructure above  $A_{c1}$  during fast heating ( $> 10 \text{ }^\circ\text{C/s}$ ), according to the literature review.

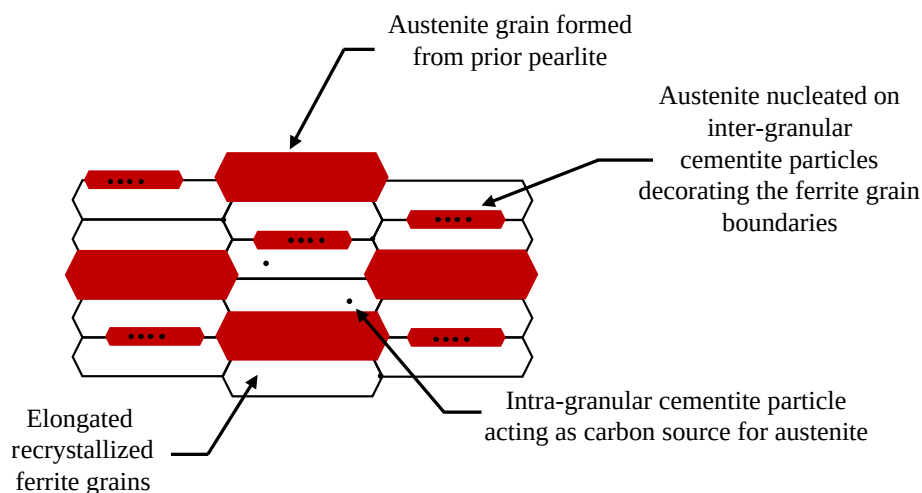


Figure I.33: Schematic representation of the genesis of a banded microstructure above  $A_{c1}$  during fast heating ( $> 10 \text{ }^\circ\text{C/s}$ ).

The banded morphology was first attributed to the initial elongated shape of the carbon-rich phases (pearlite, martensite, ...) inherited from the cold-rolling process [BVS22; Bel+19; Chb+14; HPM04; Li+13; MGF11; Mor19; Tei+21; TM18]. The austenite forming from these elongated islands inherits this elongated shape, as schematized in Figure I.33.

Then, authors claim that this banded layout is emphasized by the concomitance of the ferrite recrystallization and the austenite transformation:

- It was first shown that migrating boundaries are inappropriate nucleation sites [HPM04; Li+13]. Using high heating rates ( $> 10 \text{ }^\circ\text{C/s}$ ), ferrite recrystallization is ongoing when austenite nucleates. This hinders the evenly distributed austenite nucleation at ferrite

grain boundaries. The mechanisms of the necklace morphogenesis (I.3.1) are not activated and the banded morphology inherited from the elongated austenite island formed from the carbon-rich phases is maintained.

- When observed in the ferrite matrix, clusters of cementite particles are identified as the second order cause for the banded microstructure. When recrystallization and austenite formation are concomitant (using either intermediate or high heating rates), most of the cementite particles in inter-granular clusters stay at ferrite grain boundaries, as no recrystallization redistribute them. Thus, the cluster of inter-granular cementite particles offers many favorable nucleation sites aligned with the cold-rolling direction [BVS22; Bel+19; Chb+14; Li+13; Tei+21; TM18]. The austenite nucleated on these clusters inherits their elongated shape, as represented in Figure I.33.

In addition, Mohanty et al. [MGF11] claimed that the carbon diffusion is affected by the heating rate. Higher heating rates mean less time for diffusion. Using intermediate or fast heating rates ( $> 10$  °C/s), carbon is expected to diffuse only at short distances. This limits once again the nucleation at ferrite grain boundaries, but also the austenite growth along the recrystallized ferrite grains.

Under fast heating ( $> 100$  °C/s), the still fragmented cementite particles are less stable, and austenite nucleates and grows quickly, while cementite dissolves. Bandi et al. [BVS22] highlight the absence of carbon enrichment at ferrite grain boundaries, as no spheroidization occurs. The nucleation of austenite at ferrite grain boundaries is restricted and austenite growth from carbon-rich zones is not guided in the ferrite grain boundaries.

- Authors [BVS22; Bel+19; TM18] also claim that the still deformed or recovered ferrite offers a dense and efficient diffusion network for carbon, thanks to their high dislocation density (light grey in Figure I.32). The austenite growth is expected to be easier in the elongated deformed grains. The austenite growth is guided along the elongated ferrite grains, which tends to accentuate the banded morphology.
- Even more subtle details are reported to affect the morphogenesis during fast heating ( $> 100$  °C/s), such as the manganese segregation. First, as already exposed, the carbon-rich phases are located in manganese segregation bands. As manganese is a  $\gamma$ -stabilizer, the austenite formation is catalyzed in the segregation bands. Then, the ongoing recrystallization is expected to be strongly delayed in the segregation bands by solute-drag, but easier in manganese-poor regions [BVS22; TM18]. As exposed above, the austenite growth along the cold-rolling direction is helped in the deformed ferrite in the manganese-rich regions, while the austenite growth in the normal direction is limited by the recrystallized grains in the manganese-poor regions.

In addition, the austenite growing fast in bands constrain the recrystallizing ferrite grains [BVS22; Chb+14; Li+13]. The recrystallized ferrite grains finally adopt a banded shape, as schematized in Figure I.33, limited in their normal growth by austenite bands and following the manganese-poor bands.

- In the numerical work of Zhu et al. [ZM15] on a DP600 grade steel, the 2D Phase-Field simulations accurately reproduces the banded morphology after heating at 100 °C/s, as shown in Figure I.31 (b). The simulated microstructure shows elongated austenite, as well as inter- and intra- granular austenite nuclei. This work confirms the role of pearlite

islands, as they are shown to transform rapidly into elongated austenite bands. But, as already mentioned in the previous subsection, the morphology of the austenite forming from pearlite is weakly sensitive to the heating rate.

Contrary to the authors cited previously, the explanation given by Zhu et al. [ZM15] for the banded microstructure is purely diffusive and ignores any interaction with ferrite recrystallization. Similar conclusions are drawn in the work of Rudnizki et al. [Rud+11].

### I.3.3 Effect on the austenite formations kinetics

As presented in Section I.2.4, the heating rate not only affects the final morphology of the austenite, but also the kinetics of the austenite transformation. As illustrated in Figure I.27, the higher the previous heating rate, the faster the austenite formation kinetics and the higher the austenite fractions at the end of the intercritical annealing [BVS22; Bel+19; Chb+14; HPM04; Li+13; MGF11; Mor19; Tei+21; TM18].

Several theories are available in the literature to explain these effects. Authors often put forward the carbon diffusion, the austenite nucleation and the austenite growth as potential mechanisms. Yet, no clear consensus is reached to explain the observed trend. Here are the main ideas proposed in literature and their main contradictions.

Working with martensite as the carbon-rich phase, Bellavoine et al. [Bel+19] observe cementite particles precipitation in martensite islands along the annealing. The higher the heating rate, the smaller and the higher the spatial density of the cementite particles in the tempered martensite. As cementite particles are preferential nucleation sites, higher heating rates increase the number of nucleation sites and reduce the diffusion distances, which is expected to increase the transformation kinetics in carbon diffusion controlled phase transformation.

Similarly, using fast heating rates ( $> 100$  °C/s), Bandi et al. [BVS22] argue that the still fragmented cementite particles in pearlite are more efficient nucleation sites. Such particles are expected to be less stable than spheroidized cementite particles. Consequently, still fragmented cementite particles should dissolve faster. In addition, the presence of deformed ferrite with high dislocation density or recovered ferrite with dislocation substructures is assumed to accelerate carbon diffusion and, consequently, austenite formation [BVS22; Bel+19; Chb+14; TM18].

On the contrary, using low heating rates ( $< 1$  °C/s), the recrystallization completed before austenite formation leads to large dislocation-free ferrite grains. Bandi et al. [BVS22] claim that the diffusion network, reduced to the ferrite boundaries, is coarser and, thus, less efficient. The large ferrite grain size makes the carbon diffusion distances longer. The lower efficiency of carbon diffusion is believed responsible for the slowest austenite growth kinetics.

When authors observed inter-granular clusters of cementite particles in the initial microstructure [Li+13; Tei+21; TM18], they highlight that most of these cementite particles stay at ferrite grain boundaries during fast heating ( $> 10$  °C/s). These particles remain favorable nucleation sites. On the contrary, under slow heating ( $< 1$  °C/s), such particles can become intra-granular particles, which are inefficient nucleation sites, due to the ferrite recrystallization.

From a thermo-kinetics point of view, Chbihi et al. [Chb+14] state that, under fast heating (100 °C/s), the driving force for austenite growth and the carbon diffusion are enhanced and promote high interface velocity without redistribution of manganese.

The authors cited above explain the faster austenite formation kinetics when using fast heating rates ( $> 10$  °C/s) through the efficiency of carbon diffusion and its effect on the austenite nucleation. Such arguments rely on the assumption that the austenite formation kinetics is led by the diffusion of carbon. Though, several authors argue that the austenite formation kinetics is

mainly controlled by the diffusion of substitutional element, usually manganese [Lai+16; Mor19; SDM81; Tei+21].

In a previous PhD work, Moreno et al. [Mor19; Tei+21] studied the annealing of an industrial DP600 steel. The initial microstructure is a cold-rolled ferrite-pearlite mixture with clusters of inter-granular cementite particles dispersed in the deformed ferrite matrix. Their numerical work proposes to investigate separately the growth of austenite from these two types of cementite aggregates. Contrary to the growth of austenite from pearlite bands, the growth of austenite from the clusters of cementite particles is shown to be sensitive to the heating rate.

Figure I.34 plots the total austenite transformation kinetics of the studied DP600 steel along annealing at 800 °C using a low (a) and a fast (b) heating rate. The austenite fractions simulated for the simplified ternary nominal composition with the DICTRA module of the Thermo-Calc software (3 °C/s in blue and 30 °C/s in red) are compared to austenite fractions obtained from HEXRD experiments (in black). Their simulations successfully reproduced experimental trends, as the higher final austenite fraction when using higher heating rates. Authors finally attribute the effect of the heating stage to the kinetics of austenite formation from the inter-granular cementite particles.

The simulated kinetics are significantly faster than the experiments and their study had strong assumptions. No interaction is considered between the austenite growing from the pearlite islands and the austenite growing from the inter-granular cementite particles (no carbon transfer, no impingement). The simulations only account for mean composition of cementite particles, though their study highlights a significant impact of the composition of cementite particle on the austenite formation kinetics.

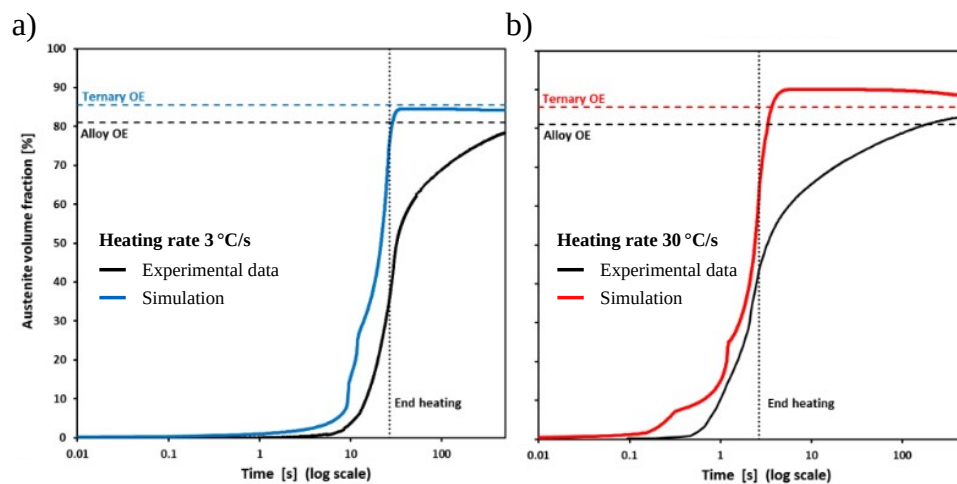


Figure I.34: Austenite transformation kinetics of an industrial DP600 steel cold rolled at 60 % annealed at 800 °C using a low (a) and a fast (b) heating rate. Austenite fractions simulated for the simplified ternary nominal composition with the DICTRA module of the Thermo-Calc software considering two separated subsystems (in color) are compared to austenite fractions obtained from HEXRD experiments (in black). (adapted from [Mor19])

### I.3.4 Conclusions on the interactions between ferrite recrystallization and phase transformation

The investigation of the interactions between the ferrite recrystallization and the austenite formation is complex, as it necessitates understanding a multitude of mechanisms influencing each other. Carbon diffusion, spatial distribution of the carbon sources and austenite nucleation are the mechanisms most often highlighted in the literature involved in the interactions between the ferrite recrystallization and the austenite formation.

The complexity of such investigation is increased by the sensitivity of the studied mechanisms to the initial microstructure, the nominal composition of the studied steel or the annealing parameters (heating rate and temperature). The main observed mechanisms depend on these parameters leading to an apparent disagreement between authors.

This literature review shows that the concomitance of the recrystallization and austenite formation strongly affects the final morphology of the microstructure. Recrystallization is widely shown to affect the spatial distribution of the austenite nucleation sites. In addition, when observed in the initial microstructure, inter-granular cementite particles in the ferrite matrix are reported as crucial to explain the morphogenesis.

From a kinetics point of view, no clear consensus is reached among the authors. Many authors discuss carbon diffusion and how recrystallization can affect its efficiency. Though, other authors claim that austenite formation is controlled by substitutional element diffusion, usually manganese, instead of carbon. Lastly, Moreno et al. [Mor19; Tei+21] suggested that the dissolution kinetics of the inter-granular cementite particles is responsible for the higher final austenite fraction reached using a higher heating rate, based on a numerical investigation. But the simulated kinetics were far too fast.

The understanding of the effect of the heating rate on the austenite formation kinetics still needs further investigation. The Chapter III of the present PhD work aims to bring new experimental insights on the interaction between ferrite recrystallization and austenite formation. The behavior of the austenite formation from pearlite islands and inter-granular cementite particles is closely investigated to further discuss the work of Moreno et al. [Mor19; Tei+21]. Based on the experimental conclusions of Chapter III, Chapter IV proposes a numerical study of the austenite formation thermo-kinetics.

## I.4 Modeling the austenite formation

This section reviews the modeling solution proposed in literature for austenite formation, known to be a diffusive phase transformation usually described by a nucleation and growth process (I.2).

Austenite nucleation is rarely detailed in literature. In several studies, the simulations starts after austenite nucleation and only growth is investigated [Cou+23; Miy+10; Mor19; Oll+17; Tei+21; Wu+20]. Considering austenite nucleation at recrystallized ferrite grain boundaries, the site saturation hypothesis (simultaneous nucleation at all sites) or the classical nucleation theory (gradual nucleation driven by a nucleation flux) were used by Zhu et al. [ZM15]. For austenite nucleation at ferrite-pearlite grain boundaries, the site saturation hypothesis is also used [ZM15] and the nucleation site density can be evaluated using pearlite inter-lamellar spacing [CCdA01; RGF83]. Such modeling strategies require substantial experimental data, such as inter-lamellar spacing or carbide density. The driving force for nucleation must be either evaluated empirically [CCdA01; RGF83] or calculated using thermodynamic databases [Lai+16; Mar+20; ZM15].

The following review focuses on modeling the austenite growth or global kinetics.

### I.4.1 Empirical laws

The Johnson-Mehl-Avrami-Kolmogorov formalism describes empirically nucleation-growth processes [Avr39; JM39; Kol37]. Under isothermal conditions,  $Y(t)$  is defined as  $\frac{f(t)}{f_{max}}$ , with  $f(t)$  the current transformed fraction and  $f_{max}$  is the maximum fraction transformed. The JMAK model describes the evolution of  $Y$  as a function of time ( $t$  in s) by:

$$Y(t) = 1 - \exp((-bt)^n) \quad (\text{I.8})$$

Where  $n$  is the Avrami exponent, describing the nucleation type, and  $b$  is the rate constant (in  $s^{-n}$ ), given as a function of temperature  $T$  as follows:

$$b(T) = b_0 \exp\left(\frac{-Q}{RT}\right) \quad (\text{I.9})$$

with  $b_0$  a constant (in  $s^{-n}$ ),  $Q$  the activation energy of the transformation (in J/mol) and  $R$  the gas constant ( $8.314 \text{ J.K}^{-1}.\text{mol}^{-1}$ ).

This model was adapted by Denis et al. [DFS92] to consider anisothermal conditions (continuous heating for instance). The heating stage is modeled by a succession of isothermal stages during an increment of time  $\Delta t$ . Later, Ollat et al. [Oll+17] used a differential form of the JMAK model, written as follows:

$$\frac{dY}{dt} = (nb(t))^n t^{n-1} (1 - Y(t)) \quad (\text{I.10})$$

to predict the austenite formation kinetics during continuous heating using various heating rates for a recrystallized DP1000 grade steel. The initial microstructure contains equiaxed ferrite grains and aggregates of spheroidized cementite particles. Figure I.35 plots the kinetics predicted by the differential JMAK model (in dashed lines). The parameters were fitted on data obtained from dilatometry experiments (in solid lines).

This empirical model usually reproduces well the sigmoidal shape and final saturation of transformations lead by nucleation and growth, such as ferrite to austenite transformation (Figure I.35) [KPM14; KPM13; Oll+17], but also ferrite recrystallization [HPM04; KPM14; KPM13; Li+13; Oll+17].

The JMAK model is an interesting tool to model quickly the austenite formation kinetics. As a widely spread model, the literature offers plenty of fitted parameters and the JMAK law is a useful first model to compare a current study with literature.

However, the kinetics parameters are highly dependent on the empirical data established on materials with very specific compositions and initial microstructures. As those parameters have no direct physical basis, their extrapolation to other materials is often disappointing. Moreover, phase volume fraction is the sole microstructural feature described by this law.

### I.4.2 Full-field sharp interface models

Full-fields models describe the local composition field in all phases. Sharp interface models consider a discontinuity in properties, especially solute concentration and crystallography. The parameters of such models are thermodynamic or mobility data and microstructural features, making such models more robust to extrapolation.

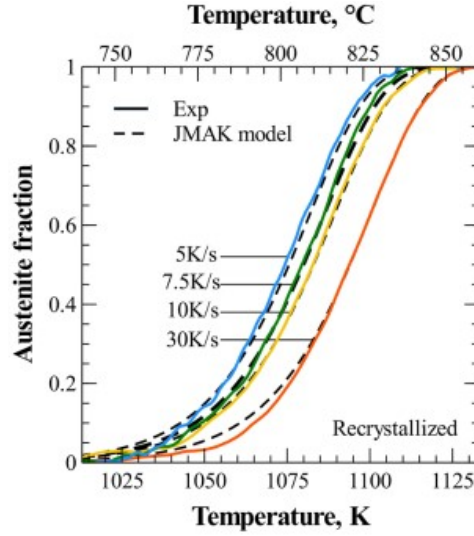


Figure I.35: Austenite formation kinetics predicted by a differential JMAK model (dashed lines), compared to experimental data (dilatometry, in solid line), during continuous heating using various heating rates of a recrystallized DP1000 grade steel. The initial microstructure contains equiaxed ferrite grains and aggregates of spheroidized cementite particles. (from [Oll+17])

#### I.4.2.1 Diffusion-controlled models

A first approach considers the austenite growth as diffusion-controlled, i.e. the growth rate is limited by the diffusion of atoms [Gou+15]. The interface is supposed to admit a Local Equilibrium, defined in I.2.3.1. The migration of the interface and the new chemical properties of the phases are computed by solving Fick's equation for all alloying elements in all phases.

Analytical models solve mathematically those equations [Aar75] but require oversimplification, such as constant temperature, simple geometry (planar geometry and semi-infinite phases), binary Fe-C systems [ARA94; AA96]. These simplifications strongly limit the investigation.

More complex systems (multi-constituent systems, spherical geometry, finite volume of phase) are modeled using semi-analytical models [Eno+18; WPE81]. The mathematical resolution is less rigorous, as simplified composition profiles are assumed.

Wycliffe et al. [WPE81] propose a model for austenite growth in ferrite after pearlite transformation, considering both planar and spherical geometries. Zener's approximation [Zen49] is used, i.e. the composition profiles are locally linearized. Figure I.36 represents the composition profile of carbon (a, c, e) and manganese (e, d, f) along the austenite growth during isothermal holding. In the initial state (Figure I.36 a and b), austenite contains all the carbon. The manganese profile is considered to be flat over the microstructure. Following the austenite growth steps described by Speich et al. [SDM81] (Figure I.19), the austenite growth is first modeled considering the LENP mode (Figure I.36 c and d), until carbon is homogeneous in austenite. Then, the austenite growth is modeled with the LEP mode (Figure I.36 e and f) with the partition of manganese in austenite.

Thus, the growth mode transitions described in Subsection I.2.3 are predicted. As a result, the model gives the time-dependent tie-line, interface position and velocity, as well as the simplified composition profiles computed at every time step. The computation of the simulation is expected to be quite fast, as no discretization of the space is needed.

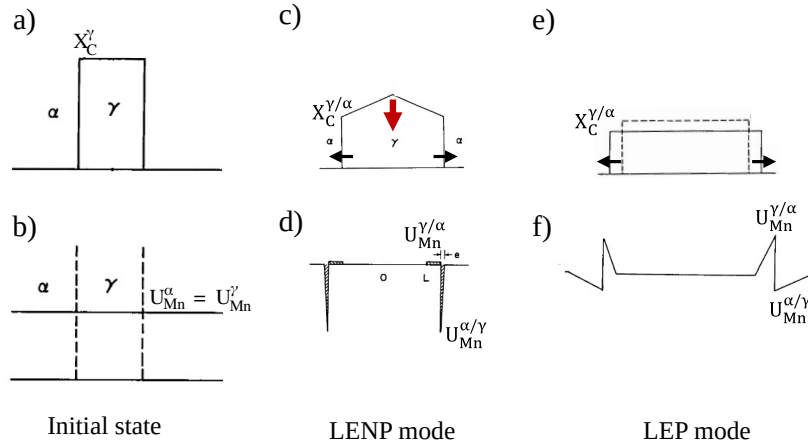


Figure I.36: Evolution of the simplified composition profile of carbon (a, c, e) and manganese (e, d, f) during the austenite growth in the surrounding ferrite in a Fe-C-Mn steel during isothermal holding proposed by Wycliffe et al. [WPE81]. From the initial state (a and b), the austenite growth is modelled considering the LENP mode (c and d), until carbon is homogeneous in austenite. Then, the austenite growth is modeled with the LEP mode (e and f) with partition of manganese in austenite.

Without explicit solution, the diffusion equations can be solved numerically using discretization of time and space. The commercial Thermo-Calc software and its module DICTRA offers a full numerical treatment of the diffusion equations in one dimension, using planar, cylindrical or spherical geometry. This numerical tool is presented in more details in Chapter II. The chemical potentials of species are computed with Thermo-Calc databases. The diffusion coefficients are computed using the mobility databases and accounting of cross-terms and local composition, making the study of multi-component systems possible. Nevertheless, most systems studied using DICTRA in the literature are ternary [Lai+16; Liu+91; Oll+17; Tei+21; Wu+20] or sometimes quaternary [Mar+20; Wei+13]. Considering multi-constituent systems is complex and is often detrimental to the numerical convergence. Though, we manage such simulation in a multi-constituent system in Chapter IV.

Numerous results of DICTRA simulations were already presented in this literature review (Figure I.20 , Figure I.23, Figure I.24, Figure I.25, Figure I.26, Figure I.34). These simulations are very interesting to understand the austenite formation from a thermo-kinetic point of view. However, DICTRA simulations are known to be complex to initialize when studying phase transformations in multi-component systems. In addition, only simple geometries (planar, cylindrical or spherical) can be implemented. Phase transformation in realistic microstructures cannot be simulated using this tool.

#### I.4.2.2 Interface-controlled models

In the previous sub-subsection, the transformation is assumed to be controlled by the diffusion of carbon or alloying elements. In such case, the mobility of the ferrite/austenite interface is considered to be infinite. During the  $\alpha \rightarrow \gamma$  phase transformation, a change in crystal structure (from bcc to fcc) occurs in addition to redistribution of interstitial and substitutional elements. Sometimes, the transformation is assumed to be controlled by the mobility of the interface

[Gou+15; Oll+17]. The elements are considered to diffuse at an infinite rate and the migration of the interface is limited by the reorganization of the crystallographic lattice, the so-called interface friction. This approach was introduced by Christian [Chr02].

During an interface-controlled phase transformation, the interface velocity  $v$  is given as the product of the driving force for the transformation  $\Delta G$  and the interface mobility  $M$ . The interface mobility is usually assumed to follow an Arrhenius law.

### I.4.2.3 Mixed-mode models

The diffusion-controlled and interface-controlled approaches represent two limit cases for modeling the behavior of the ferrite/austenite interface. The mixed-mode model combines the two visions [Gou+15; Oll+18]. It was first developed for  $\gamma \rightarrow \alpha$  transformation [BS09; BS07; KSvdZ97; SvdZ04]. The mixed-mode approach accounts for deviation from equilibrium, due to the friction effect that slows down the interface. In binary Fe-C systems, the driving force for the transformation  $\Delta G$  becomes:

$$\Delta G = \chi \left( x_C^{\gamma/\alpha} - x_C^{\gamma_{int}} \right) \quad (\text{I.11})$$

With  $\chi$  a proportionality coefficient,  $x_C^{\gamma/\alpha}$  the carbon content in austenite at equilibrium and  $x_C^{\gamma_{int}}$  the actual carbon content in austenite at the interface. One can quantify the mixed-mode character of the current transformation using the parameter  $S = \frac{x_C^{\gamma/\alpha} - x_C^{\gamma_{int}}}{x_C^{\gamma/\alpha} - x_C^0}$ , with  $x_C^0$  the nominal carbon content. When  $S$  equals 0, the transformation is diffusion-controlled. On the contrary,  $S$  equals 1 when the transformation is interface-controlled.

The mixed-mode approach was adapted to model the  $\alpha \rightarrow \gamma$  transformation [MBS15; Oll+18]. Using the formalism from Equation I.11, phase transformations can be modeled only in binary Fe-C systems. To model the  $\alpha \rightarrow \gamma$  transformation in ternary systems, one must assume interface conditions. Mecozzi et al. [MBS15] assumed PE interface conditions – only carbon chemical potential is equal through the interface. Ollat et al. [Oll+18] considered LENP interface conditions as more accurate based on their work in [Oll+17].

In their work, Ollat et al. [Oll+18] compared mixed-mode simulations (in dashed lines in Figure I.37) to experimental results obtained from dilatometry experiments (in solid lines in Figure I.37) on a recrystallized DP1000 grade steel. Yet, their study on the parameter  $S$  highlighted a critical annealing temperature, 800 °C, under which the phase transformation was interface-controlled. Above this temperature, the phase transformation showed a mixed-mode behavior.

In [Oll+18], the mixed-mode assumption is presented as a relevant tool to account for multi-component solute drag or transitions from carbon to substitutional diffusion control, as the simulations reproduced well the experimental data. However, those results were obtained by fitting the mobility parameters – pre-exponential factor and activation energy of the Arrhenius law – to the studied steels. Thus, the presented model relies on a preliminary calibration on a single annealing. This model is inadequate for the study of other grades of steel. Besides, the mixed-mode approach accounts only for the crystal friction. Models accounting for other phenomena, such as solute drag, and compatible with the mixed-mode model are proposed in the literature for the  $\gamma \rightarrow \alpha$  transformation [Gou+15; HS76; Liu97].

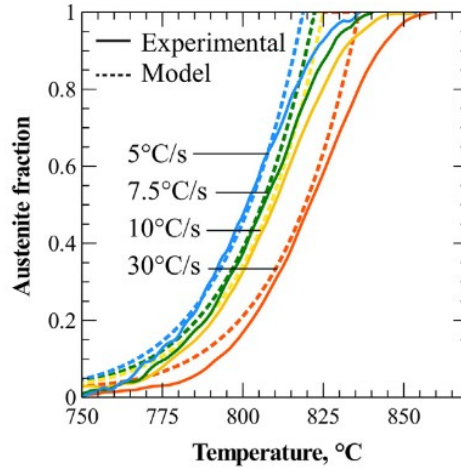


Figure I.37: Austenite formation kinetics predicted by a mixed-mode model (dashed lines), compared to experimental data (dilatometry, in solid line), during continuous heating using various heating rates of a recrystallized DP1000 grade steel. The initial microstructure contains equiaxed ferrite grains and aggregates of spheroidized cementite particles. (from [Oll+18])

#### I.4.2.4 Cellular Automaton (CA)

Cellular Automaton (CA) [BMS10; Mad+13; ZR13] are 2D or 3D Full-field models. In such models, space is discretized in cells. The current state of a cell depends on the state of the neighboring cells. In polycrystal modeling, a cell belongs to a sole grain. Boundary cells, having neighbors in different grains are clearly defined, making CA models sharp-interface models. The boundary position is updated at each time increment by Euler integration, after computation of the interface velocity.

These are interesting numerical tools for microstructural evolution simulations. They were used to study ferrite recrystallization, pearlite to austenite transformation, cementite to austenite transformation and ferrite to austenite transformation. Realistic final microstructures sensitive to the annealing temperature, are predicted by the CA models.

In the work of Zheng et al. [ZR13], a 2D CA model is implemented to investigate concurrent ferrite recrystallization and austenitic transformation during intercritical annealing of cold-rolled DP steels. The simulations reproduce the typical necklace and banded morphology using different heating rates and highlight the role of recrystallization in the distribution of the austenite nucleation sites, as described in Section I.3.

However, initial microstructures are often polygonal grains surrounded by pearlite, created using Voronoi cells. The use of CA models is also limited by their ability to deal with fine interface conditions, such as LENP to LEP transition. In addition, computation time is always a crucial parameter for CA simulations. Going from a 2D to a 3D simulation considerably increases the computation time [BMS10].

#### I.4.3 Phase Field (PF) models

Similarly to CA models, Phase Field (PF) models [AM10; Rud+11; ZM15] are 2D or 3D Full-field models used to investigate the evolution of microstructures.

PF models identify each grain by a phase-field parameter, which is equal to 1 inside the grain and 0 outside. As the phase-field parameters are continuous functions of space, PF models are diffuse interface models. A set of properties (phase, crystallographic orientation, ...) are attributed to each grain. The temporal evolution of the phase-field parameters is computed by the superposition of pairwise interactions with the neighboring grains.

PF models are powerful numerical tools dealing with complex microstructures, as the initial state can be taken from experimental micrographs. Azizi-Alizamini et al. [AM10] successfully simulated austenite formation from carbide dissolution in an ultra-fine ferrite-cementite aggregate. In particular, the austenite growth along the ferrite grain boundaries and the interaction between carbides was well captured and showed the effect on the morphology of the final austenite grains. However, the model is limited to the study of the binary Fe-C system. Zhu et al. [ZM15] reproduced with fairly good accuracy their experimental transformation kinetics using a 2D PF model, even though carbide dissolution was not considered. Their model was sensitive to heating rate and produced realistic final microstructures (Figure 31).

Despite their interesting capacity to deal with complex microstructures, PF models are computationally very expensive. The complexity of the system is often strongly reduced to overcome the computational cost. Usually, only carbon diffusion is considered, as either only the Fe-C binary system is studied [AM10] or the LENP or PE is assumed [Rud+11]. Still, Zhu et al. [ZM15] introduced solute drag effect to take substitutional element diffusion into account.

More recently, the PF model proposed by Mathevon et al. [Mat20] drives the interface migration by the minimization of the Gibbs energy of the entire system. Their Gibbs Energy Minimization (GEM) model was applied to Fe-C-Mn and Fe-C-Mn-Cr systems to simulate the  $\alpha + (\text{Fe,Mn,Cr})_3\text{C} \rightarrow \gamma$  phase transformation. To save computation time, the interactions between the substitutional elements in multi-component systems are neglected. The local Gibbs energy is assumed to be the linear combination of the energy in the corresponding binary systems. Such implementation imposes no equilibrium conditions at the interface while including diffusion within the interface. At each time increment, the global Gibbs energy of the systems is computed depending on the position of the interface. The new interface position is chosen as the one that minimizes the global Gibbs energy as a function of the interface position. Their computation time is claimed 60 times less than DICTRA simulations. Contrary to the PF models presented above, this model is only 1D, making possible the account for more complex systems. The microstructure evolution cannot be investigated. Only the austenite formation kinetics and composition profiles are obtained from this model.

#### I.4.4 Machine learning

In the past few years, machine learning approaches appeared to predict phase transformation kinetics, microstructures and mechanical properties. Different machine learning techniques can be used, such as Artificial Neural Networks, Multilayer Perceptron Regressors, k-Nearest Neighbors, Bagging, or Random Forests [Gen+20; HBB20].

Such approaches significantly reduce computation time, once appropriately trained. Geng et al. [Gen+20] successfully used machine learning techniques to model the Continuous Cooling Transformation diagram. The inputs of the model are the chemical composition, the austenitizing temperature and the cooling rate. The model is claimed to be able to generalize outside the range of the training database and to be more accurate in predicting transformation temperatures than commercial software.

Contrary to physically-based models, machine learning is statistically-based. Such approach needs an initial dataset to correlate input attributes to output attributes. The training dataset can be experimental data, as in [Gen+20], or simulation data, as in [HBB20]. Preparing the training dataset is a crucial and hard work and is one of the main limitations of the machine learning approaches. The quality of the initial dataset makes the quality of the model. Creating the dataset can be time-consuming when using experimental data or computationally expensive numerical simulations.

#### I.4.5 Conclusions on phase transformations modeling

The literature reports several modeling solutions for austenite formation.

2D or 3D models such as many Cellular Automaton and Phase Field models are very useful to investigate the evolution of the microstructures. But such simulations have often high computation costs. To save on computation time, the chemistry of the studied system is often simplified to binary or subjected to restrictive conditions on the substitutional element in ternary systems. Considering these arguments, these models do not suit our objectives.

With 1D full-field simulation coupled to the Thermo-Calc databases, DICTRA seems a relevant numerical tool to better understand the thermo-kinetics of the austenite formation in multi-component systems and the interaction between substitutional elements.

Chapter IV presents our DICTRA simulations accounting for our new experimental insights detailed in Chapter III and considering up to quinary systems. The conclusions drawn along the experimental work in Chapter III and the numerical investigation in the first section of Chapter IV justify in detail the choices for the final modeling strategy. Yet, arguments can already be stated.

As the model should be robust to annealing parameters and steel chemistry, models using fitted parameters (JMAK and mixed-mode models) are avoided. In particular, the Machine Learning solutions are not implemented due to the high amount of data needed to obtain an accurate prediction.

Finally, the 1D PF model proposed by Mathevon et al. [Mat20] seems quite efficient to model the austenite formation kinetics, even in multi-component systems. The evolution of the composition profile is also a result of the simulation. However, the model proposed by Wycliffe et al. [WPE81] outputs the same variables. The simplified composition profile certainly reduces the precision of the results. But the gain in computation time is expected to justify this loss of precision. Yet, Wycliffe's model works only for ternary systems. In Chapter IV, we present our new predictive physically-based model, which generalizes Wycliffe's approach to multi-component systems.

### I.5 Summary

Recovery and recrystallization are closely linked phenomena as they compete for the same driving force. Besides, the SIBM theory attributes the recrystallization "nucleation" to recovery. Consequently, the experimental characterization of recovery and recrystallization often uses the same methods and it can be difficult to decorrelate their effect. The current thesis aims to improve and validate in depth the new time-resolved technique to follow recrystallization proposed in the recent work of Moreno et al. [Mor+18]. The developed method, detailed in Chapter II, uses in situ HEXRD experiments and requires no interrupted and time-consuming post-mortem experiments.

During the heating stage of intercritical annealing, ferrite recrystallization interacts with austenite formation. The study of these interactions is complex, as it involves carbon diffusion, spatial distribution of the carbon sources and austenite nucleation, which influence each other. The literature widely shows that the concomitance of ferrite recrystallization and austenite formation strongly affects the final morphology of the microstructure. Recrystallization affects the spatial distribution of the austenite nucleation sites, such as inter-granular cementite particles.

From a kinetics point of view, a higher heating rate leads to a higher final austenite fraction and no clear consensus explains this observation. Discussions in literature mainly involve carbon diffusion and how recrystallization can affect its efficiency. Though, some authors claim that austenite formation is controlled by substitutional element diffusion, usually manganese, instead of carbon. Instead, Moreno et al. [Mor19; Tei+21] claim that the dissolution kinetics of the inter-granular cementite particles is responsible for the observed effect. Chapter III is dedicated to the further investigation of the effect of the heating rate on the austenite formation kinetics. New experimental insights will be provided on the interaction between ferrite recrystallization and austenite formation.

DICTRA simulations are identified as relevant numerical tools to better understand the thermo-kinetics of the austenite formation in multi-component systems and the interaction between substitutional elements. The present literature review already presents several conclusions from thermo-kinetic analysis of austenite formation. In particular, this review details the thermo-kinetic analysis of Moreno et al. [Mor19], considering two closed subsystems, one containing the pearlite islands, the other the cementite particles. This interesting approach reproduces the excess of the OE fraction observed experimentally, but it suffers from several limitations. In particular, the hypothesis of closed subsystems is probably too strong, as our recent numerical investigation shows interactions between austenite islands through carbon diffusion in the ferrite matrix. Chapter III discuss further these thermo-analyses and hypotheses based on our experimental investigation. Our conclusions guide the choices for the final modeling strategy in Chapter IV.

Finally, the model proposed by Wycliffe et al. [WPE81] was shown to be an efficient model for the austenite formation kinetics, in terms of computation time, thanks to the simplified composition profiles. In Chapter IV, we extend this model to multi-component systems.



---

## Chapter II

# Experimental and simulation methods

---

J'en veux encore, même si je  
comprends pas  
Pourquoi je change, et  
quelquefois  
J'ai tellement peur que la nuit ne  
vienne pas  
Car quand je dors, je rêve de ça  
De tout comprendre et de savoir  
pourquoi  
[...]  
J'voudrais tout savoir  
Et voir dans le noir

---

*Tout savoir*  
*Adé*

II.1	Studied materials . . . . .	59
II.2	Thermal treatments . . . . .	61
II.3	Optical microscopy . . . . .	62
II.3.1	Metallographic preparation . . . . .	62
II.3.2	Optical observations . . . . .	62
II.3.3	Phase fraction quantification . . . . .	62
II.4	Scanning Electron Microscopy . . . . .	63
II.4.1	Metallographic preparation . . . . .	63
II.4.2	Secondary Electron Imaging . . . . .	64
II.4.3	Electron BackScattering Diffraction . . . . .	64
II.5	Transmission Electron Microscopy . . . . .	67
II.5.1	Sample preparation . . . . .	67
II.5.2	Energy-Dispersive X-ray Spectroscopy . . . . .	68
II.6	Wavelength-Dispersive Spectrometry . . . . .	69
II.7	Inductively Coupled Plasma Optical Emission Spectroscopy . . . . .	70

II.8	Vickers Micro-Hardness . . . . .	70
II.9	High Energy X-Ray Diffraction . . . . .	72
II.9.1	Experimental set-up . . . . .	73
II.9.2	Diffraction pattern analysis . . . . .	74
II.9.2.1	Rietveld analysis . . . . .	74
II.9.2.2	Isolated Diffraction Spot Tracking . . . . .	76
II.9.2.2.1	Methodology . . . . .	76
II.9.2.2.2	Validation of the IDST method . . . . .	78
II.9.2.2.3	Conclusion on recrystallized fraction quantified by IDST . . . . .	83
II.10	Phase transformation modelling: approach and tools . . . . .	83
II.10.1	CALPHAD method . . . . .	83
II.10.2	Numerical tools . . . . .	84

This PhD work aims to understand and propose a physically-based model of the austenite formation kinetics in cold-rolled steel during industrial annealing. To do so, we investigate the metallurgical mechanisms, such as recrystallization, cementite coarsening and dissolution and austenite formation, as well as their interactions, occurring during industrial annealing. This chapter presents the studied materials as well as the experimental and simulation methods implemented to this end.

Our experiments mainly consist in industrial annealing simulations in a dilatometer. We investigate austenite formation during strategically-chosen thermal treatments starting from different initial states, either in situ or post mortem (after interrupted treatments) and using several characterization techniques.

During the experimental annealing simulations, the treatments are interrupted at strategic temperatures to observe the current microstructure, using optical microscopy and Scanning Electron Microscopy (SEM) in Secondary Electron imagery mode. The recrystallization progress is tracked using Electron BackScattering Diffraction (EBSD) as well as micro-Vickers Hardness measurements. Advanced techniques for local chemical analysis were employed to support discussions in Chapter IV. Carbon content in austenite islands is mapped using Wavelength-Dispersive Spectrometry (WDS) and chemical composition of cementite particles is measured using Energy-Dispersive X-ray Spectroscopy (EDXS).

In situ High Energy X-Ray Diffraction (HEXRD) experiments were performed on the P07 synchrotron beamline on PETRA III at DESY in Hamburg. These in situ experiments first aimed to obtain the austenite formation kinetics during the annealing treatment. A careful analysis of the collected data led us to develop a new method using HEXRD to investigate recrystallization. The method is detailed and discussed in the present chapter. Thanks to this method, we follow simultaneously ferrite recrystallization and austenite formation in situ in a single experiment with a high time-resolution. Our method makes possible the investigation of their interaction during the annealing treatment, as presented and discussed in Chapter III.

This chapter dedicated to methods also details the commercial computational tools for phase transformation simulation and thermodynamic databases used to model cementite dissolution and austenite formation during the thermal treatments. The Thermo-Calc software and its module DICTRA are briefly presented in this Chapter, while the full configurations of performed simulations are detailed in Chapter IV.

## II.1 Studied materials

All steels studied in this PhD work were provided by ArcelorMittal Maizières Research at the cold rolled state.

This chapter presents our new method to determine recrystallization kinetics. The method is validated from the study of two model steels designed for this purpose, ultra-low carbon ferritic steels (0.001 wt% C) with two levels of manganese, 0.5 wt% Mn and 2.0 wt% Mn respectively. These two steels are labeled Mn05 and Mn20 in the following.

The study on interactions between ferrite recrystallization and austenite formation, detailed in Chapter III, required the production of three model steels. The aimed chemical compositions and the studied thermal cycles are designed to reach an intercritical domain and to produce a Dual-Phase steel after cooling. The first studied steel corresponds to an industrial DP600 grade, called DP600 in the following. The two other steels are designed based on the DP600 grade. Niobium is added to slow down the recrystallization kinetics and to force its interaction with

austenite formation. Two niobium levels are used, 0.015 wt% Nb and 0.030 wt% Nb. These steels are referred as DP600Nb15 and DP600Nb30 respectively.

The full chemical compositions of the studied steels are reported in Table II.1, in weight percent (wt%).

Label	C	Mn	Si	Cr	Nb	Ti	P	S	N
Mn05	0.001	0.5	0.03	< 0.002	< 0.002	< 0.002	0.002	< 0.0005	< 0.001
Mn20	0.001	2.0	0.03	< 0.002	< 0.002	< 0.002	0.002	0.0006	0.0015
DP600	0.1	1.9	0.2	0.2	< 0.002	< 0.002	0.003	0.0007	< 0.001
DP600Nb15	0.1	1.9	0.2	0.2	0.015	0.020	0.003	0.0007	< 0.001
DP600Nb30	0.1	1.9	0.2	0.2	0.030	0.020	0.003	0.0007	< 0.001

Table II.1: Chemical composition of the five studied steels in weight percent (wt%)

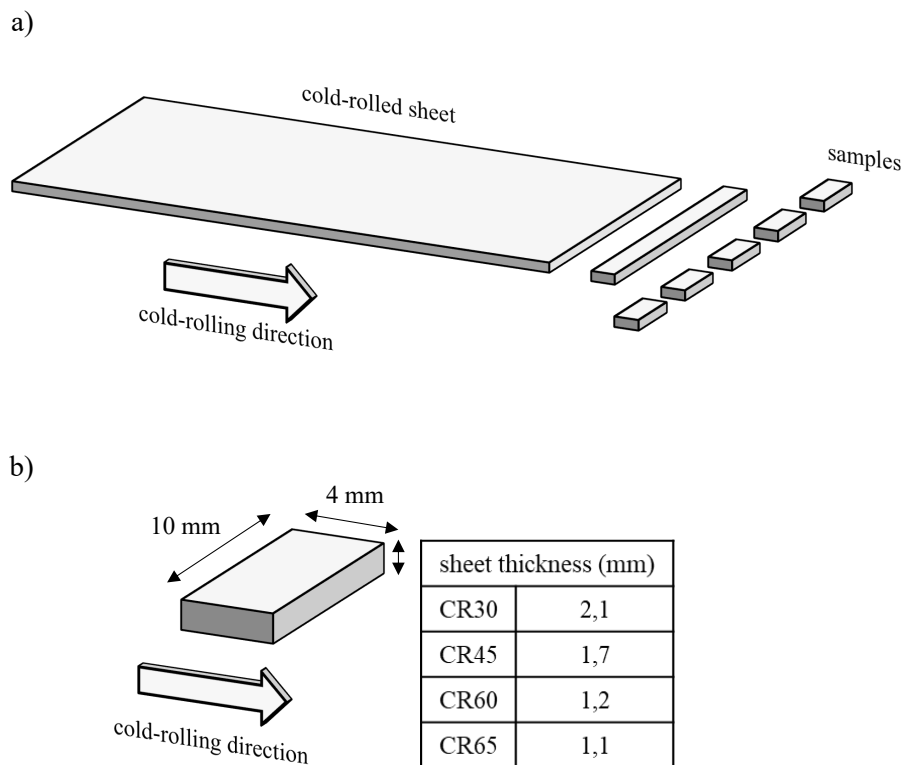


Figure II.1: Schema of samples cut down from the cold-rolled sheets (a) and dimensions of the samples (b)

The ingots of the studied steels were elaborated in a vacuum induction melting pilot furnace, and further hot-rolled. The thickness of sheets after this operation was 3.2 mm. The sheets were cold-rolled in a laboratory mill, to four final cold-rolling ratio: 30 %, 45 %, 60 % and 65 %. After cold-rolling, the samples are labeled CRxx, with xx the cold-rolling ratio.

This work investigates austenite formation during industrial annealing, either in situ or post mortem (after interrupted treatments), using several techniques. We perform several thermal treatments in a dilatometer on parallelepipedal samples, cut down from the cold-rolled sheets

(Figure II.1 (a)), to simulate industrial thermal schedules. The final sample and its dimensions are represented in Figure II.1 (b).

## II.2 Thermal treatments

Annealing simulations are performed using commercial Bähr DIL805 A/D dilatometers available at ArcelorMittal Research Center and Deutsches Elektronen-Synchrotron (DESY) facilities. At ArcelorMittal Maizières Research, the thermal treatments were conducted by Carla Oberbillig.

The samples are placed in a closed chamber under secondary vacuum, pictured in Figure II.2 (a), and hold by two quartz rods. The samples are heated by induction at high frequency and cooled by helium injection through the induction coil. A K-type thermocouple, spot welded on the sample as schematized in Figure II.2 (b), regulates the heating power during the thermal treatment.

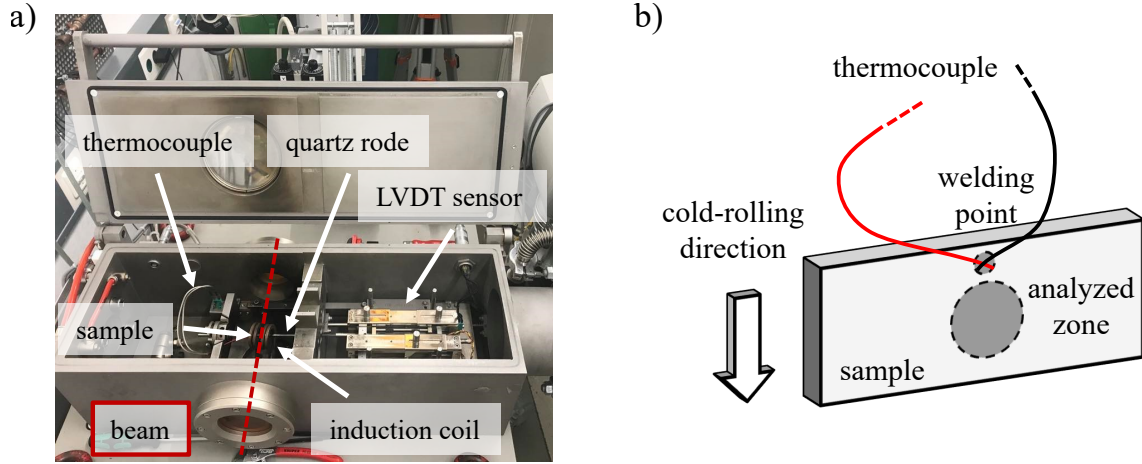


Figure II.2: Bähr dilatometer available at DESY facilities (a) and position of the welded thermocouple and analyzed zone on a sample studied by HEXRD (b). A dashed red line represents the beam path.

Most of the simulated thermal treatments presented in this manuscript consist in intercritical annealing. In the intercritical range, the austenite fraction is very sensitive to the temperature. Our study on austenite formation kinetics during intercritical annealing requires high precision and repeatability of temperature measurement and regulation.

K-type thermocouples and their connectors in the dilatometer introduce intrinsic uncertainties estimated at  $\pm 2.2$  °C and  $\pm 1$  °C respectively [Mor19; Nak04]. During the study, wrong temperature acquisitions made some experiments unexploitable. A meta-analysis of our experiments led us to think that a K-type thermocouple used at DESY facilities in 2021 could have been poorly welded, introducing an additional bias on the temperature measurement.

As most of the experiments were carried out twice, dubious experiments were ruled out. The temperature acquisition is controlled, a posteriori, following the electrical power provided by the dilatometer. As the transition from ferro- to para- magnetic state is detrimental to heating by induction, maintaining the heating rate requires a burst of electrical power. By systematically plotting the electrical power as a function of the temperature, one can precisely identify the Curie magnetic transition of the steel. The temperature is considered correctly acquired and

regulated when the temperature of electrical power burst matches the Curie temperature. This procedure ensures the correct acquisition of all the experiments presented in this manuscript.

## II.3 Optical microscopy

The microstructures in samples are preliminary observed using optical microscopy, either prior any thermal treatment (as cold-rolled) or after interrupted or full annealing.

### II.3.1 Metallographic preparation

The samples are coated in epoxy resin (transverse cut of the dilatometer sample, pictured in Figure II.3 (a), or sagittal cut of the cold rolled sheet). Then, the samples are polished with silicate grid paper down to  $1\mu\text{m}$ .

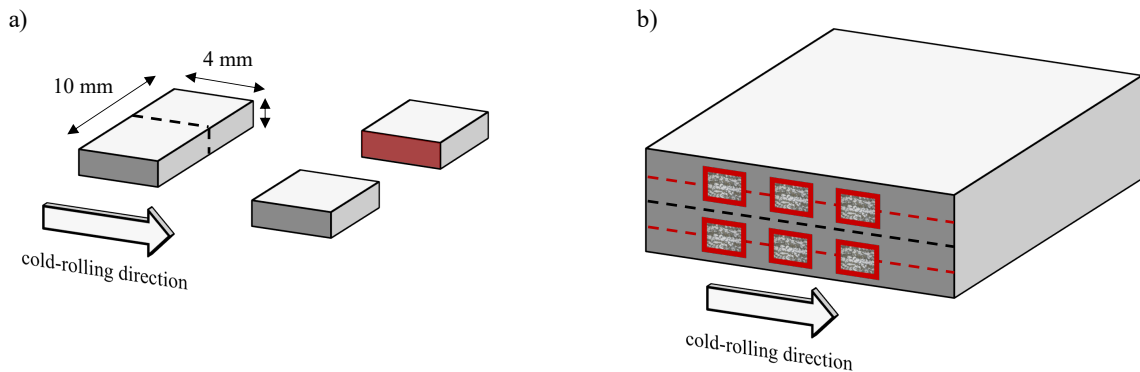


Figure II.3: The dilatometer samples are cut in the transverse direction for microscopy (a). The observed surface is colored in red. Microscopical observations are performed at sheet quarter thickness (b).

The samples were etched using either a diluted Picral solution (4 % picric acid and 96 % ethanol), or a Metabi solution (4 g metabisulfite and 100 ml distilled water). The Picral etchant reveals cementite. Martensite is colored in brown by the Metabi solution, while ferrite appears white.

### II.3.2 Optical observations

The observations were performed by Carla Oberbillig at ArcelorMittal Research Center using ZEISS microscopes at magnification  $\times 100$ . The samples are analyzed at sheet quarter thickness, as illustrated in Figure II.3 (b).

### II.3.3 Phase fraction quantification

The phase fraction is quantified by image analysis using the Aphelion software (DEV 4.5.0, 64 bit version). The optical micrographs are segmented using a threshold on their red, green or blue color channel.

Austenite fraction is quantified after Metabi etching to color martensite (austenite before quenching).

In a previous PhD work [Mor19], the studied DP600 CR60 presents to main carbon sources: pearlite and cementite particles isolated in the ferrite matrix (mainly intergranular). The fraction of pearlite and isolated cementite particles are quantified after Picral etching to reveal cementite particles and pearlite. The segmentation of the image gives the total fraction of pearlite and cementite particles. Then, the isolated cementite particles are erased from the segmentation by hand using a morphological criterion. After this procedure, the fraction of pearlite in the microstructure is obtained. The fraction of isolated cementite particles is obtained by subtracting the pearlite fraction to the total fraction of pearlite and isolated cementite particles.

Figure II.4 (a) shows the original micrograph of the studied DP600Nb15 CR65 in the cold-rolled state. The ferrite matrix is in light grey and pearlite and isolated cementite particles are in dark grey. Figure II.4 (b) shows in red the segmentation of pearlite. Isolated cementite particles removed from the previous segmentation are in dark grey.

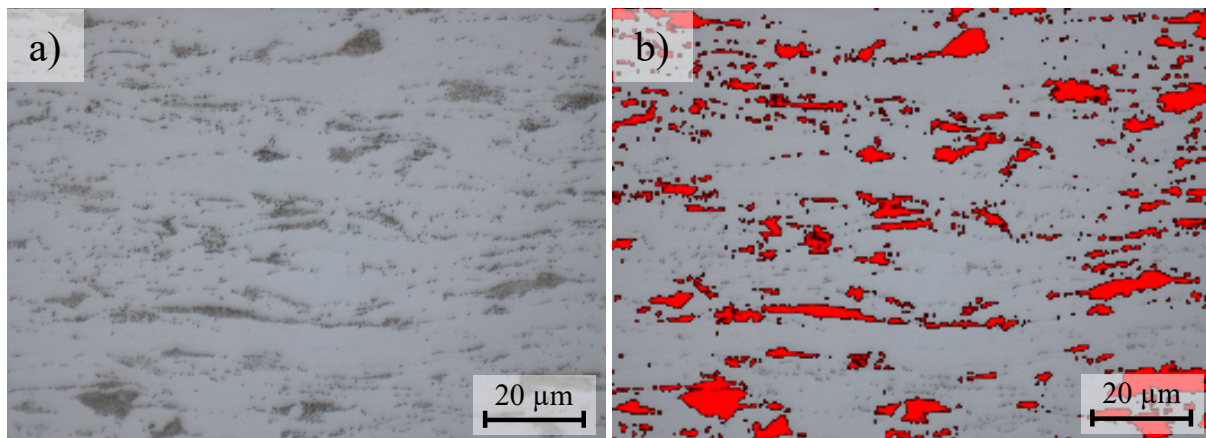


Figure II.4: Optical micrograph of the DP600Nb15 CR65 in the cold-rolled state (a) and segmentation of pearlite in red (b). Isolated cementite particles, seen in (b) in dark grey, are erased from the segmentation on morphological base.

## II.4 Scanning Electron Microscopy

Scanning Electron Microscopy (SEM) is used to observe and quantify the evolution of the microstructures in the studied steels during the thermal cycles after interrupted heat treatments. The samples are analyzed at sheet quarter thickness, as in optical microscopy (Figure II.3 (b)).

### II.4.1 Metallographic preparation

After optical observations, the finest scratches are removed using colloidal silica suspension solution. The samples are cleaned in an ultra-sonic methanol bath.

The samples are etched using either a Picral solution (4 % picric acid and 96 % ethanol) or a Nital solution (2 % HNO<sub>3</sub> and 98 ml ethanol). The Picral and Nital etchants reveal the carbides and ferrite grain boundaries respectively.

### II.4.2 Secondary Electron Imaging

The evolution of the microstructure during the intercritical annealing is observed using a JEOL IT300 in Secondary Electron (SE) imagery mode. These observations were performed by Carla Oberbillig at ArcelorMittal Research Center. The acceleration tension is set at 15 keV and the Working Distance between 7.5 and 9 mm. Various magnifications are used (x 1000, x 2000, x 5000).

### II.4.3 Electron BackScattering Diffraction

EBS is used to determine the recrystallization state of the samples after interrupted annealing. The obtained recrystallization kinetics are used to validate our new time-resolved methodology based on HEXRD experiments.

EBS maps are realized using a IT800 SHL (AMMR021725) equipped with Oxford Symmetry2 (AMMR24524) and Ultimax100 (AMMR24523). These maps were acquired by Giuseppe Sollazzo at ArcelorMittal Research Center. The acceleration tension is set at 20 keV and the Working Distance at 20 mm.

The SEM/EBS maps are post-processed to show the Grain Orientation Spread (GOS), using the AZtec Crystal software. The GOS describes the standard deviation of disorientation in a grain. A high GOS indicates a high density of crystalline defaults [Mor+18; Rad15]. The recrystallized grains show a GOS typically less than 1.5 °. In contrast, the old, deformed ferrite grains show a GOS greater than 1.5 °. Considering the size of the recrystallized grains and the precision needed to investigate the GOS, a compromise was found between a magnification set at x 300 and an acquisition step at 3 µm.

In the study presented here, annealing simulations are performed on our ultra-low carbon steels and consists in isothermal holding at 650 °C after fast heating at 100 °C/s. The holding was interrupted after 0 s, 5 s, 10 s, 15 s, 20 s and 50 s treating the Mn05 CR65 and after 0 s, 25 s, 100 s, 200 s, 300 s and 400 s treating the Mn20 CR65. The holding stage is followed by gas quenching (He) to stop the recrystallization and freeze the microstructure.

For our study, we defined grain boundaries at 10 ° of misorientation (High Angle Grain Boundaries [HH95; Doh+97]) and recrystallized grains as ferrite grains with a GOS less than 3 °. A SEM/EBS map of the Mn20 CR65 steel annealed 100 s at 650 °C, post-processed to show the GOS, is shown in Figure II.5. The non-recrystallized grains appear in green and red grains, highlighting a GOS higher than 3 °. On the contrary, the recrystallized grains, colored in blue, shows a low GOS (< 3 °). The recrystallized grains represent 38 % of the microstructure.

This method is very sensitive to the threshold chosen for grain boundaries misorientation, which defines the grains, and for the GOS, which defines the recrystallized grains. Figure II.6 shows the Inverse Pole Figure (IPF) map (a) and GOS maps (b, c) of the Mn20 CR65 after 200 s at 650 °C. The GOS map in (b) highlight grains with a GOS lower than 3 °, while (c) highlights grains with GOS up to 5.5 °. White arrows show grains with subgrains. As exposed in Chapter I, theories, such as Strain Induced Boundary Migration theory [HH95; Hum97; ZBD06; Vat+96], attributes the nucleation of new recrystallized grains to recovery. Cells and sub-grains formed during recovery can reach a critical size by migration of Low Angle Grain Boundaries (LAGB), with a misorientation lower than 10 ° to 15 °, and become nuclei for recrystallized grains [HH95; Hum97]. Consequently, recrystallized grains can show subgrain boundaries. But, subgrains show different crystal orientations and belong to the same grain. Consequently, the GOS of the grain is highly increased, up to the misorientation of the LAGB between subgrains. The recrystallized fraction estimated in Figure II.6 (b) is 60 %, while it reaches 66 % in Figure II.6 (c).

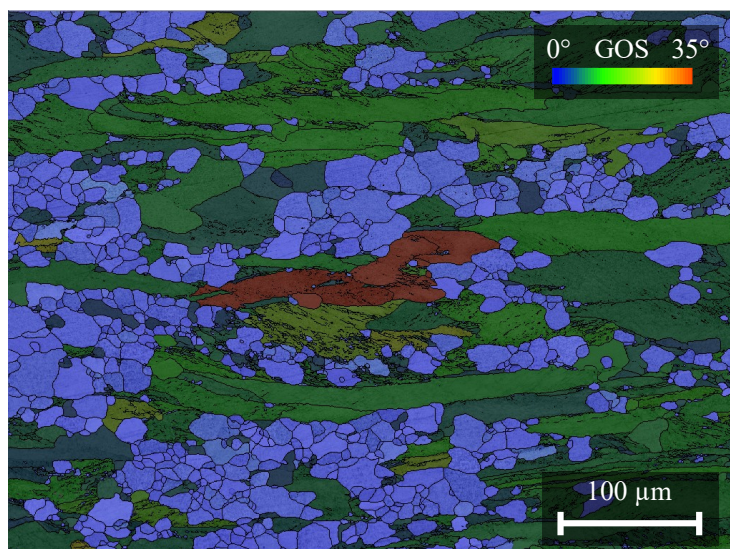


Figure II.5: SEM/EBSD map (magnification  $\times 300$ ) of the Grain Orientation Spread (GOS) in the Mn20 CR65 steel after 100 s at 650 °C.

This method is also very sensitive to the surface state. Figure II.7 shows the IPF map (a) and GOS maps (b,c) of the Mn05 CR65 after 20 s at 650 °C. The GOS map in (b) highlights grains with a GOS lower than 3 °, while (c) highlights grains with GOS up to 10 °. The IPF map highlights a poor surface state. Our samples are ultra-low carbon steels with a fully ferrite matrix. The studied samples show various progress in ferrite recrystallization. Consequently, our samples show very low mechanical properties, making the polishing step delicate. A poor surface state introduces crystalline defaults close to the surface and increases the GOS of the grains. Consequently, the grains with a GOS lower than 3 ° represents only 3 % of the microstructure in Figure II.7 (b). Considering GOS up to 10 °, Figure II.7 (c) highlights grains with recrystallized morphologies and GOS higher than 3 °. Grains with a GOS up to 10 ° represents 75 % of the microstructure in Figure II.7 (c).

The method also suffers from a statistical issue. The studied steels are ultra-low carbon steels with few alloying elements. The studied microstructures show very large grains. Figure II.8 shows a GOS map in the Mn05 CR65 after 10 s at 650 °C. A very large deformed grain takes up the entire lower part of the map. This grain is at least 430  $\mu\text{m}$  large. This method requires an acquisition step small enough to ensure precision on the GOS and detection of the very beginning of recrystallization with very small grains. Considering the large studied grains, ensuring statistics requires very large maps. Having both small acquisition steps and large maps leads to very long acquisition time. We had to find a compromise between these different constraints and to analyze critically the results obtained.

The studied Mn05 CR65 shows the largest grains, as its manganese content is the lowest. Though the grains are certainly too large, the estimated fractions are plotted in the following, with the corresponding large uncertainties. Two SEM/EBSD maps on the Mn05 CR65 after 5 s at 650 °C were acquired. The post-processed GOS maps are shown in Figure II.9. The recrystallized fraction is estimated at 4 % in (a) and 9 % in (b).

Considering the limitations exposed above, the uncertainty on the recrystallized fraction obtained from the present method is estimated around 10 % (sensitivity to threshold and statistic

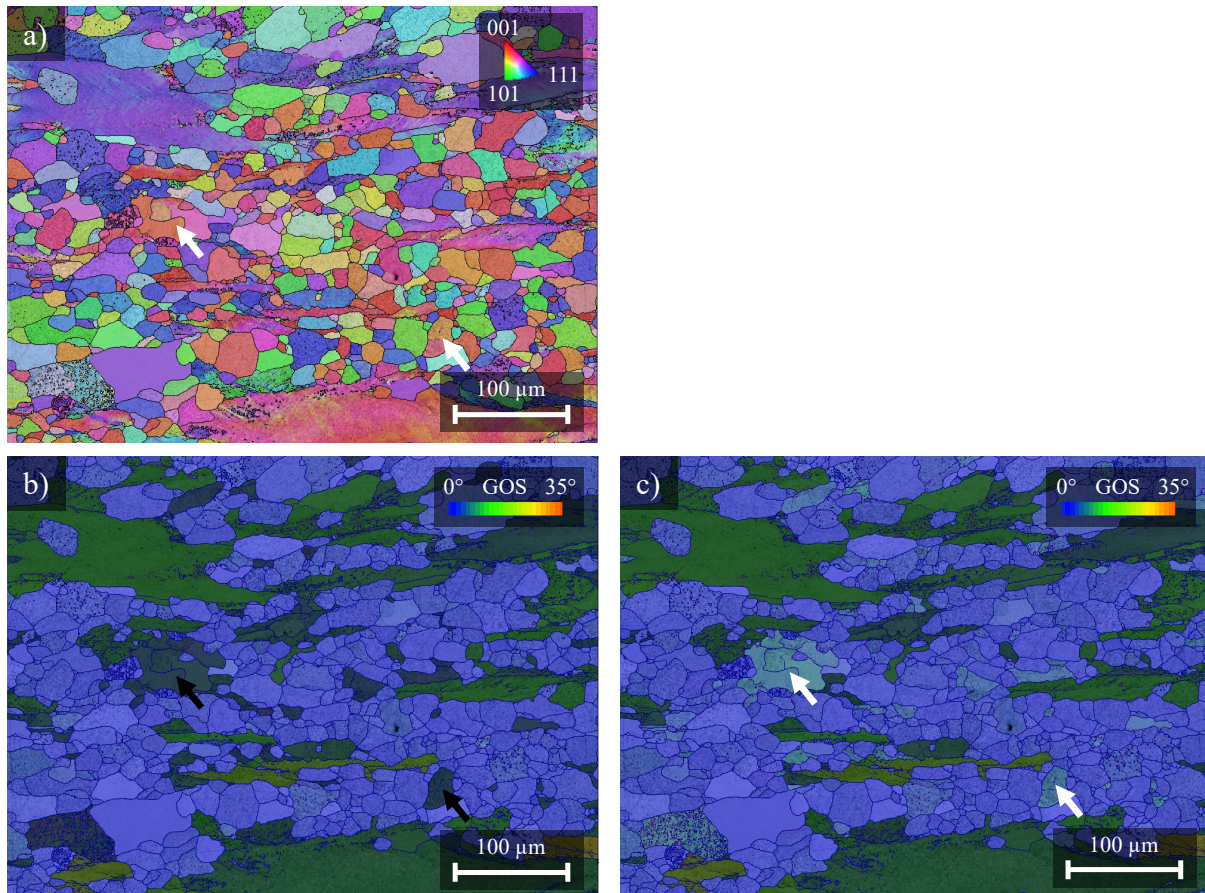


Figure II.6: IPF map (a) and GOS maps (b,c) (magnification  $\times 300$ ) of the Mn20 CR65 steel after 200 s at 650 °C. (b) highlights grains with a GOS lower than 3 °. (c) highlights grains with a GOS lower than 5.5 °. White arrows show recrystallized grains with subgrains.

error). Concerning the large error introduced due to the surface state of the sample, as seen in Figure II.7, the recrystallized fraction is first estimated using the systematic parameters (grain boundaries misorientation upper than 10 ° and GOS lower than 3 °). Then, the map is post-processed again using a GOS threshold set at 10 ° and the fraction is plotted with a black circle.

Figure II.10 shows the recrystallized fractions estimated from our SEM/EBSD maps (maps not already presented in this section can be found in A) in the studied Mn05 CR65 (a) and Mn20 CR65 (b) steels. In both steels, the recrystallized fraction globally increases with annealing time, depicting well the recrystallisation progress. In the Mn05 CR65 steel, the microstructure is almost completely recrystallized after 50 s, while the Mn20 CR65 takes more than 300 s to recrystallize. Alloying elements as manganese are known to delay recrystallization [HPM04; Oll+17].

The method presented in this section is used to estimate the recrystallized fraction from SEM/EBSD maps. Uncertainties on the estimated fraction comes from the sensitivity of the method to the quality of the studied surface state, the size of the studied surface and the

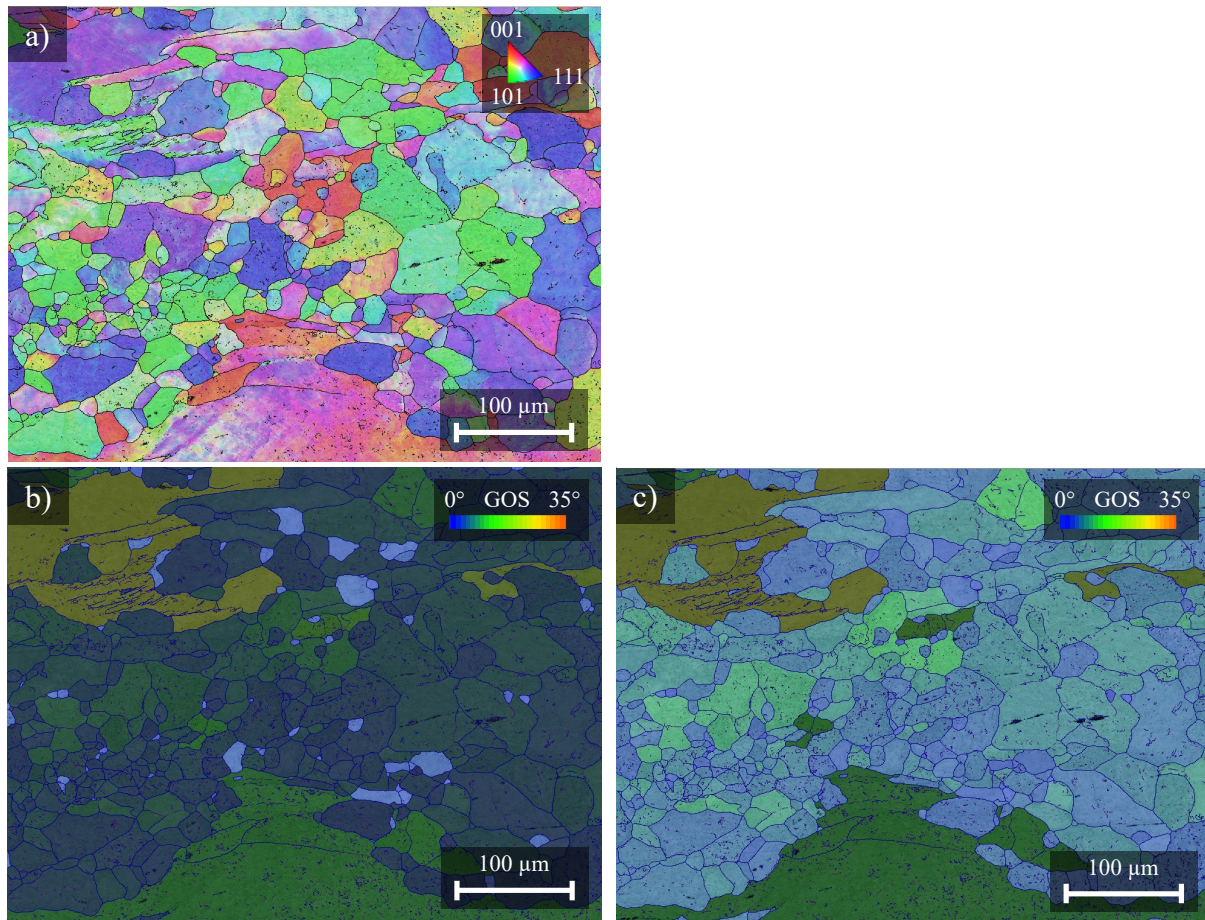


Figure II.7: IPF map (a) and GOS maps (b,c) (magnification  $\times 300$ ) of the Mn05 CR65 steel after 20 s at 650 °C. (b) highlights grains with a GOS lower than 3 °. (c) highlights grains with a GOS lower than 10°.

misorientation defining grains. Considering the typical grain size in our studied steels, especially the lower alloyed one (Mn05 CR65), this method is not the most suited. Though, it gives an estimation of the recrystallized fractions, used in the following for validation of our new method using HEXRD to investigate recrystallization.

## II.5 Transmission Electron Microscopy

The chemical composition of cementite particles is investigated by Transmission Electron Microscopy (TEM) experiments carried out on a JEOL 2100F by Patrick Barges and Daniela Obriot at ArcelorMittal Research Center.

### II.5.1 Sample preparation

The chemical composition measurements are done on replica. After SEM observations, the samples are extracted from the epoxy-resin shell and further polished using grinding paper to

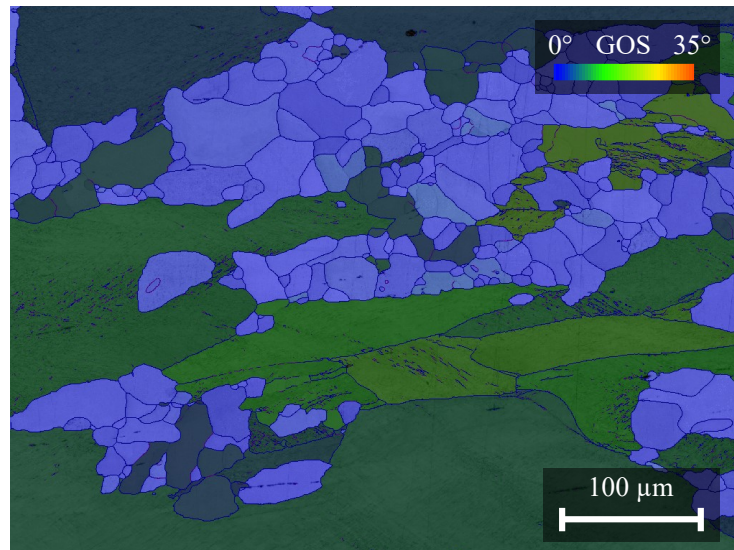


Figure II.8: SEM/EBSD map (magnification x 300) of the Grain Orientation Spread (GOS) in the Mn05 CR65 steel after 10 s at 650 °C.

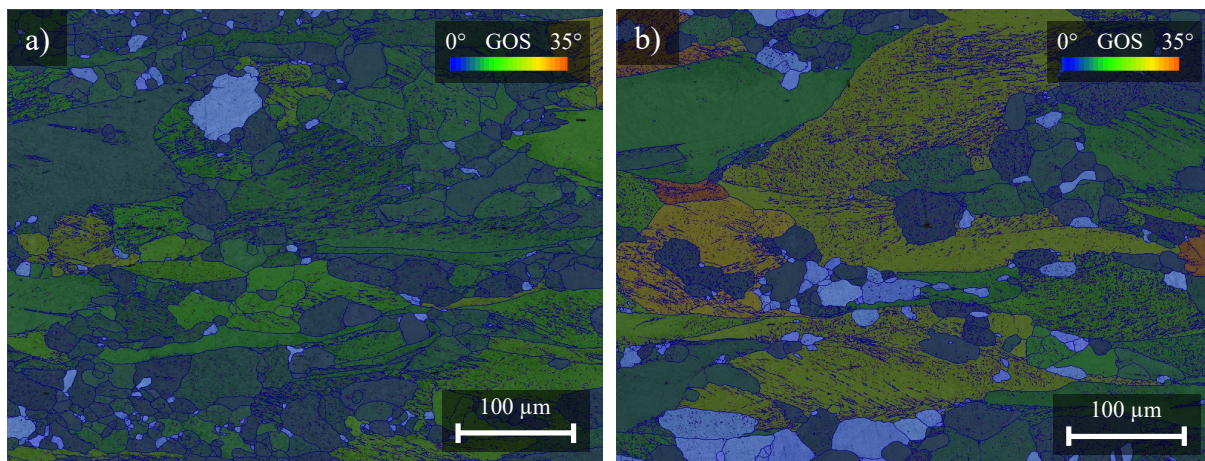


Figure II.9: SEM/EBSD maps (magnification x 300) of the Grain Orientation Spread (GOS) in the Mn05 CR65 steel after 5 s at 650 °C. The recrystallized fractions are estimated at 4 % in (a) and 9 % in (b).

reach a thickness around 70 μm. Discs of 3 mm diameters are punched out the specimen, before being electro-polished. A thin carbon layer, about 30 nm thick, is vaporized on the specimen. This carbon layer is extracted using a Niteau solution, composed of 20 % of nitric acid and 80 % of distilled water, and placed on a copper grid.

### II.5.2 Energy-Dispersive X-ray Spectroscopy

The electron beam is accelerated at 200 keV. The manganese and chromium compositions of the studied cementite particles are measured by Energy-Dispersive X-ray Spectroscopy (EDXS)

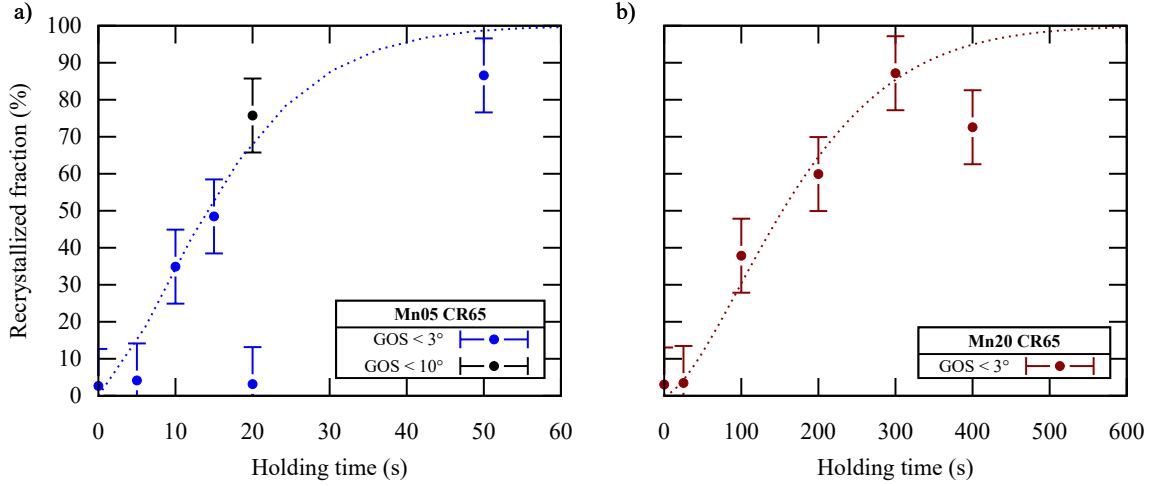


Figure II.10: Recrystallized fraction obtained from SEM/EBSD maps during annealing at 650 °C of the studied Mn05 CR65 (a) and Mn20 CR65 (b) as a function of the annealing time. We consider as grain boundaries, boundaries with a misorientation higher than 10 °. We consider as recrystallized, grains with a GOS lower than 3 ° (in blue (a) or red (b)). Samples with poor surface state are post treated twice. The second post treatment considers GOS up to 10 °. The obtained recrystallized fraction is then plotted in black. Trends curves are plotted in dotted lines.

with the Cliff-Lorimer method with absorption. The particles are verified to be cementite using crystallographic analysis by electron diffraction. Cementite is identified by the space group  $Pnma$  and lattice parameters  $a = 5.069 \text{ \AA}$ ,  $b = 6.736 \text{ \AA}$  and  $c = 4.518 \text{ \AA}$ . The measurements are performed using a Brüker Silicon Drift Detector with a  $30 \text{ mm}^2$  collector plate. The energy resolution for manganese is 127 eV. The carbon composition of cementite is set at 6.67 wt% (25 at%), as expected in cementite, even alloyed. The results of these measurements are presented in Chapter III.

## II.6 Wavelength-Dispersive Spectrometry

The chemical homogeneity in the microstructure is studied by mapping the carbon and manganese content on SEM samples.

The chemical composition is locally analyzed by Wavelength-Dispersive Spectrometry (WDS). The electron beam is focused on the studied zone. The electron beam interacts with the sample in  $1 \text{ }\mu\text{m}^3$  volume, defining the spatial precision of the technique. The interaction of electrons and atoms produces X-rays, whose wavelength depends on the interacting atom. A map of the chemical content is obtained by scanning the sample and analyzing the wavelength of the X-rays.

The maps were acquired by Daniela Obriot at ArcelorMittal Research Center, using a CAMECA SX 100 and a EJOL JXA-8530F Plus with a from 3 kV to 30 kV acceleration tension and a maximum 2  $\mu\text{A}$  current. The results of the measurements are presented in Chapter III.

## II.7 Inductively Coupled Plasma Optical Emission Spectroscopy

The precipitation state of the NbC precipitates is quantified in the niobium micro-alloyed steels by Inductively Coupled Plasma Optical Emission Spectroscopy (ICP-OES). These chemical analyses were performed by Mathieu Cholvin at ArcelorMittal Research Center.

A sample (Figure II.1) is dissolved by electrolysis in a methanol solution containing salicylic acid and lithium chloride. The solution is then filtered using a polycarbonate membrane (porosity size of 0.2  $\mu\text{m}$ ). Then, the filter is dissolved using an acid solution (perchloric acid, hydrochloric acid and hydrofluoric acid) to obtain a dry residue. This residue is finally dissolved in hydrochloric acid. This final solution is analyzed by ICP-OES and compared to standard solutions.

## II.8 Vickers Micro-Hardness

Vickers micro-hardness measurements were also conducted to determine the recrystallization kinetics in the ultra-low carbon ferritic steels Mn05 CR65 and Mn20 CR65, presented in Section II.1, after interrupted annealing treatments.

The Vickers micro-hardness measurements are performed using the Buehler MicroMet 5104 and Mitutoyo HM-100 series devices, available at ArcelorMittal Research Center. These experiments were carried out by Carla Oberbillig. After optical and SEM observations, the Vickers micro-hardness of the samples are measured using a 1 kg testing mass and 10 s indenting time, at the quarter thickness of the sample.

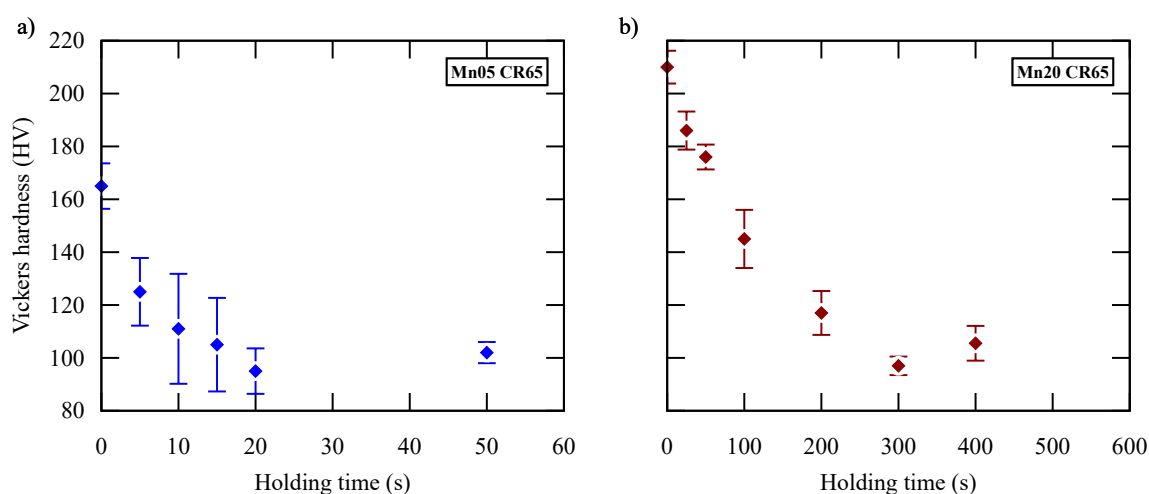


Figure II.11: Vickers micro-hardness during annealing at 650  $^{\circ}\text{C}$  of the studied Mn05 CR65 (a) and Mn20 CR65 (b)

We indented ten times each sample. Figure II.11 plots the mean Vickers micro-hardness measured in the studied Mn05 CR65 (a) and Mn20 CR65 (b) steels. The standard deviation of the ten measurements of each sample is indicated by error bars. In both steels, the Vickers micro-hardness mainly decreases. In the Mn05 CR65, the hardness at the beginning of the holding at 650  $^{\circ}\text{C}$  is 165 HV, much lower than 210 HV in the Mn20 CR65. The lowest hardness is around 95 HV, measured after 20 s in the Mn05 CR65 and 300 s in the Mn20 CR65. After

50 s, in the Mn05 CR65, and 400 s in the Mn20 CR65, the hardness slightly increases up to 105 HV.

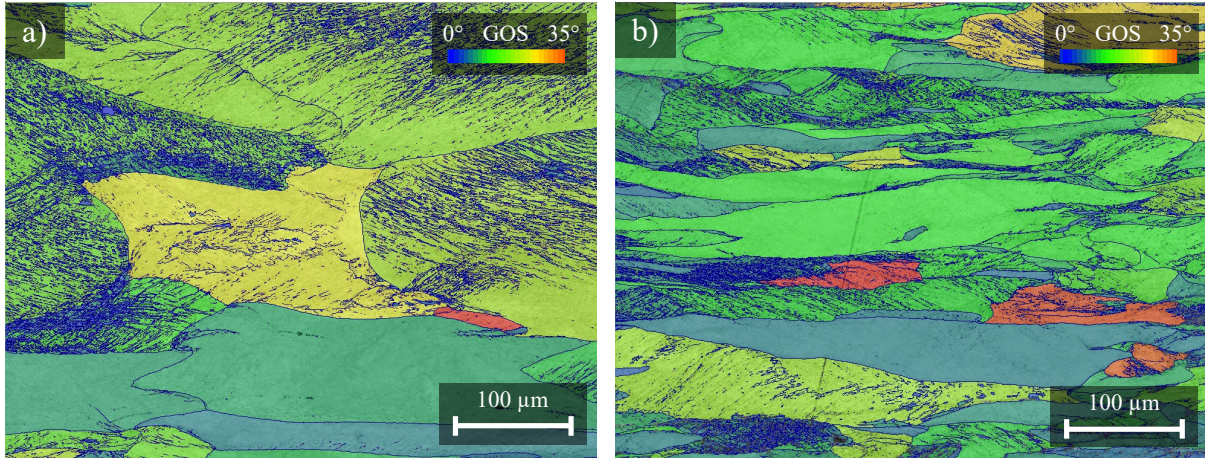


Figure II.12: GOS maps (magnification x 300) in the Mn05 CR65 (a) and Mn20 CR65 (b) steels heated up to 650 °C and gas quenched (0 s holding).

The lower hardness in the Mn05 CR65 at the beginning of the holding at 650 °C is attributed to a larger grain size. Figure II.12 shows GOS maps in the Mn05 CR65 (a) and Mn20 CR65 (b) steels heated up to 650 °C and quenched (0 s holding). The Mn05 CR65 sample (a) shows much coarser grains than the Mn20 CR65 sample (b). As explained in literature [HH95; Chr02; LFZ19], solutes, as manganese, limit both dislocation movement and boundary migration. During hot-rolling in the austenitic domain, new grains form by dynamic recrystallization. As the deformation continues, the dislocation density in the recrystallized grains increases, decreasing the driving force for grain growth. As a consequence, the growth of recrystallized grains may stop. By decreasing the boundary mobility, manganese limits further recrystallized austenite grain growth and leads to smaller austenite grains. Smaller austenite grains then offer a higher density of nucleation sites for ferrite formation. Combined with the lower boundary mobility, higher manganese content is expected to lead to smaller ferrite grain size in our ferritic steel at room temperature after the hot-rolling process.

Larger grain size in the Mn05 CR65 also leads to larger uncertainties. Larger grains mean fewer grains in the indented zone and less statistics. This leads to a wider spread of the measurements.

Hardness is a mechanical property affected by both recovery and recrystallization [HH95]. At the very beginning of the annealing, hardness catches the end of recovery. This can also partially explain the lower hardness in the Mn05 CR65 at the beginning of the holding at 650 °C. It also affects the recrystallization kinetics shape estimated from hardness measurements. Recrystallization makes mechanical properties drop sharper than recovery. Once recrystallization has begun, hardness drop is mainly attributed to recrystallization [OMG08]. Recovery is supposed to account for a small part of this drop.

Then, the recrystallized fraction is estimated from the hardness measurements using the following formula [OMG08]:

$$f_{Recx}(t) = \frac{HV(t) - HV_{0s}}{HV_{min} - HV_{0s}} \quad (\text{II.1})$$

with  $HV(t)$ , the hardness after a time  $t$  at  $650\text{ }^\circ\text{C}$ ,  $HV_{0s}$ , the hardness at  $650\text{ }^\circ\text{C}$  (0 s holding), and  $HV_{min}$ , the minimum hardness measured on the sample.

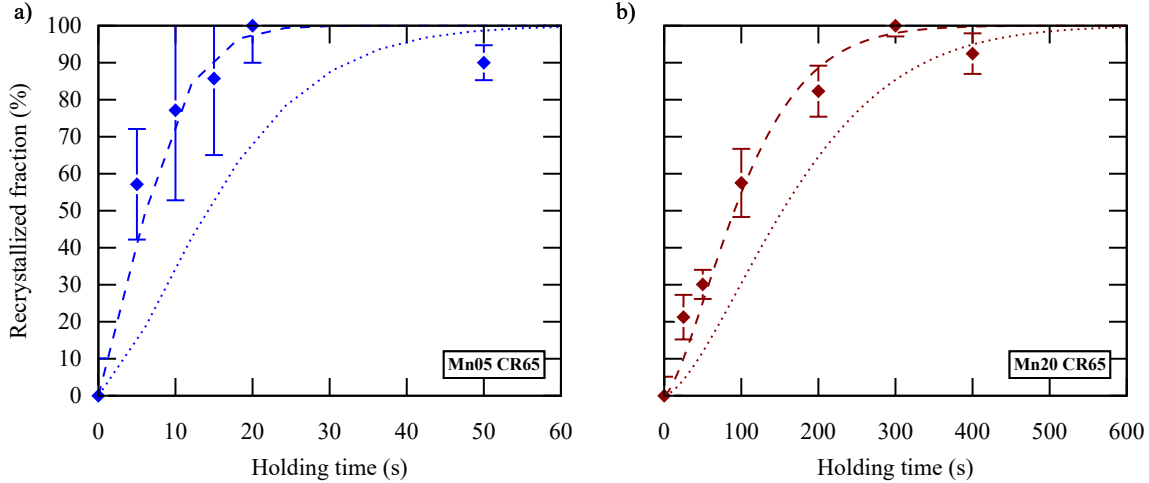


Figure II.13: Recrystallized fraction obtained from Vickers micro-hardness measurements during annealing at  $650\text{ }^\circ\text{C}$  of the studied Mn05 CR65 (a) and Mn20 CR65 (b). Trend curves are plotted in dashed lines. The trend curves of the SEM/EBSD measurements (dotted lines) are plotted as reference.

Figure II.13 plots the recrystallized fractions estimated with the above formula. In both steels, the recrystallized fraction mainly increases with holding time. According to these results, full recrystallization occurs after 20 s in the Mn05 CR65 and 300 s in the Mn20 CR65. After 50 s, in the Mn05 CR65, and 400 s in the Mn20 CR65, the recrystallized fraction slightly decreases down to 90 %. This is due to the final slight increase in hardness. Still, our previous study of recrystallization kinetics using SEM/EBSD shows that the microstructure is not fully recrystallized after 20 s in the Mn05 CR65 and 300 s in the Mn20 CR65. On the contrary, it highlights fully recrystallized microstructures after 50 s, in the Mn05 CR65, and 400 s in the Mn20 CR65.

In this section, recrystallization kinetics were estimated from post-mortem Vickers micro-hardness measurements. The large grain size in our samples, especially in the Mn05 CR65, widens the uncertainties of such hardness measurements. Both recovery and recrystallization affect hardness. As recovery and recrystallization cannot be decorrelated, the recrystallization kinetics shape at the beginning of the annealing is altered. These results confirm the trends obtained by SEM/EBSD and provide an alternative base for the validation of our new time-resolved methodology based on HEXRD experiments.

## II.9 High Energy X-Ray Diffraction

In situ High Energy X-Ray Diffraction (HEXRD) experiments are conducted on PETRA III - P07 beamline at the Deutsches Elektronen Synchrotron (DESY) facilities in Hamburg (Germany).

Experiments performed in 2016 (proposal I-20160160 EC) and results from the PhD work of Moreno [Mor19] were reused. Around 200 new experiments were carried out during this study, split in two beamtimes in 2021 (proposal I-20200450 EC) and 2022 (proposal I-20220239 EC). These experiments were performed by Guillaume Geandier, Marc Moreno, Sébastien Allain, Julien Teixeira, Cécile Rampelberg, Juan Macchi, Miguel Costa Salazar and Clélia Couchet.

### II.9.1 Experimental set-up

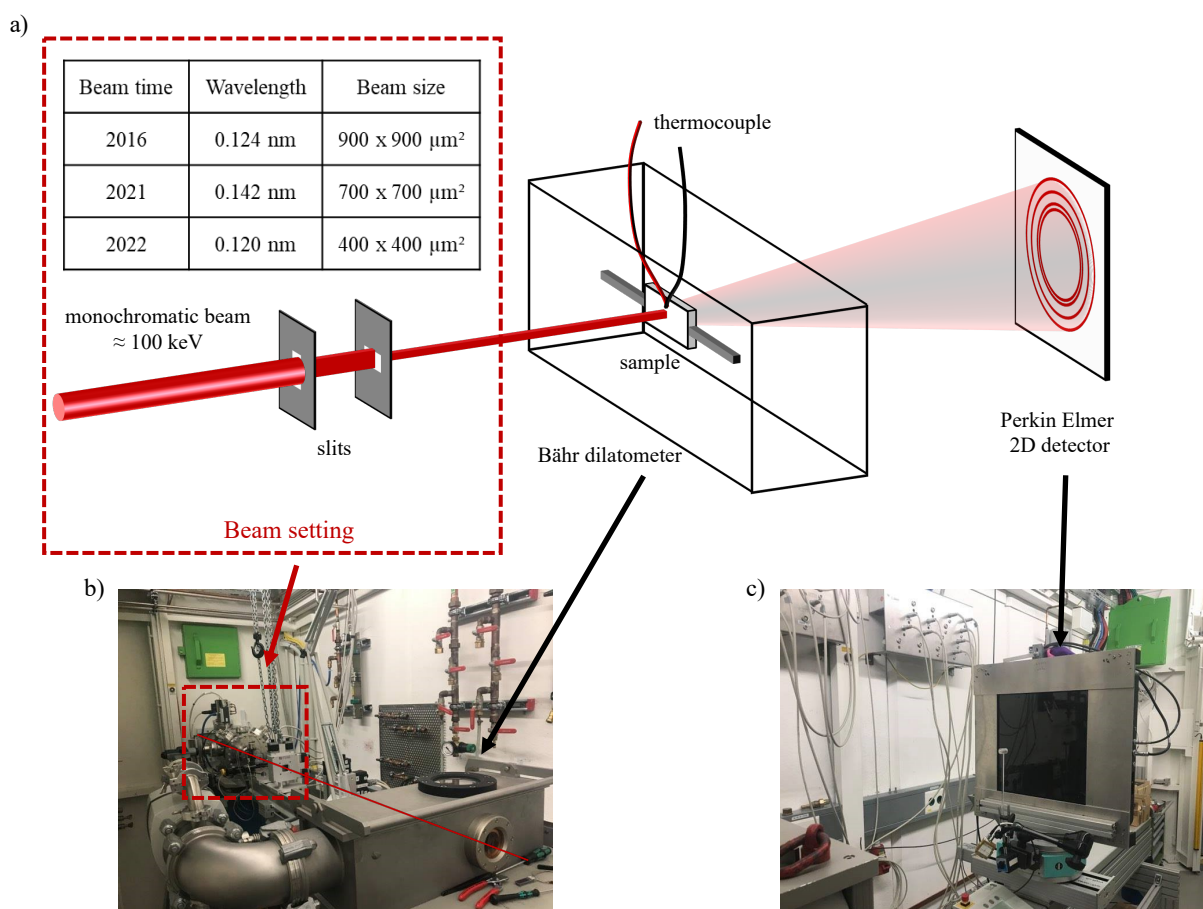


Figure II.14: Schema (a) and pictures (b,c) of the in situ High Energy X-Ray Diffraction (HEXRD) experiment setup used on the PETRA III - P07 beamline at the DESY facilities.

The experimental setup is represented in Figure II.14 (a). A X-Ray beam of high energy ( $\approx 100$  keV) is made monochromatic by a silicon monochromator and shaped by slits. The beam goes through the sample placed in a Bähr DIL805 A/D dilatometer, used to simulate thermal cycles (see Section II.2). The diffracted beams produce typical Debye-Scherrer (DS) rings (Figure II.15 (a)) on the planar Perkin-Elmer (PE) detector placed downstream. Such detector offers a low ratio between background noise and signal intensity. Combined with the high flux from the synchrotron source, in situ high quality acquisitions are possible at high acquisition rates (up to 10 Hz) during the thermal treatment.

The interaction volume ( $\approx 1 \text{ mm}^3$ ) offers a large investigation zone, ensuring representativity of the bulk material, contrary to more local observations (SEM). Continuous ring patterns are expected, due to the fine grain size in the studied steels, at least in the early stages of the thermal cycles. After ferrite recrystallization has begun, diffraction spots are observed on the continuous DS rings. These spots are analyzed to follow the recrystallization process, as presented in the following.

The detector is installed such that the five first rings of ferrite are fully observed on the collected diffraction patterns. The sample-detector distance depends on the beam energy. The higher the energy, the narrower the diffraction angles.

## II.9.2 Diffraction pattern analysis

During each experiment, between 700 to 3500 diffraction patterns were collected. Automated numerical tools were necessary to analyze systematically the diffraction pattern.

### II.9.2.1 Rietveld analysis

The phase fractions are measured using conventional Rietveld refinements, performed on 1D  $2\theta$  versus intensity profiles, as plotted with black circles in Figure II.15 (b, c). For the considered experiments, a complete azimuthal integration of each 2D DS ring pattern is performed using PyFAI [Ash+15].

A precise instrumental calibration is crucial to determine the center of the ring patterns, as well as to correct the ellipticity of the rings, due to the relative position of the PE detector and the sample. A  $\text{LaB}_6$  powder is chosen as calibrant, as its diffraction patterns are well known at room temperature. A capillary filled with strain-free  $\text{LaB}_6$  powder is installed in the experimental setup and diffraction patterns are collected at room temperature. The position and parallelism of the detector are evaluated through the identification of the  $\text{LaB}_6$  rings using PyFAI [Ash+15]. These parameters are input for systematic correction and azimuthal integration of the studied diffraction patterns.

A Rietveld refinement is performed on each 1D diffraction pattern of the studied experiments, using the FullProf software developed by Carvajal et al. [Rod93]. From instrumental (beam wavelength) and structural (phases crystallography, ...) inputs, a theoretical 1D diffraction profile, in red line in Figure II.15 (b, c), is adjusted on the experimental one using a Weighted Least Squares method.

The experimental 1D diffractograms, in black circles in Figure II.15 (b, c), are analyzed in the  $2\theta$  range  $2.5^\circ - 10.0^\circ$ , so that only full rings are considered. We model diffraction peaks using pseudo-Voigt functions. The fitting process outputs phase structural parameters: lattice parameters, scale factors, peak widths, strains and overall isotropic temperature factor. Phase fractions in multi-phased materials are secondary outputs of the fitting process, linked to the diffraction peak intensities, as detailed in Rietveld's work [Rie69].

The confidence in outputs relies on the quality of the fit, as it conditions the deconvolution of contributions to the diffraction peak aspect, such as experimental broadening and density of crystalline defects. For each experiment analyzed, a first diffractogram is fitted manually to ensure the reliability of the fitting parameters. The full batch is then fitted automatically using the fitted parameters as starting values in the fitting process of the following diffractogram. The parameters are fitted in the same user-defined order.

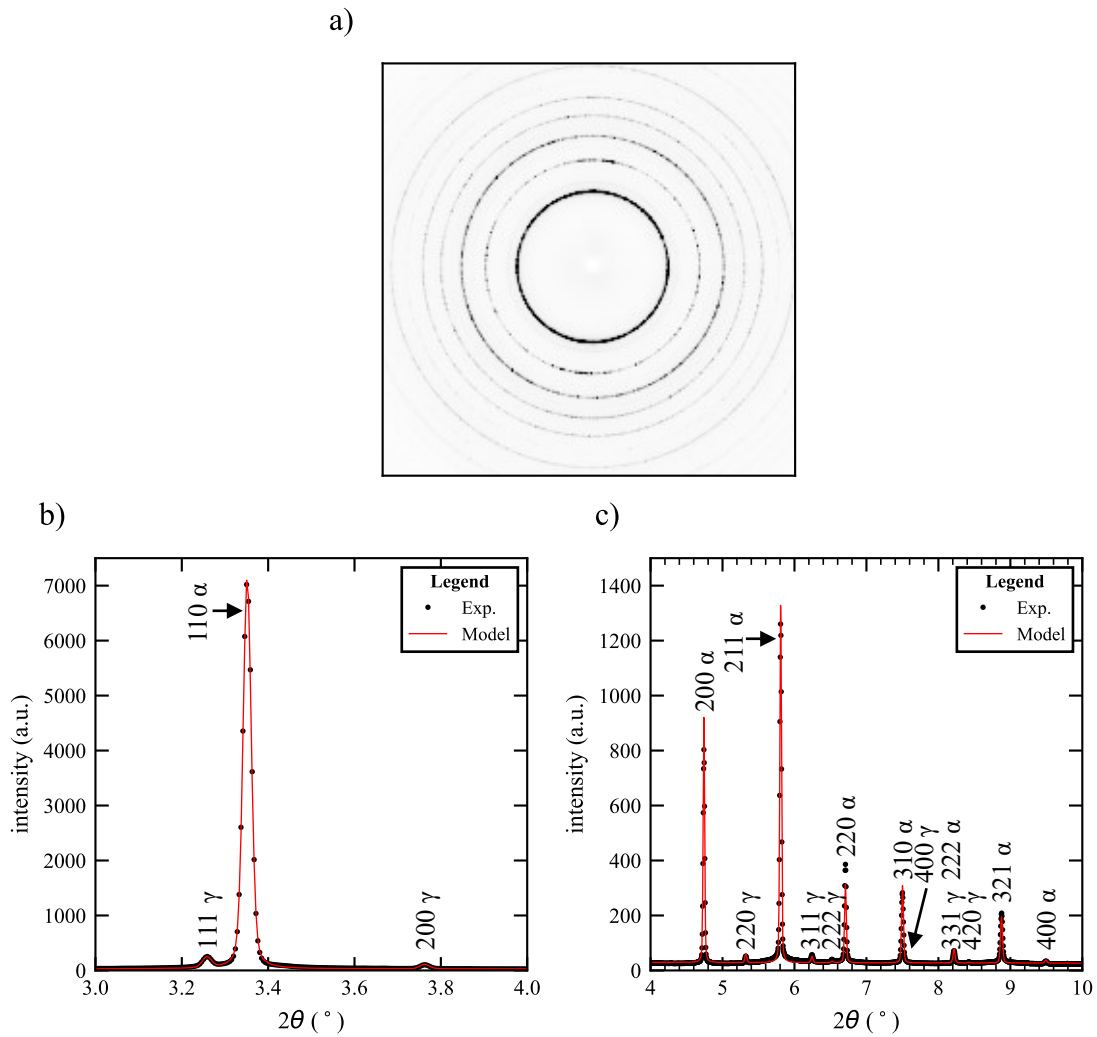


Figure II.15: Debye-Scherrer rings (a) and 1D diffraction patterns (b, c) during the annealing of the DP600 CR65 at 800 °C. The experimental 1D diffraction pattern is plotted with black circles and the fitted theoretical diffraction pattern is plotted with a red line. The temperature and the axis scales are chosen to show the diffracting planes of ferrite and austenite.

Two crystal systems are considered: body centered cubic  $I m\bar{3}m$ , corresponding to ferrite, and the face centered cubic  $F m\bar{3}m$ , corresponding to austenite. Cementite is not systematically investigated by HEXRD. This point is further discussed in Chapter III.

We use two main outputs in the present work. The ferrite lattice parameter is used to correlate the diffractograms (and associated results from the fitting process) to the data collected by the dilatometer during the thermal cycle. The precise estimation of the temperature of the sample corresponding to a 2D diffractogram is crucial. This is done by identifying well known metallurgical phenomena, here, the expansion of the lattice during heating. This process leads to a temperature uncertainty, given by  $\Delta T = \pm \text{heating rate}/\text{acquisition rate}$  [Nak04; Esi+14].

Using an acquisition rate of 10 Hz during the heating stage, the temperature uncertainty is estimated at 0.3 °C during slow heating (3 °C/s) and 3 °C during fast heating (30 °C/s). Then, the phase fraction, estimated from the peak fitting, are plotted against the experimental time and temperature of the sample, to study the phase transformation kinetics. The uncertainty on the phase fraction due to the quality of the peak fitting is estimated at only 1 %. Finally, the Rietveld analysis is supposed to be used under powder diffraction conditions. These conditions are not fulfilled in our poly-crystalline materials. Especially, during the holding stage, diffraction spots appear on the Debye-Scherrer rings of both austenite and ferrite, as observed in Figure II.15 (a). As a consequence, the 1D diffractogram obtained by integration differs in shape from one in powder diffraction conditions. Figure II.15 (c) shows that the model peaks for powder diffraction either under-estimate (peak (220) of ferrite) or over-estimate (peak (200) of ferrite) the experimental diffraction peaks. The induced error on the austenite fraction is hard to quantify, as the computed fraction on our material should be compared to the fraction computed in a similar material fulfilling the powder diffraction condition. Though we cannot estimate this error, we feel confident on our fraction estimation. We reproduced several times our experiments across three campaigns with several experimenters and found our experiments to be perfectly repeatable (see B).

### II.9.2.2 Isolated Diffraction Spot Tracking

During this PhD work, we developed a new methodology to study in situ the recrystallization of the studied steels. This method estimates the recrystallized fraction as a function of time and temperature.

**II.9.2.2.1 Methodology** Inspired from the work of Moreno et al. [Mor19; Mor+18], a new method to study in real-time recrystallization of industrial polycrystals is developed. As in Moreno's work [Mor19; Mor+18], HEXRD is used without rotation of the sample. Our new method, entitled Isolated Diffraction Spot Tracking (IDST), is based on the tracking of diffraction spots appearing on the continuous Debye-Scherrer ring, due to newly recrystallized grains, as explain is the previous literature review in I.1.2. Contrary to Moreno's method, being a 1D method by design (starting with an azimuthal integration), the IDST method is a full 2D characterization method. As shown in the following, a larger variety of information can be extracted with high statistics.

Figure II.16 shows diffraction patterns of the Mn20 CR65 steel at room temperature (Figure II.16 (a)) and after 550 s annealing at 650 °C (Figure II.16 (b)). Before treatment (Figure II.16 (a)), the Debye-Scherrer rings are smooth and continuous. After 550 s at 650 °C (Figure II.16 (b)), high-intensity spots appear on the Debye-Scherrer rings. The intensity of these spots increases with the size of the corresponding grains. A similar approach has been used to track a few grains by 3DXRD [Pou+11; Lau+03; Lau+06]. The method presented here is dedicated to the study of polycrystalline samples close to industrial products.

The IDST method involves a systematic tracking of diffraction spots appearing on the continuous DS rings. This tracking is performed a posteriori, once the experiments are completed. The TRACK software, from the start-up APREX SOLUTIONS, offered a ready-to-use numerical tool for object detection and tracking on video.

The images collected by the Perkin-Elmer detector are imported into TRACK (16-bit TIFF format). Filters can be used to smooth, increase the contrast or invert the imported images.

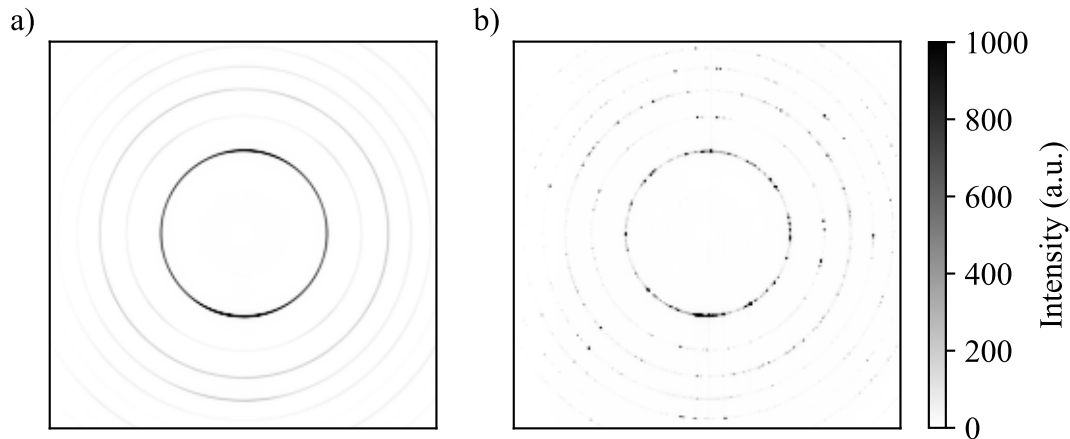


Figure II.16: Diffraction patterns of the Mn20 CR65 steel (a) at room temperature, (b) after 550 s at 650 °C.

These filters have been used only as a visual guide in the user interface, so as not to alter the information contained in the images.

Our 2D characterization method is composed of two main steps. First, the detection step consists in isolating the diffraction spots from the continuous background ring as well as from the other spots. The spots are detected on each diffraction image individually. Then, the tracking step involves the labelling of each detected spot and their identification from one image to another.

In the framework of this study, the diffraction patterns are grey-scale images (16 bits). The detection step consists in the application of several grey scale thresholding. The thresholds can be applied at different spatial scales, to help discriminate similar objects on different backgrounds. The simple threshold is applied to the whole image. Using a global, regional and/or local threshold implies the definition of a typical spatial size and a threshold factor. For each image, the detection step starts with the application of a simple threshold to erase the continuous background noise. Local thresholding is then applied to detect local maxima. It distinguishes nearby spots. Figure II.17 shows a model 1D intensity profile containing 4 numbered peaks. Simple thresholding, shown as a red line eliminates the low-intensity peak 1, which represent background noise. This thresholding detects peak 2, but peaks 3 and 4 are confused, as they are too close to each other. In this case, no simple thresholding is able to distinguish peaks 3 and 4 without eliminating peak 2. Local thresholding is therefore necessary. A window, outlined in black lines in Figure II.17, defines a Region Of Interest (ROI) and is used to scan the image. The mean intensity over the ROI, plotted in blue, is multiplied by a user-defined constant, 1.5 in the figure, constituting the local threshold, drawn in green.

The software detects the pixel cloud composing the spot. This is the appropriate method for small objects. The position of the maximum intensity defines the position of the spot. A minimum distance of one pixel is imposed between objects. Combined with local threshold, this distance helps to separate nearby spots.

The tracking step, schematized in Figure II.18, ensures that the detected objects are recognized from an image to the other. Recrystallization spots are not very mobile, meaning their position on the diffraction pattern is almost fixed. The "Nearest" tracking method is an option from the Track software to deal with such object tracking. With this method, an object detected

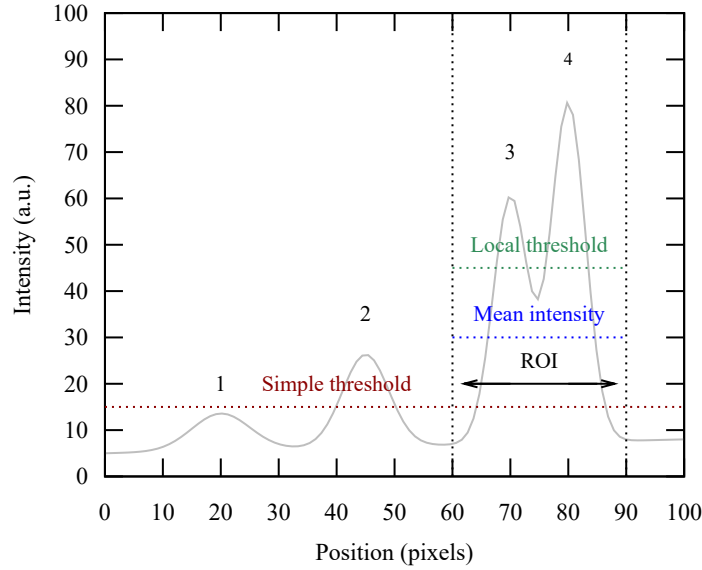


Figure II.17: 1D example of the detection step in the IDST method. The simple threshold (in red) erases the background noise. The local threshold (in green) is calculated based on the local mean intensity (in blue) and separates nearby local maxima.

at position  $(x; y)$ , represented by a black spot in Figure II.18, on the image  $n$  is searched for in the ROI  $(x \pm r; y \pm r)$  on the image  $n + 1$ , with  $r$  the searching radius. If the object is not found, represented by a green spot in Figure II.18, it is searched in the region  $(x \pm \Delta n \times r; y \pm \Delta n \times r)$  on image  $n + \Delta n$ . A maximum value of  $\Delta n$  has been set at 10. Beyond  $n + \Delta n_{\max}$ , the software considers that the object disappeared. However, widening the search field in the event of momentary object loss is not appropriate in the case of small, sometimes close and virtually stationary objects. Spots can be confused with this method. The Slow or fixed objects option was therefore used to maintain the search radius. The spot is searched in the region  $(x \pm r; y \pm r)$  on image  $n + \Delta n$ . For each object tracked, a trajectory contains the information about the object, such as the maximum intensity, the position or the area, as a function of time. For each detected spot on a current frame, the position is compared to the position of the identified spot on the previous frame. If a corresponding spot is found, the track is updated, else a new spot is considered to have appeared and new track is created.

When a new spot is detected, an identification number is attributed and different features, such as the maximum intensity, the mean intensity, the size, the position, . . . , can be evaluated and saved in a CSV file. Another CSV file lists the quantity of detection and trajectory for each image.

**II.9.2.2.2 Validation of the IDST method** During the validation process, we study ferrite recrystallization in the ultra-low carbon ferritic steels Mn05 and Mn20, presented in Section II.1, during annealing treatments (see Section II.2). We compare the fractions of recrystallized ferrite obtained using our new method (experiments carried out in 2021) to fractions obtained from SEM/EBSD maps, presented in Section II.4.3, or from Vickers micro-hardness measurements, presented in Section II.8.

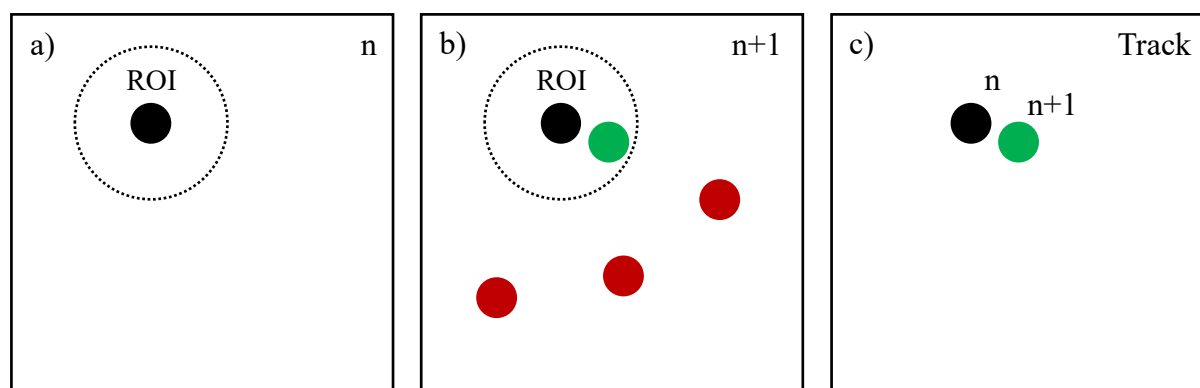


Figure II.18: Build of a track. An object (black spot) is detected at on the frame  $n$  and a ROI is defined (limited by a dashed circle) (a). On the next frame  $n + 1$ , an object detected in the searching region (green spot) is identified as the same object (b). The resulting track contains the information (position, intensity, size, ...) of the object over time (c).



Figure II.19: Detected spots (circled in blue) on the diffraction pattern of the Mn20 CR65 after 100 s at 650 °C.

Figure II.19 shows the diffraction patterns of the Mn20 CR65 collected after 100 s annealing at 650 °C and heated at 100 °C/s. The TRACK software detects 204 diffraction spots, circled in blue in the figure. Some spots, as seen in the zoom on the (110) ring, have an intensity near to the background intensity of the ring.

Considering our polycrystal materials and their typical grain size, we consider that diffraction conditions are close to powder diffraction conditions. Powder diffraction relies on random orientation of crystallites. A given Bragg plane  $hkl$  diffracts X-rays with a characteristic  $2\theta$  angle according to the Bragg relation. The higher the diffraction angle, the larger the ring on the

detector. The X-ray photons spread over a wider area, which locally decreases the ring intensity. Due to crystal symmetries, several planes diffract X-rays with the same  $2\theta$  angle, forming plane families. The number of planes in a family, diffracting X-rays in the same diffraction ring, gives the reflection multiplicity. The higher the multiplicity, the more X-ray photons diffracted in the  $2\theta$  angle corresponding to the family. Despite the high quantity of grain illuminated, our diffraction conditions are not perfect powder diffraction conditions. Due to cold-rolling, texture may appear [HH95]. In textured materials, grains are no more randomly oriented in the material and specific orientation are overrepresented. Diffraction rings corresponding to this orientation are brighter. Due to various diffraction angles, reflection multiplicity and texture, diffraction rings have various relative intensities. We successfully detect spots on various background intensities on a same image using the local thresholding.

Figure II.20 shows the number of detected spots (in black line) and the number of tracked spots (in green line), i.e. identified as one object and memorized, during the annealing of the Mn05 CR65 (a) and Mn20 CR65 (b). We identify two stages.

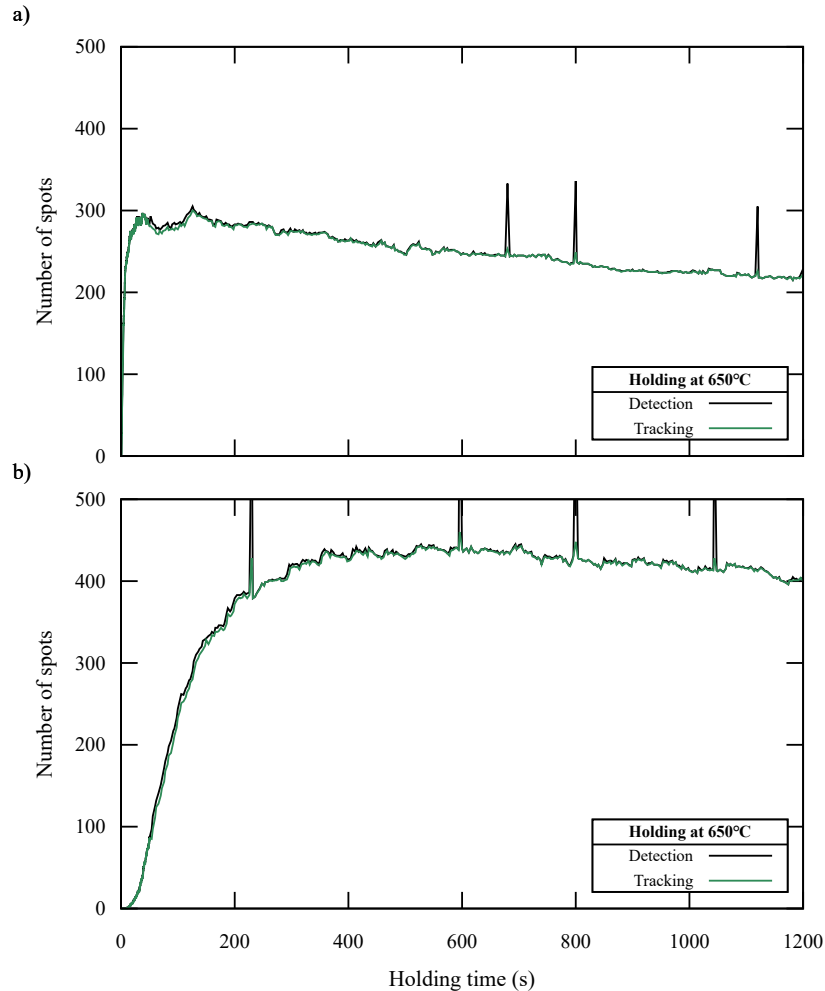


Figure II.20: Number of detected (black line) and tracked spots (green line) during the holding stage at 650 °C of the Mn05 CR65 (a) and Mn20 CR65 (b).

First, in both studied steels, the number of detected spots and the number of tracked spots increase with time up to a maximum around 300 spots after 50 s in the Mn05 CR65 and 440 spots after 550 s in the Mn20 CR65. During this stage, the curves present a sigmoidal shape.

In a second stage, the number of detected spots and the number of tracked spots slowly decrease. In both studied steels, the number of detected spots and the number of tracked spots are very close. Almost all detected spots on a current image are associated to another on the previous or following image, showing the quality of the tracking.

In the following, the number of tracked spots is used to quantify the recrystallization. The quantity of detected spots is considered less accurate as it could contain artifacts (objects outside rings often present on a single image).

During this study, the intensity, the area and the position of the detected spots are followed. These results are not presented nor used in the present manuscript. Yet, we are currently working on these results to bring our method to the next level and perform systematic individual grain growth investigation of the diffracting grains.

The number of spot is assumed proportional to the recrystallized fraction [Mor+18; Pou+11; Lau+03; Lau+06]. The lower number of spots in the Mn05 CR65 (Figure II.20) is attributed to the larger grains as shown by our SEM/EBSD observations (Figure II.12). The studied samples are considered fully recrystallized when the maximum of spot detection is reached, supported by our SEM observations. The decrease in detected spot number is attributed to grain growth. Grain growth means less and coarser grains in the studied volume, i.e. less grains could diffract.

The recrystallized fraction is calculated from the IDST results as the current number of tracked spots divided by the maximum number of spots detected during the considered experiment.

Figure II.21 plots the recrystallized fractions estimated by the IDST method (in solid line), by SEM/EBSD maps (in circles) and by Vickers micro-hardness measurements (in diamonds) during annealing at 650 °C of the Mn05 CR65 (a) and Mn20 CR65 (b).

The time resolution of the recrystallization kinetics obtained with the IDST method is higher by construction than using SEM/EBSD observations or Vickers micro-hardness measurements. The IDST method gives an estimation of the recrystallized fraction every 0.33 s during the first minute of the annealing and every second then, up to the end of the treatment, obtained from a single experiment lasting around twenty minutes. On the contrary, ex situ methods, as SEM/EBSD or hardness, give six estimations of the recrystallized fraction, each. Each estimation needed an interrupted thermal treatment, the sample preparation and the ex situ experiment (SEM/EBSD map or hardness measurement). These total of twelve estimated fraction represent several days of work.

In both studied steels, the recrystallization kinetics given by the IDST method increases with a sigmoidal shape, as expected from literature [HH95; OMG08; Rei52; Mor+18].

In the Mn05 CR65, the recrystallized fraction starts increasing after 1 s at 650 °C. The estimated recrystallized fraction increases fast at first. The increase slows down and the recrystallized fraction stagnates from 40 s at 650 °C around 97 % with local fluctuations about  $\pm 2$  %. The recrystallized fractions estimated from the IDST method coincide almost perfectly with the fractions estimated with Vickers micro-hardness measurements. On the contrary, fractions estimated from SEM/EBSD maps are far lower, except at the very end of recrystallization.

In the Mn20 CR65, the recrystallized fraction increases from 10 s at 650 °C, up to 400 s where the fractions stagnate around 98 % with local fluctuations about  $\pm 2$  %. The recrystallized fractions estimated from the IDST method are close to the fractions estimated with the ex situ methods.

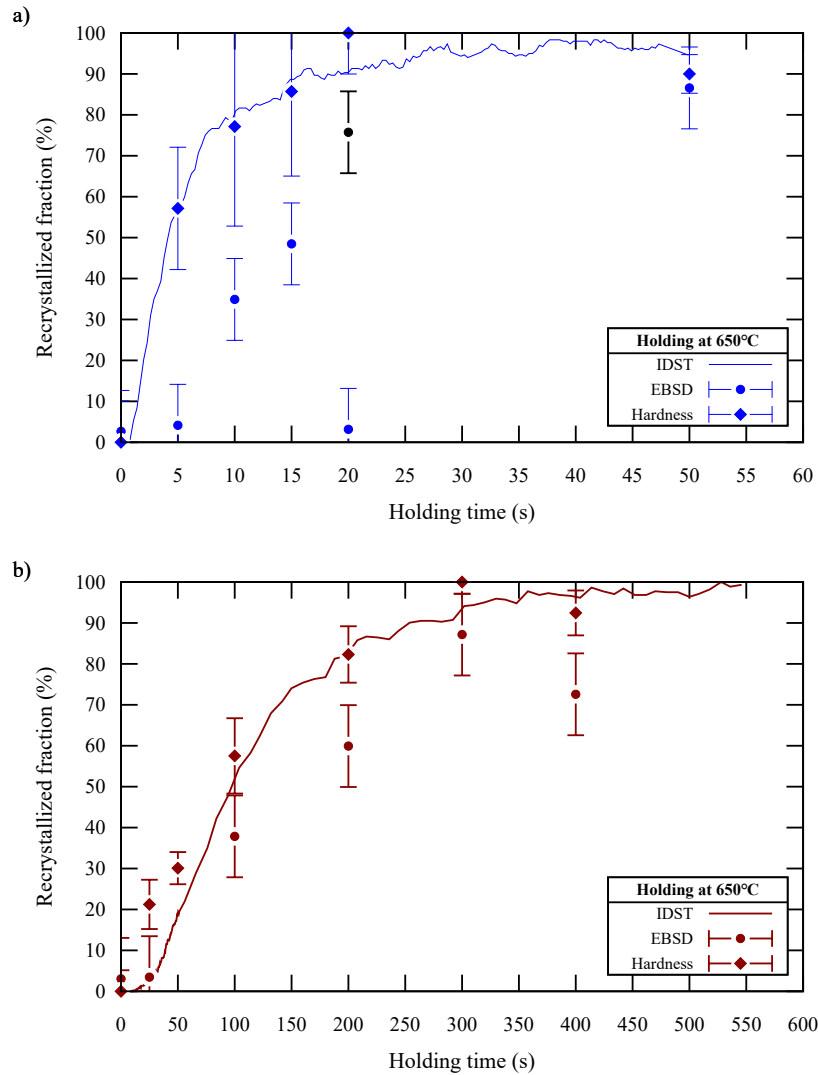


Figure II.21: Recrystallized fractions obtained by the IDST method (in solid line), by SEM/EBSD maps (in circles) and by Vickers micro-hardness measurements (in diamonds) during annealing at 650 °C of the Mn05 CR65 (a) and Mn20 CR65 (b).

In both studied steels, the fractions estimated with the IDST method and Vickers micro-hardness are very close. The fractions estimated with the SEM/EBSD maps are often lower. As explained in Section II.4.3, our SEM/EBSD observations suffer from a lack of grain statistic due to the large grain size, especially in the Mn05 CR65. Our hardness measurements offer a better statistic, as ten measurements were performed on each sample. The IDST method investigate the larger volume (beamsize  $700 \times 700 \mu\text{m}^2$ ) ensuring the grain statistics.

In addition to the prolongation of recrystallization, the excellent time resolution of the IDST method highlights its delay, expected from literature [LFZ19].

These observations validate the fractions estimated with our IDST method. We estimate the uncertainty of the IDST method using the fraction fluctuations during stagnation, i.e.  $\pm 2\%$ .

**II.9.2.2.3 Conclusion on recrystallized fraction quantified by IDST** We presented a new 2D method to investigate in situ the recrystallization process. This method, called Isolated Diffraction Spot Tracking IDST, inspired from 3DXRD and the RPC method detailed in [Mor19; Mor+18], is based on the detection and tracking of diffraction spots of high intensity, originating from newly recrystallization grains.

We used this method to follow recrystallization in cold rolled ultra-low carbon ferritic steels during annealing. Recrystallized fractions estimated with the IDST method were successfully compared to fractions obtained by more conventional method, such as Vickers micro-hardness measurements or SEM/EBSD observations.

The IDST method offers an excellent time resolution, contrary to more conventional ex situ methods. The method investigates larger volumes, ensuring a large grain statistic, contrary to SEM/EBSD measurements.

In the next chapter, we use the IDST method to follow recrystallization during the intercritical annealing of DP steel semi-product. Our new method makes possible a deep investigation of interactions between ferrite recrystallization and austenite formation.

## II.10 Phase transformation modelling: approach and tools

The literature review in Chapter I offered various approach to model phase transformations. Empirical and physically-based models were presented. Among physically-based models, several interface mathematical description, sharp interfaces or phase-field were studied. Different interface behaviors, such as diffusion-controlled, interface-controlled or mixed mode, were also highlighted.

In the present work, the studied phase transformations are modeled using physically-based models with sharp interface. The ferrite to austenite phase transformation is known to be diffusion controlled [Fon15]. Supported by the previous work on diffusive phase transformation exposed in Chapter I [Mor19; Tei+21], a thermo-kinetic approach was chosen to better understand the physical mechanisms taking place during the phase transformation.

### II.10.1 CALPHAD method

As shown in the literature review, a thermodynamic approach to model diffusive phase transformation relies on the computation of thermodynamic equilibria. Chemical potentials need to be determined as a function of local chemical composition and temperature. Moreover, experiments to determine diffusion data, such as diffusion coefficients, are laborious and time-consuming, even in binary systems [Bor+00]. Besides, such coefficients are specific to the studied system, as gradient compositions of an element were shown to affect the diffusion of other solute elements [Dar42; Dar49].

The CALculation of PHase Diagrams (CALPHAD) method, later extended to refers also to Computer Coupling of Phase Diagrams and Thermochemistry, offers a solution to compute the thermodynamic equilibria. The method is based on experimental and theoretical data on phase equilibria and thermodynamic properties in binary or ternary systems. The main benefit from this method is the computation of equilibria in multi-component systems (more than four elements) using the data on lower systems and physically-based models, considering the crystallography, bounding type or magnetic properties. This strategy limits the number of experiments to be carried out, as well as the amount of data to be stored in databases. Thermodynamic

and mobility data arise from the common work of the Scientific Group Thermodata Europe community [Sun].

The elements in the system, as well as the studied phases must be defined first. Relevant thermodynamic data for the studied system are collected in the database. The Gibbs Free Energy of each phase is computed using a mathematical model and the collected data. The thermodynamic equilibria are deduced from the Gibbs free energy depending on the equilibrium hypotheses on the system (Para-Equilibrium, Local Equilibrium, Ortho-Equilibrium), giving finally the chemical and thermodynamic properties of the considered phases. Similarly, mobility data are stored in databases. The relevant data for the studied system are collected and the diffusion parameters, such as inter-diffusion coefficients, are computed from atomic mobilities.

### II.10.2 Numerical tools

The Thermo-Calc software is a commercial numerical tool using this method. Both graphical and console user interface are available. In this work, the 2020b version of the Thermo-Calc software was used in Console mode. The thermodynamic data are taken from the TCFE9 database.

DICTRA is the Add-on module of the Thermo-Calc software dedicated to the modelling of multicomponent diffusion-controlled phase transformation. This Diffusion module is based on the CALPHAD method and the multicomponent diffusion equations. The diffusion equations are solved in 1D under user-defined geometries. The available geometries are, then, planar, cylindrical, or spherical. The mobility data are taken from the MOBFE4 database.

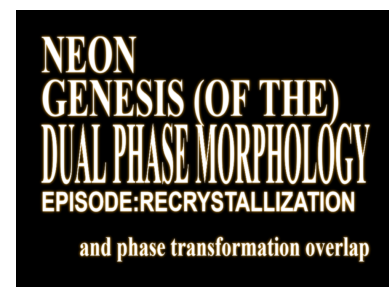
For more details on the Thermo-Calc software or its DICTRA module, the reader may refer to the documentation made available by the Thermo-Calc society, as well as the very complete work of Anderson et al. [And+02].

---

## Chapter III

# Interaction between recrystallization and austenite formation investigated by in situ HEXRD experiments

---



*Marco Freire*

III.1 Effect of the heating rate on the austenite transformation . . . . .	88
III.1.1 Materials and methods . . . . .	89
III.1.2 Results . . . . .	89
III.1.2.1 Initial microstructure . . . . .	89
III.1.2.2 Chemical composition of cementite particles . . . . .	90
III.1.2.3 Austenite growth from the two identified cementite aggregates . . . . .	93
III.1.2.4 Carbon homogeneity across austenite . . . . .	94
III.1.2.5 Kinetics of ferrite recrystallization and austenite formation . . . . .	96
III.1.2.6 Microstructure at the end of the heating stage . . . . .	102
III.1.3 Discussions . . . . .	103
III.1.3.1 Proposed mechanisms for austenite formation during the heating stage . . . . .	103
III.1.3.2 Influence of the composition of cementite particles on their dissolution kinetics . . . . .	106

III.1.3.3	Influence of heating rate on the ferrite recrystallization kinetics .	108
III.1.3.4	Influence of the heating rate on the austenite microstructure . .	108
III.1.3.5	Influence of the heating rate on the austenite formation kinetics during the holding stage . . . . .	109
III.1.4	Conclusion on ferrite recrystallization and austenite formation interaction induced by heating rate . . . . .	110
III.2	Effect of the micro-alloying and cold-rolling ratio on the austenite transformation	111
III.2.1	Materials and methods . . . . .	112
III.2.1.1	Description of the niobium micro-alloyed samples . . . . .	112
III.2.1.2	Description of the cold-rolled samples . . . . .	114
III.2.2	Results . . . . .	114
III.2.2.1	Experiments on niobium micro-alloyed grades . . . . .	114
III.2.2.1.1	Initial microstructure . . . . .	114
III.2.2.1.2	Microstructure at the end of the heating stage . . . . .	116
III.2.2.1.3	Kinetics of ferrite recrystallization and austenite formation . . . . .	116
III.2.2.2	Experiments on the DP600 with various cold-rolling ratios . . .	119
III.2.2.2.1	Initial microstructure . . . . .	119
III.2.2.2.2	Microstructure at the end of the heating stage . . . . .	121
III.2.2.2.3	Kinetics of ferrite recrystallization and austenite formation . . . . .	122
III.2.3	Discussions . . . . .	124
III.2.3.1	Effect of niobium micro-alloying and cold-rolling on the initial microstructure . . . . .	124
III.2.3.2	Ferrite recrystallization control . . . . .	125
III.2.3.3	Austenite morphology strongly affected by ferrite recrystallization	127
III.2.3.4	Austenite formation kinetics driven by thermo-kinetics . . . . .	128
III.2.4	Conclusion on ferrite recrystallization and austenite formation interaction induced by niobium micro-alloying and cold-rolling ratio . . . . .	130
III.3	Conclusions on the interaction between ferrite recrystallization and austenite formation . . . . .	132

As discussed in Chapter I, the microstructure morphogenesis during the whole production of Dual Phase steels is crucial for steelmakers, as it controls their mechanical properties [All+15; Pus+15; Sco+17]. In this process, the final annealing step is decisive and typical "necklace" or "banded" microstructures can be obtained during intercritical annealing using either low or high heating rates (typically between 1 °C/s and 50 °C/s and depending on the heating technology on the production lines). It is also well established that faster heating leads to a faster austenite formation kinetics and a higher overshoot from Ortho-Equilibrium (OE), i.e. the fraction of austenite temporarily exceeds the OE fraction during the isothermal holding. The following cooling steps strongly impact the fraction of phases (ferrite, bainite and martensite) but the final morphology is mainly inherited from the heating stage.

These microstructural and kinetics effects strongly depend on the distribution of alloying elements in the microstructure prior to annealing, more generally called inheritance effect. For instance, the morphology of the microstructure depends on manganese micro-segregation bands (related to casting conditions) or the distribution of carbon sources (pearlite, cementite, martensite, bainite phases inherited from hot-rolling conditions), acting as austenite nucleation sites (related to the as-cold-rolled microstructure). The relative effect of these distributions is still a bone of contention in the literature.

In the same way, the literature review in Chapter I reports several metallurgical mechanisms, by which ferrite recrystallization and austenite formation interact. Ferrite recrystallization is claimed to affect the spatial distribution of carbon sources, the dislocation density, carbon diffusivity and diffusion distances.

The present Chapter tries to challenge the conclusions drawn above from an experimental point of view but also the influence of the interactions between ferrite recrystallization and austenite formation.

In the first section, the experiments we carried out to study the influence of the heating rate on the studied DP600 grade steel during the intercritical annealing are presented. We combine post-mortem microstructure investigations after interrupted thermal treatments and in situ experiments, as disclosed in Chapter II. To begin, we present our investigations of the growth of austenite from the two identified cementite aggregates (inter-granular cementite particles and pearlite islands) as done in [Mor19; Tei+21], using microscopy (optical, Scanning Electron Microscopy (SEM) and Transmission Electron Microscopy (TEM)), as well as chemical characterization techniques (Energy-Dispersive X-ray Spectroscopy (EDXS) and Wavelength-Dispersive Spectrometry (WDS)). Then, our study on the concomitant kinetics of ferrite recrystallization and austenite transformation thanks to in situ High Energy X-Ray Diffraction (HEXRD) experiments is described and discussed. Ferrite recrystallization and austenite formation kinetics are determined using the Isolated Diffraction Spot Tracking (IDST) method and Rietveld refinements respectively.

In such experiments, the concomitance of ferrite recrystallization and austenite formation is due to the heating rate, as schematized in Figure III.1. In literature, the acceleration of the austenite formation with the heating rate is attributed either to recrystallization, through mechanisms cited above.

In the second section of this chapter, we designed judicious experiments to decorrelate the heating rate and the concomitance of ferrite recrystallization and austenite formation, to go further in the discussion. The heating rate is fixed to maintain the conditions for thermo-activated mechanisms, but we use new alloys with higher niobium micro-alloying [All+20; Son+14; Ver+09] and the reference DP600 steel with lower cold-rolling ratio [HH95; Rei52] in order to delay ferrite recrystallization, as schematized in Figure III.1. This study helps to

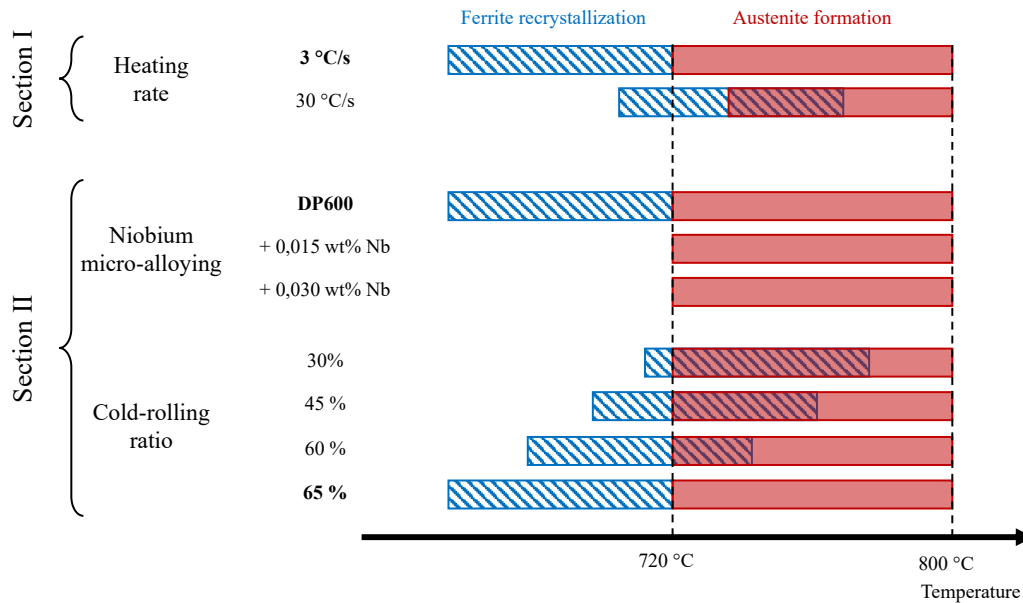


Figure III.1: Schematic representation of the experimental strategy developed in this thesis. The different annealing conditions are compared in terms of ferrite recrystallization and austenite formation. In Section III.1, the mechanisms are controlled by the heating rate and, in Section III.2, by niobium micro-alloying and cold-rolling ratio. The parameters of the reference experiment are highlighted in bold font (non-micro-alloyed DP600 steel composition annealed at 3 °C/s up to 800 °C during 10 min, after 65 % cold-rolling).

discuss several hypotheses from literature and highlights whether or not the concomitance of the two studied mechanisms has a significant effect, at least from a kinetic point of view. The conclusions drawn and mechanisms suggested by our experimental work support our final choices for our numerical investigations and our physics-based model, both detailed in the following Chapter IV.

### III.1 Effect of the heating rate on the austenite transformation

As exposed in introduction, literature (see Chapter I) widely shows that heating rate controls both the morphology of the austenite microstructure and the kinetics of austenite formation. Higher heating rates delay ferrite recrystallization making it overlap with austenite formation possible. In literature, several metallurgical mechanisms, by which ferrite recrystallization and austenite formation interact are proposed, underestimating other purely thermo-kinetics effect.

This section aims to discuss these different mechanisms on experimental basis. We investigate the austenite formation and its interactions with ferrite recrystallization during the intercritical annealing of a cold-rolled ferrite-pearlite microstructure for DP600 production. The growth of austenite from the two identified cementite aggregates (inter-granular cementite particles and pearlite islands) is further studied. We discuss the relevance of the division in closed subsystems for the investigation of austenite formation kinetics used in [Mor19]. We establish ferrite recrystallization kinetics and austenite formation kinetics from in situ HEXRD experiments. We finally discuss the effect of the heating rate on both the austenite formation kinetics and the

	C	Mn	Si	Cr	Nb
Aimed	0.1	1.9	0.2	0.2	< 0.002
Measured	0.092	1.83	0.225	0.193	< 0.002

Table III.1: Aimed and measured nominal composition (wt%) of the studied DP600 steel.

austenite morphology. This section mainly shows that our experimental findings are consistent with the ones already reported in the literature, with our steel, while proposing in-depth analyses of microstructures and kinetics enabled by cutting-edge techniques to ensure the nature of the mechanisms at work (interface conditions in particular).

### III.1.1 Materials and methods

This section focuses on ferrite recrystallization and austenite formation in a conventional DP600 grade, with a cold-rolled ferrite-pearlite microstructure, during the intercritical annealing. The aimed and measured nominal composition of the studied DP600 is reported in Table III.1. The experiments of the present section are performed on 65 % cold-rolled samples. More details are given in Chapter II. This studied steel is referred as DP600 CR65 in the following.

Two heating rates are studied: 3 °C/s, referred as low heating rate and taken as reference scenario in the following, and 30 °C/s, referred as high heating rate. These heating rates were chosen for their industrial relevance. The heating stage is followed by an isothermal holding at 800 °C for 10 min.

We simulated annealing treatments during HEXRD experiments on the synchrotron beamline PETRA III - P07 at the DESY facility (Hamburg). The recrystallization progress is monitored using the IDST method. The austenite fraction during the annealing is obtained using the Rietveld analysis. Microstructural evolutions are studied post-mortem using optical microscopy and SEM. Mean sizes of ferrite grains, pearlite islands and austenite islands are measured on the micrographs presented in this Section in the cold-rolling direction, giving their length, and in the direction normal to the cold rolling direction, giving their thickness. Mean sizes are estimated from ten measurements, ensuring a precision of 0.1  $\mu\text{m}$ . Chemical composition in cementite particles is quantified using EDXS in TEM. Silicon is almost not soluble in cementite. Despite the silicon in the nominal composition, the composition of cementite particles in silicon is not studied. Carbon homogeneity across austenite is investigated by WDS.

### III.1.2 Results

This subsection presents our experimental results. First, the initial microstructure is characterized. Then, the evolution in the microstructure (composition of cementite particles, austenite growth, austenite carbon content) is studied during the heating stage. We present in detail the results from our HEXRD experiments. Finally, we describe the microstructure at the end of the heating stage. These results are discussed together in the following Subsection III.1.3.

#### III.1.2.1 Initial microstructure

A SEM micrograph of the initial microstructure, i.e. in the cold-rolled state, of the studied DP600 CR65 steel is shown in Figure III.2. The microstructure contains deformed ferrite grains (2.6  $\mu\text{m}$  thick), indicated by white arrows, and pearlite islands (2.7  $\mu\text{m}$  thick) elongated in the

cold-rolling direction (17.9  $\mu\text{m}$  long), indicated by red arrows. Inter-granular cementite particles, indicated by black arrows, are observed in the ferrite matrix. They are often in elongated clusters grouping few of them (3 to 5 particles). The initial microstructure shows an elongated shape in the cold-rolling direction.

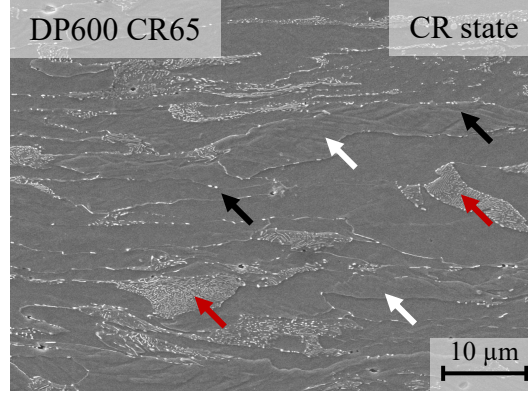


Figure III.2: SEM/SE micrograph of the microstructure of the DP600 CR65 steel in the cold-rolled state (Picral and Nital etching). Cementite particles (either in pearlite or in the matrix) are in white contrast and ferrite in dark contrast.

The initial volume fraction of pearlite, written  $f_P$  in the following, was evaluated at 16 % by image analysis in the previous PhD work of Moreno [Mor19]. During their investigation of the studied steel, they found that pearlite formed around 570  $^{\circ}\text{C}$ . In this condition, using the Hultgren's extrapolation of  $A_{cm}$  [Hul20] and the nominal composition of the studied steel, the average carbon composition of pearlite is estimated at  $X_C^P = 1.78 \text{ at}\%$  (0.39 wt%). The carbon balance of the studied steel in the initial state is written as follows:

$$\underbrace{X_C^0}_{0.46 \text{ at}\%} = f_P \times \underbrace{X_C^P}_{1.78 \text{ at}\%} + f_{CP} \times \underbrace{X_C^{CP}}_{25 \text{ at}\%} + f_{\alpha M} \times \underbrace{X_C^{\alpha M}}_{\approx 0 \text{ at}\%} \quad (\text{III.1})$$

With  $X_C^0 = 0.46 \text{ at}\%$  the nominal carbon content,  $f_{CP}$  the initial molar fraction of inter-granular cementite particles and  $X_C^{CP} = 25 \text{ at}\%$  their carbon content,  $f_{\alpha M}$  the fraction of the ferrite matrix and  $X_C^{\alpha M}$  its carbon content. By assuming that the ferrite matrix contains almost no carbon ( $X_C^{\alpha M} \approx 0 \text{ at}\%$ ), the molar fraction of the inter-granular cementite particles is estimated at  $f_{CP} = 0.70 \%$ . Considering the molar volumes of the phases, the initial volume fraction of the inter-granular cementite particles is estimated at 2.3 % in the DP600 CR65 steel.

In such configuration, the pearlite islands initially contain  $f_P \times X_C^P / X_C^0 = 62 \%$  of the carbon available in the system. Despite their small volume fraction, inter-granular cementite particles contain 38 % of the carbon available.

### III.1.2.2 Chemical composition of cementite particles

Figure III.3 shows TEM images of cementite particles extracted by replica in a DP600 CR65 sample during slow heating (3  $^{\circ}\text{C}/\text{s}$ ) interrupted at 710  $^{\circ}\text{C}$ , before austenite formation. The extracted particles, in bright white in (a), are identified either as cementite particles from pearlite islands (c), when found locally in high spatial density, or cementite particles isolated in the matrix (b), found mainly inter-granular.

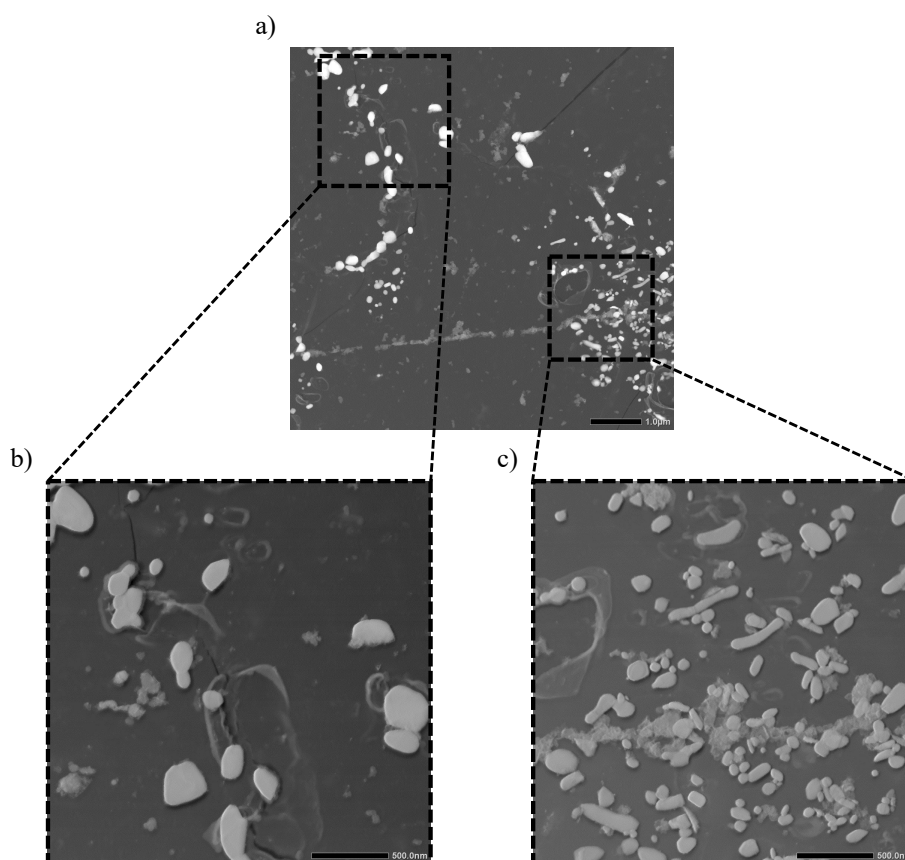


Figure III.3: TEM images of cementite particles extracted by replica in a DP600 CR65 sample heated at  $3\text{ }^{\circ}\text{C/s}$  up to  $710\text{ }^{\circ}\text{C}$  and gas quenched (He). The extracted particles (a) were identified either as cementite particles from pearlite islands (c) or cementite particles isolated in the matrix (b).

The previous PhD work of Moreno et al. [Mor19; Mor+19] highlighted the enrichment in manganese and chromium in cementite during the heating stage using low heating rate ( $3\text{ }^{\circ}\text{C/s}$ ). But in their study, the cementite particles in pearlite and isolated in the matrix were not distinguished. On the contrary, no significant enrichment was observed using a higher heating rate ( $30\text{ }^{\circ}\text{C/s}$ ). In the present study, we measure the manganese and chromium content of cementite particles isolated in the matrix only. In addition, we performed our measurement on replica, contrary to [Mor+19], so that the surrounding ferrite does not interact with the measurement (dilution effect).

Isolated cementite particles are studied in a sample heated up to  $710\text{ }^{\circ}\text{C}$  at  $3\text{ }^{\circ}\text{C/s}$  (and quenched) to simulate the enrichment during slow heating. The cementite particles in the heated sample are labeled "Enriched" in the following. These particles are also studied without enrichment in an as-cold-rolled sample, i.e. non heat treated sample. Cementite particles in the latter sample are considered representative of the ones in fast heated samples, as no enrichment is supposed to occur [Mor+19], and labeled "non-enriched" in the following.

Figure III.4 shows the manganese and chromium compositions of 22 cementite particles analyzed in the as-cold-rolled sample (in green) and 9 in the sample heated up to  $710\text{ }^{\circ}\text{C}$  at  $3\text{ }^{\circ}\text{C/s}$  (in blue).

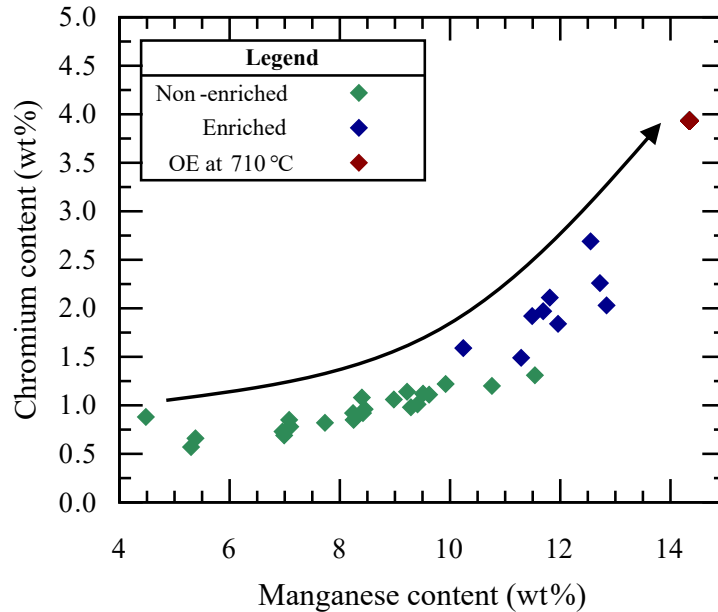


Figure III.4: Manganese and chromium composition of 22 isolated carbides analyzed in the initial state sample (non-enriched particles in green) and 9 isolated carbides in the sample heated up to 710 °C at 3 °C/s (enriched particles in blue). OE (in red) stands for Ortho-Equilibrium.

The non-enriched cementite particles in the as-cold-rolled sample (in green) presents manganese composition between 4.5 wt% and 11.5 wt%. Their chromium composition is between 0.9 wt% and 1.3 wt%. These compositions are in good agreement with [Mor+19], observing cementite particles with manganese compositions between 6 wt% and 8 wt% and chromium compositions around 0.5 wt% in the as-cold-rolled state. In the sample heated up to 710 °C (in blue), the enriched cementite particles present both higher manganese and chromium compositions. They contain between 10.2 wt% and 12.8 wt% of manganese and between 1.5 wt% and 2.7 wt% of chromium. Once again, these measurements agree with [Mor+19], showing manganese compositions between 3 wt% and 8 wt% and chromium compositions between 1 wt% and 3 wt% after slow heating.

The manganese and chromium cementite content at OE at 710 °C is plotted with a red diamond in Figure III.4. The manganese composition of the non-enriched particles (in green in Figure III.4), i.e. cementite particles in an as-cold-rolled DP600 CR65 sample, lays in a wide range (7 wt% wide) but remains at least 2 wt% lower than the OE content at 710 °C. The chromium content is far less dispersed (0.4 wt%) and is much lower than the OE (3 wt% less). On the contrary, the cementite composition of the enriched particles (in blue in Figure III.4), the manganese composition rises up very close to the OE composition (14.3 wt%). In the same way, the chromium composition is systematically higher than in the as-cold-rolled sample and increases up to 2.7 wt%, only 1.2 wt% lower than the OE composition. The cementite composition of the particles after slow heating (in blue) tends to get closer to the OE cementite composition at 710 °C, as indicated by the black arrow. The latter also highlights that higher enrichment in manganese is correlated with higher enrichment in chromium.

In both samples, manganese and chromium concentrations inside the cementite particle are

much higher than the nominal composition of the steel (1.9 wt% in manganese and 0.2 wt% in chromium). The initial enrichment of cementite particles in the as-cold-rolled state comes from the coiling operation after hot rolling [Mor+19; TK87]. This stage corresponds to a slow cooling stage after the pearlitic transformation.

### III.1.2.3 Austenite growth from the two identified cementite aggregates

As shown in III.1.2.2 and in [Mor19; Tei+21], cementite is present either in pearlite islands or in isolated cementite particles (Figure III.3). Both were identified as nucleation sites for austenite in the literature.

The formation of austenite from one or another of the two cementite aggregates (pearlite or cementite particles) is followed on optical micrographs, shown in Figure III.5. A DP600 CR65 sample is heated at 3 °C/s up to 750 °C (a), 760 °C (b), 780 °C (c) and 800 °C (d) and gas quenched (He). The Metabi etchant reveals martensite (austenite before quenching) in brown and ferrite is in white. The origin of the austenite (pearlite or cementite particles) is determined on morphological basis and their fraction is counted separately by image analysis (detailed in Chapter II).

Elongated bands of austenite are supposed to have nucleated and grown on a pearlite island. Its fraction is written  $f_{\gamma}^P$  in the following (P for pearlite). The thin films of austenite at the ferrite grain boundaries are supposed to have nucleated and grown on inter-granular cementite particles. Its fraction is written  $f_{\gamma}^{CP}$  in the following (CP for cementite particle). This identification based on morphology, as well as the separation in closed subsystems in [Mor19; Tei+21], supposes that no carbon flux exists from one austenite structure to another. This is a strong hypothesis, as carbon have ways to diffuse either through ferrite, as shown by Miyamoto et al. [Miy+10], Wu et al. [Wu+20] and one of our studies [Cou+23], or through austenite, especially after the percolation of the austenite network.

The microstructures at 750 °C (a) and 760 °C (b) are very similar. In both microstructures, the ferrite matrix is formed of large equiaxed grains. The matrix is already fully recrystallized when austenite forms, as expected during slow heating [BVS22; Bel+19; Chb+14; HPM04; Li+13; MGF11; Mor19; Tei+21; TM18]. Large austenite-rich zones elongated in the cold-rolling direction, indicated by red arrows, are easily observed and identified as previous pearlite islands. Smaller and thin austenite grains, identified by black arrows, are observed along the boundaries of recrystallized ferrite grains. These inter-granular austenite films start to form the so-called "necklace" structure. They are attributed to austenite forming from the dissolution of inter-granular cementite particles [Bel+19; Chb+14; Li+13; Tei+21; TM18]. At 780 °C (c), the microstructure is more homogeneous. Some elongated austenite grains are still observed (red arrows). The inter-granular austenite films (black arrows) are thicker and cover almost all the ferrite grain boundaries. After 780 °C, the origin of the austenite is hard to identify on the sole morphological basis. At 800 °C (d), no clear morphological distinction can be made between austenite from pearlite islands and austenite from inter-granular cementite particles.

The austenite fractions evaluated from these micrographs are plotted in Figure III.6. The fraction of austenite in elongated bands is plotted using red filled diamonds, while the fraction of austenite thin inter-granular films is plotted using black open diamonds. The total austenite fraction is plotted using blue open diamonds. The austenite fractions are compared to the expected theoretical LENP fractions, computed with Thermo-Calc considering Local Equilibrium with Negligible Partitioning (LENP) interface conditions, with no carbon or substitutional gra-

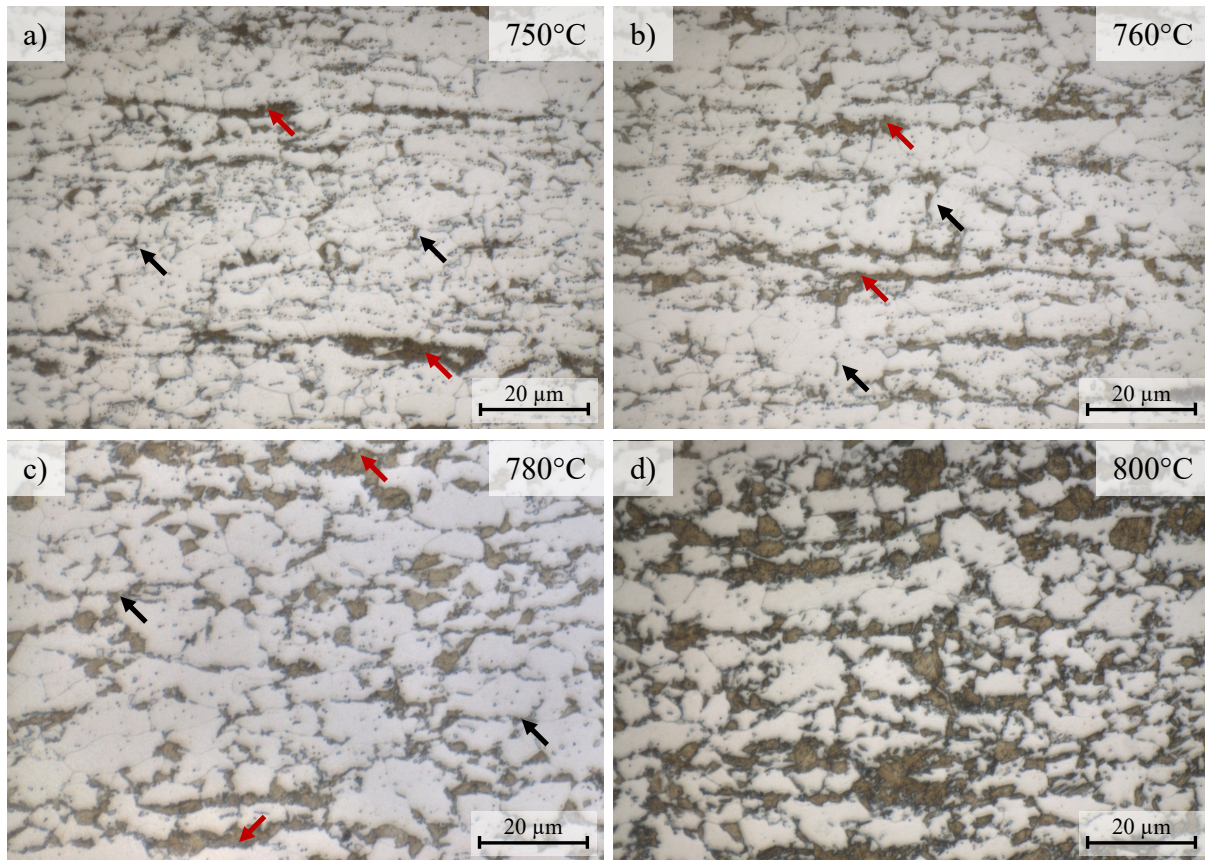


Figure III.5: Optical micrographs (Metabi etching) of DP600 CR65 samples heated at 3 °C/s up to 750 °C (a), 760 °C (b), 780 °C (c) and 800 °C (d) and quenched. The ferrite appears in white and austenite (martensite after quenching) is colored in brown. Examples of thin austenite grains, attributed to austenite forming from the dissolution of inter-granular cementite particles, are identified by black arrows. Examples of elongated austenite grains, identified as previous pearlite islands, are indicated by red arrows.

dient in austenite nor in ferrite. This computation is performed using the full measured nominal composition of the studied DP600 (Table III.1).

As observed earlier in the initial microstructure, pearlite islands represent 16 %, while the volume fraction of isolated cementite particles is only 2.3 %. All during heating at 3 °C/s, the fraction of austenite in elongated bands, i.e. attributed to pearlite islands transformation, or in thin films, i.e. attributed to isolated cementite particle dissolution, are surprisingly equal. Both fractions increase from 5 % at 750 °C to 14 % at 780 °C. The total fraction estimated by optical micrography increases from 10 % at 750 °C to 50 % at 800 °C and gets closer to the theoretical LENP fraction (different by 6 % at 800 °C).

#### III.1.2.4 Carbon homogeneity across austenite

Although isolated cementite particles contain 38 % of the carbon available in the steel (astoundingly high considering their low volume fraction), it is still less than the carbon contained

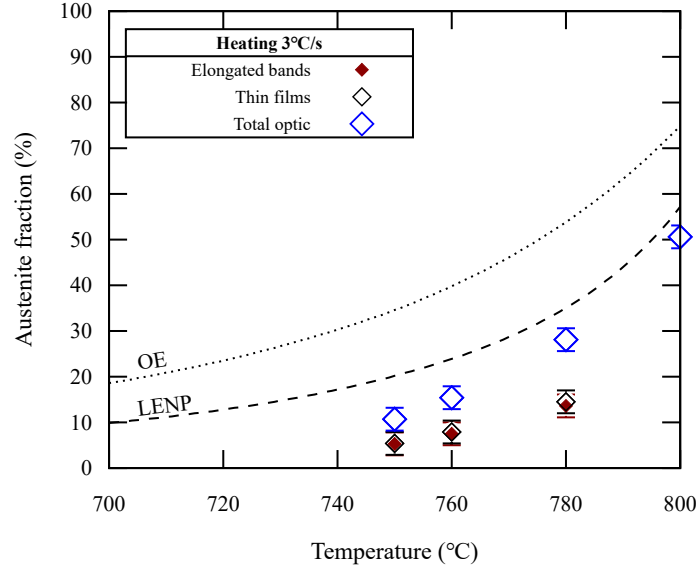


Figure III.6: Austenite fraction during heating at 3 °C/s of a DP600 CR65 sample. The fraction of austenite in elongated bands ( $f_{\gamma}^P$ ) is plotted with red filled diamonds. The fraction of austenite in thin inter-granular films ( $f_{\gamma}^{CP}$ ) is plotted with black open diamonds. The total austenite fraction evaluated from optical micrographs by image analysis is plotted with blue open diamonds.

in pearlite islands (62 % of the carbon available). The initial difference in carbon content in these cementite aggregates makes very surprising the equal austenite volume fraction formed from them, as observed above.

Two extreme hypotheses can explain this. Either the carbon content in austenite depends on its origin (austenite formed from the transformation of pearlite bands would be richer in carbon than austenite formed from the dissolution of isolated cementite particles), or a carbon transfer homogenizes carbon across austenite. The first hypothesis leads to the method used in the work of Moreno et al. [Mor19; Tei+21], using closed subsystems and each containing one of the two cementite aggregates. The second hypothesis makes the separation in closed subsystems irrelevant, as the carbon in austenite homogenizes.

To decide between these hypotheses, the carbon homogeneity across the austenite is investigated by WDS. Figure III.7 shows carbon content maps of DP600 CR65 samples heated at 3 °C/s up to 760 °C (a) and 780 °C (b) and gas quenched (He). In both maps, the carbon content is heterogeneously distributed in carbon-rich zones. Red spots are observed, in higher quantity at 760 °C (a). These spots indicate very localized regions with a carbon content estimated at 6.6 wt%. They are attributed to undissolved cementite particles.

Local carbon measurements (around 10 in each case) were performed in austenite in elongated bands (red filled diamonds) or in thin intergranular films (black open diamonds) on our DP600 CR65 samples heated at 3 °C/s up to 760 °C and 780 °C. The mean carbon contents obtained from these local WDS measurements are plotted in Figure III.8.

At 760 °C, the fraction of austenite in elongated bands is  $7.5 \pm 2.5$  %, as shown in Figure III.6, lower than the initial pearlite fraction (16 %). The transformation of pearlite bands is not com-

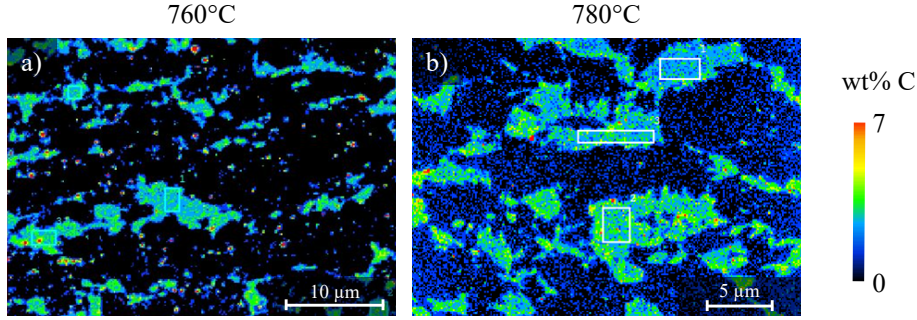


Figure III.7: Carbon content maps obtained by WDS on DP600 CR65 samples heated at 3 °C/s up to 760 °C (a) and 780 °C (b) and gas quenched (He).

pleted. The elongated austenite bands show a carbon content around  $w_C^{\gamma P} = 0.36 \pm 0.02$  wt% (Figure III.8). Considering the precision of the measurement, this is consistent with the carbon content of pearlite domains (0.39 wt%), calculated using the Hultgren’s extrapolation of Acm [Hul20]. Austenite in thin inter-granular films is found with a far lower carbon content, around  $w_C^{\gamma CP} = 0.21 \pm 0.07$  wt% (Figure III.8). The carbon mass balance considering the untransformed pearlite, the austenite in elongated bands and the austenite in thin inter-granular films shows a discrepancy in carbon compared to the total carbon content (0.092 wt%):

$$(f_P - f_{\gamma P}) \times \underbrace{w_C^P}_{0.39 \text{ wt}\%} + f_{\gamma P} \times w_C^{\gamma P} + f_{\gamma CP} \times w_C^{\gamma CP} = 0.075 \text{ wt}\% \quad (\text{III.2})$$

The lack of carbon is explained by undissolved isolated cementite particles observed at this temperature (Figure III.7 a). Such observations after heating up to 760 °C mostly support the hypothesis of closed subsystems in [Mor19; Tei+21].

On the contrary, at 780 °C, the austenite in elongated bands present a carbon content around  $w_C^{\gamma P} = 0.34 \pm 0.02$  wt%, close to the carbon content of the austenite in inter-granular films, around  $w_C^{\gamma CP} = 0.36 \pm 0.02$  wt% (Figure III.8). Using the austenite fractions obtained by image analysis of optical micrographs (Figure III.6), the global carbon balance is verified. At this temperature, carbon behavior is completely different, as it is equally shared between elongated bands and inter-granular films. This configuration highlights a carbon homogenization across austenite, which is in contradiction with the analysis in closed subsystems conducted in [Mor19; Tei+21].

### III.1.2.5 Kinetics of ferrite recrystallization and austenite formation

As exposed in the literature review of Chapter I, the austenite formation kinetics is affected by the heating rate, which influences the interactions between ferrite recrystallization and austenite formation. To better understand these interactions, we perform in situ HEXRD experiments, simulating annealing treatments on our DP600 CR65 steel, using a low heating rate (3 °C/s) and a high heating rate (30 °C/s).

Figure III.9 shows an enlargement of the HEXRD 2D patterns at 625 °C (a, b), 700 °C (c, d), 750 °C (e, f), 775 °C (g, h) and 800 °C (i, j) during the heating stage at 3 °C/s (a, c, e, g, i) and 30 °C/s (b, d, f, h, j) of the DP600 CR65 steel. The diffracting phases and planes are indicated on the corresponding diffraction rings.

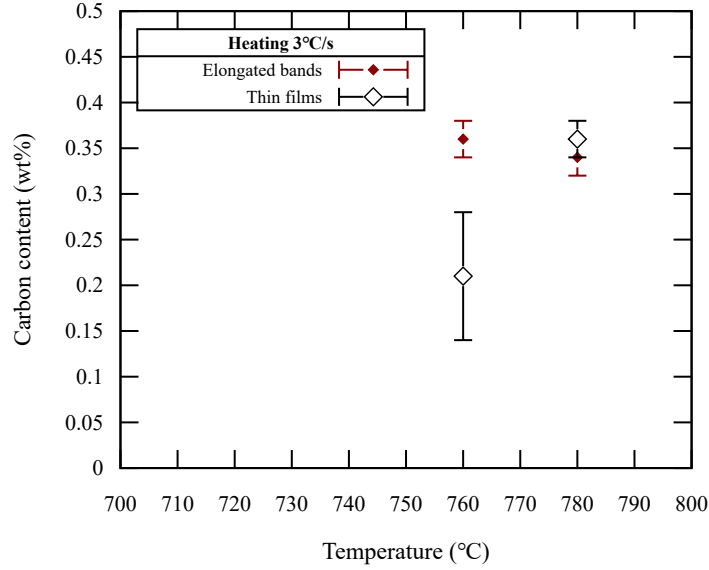


Figure III.8: Mean carbon contents obtained from WDS measurements in austenite in elongated bands (red filled diamonds) or in thin intergranular films (black open diamonds) on DP600 CR65 samples heated at 3 °C/s up to 760 °C and 780 °C and gas quenched (He).

At 625 °C (Figure III.9 a and b), only diffraction rings corresponding to ferrite are observed, regardless the heating rate. The rings are continuous (no diffraction spot is observed). Cementite fraction mass fraction  $f_\theta$  is very low in the steel. Considering that there is no carbon in ferrite, the following carbon mass balance applies:

$$\underbrace{w_C^0}_{0.1 \text{ wt\%}} = f_\theta \times \underbrace{w_C^\theta}_{6.67 \text{ wt\%}} + f_\alpha \times \underbrace{w_C^\alpha}_{\approx 0 \text{ wt\%}} \quad (\text{III.3})$$

With  $w_C^0$ ,  $w_C^\theta$  and  $w_C^\alpha$  the nominal, cementite and ferrite carbon content (in wt%) and  $f_\alpha$  the mass fraction of ferrite, predicts a mass fraction of cementite around 1.5 %. Due to this low fraction, the diffraction rings of cementite cannot be observed in Figure III.9. Their detection requires to adapt the scale to observe low diffraction intensities. Figure III.10 shows a part of the 1D diffractogram at 625 °C (blue) and 780 °C (red) during the heating stage using the low heating rate (3 °C/s) of annealing of a DP600 CR65 sample. Using a logarithm scale for the intensity, diffraction peaks corresponding to cementite, indicated by arrows, can be observed at 625 °C. Those peaks are no more visible at 780 °C.

Ferrite is still the main phase to diffract significantly to be observed at 700 °C (Figure III.9 c and d). Numerous bright diffraction spots, indicated by blue arrows in Figure III.9 c, are observed on the diffraction rings of ferrite, while heating at 3 °C/s. On the contrary, ferrite diffraction rings remain continuous, while heating at 30 °C/s, as shown in Figure III.9 d.

In addition to ferrite, austenite diffracts at 750 °C regardless the heating rate (Figure III.9 e and f). Diffraction spots are still observed on ferrite diffraction rings during slow heating (Figure III.9 e). At this higher temperature, diffraction spots, indicated by green arrows in Figure III.9 f, are finally observed on ferrite diffraction rings during fast heating. For both heating rates, austenite diffraction rings are continuous.

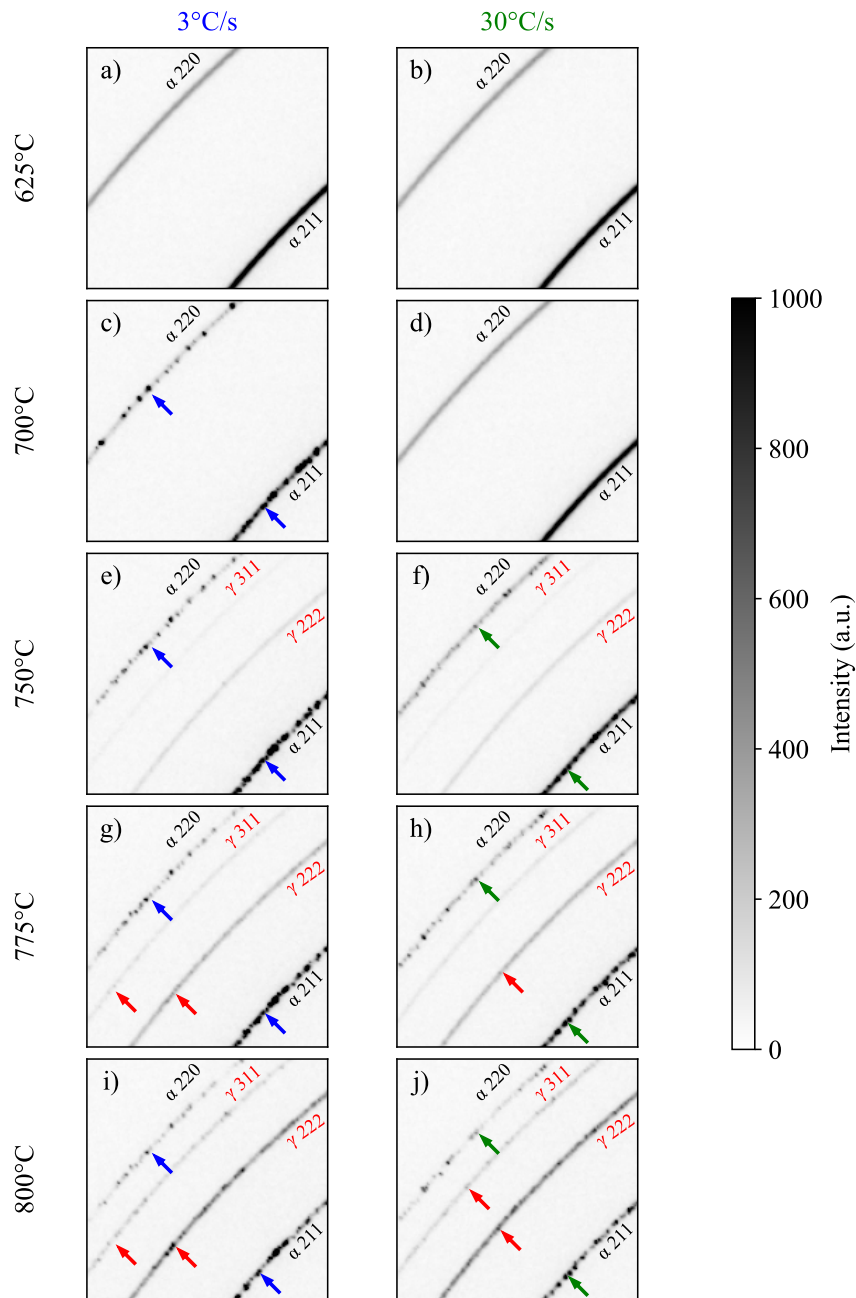


Figure III.9: Partial diffraction patterns at 625 °C (a, b), 700 °C (c, d), 750 °C (e, f), 775 °C (g, h) and 800 °C (i, j) during the heating stage at 3 °C/s (a, c, e, g, i) and 30 °C/s (b, d, f, h, j) of the DP600 CR65. The diffracting phase and planes are indicated on the corresponding diffraction ring. Arrows indicate diffraction spots on diffraction rings.

At 775 °C, bright diffraction spots appear on diffraction rings of austenite, indicated by red arrows in Figure III.9 g and h. On the contrary, the diffraction spots on ferrite diffraction rings fade out.

At the end of the heating stage (800 °C), numerous bright spots are observed on austenite



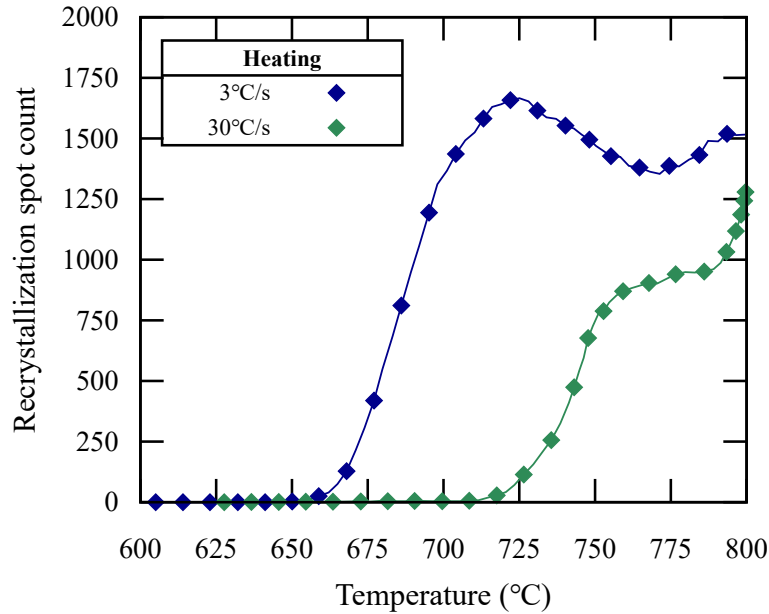


Figure III.11: Number of diffraction spots tracked during the heating stage of the intercritical annealing of the DP600 CR65 at 3 °C/s (blue) and 30 °C/s (green).

growth, as discussed in Chapter II, and austenite formation, which starts at 725 °C, as shown in Figure III.12 (b).

From 775 °C, diffraction spots are detected on both ferrite and austenite diffraction patterns, regardless the heating rate, as shown in Figure III.9 (g, h, i and j). The final increase in detected diffraction spots in Figure III.12 (a) is mainly due to diffraction spots on austenite rings. After 775 °C, the count of diffraction spots is no more representative of the ferrite recrystallization progress.

From these observations, primary recrystallization kinetics is estimated using the number of spots between the beginning of recrystallization and the end of the first increase of the number of detected spots. As explained in Chapter II, the recrystallized fraction is calculated as the current number of detected diffraction spots divided by the maximum number of detected diffraction spots. The ferrite recrystallization kinetics during heating at 3 °C/s (blue) and 30 °C/s (green) are plotted in Figure III.12 (a). Both recrystallization kinetics show a typical shapes of recrystallization kinetics, as expected from literature [HH95; Mor+18; OMG08; Rei52]. The beginning of ferrite recrystallization is delayed by 65 °C because of the fast heating. During slow heating, ferrite recrystallization is complete when the austenite formation starts at 725 °C (Figure III.12 a and b). On the contrary, ferrite recrystallization and austenite formation overlap during fast heating.

Figure III.12 (b) and (c) show the austenite weight fraction estimated by Rietveld refinement from in situ HEXRD experiments during the heating and isothermal holding stages respectively. The austenite fractions are compared to the expected theoretical LENP and OE fractions, computed with Thermo-Calc using the full nominal composition of the studied steels. The first one, plotted with a black dashed line, is the austenite fraction computed considering LENP interface conditions. The second one, plotted with dotted lines, is the austenite fraction at OE. These

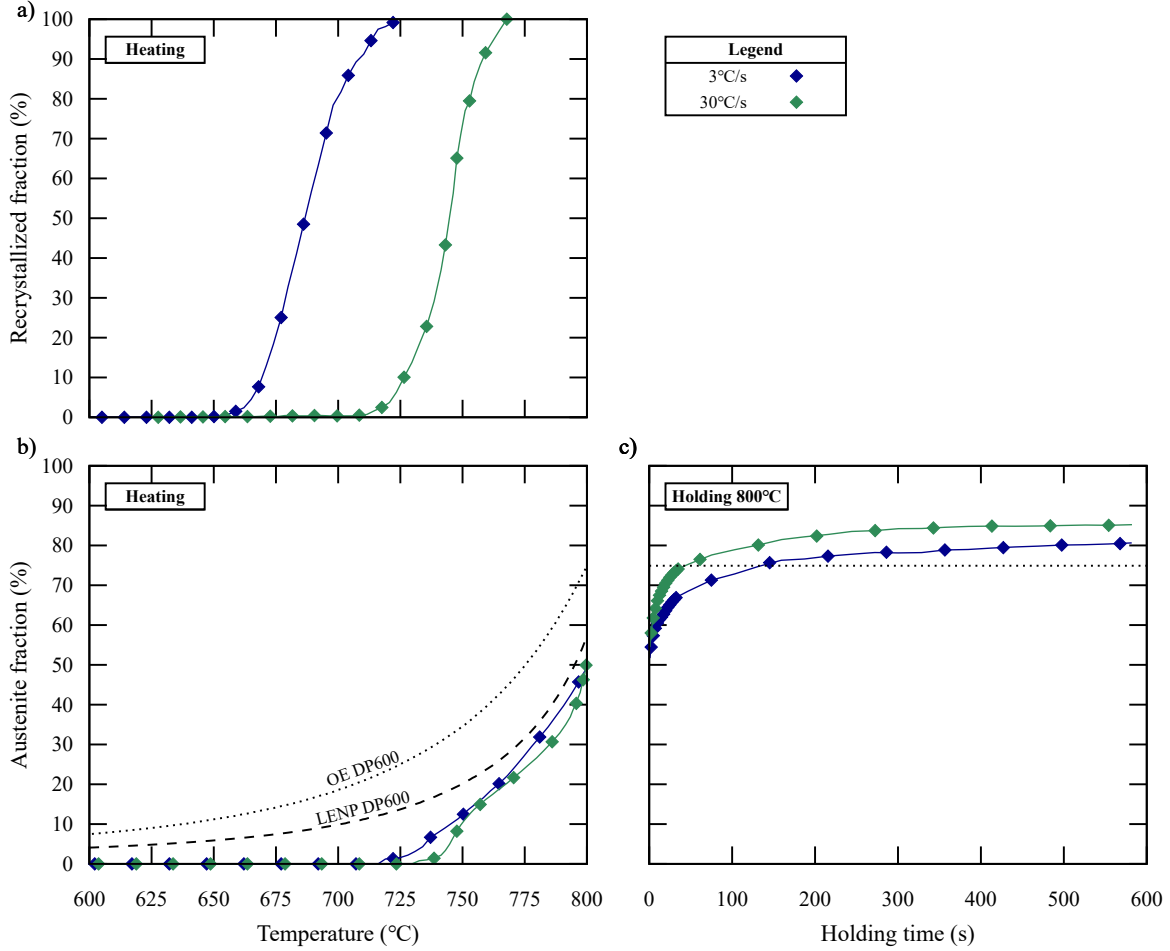


Figure III.12: Recrystallization (a) and austenite formation (b and c) kinetics during the inter-critical annealing of the DP600 CR65 at 3 °C/s (blue) and 30 °C/s (green) followed by HEXRD (IDST and Rietveld post-processes respectively). Fractions are plotted during the heating (a and b) and isothermal holding (c) stages.

computations are performed using the full measured nominal composition of the studied DP600 (Table III.1).

The austenite fraction is a direct output from the Rietveld refinement, as described in Chapter II. The uncertainty on the austenite fraction due to the Rietveld refinement is estimated at 1 %. As their mass fraction is very low, our refinement does not account for cementite. Only ferrite and austenite are studied. The austenite fractions are plotted with a total uncertainty estimated around 3 % before and 1 % after complete dissolution of cementite. However, during our several HEXRD experiment campaigns (2016 and 2022), we reproduced the experiments presented here. As shown in B, our results show an almost perfect repeatability. Consequently, we feel legitimate to study the most subtle variations in measured kinetics.

During slow heating stage (in blue in Figure III.12 (b)), the austenite weight fraction increases almost monotonously from 720 °C to the end of the heating stage at 800 °C. The austenite fraction

is first far from the theoretical LENP fraction ( $T < 750\text{ °C}$ ) but becomes closer to this theoretical limit, from  $775\text{ °C}$  to  $800\text{ °C}$ . Still, between  $775\text{ °C}$  and  $800\text{ °C}$ , the experimental fraction is 4 % lower in average than the theoretical LENP.

During fast heating experiment (in green in Figure III.12 (b)), the austenite is first detected at  $740\text{ °C}$ . Contrary to slow heating, the austenite fraction increases in two steps during fast heating. First, the austenite fraction increases rapidly from 0 % to 10 % between  $740\text{ °C}$  and  $750\text{ °C}$ . At  $750\text{ °C}$ , the austenite fraction is equal in the samples heated at  $3\text{ °C/s}$  and  $30\text{ °C/s}$ . After  $750\text{ °C}$ , the austenite fraction follows closely the austenite fraction during slow heating (less than 5 % gap). The austenite fraction during fast heating is always lower than during slow heating. Thus, as the austenite fraction seems to depend mainly on the temperature, the austenite formation kinetics as a function of time is much faster during fast heating.

At the end of the heating stage, the austenite fraction reaches 50 % regardless the heating rate.

During the isothermal holding (Figure III.12 (c)), the austenite fraction continues to increase, but the transformation rate decreases progressively. During the isothermal holding, the austenite fraction in the sample heated at  $30\text{ °C/s}$  (in green) is always higher than in the sample heated at  $3\text{ °C/s}$  (in blue). The austenite fraction increases faster in the sample heated at  $30\text{ °C/s}$  in the first 20 s of the holding stage. After 20 s at  $800\text{ °C}$ , the austenite fraction is 64 % in the sample heated at  $3\text{ °C/s}$ , while 70 % in the fast heated sample. After 20 s holding, a 5 % gap is maintained between the two samples. In both samples, the austenite fraction finally "overshoots" the austenite fraction calculated at OE (75 %). The higher the heating rate, the higher the overshoot.

### III.1.2.6 Microstructure at the end of the heating stage

Optical micrographs after etching of the microstructures at  $800\text{ °C}$  after slow (a) and fast heating (b) are shown in III.13.

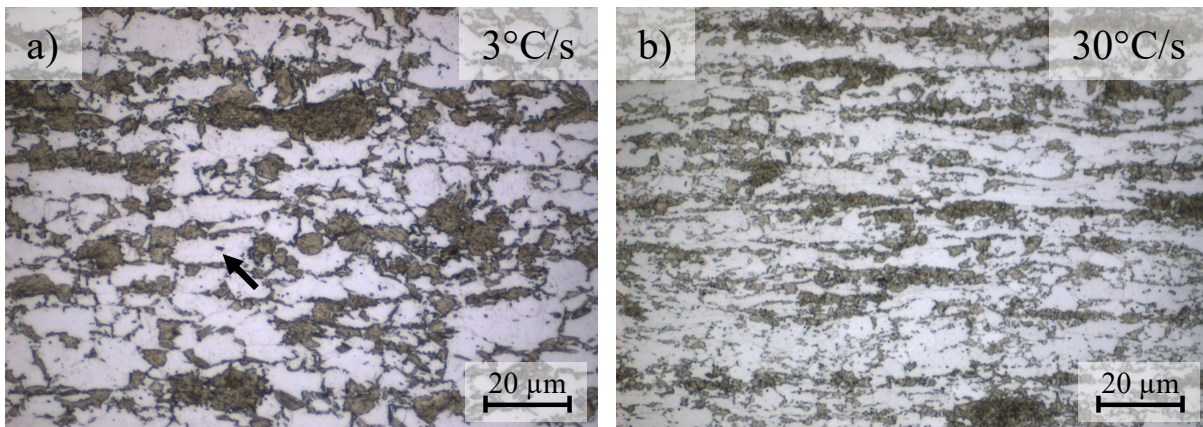


Figure III.13: Optical micrographs of the microstructure of a DP600 CR65 at  $800\text{ °C}$  at the end of heating stage after slow (a) and fast heating (b).

At the end of the heating stage ( $800\text{ °C}$ ), the microstructure after slow heating (a) is characterized by large recrystallized ferrite grains ( $5\text{ μm}$  thick), in white, and austenite (martensite after quenching, in brown). The austenite fractions are estimated by image analysis, as detailed

in Chapter II. Austenite represents 50 % of the microstructure and is either in large grains (10.4  $\mu\text{m}$  thick and 28.3  $\mu\text{m}$  long) or thin films at ferrite grain boundaries. The mean distance between austenite islands (regardless their morphology) is evaluated around 11  $\mu\text{m}$ . Rare small austenite grains, indicated by a black arrow, are observed in recrystallized grains. On the contrary, the microstructure after fast heating (b) consists of numerous smaller recrystallized ferrite grains (3.8  $\mu\text{m}$  thick) and austenite. The ferrite phase keeps an elongated form in the cold-rolling direction. The austenite phase represents 50 % of the microstructure, as after slow heating. However, austenite is in smaller grains (4.6  $\mu\text{m}$  thick), either grouped in islands elongated (33  $\mu\text{m}$  long) in the cold-rolling direction or dispersed in the fine recrystallized ferrite matrix. The mean distance between austenite islands (regardless their morphology) is evaluated around 8  $\mu\text{m}$ .

These typical sizes are summarized in Table III.2.

Heating rate	Ferrite grain thickness	Austenite grain thickness	Austenite islands length	Distance between austenite islands
3 $^{\circ}\text{C}/\text{s}$	5 $\mu\text{m}$	10.4 $\mu\text{m}$	28.3 $\mu\text{m}$	11 $\mu\text{m}$
30 $^{\circ}\text{C}/\text{s}$	3.8 $\mu\text{m}$	4.6 $\mu\text{m}$	33 $\mu\text{m}$	8 $\mu\text{m}$

Table III.2: Typical mean sizes in the microstructure at the end of the heating stage of the studied DP600 depending on the heating rate.

In slow heated samples (Figure III.5 and Figure III.13 a), rare small austenite grains are found in recrystallized ferrite grains. Such grains are attributed to austenite nucleation on rare cementite particles, crossed by moving interfaces and trapped in recrystallized grains [Bel+19; Chb+14; Mor19; Tei+21].

### III.1.3 Discussions

In this subsection, we discuss the results presented in the previous Subsection III.1.2. Mainly based on our experiments on the slow heating samples, we propose a description of the mechanisms during the heating stage. Then, the influence of substitutional elements, more specifically the cementite enrichment, is questioned. Finally, we discuss the influence of the heating rate on the recrystallization kinetics, the austenite microstructure and the austenite formation kinetics during the isothermal holding stage.

#### III.1.3.1 Proposed mechanisms for austenite formation during the heating stage

First, we observe the expected influence of the heating rate on the beginning of the austenite formation. Our HEXRD experiments (Figure III.12 b) show that the transformation is delayed from 720  $^{\circ}\text{C}$ , during slow heating (3  $^{\circ}\text{C}/\text{s}$  in blue), to 740  $^{\circ}\text{C}$ , during fast heating (30  $^{\circ}\text{C}/\text{s}$  in green), as already observed in [Mor19; Tei+21]. Up to 750  $^{\circ}\text{C}$ , the austenite formation kinetics depends on the heating rate. Figure III.14 schematizes the sequence of mechanisms for austenite formation that our experiments highlight during slow heating (3  $^{\circ}\text{C}/\text{s}$ ).

During slow heating, our experiments confirm a growth of austenite in two closed subsystems at the beginning of the phase transformation, as proposed by Moreno et al. [Mor19; Tei+21].

Before 760  $^{\circ}\text{C}$ , Figure III.14 depicts a fully recrystallized ferrite matrix. The ferrite recrystallization kinetics obtained from HEXRD experiments (Figure III.12 a) supports that ferrite

recrystallization is complete when austenite formation starts at 720 °C (Figure III.12 b). Optical micrographs in Figure III.5 show that austenite grows in a fully recrystallized ferrite matrix.

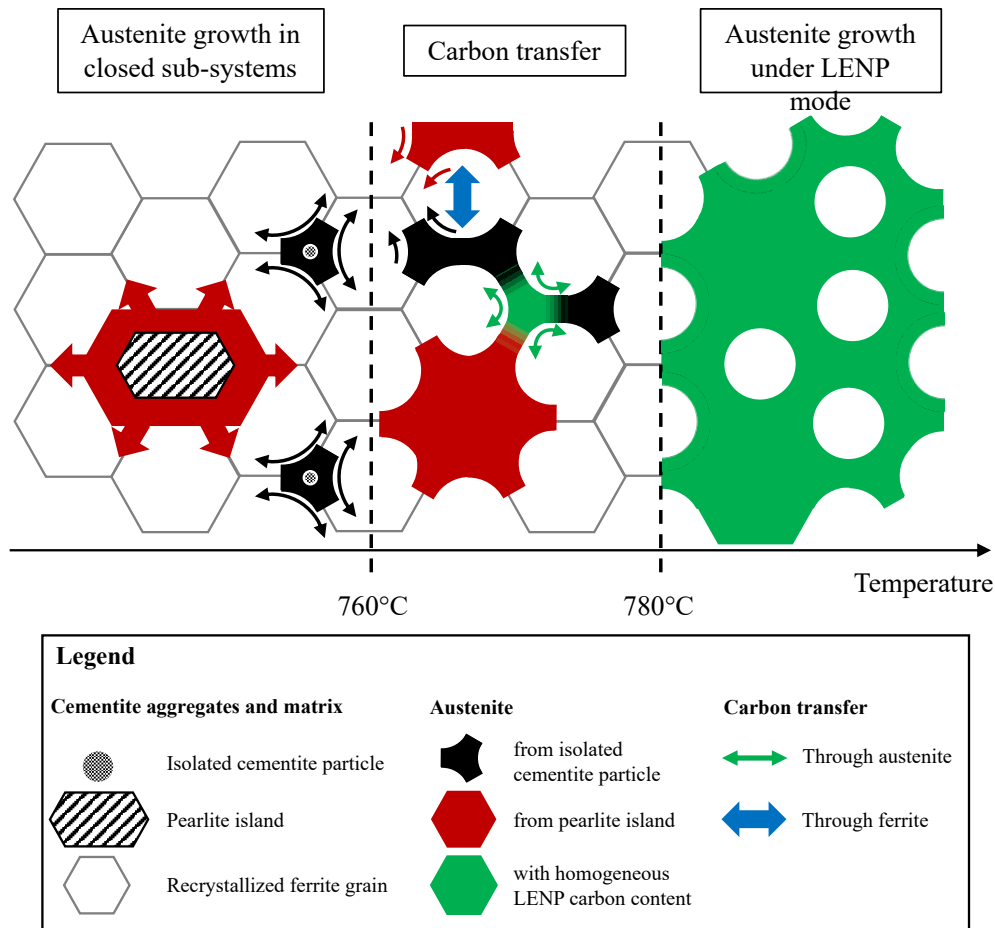


Figure III.14: Schematic representation of austenite formation mechanisms during slow heating (3 °C/s, reference scenario)

Pearlite islands, represented by elongated hatched hexagons in Figure III.14, and isolated cementite particles, represented by dotted circles in Figure III.14, are the two main carbon sources in the studied DP600 CR65, as supported by SEM micrographs of the initial microstructure (Figure III.2) and the carbon content maps obtained by WDS (Figure III.7).

Although pearlite contains 62 % of the available carbon (III.1.2.1), the fraction of austenite forming from these two cementite aggregates (pearlite islands and isolated particles) is equal, as shown by the austenite fractions plotted in Figure III.6. The measurements of carbon content by WDS (Figure III.8) and the carbon content maps (Figure III.7) show that the carbon content of austenite forming from pearlite bands is close to pearlite carbon content (0.39 wt%). The carbon content is maintained during the pearlite transformation and the pearlitic subsystem, containing the pearlite bands, can be considered as a closed subsystem, as proposed in [Mor19; Tei+21]. In addition, the carbon content in austenite in thin films (in black opened diamonds in Figure III.8), attributed to the dissolution of isolated cementite particles, is significantly lower than the carbon content in austenite formed from pearlite islands (in red filled diamonds in

Figure III.8). This observation tends to show that the austenite in thin films follows a growth kinetics different from the austenite forming from pearlite, as shown by previous numerical work [Cou+23; Mor19; Tei+21]. Thus, our study supports that, during the transformation of pearlite and the dissolution of isolated cementite particles (under 760 °C), the austenite formation can be studied separately, considering closed subsystems in the reference scenario (slow heating at 3 °C/s).

At higher temperatures, our experiments suggest a carbon transfer between the austenite formed from pearlite islands and the austenite formed from isolated cementite particles. At 780 °C, our austenite fraction measurements still show an equal fraction of austenite formed from pearlite islands (in red filled diamonds in Figure III.6) and austenite formed from isolated cementite particles (in black opened diamonds in Figure III.6). However, as shown by our carbon content maps (Figure III.7) and carbon content measurements (Figure III.8), carbon is now equally shared between austenite formed from pearlite islands (in red filled diamonds in Figure III.8) and austenite formed from isolated cementite particles (in black opened diamonds in Figure III.8). This surprising observation, differing from the one at 760 °C, indicates a change in the austenite formation behavior. With both close austenite fractions and carbon content, the carbon is now equally distributed between austenite in elongated bands, attributed to pearlite transformation, and austenite in thin intergranular film, attributed to the dissolution of isolated cementite particles. This equal distribution is far from the initial one (62 % in pearlite and 32 % in the isolated cementite particles).

Between 760 °C and 780 °C, Figure III.14 depicts austenite formed from pearlite islands, in red, and austenite formed from isolated cementite particles, in black, during slow heating. Both are growing in the fully recrystallized ferrite matrix.

The highlighted carbon transfer and homogenization may occur through ferrite, as symbolized by a blue arrow in Figure III.14. Carbon transfer through ferrite was highlighted during austenite formation from cementite particles in [Miy+10; Wu+20]. They show that austenite nucleated on a cementite particle not only grow by the dissolution of the aforesaid particle. Cementite particles may dissolve without being austenite nucleation sites, by transferring their carbon to growing austenite through ferrite. Yet, these studies focus on cementite particles. Our previous numerical investigation on the competitive growth between two austenite islands [Cou+23], exposed in Chapter I (Subsubsection I.2.3.4) highlights a carbon transfer from one austenite island to another through the ferrite matrix, due to a manganese depletion.

In addition, the austenite microstructure starts to form a connected network across the microstructure. It not only makes difficult to distinguish the origin of austenite on morphology criteria but also facilitates carbon homogenization by diffusion across austenite, represented by green arrows in Figure III.14. As a reference, randomly distributed spheres percolate when their volume reaches 30 % of the space [Pow79]. This theoretical threshold is reached around 780 °C, supported by our austenite fraction estimation from optical micrographs (Figure III.6) and HEXRD experiment (Figure III.12 b). The optical micrographs of the studied DP600 CR65 at 780 °C in Figure III.5 c) shows a well-connected austenite network, supporting that the austenite microstructure percolates between 760 °C and 780 °C. As the percolation of the austenite network occurs in the same temperature range as the highlighted carbon transfer (between 760 °C and 780 °C), it is fairly reasonable to consider that this carbon transfer also takes place by diffusion across the percolated austenite network. However, Figure III.7 (b) also highlights unconnected austenite islands at 780 °C. Despite the well-connected austenite network, such isolated austenite islands would favor carbon transfer through ferrite.

Finally, as carbon has been equally distributed in austenite, the separation in closed sub-

systems, as proposed in [Mor19; Tei+21], is made irrelevant above 780 °C. Contrary to Moreno et al. [Mor19; Tei+21], in the simulations that will be presented later on, we will choose to consider austenite as a single system above 780 °C, represented in green in Figure III.14.

At 780 °C, no more cementite is detected by HEXRD (mass fraction probably lower than 0.1 wt%), as shown by Figure III.10 and supported by [Mor19]. Only ferrite and austenite are observed. The phase transformation continues by austenite growth in ferrite, exclusively.

Figure III.12 (b) shows that, above 750 °C, the austenite fractions follow the theoretical LENP fractions, regardless the heating rate. This observation leads us to think that the austenite grows under LENP mode after the carbon transfer, as already proposed in [Chb+14; Mor19; Tei+21]. In addition, our previous numerical investigation [Cou+23], highlights that, even when considering various interface conditions in the microstructure (Local Equilibrium with Negligible Partitioning (LENP) and acrfullep), all interfaces finally show LENP conditions and only the austenite with initial LENP interface condition growth significantly, due to the carbon transfer between austenite islands.

The 5 % gap between the theoretical and experimental fractions can be explained by the uncertainty on the nominal carbon content or a slight carbon gradient in austenite. Indeed, a 10 % error on the nominal carbon content (0.09 wt% instead of 0.1 wt% - Table III.1) may introduce a 5 % error on the theoretical LENP fraction. Though we considered the measured nominal composition, the uncertainty on this measurement remains. In addition, the heating rate (3 °C/s) may be already too fast for carbon homogenization while heating, as shown in our previous numerical study on the same steel [Cou+23]. In this case, austenite can grow with LENP compositions at the interface but higher mean content, due to composition gradient. This also leads to predicted fractions lower than the theoretical LENP fractions. This last hypothesis is further discussed with DICTRA simulations in Chapter IV) but seems to explain consistently our observations. Consequently, our observations support austenite growth into a ferritic matrix above 780 °C, as one single thermodynamic system instead of the two separated and closed systems proposed in [Mor19; Tei+21], under carbon diffusion control without significant substitutional redistribution (LENP mode).

Following the theoretical LENP fraction regardless the heating rate makes the austenite formation kinetics ten times faster as a function of time using fast heating. Several arguments are available in literature (Chapter I) to explain this trend based on nuclei density and carbon diffusion. The results from the present section brings no new insight on this point.

### III.1.3.2 Influence of the composition of cementite particles on their dissolution kinetics

First, our EDXS measurements of composition of isolated cementite particles (Figure III.4) show manganese and chromium enrichment during the heating stage, as observed in the previous PhD work of Moreno [Mor19] on cementite particles in pearlite.

In the slow heated sample (in blue in Figure III.4), manganese and chromium compositions increase together. Manganese and chromium co-segregate in cementite particles. This partition of chromium in cementite is supported for instance by Marceaux dit Clément et al. [Mar+20]. Their study claims chromium as a cementite stabilizer.

The distribution of Partition to Non-partition Transition Temperature (PNTT) associated with the cementite composition measured by EDXS (Figure III.4) is computed using the criterion reported in [Miy+10]. The distribution of PNTT is computed first using only the manganese distribution, as in previous works [Mor19; Tei+21], and is plotted in Figure III.15 (a). Using

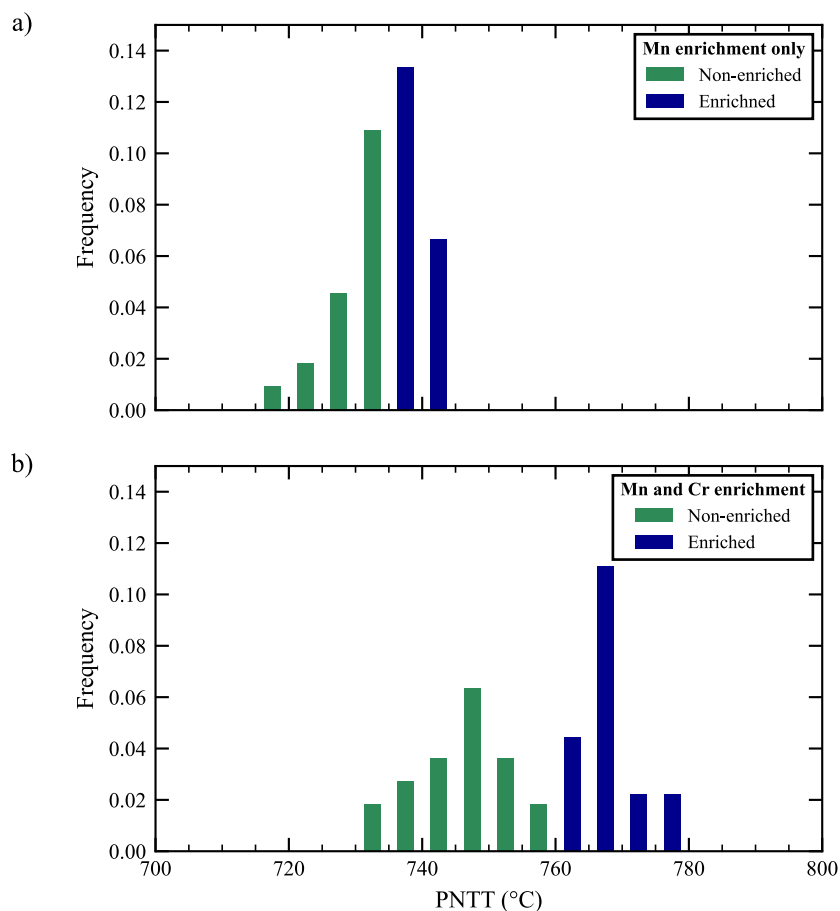


Figure III.15: Distribution of PNTT associated with the distribution of manganese and chromium composition of isolated carbides presented in Figure III.4. The distribution in green corresponds to the non-enriched particles in the as-cold-rolled sample. The distribution in blue corresponds to the enriched particles in the sample heated up to 710 °C at 3 °C/s.

only the distribution of manganese enrichment (Figure III.15 (a)), the PNTT of the non-enriched particles ranges between 715 °C and 735 °C. The PNTT of the enriched particles ranges between 735 °C and 745 °C. As exposed in the literature review (I.2.3), this enrichment shifts the PNTT to higher temperature, which delays in turn the beginning of the austenite formation from cementite particles.

Then, the distribution of PNTT is computed using both the manganese and chromium distributions and plotted in Figure III.15 (b). The PNTT of the non-enriched particles (in green in Figure III.15 b) ranges between 730 °C and 760 °C, while the PNTT of the enriched particles (in blue in Figure III.15 b) ranges between 760 °C and 780 °C. The presence of undissolved carbides at 760 °C highlighted by the carbon content map (Figure III.7 a) supports the PNTT higher than 760 °C in the sample heated at 3 °C/s up to 710 °C. Considering chromium shifts the PNTT to higher temperature, as it is known to stabilize cementite [Mar+20]. Considering chromium also scatters the measurements and widens the range of PNTT.

We used this PNTT distribution to predict the austenite fraction formed from cementite particles. Full details are provided in appendix C.

However, a sole thermo-analysis seems in contradiction with the delay of the beginning of the austenite formation (i.e. the austenite transformation starts at higher temperature at 30 °C/s than at 3 °C/s). Manganese and chromium enrichment was shown to occur during slow heating (3 °C/s), while no significant enrichment is evidenced using high heating rate (30 °C/s) [Mor19]. The distribution of PNTT of the cementite particles during slow (3 °C/s in blue) is globally higher than during fast (30 °C/s in green) heating. As shown in previous studies [Cou+23; Mor19; Tei+21], the main contribution of the isolated cementite particles to the austenite fraction is at their PNTT, temperature at which they experience fast dissolution under LENP mode (carbon diffusion control). Thus, the contribution of the isolated cementite to the austenite formation during fast heating would occur at lower temperature than during slow heating, which is in contradiction with experimental observations (Figure III.12 b). A deeper investigation, especially on a sample fast heated at 30 °C/s, is required to further discuss this point.

### III.1.3.3 Influence of heating rate on the ferrite recrystallization kinetics

As discussed above (Figure III.14), using the low heating rate (3 °C/s), the ferrite recrystallization is completed when the austenite formation starts at 720 °C. On the contrary, as expected, the delay of ferrite recrystallization by 65 °C using the high heating rate is enough to make ferrite recrystallization and austenite formation concomitant, as shown by our experimental kinetics in Figure III.12.

As exposed in the literature review in Chapter I, both recovery and recrystallization are expected to be delayed using higher heating rates [Doh+97; HH95; Mor+18; Pou+11; Rei52], and a delayed recovery could affect the recrystallization kinetics. However, one of our previous work on ferrite recovery during annealing, published in a stand-alone paper [Cou+21], shows similar decrease in dislocation density after slow (3 °C/s) and fast (100 °C/s) heating. The slightly lower level of recovery due to fast heating is considered not to significantly affect recrystallization and the influence of recovery on recrystallization is not further studied.

The effect of the concomitance of ferrite recrystallization and austenite formation using high heating rate is discussed in the following.

### III.1.3.4 Influence of the heating rate on the austenite microstructure

The optical micrograph at 800 °C after slow heating (Figure III.13 a) shows austenite and ferrite grains around twice thicker (Table III.2) than in the microstructure after fast heating (Figure III.13 b). The length of the austenite islands, mainly attributed to pearlite, is similar in both microstructure ( $\approx 30 \mu\text{m}$ , see Table III.2). Though, after slow heating (Figure III.13 a), all the recrystallized ferrite grains are surrounded by intergranular austenite grains, forming a typical necklace morphology. Besides, after fast heating, the austenite islands are thinner (Figure III.13 b), making their aspect ratios much higher after fast heating (7.1) than after slow heating (2.7). This difference in aspect of austenite islands tends to give the typical elongated shape in the cold-rolled direction of "banded" morphologies. Thus, our experiments reproduce the effect of the heating rate on the austenite morphology, exposed in the literature review in Chapter I.

As reported in Chapter I, an extensive literature, studying a wide range of initial microstructure and heating rates, gives several explanations for this change in austenite morphology with

the heating rate. Considering our initial microstructure, nominal composition and used heating rates, it is most likely that the isolated cementite particles influence the austenite morphology, as proposed in [Bel+19; Chb+14; Li+13; Mor19; Tei+21; TM18]. At this point, none of our experiments contradicts or supports the mechanisms exposed in the literature review.

### III.1.3.5 Influence of the heating rate on the austenite formation kinetics during the holding stage

Our HEXRD experiments (Figure III.12 c) show that the higher the heating rate, the faster the austenite formation kinetics during the isothermal holding. In addition, the austenite fraction at the end of the isothermal holding exceeds the OE fraction. The higher the heating rate, the higher the final fraction. Thus, our experiments reproduce well-known trends from literature [BVS22; Bel+19; Chb+14; HPM04; Kam+15; Lai+16; Li+13; MGF11; Mor19; Oll17; Tei+21; TM18; Wei+13] and exposed in the literature review (I.2.3).

Thermo-kinetics analyses [Lai+16; Mor19; SDM81; Tei+21] show that the austenite growth during the isothermal holding is governed by Local Equilibrium with Partitioning conditions at the interface, i.e. with significant redistribution of substitutional elements, mainly manganese in our studied DP600 steel. As explained in Chapter I, the austenite growth under LEP is first controlled by diffusion in ferrite, as three orders faster than in austenite. The redistribution produces a manganese gradient in the growing austenite, due to very slow diffusion in austenite. This out-of-equilibrium state often produces austenite fraction higher than the OE fraction in simulations [Cou+23; Lai+16; Mor19; SDM81; Tei+21]. Reaching the equilibrium by diffusion in austenite requires very long holding time ( $> 10^5$  s) and is not observed during our experiments, as the samples are held at 800 °C for maximum 600 s. This growth mechanism explains well the final experimental fraction exceeding the OE fraction. However, the effect of the heating rate is still not explained.

In the numerical work of Teixeira et al. [Tei+21], the difference in final austenite fraction is attributed to the growth mode of austenite formed from isolated cementite particle during the heating stage. As detailed in Chapter I (I.2.3), this growth occurs under LEP mode during slow heating. The manganese redistribution during this stage leaves a lower amount of manganese to redistribute during austenite growth under LEP mode during the isothermal holding, and less austenite is formed after slow heating.

However, this analysis is based on a strict separation of austenite formed from pearlite islands and isolated cementite particles, which is completely denied by our experiments after 780 °C. The discussion in III.1.3.1 (Figure III.14) reveals a carbon transfer from one to another between 760 °C and 780 °C and our experiments speak in favor of austenite growth without substitutional redistribution above 780 °C. Consequently, the growth under LEP mode of austenite formed from isolated cementite particle during slow heating may never occur, or, at least, is not expected to produce major redistribution.

We propose here another origin of the faster austenite transformation after fast heating, which takes into consideration the influence of the diffusion distances inside the microstructure, which are different after slow or fast heating.

Our optical micrographs (Figure III.13 and Table III.2) highlight well the finer microstructure at 800 °C after fast heating. The discussion in III.1.3.1 (Figure III.14) leads us to consider the full system from 780 °C, with austenite growth under LENP mode during the heating stage. As the austenite fraction reached at the end of the heating stage are similar regardless the heating rate (Figure III.6 and Figure III.12), a similar amount of manganese is available from

austenite growth under LEP mode during the holding stage. Thus, the austenite fraction at the end of LEP controlled by diffusion in ferrite is expected to be similar, regardless the previous heating rate. Though, a finer microstructure, as observed after fast heating, offers short diffusion path for manganese and other substitutional elements, which accelerates the austenite formation with substitutional element redistribution [BVS22; Bel+19; Chb+14; MGF11; Oll17; TM18]. Hence, the maximum austenite fraction (higher than the OE fraction) is expected to be reached earlier. Using our experimental holding time (600 s), the kinetics are stopped before the austenite fraction reaches this maximum fraction. Thus, a higher heating rate leads to a finer microstructure, i.e. faster austenite growth kinetics, and a higher austenite fraction reached at the end of the holding stage. This hypothesis is further discussed in the next section, based on new experiments, and in Chapter IV, based on simulations using our original extended version of the model proposed by Wycliffe in [WPE81] for the austenite growth during the isothermal holding stage.

A finer microstructure resulting from fast heating rate can be explained by a higher nuclei density, as discussed in III.1.3.1. Consequently, the effects of the heating rate on the austenite formation kinetics during the isothermal holding could be due to its impact on the driving force for austenite nucleation or on the concomitance of ferrite recrystallization and austenite formation, as recrystallization influences the distribution and efficiency of nucleation sites and the diffusion through dislocations (I.2.2).

### III.1.4 Conclusion on ferrite recrystallization and austenite formation interaction induced by heating rate

This section investigated the effects of the heating rate on the austenite formation, based on an extensive experimental work.

In particular, time-resolved ferrite recrystallization kinetics were produced using our innovative IDST method, developed during this PhD work and detailed in Chapter II. This method, based on in situ HEXRD experiments, combined with Rietveld refinements, makes possible a time-resolved investigation of ferrite recrystallization and austenite formation kinetics at the same time. These experiments highlighted the concomitance of ferrite recrystallization and austenite formation during fast heating (30 °C/s). On the contrary, ferrite recrystallization was shown completed at the beginning of the austenite formation using the low heating rate (3 °C/s). Though the IDST method was shown to be a powerful tool, it seems now crucial to implement a systematic separation of diffraction rings from different phases, so that the recrystallization can be safely monitored in multi-phased alloys.

We used several conventional methods such as optical microscopy, SEM and TEM, to investigate the microstructure at different scales, EDXS in TEM, to measure the chemical composition of cementite particles, or WDS to measure the carbon content across the austenite.

From this experimental work, several conclusions are drawn:

- Austenite grows from two main carbon sources: pearlite islands and isolated cementite particles. During slow heating (3 °C/s), under 760 °C, austenite growth can be studied separately considering two closed subsystems, containing the pearlite, on the one hand, and the ferrite matrix with the isolated cementite particles, on the other hand, as proposed in [Mor19; Tei+21]. Between 760 °C and 780 °C, our experiments revealed a carbon transfer between the subsystems. Consequently, their separated study is made irrelevant. Contrary to [Mor19; Tei+21], austenite growth after 780 °C is investigated as a single thermodynamic

system. during the heating stage, above 750 °C, our experimental data speak in favor of austenite growth under LENP mode, regardless the heating rate.

- The isolated cementite particles undergo both manganese and chromium enrichment during slow heating (3 °C/s). In addition, the higher the manganese or chromium content, the higher the PNTT associated to the considered particle. In particular, chromium has a strong shifting effect despite its low content in the studied steel. Considering a distribution of chemical composition of cementite particles leads to a distribution of PNTT. Despite its low content in the studied steel, chromium strongly affects the PNTT. However, our discussion shows that low heating rates promote particles enrichment and shifts their PNTT to higher temperatures, which is in contradiction with the delay of the beginning of the austenite formation with higher heating rates, observed experimentally. A deeper investigation on samples heated using our fast heating rate is required for further discussion.
- Our experiments reproduced the effect of the heating rate on the morphology of austenite. The low heating rate produced a typical "necklace" morphology, while the high heating rate produced a typical "banded" morphology. At this point, none of our observations contradicts or validates the mechanisms exposed in the literature review (I.3).
- During the holding stage, our experiments speak in favor of previous thermo-kinetic analyses, suggesting that austenite grows under LEP mode during the holding stage. We showed that the higher the heating rate, the higher the final austenite fraction. The explanation from [Mor19; Tei+21] for this trend, based of separated investigation of austenite from pearlite and austenite from isolated cementite particles, is completely denied by our experiments, showing carbon transfer in austenite. We also show that the higher the heating rate, the faster the austenite formation kinetics during the isothermal holding, as expected from literature. Considering a similar state, inherited from the growth under LENP mode during the heating stage), the finer microstructure in the fast heated sample explains both major trends observed during the isothermal holding. This last hypothesis is further discussed based on simulations in Chapter IV.

In this section, we deeply studied the mechanisms of austenite formation mainly during slow heating. A similar investigation (carbon measurements using WDS, austenite fractions from cementite particles or pearlite determined from optical micrographs) during fast heating would be interesting to extend the discussion in III.1.3.1 to fast heating stages.

Our experimental work presented in this section mainly led to new thermo-kinetic discussions. But no new argument was proposed on the possible interactions with ferrite recrystallization. To bring more elements to the discussion and draw new conclusions, we propose additional and original experiments, presented in the next section.

### III.2 Effect of the micro-alloying and cold-rolling ratio on the austenite transformation

Our experimental work from the previous section helped discuss the mechanisms of the austenite formation in the studied steel. But these experiments mainly led to discussions on thermo-kinetic aspects. In particular, the previous section exposed no new arguments concerning the possible

interaction between ferrite recrystallization and austenite formation, as both are sensitive to the heating rate.

In literature and in the previous section, the concomitance of ferrite recrystallization and austenite formation is due to the heating rate, as schematized in Figure III.1. This section aims to go further by proposing new experiments designed judiciously to decorrelate the heating rate and the concomitance of ferrite recrystallization and austenite formation. In particular, all the thermal treatments are performed with a single heating rate (3 °C/s) to prevent an impact on thermally-activated mechanisms.

The DP600 CR65 studied at 3 °C/s in the previous section is taken as a reference. Niobium micro-alloying and lower cold-rolling ratio are used to delay ferrite recrystallization and to provoke its concomitance with the austenite formation (Figure III.1). In addition, experiments on niobium micro-alloyed steels bring new elements to discuss the relevance of dispersive terms to describe the interface mobility.

### III.2.1 Materials and methods

This section further investigates ferrite recrystallization and austenite formation in a conventional DP600 grade Fe-0.1C-1.9Mn-0.2Si-0.2Cr, with a cold-rolled ferrite-pearlite microstructure, during the intercritical annealing.

The samples are heated up to 800 °C and held 10 min at this temperature. At the end of the isothermal holding stage, the samples are gas quenched (He). To prevent the impact of a difference in activation of thermally-activated mechanisms, a single heating rate, 3 °C/s, is used.

The overlap of ferrite recrystallization and austenite formation is controlled by niobium micro-alloying or cold rolling ratio. The DP600 CR65 (Fe-0.1C-1.9Mn-0.2Si-0.2Cr) studied in the previous section is used as reference.

In situ HEXRD experiments were performed. The recrystallization progress is monitored using the IDST method. The austenite fraction during the annealing is obtained using the Rietveld analysis. Microstructural evolutions are studied using optical microscopy and SEM. Mean sizes of ferrite grains, pearlite islands and austenite islands are measured on the micrographs presented in this Section in the cold-rolling direction, giving their length, and in the direction normal to the cold rolling direction, giving their thickness. Mean sizes are estimated from ten measurements, ensuring a precision of 0.1 µm.

More details on the studied materials and the methods used are given in Chapter II.

#### III.2.1.1 Description of the niobium micro-alloyed samples

As presented in Chapter II, two niobium micro-alloyed grades, with 0.015 wt% Nb, labelled DP600Nb15 CR65, and 0.030 wt% Nb, labelled DP600Nb30 CR65, are produced based on DP600 grade, i.e. with the same targeted carbon and substitutional element content. Using niobium micro-alloying to control the overlap of ferrite recrystallization and austenite formation, the cold-rolling ratio is set at 65 % as in the reference scenario.

The austenite fractions are compared to the expected theoretical LENP and OE fractions, computed with Thermo-Calc. The first one, plotted with a black dashed line, is the austenite fraction computed considering LENP interface conditions. The second one, plotted with dotted lines, is the austenite fraction at OE.

Despite the same targeted composition, the real carbon and substitutional element content is slightly different from a grade to another once elaborated. Consequently, the equilibria (OE

Label		C	Mn	Si	Cr	Nb
DP600	Aimed	0.1	1.9	0.2	0.2	< 0.002
	Measured	0.092	1.83	0.225	0.193	< 0.002
DP600Nb15	Aimed	0.1	1.9	0.2	0.2	0.015
	Measured	0.088	1.73	0.224	0.196	0.014
DP600Nb30	Aimed	0.1	1.9	0.2	0.2	0.030
	Measured	0.081	1.75	0.230	0.196	0.028

Table III.3: Aimed and measured nominal composition (wt%) of the studied steels. Values for the DP600 have already been disclosed in Table III.1.

and LENP) considering the measured nominal composition of the steels are different from one another. Figure III.16 plots the austenite fraction at OE, in dotted lines, and theoretical LENP, in dashed lines, computed with Thermo-Calc, considering the measured nominal composition of the DP600 (blue diamonds), the DP600Nb15 (blue triangles) and the DP600Nb30 (inverted blue triangles) respectively.

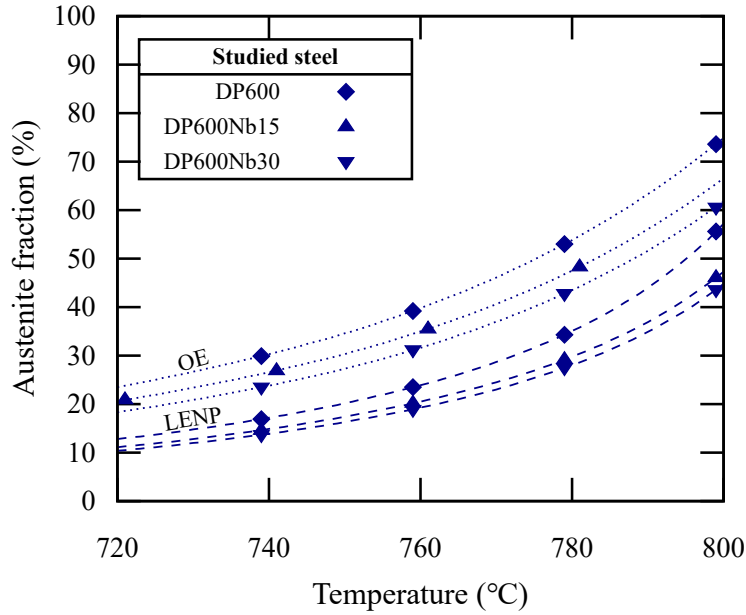


Figure III.16: Austenite fractions at Ortho-Equilibrium (OE), in dotted lines, and theoretical Local Equilibrium with Negligible Partitioning (LENP), in dashed lines, considering the measured nominal composition of the DP600 (blue diamonds), the DP600Nb15 (blue triangles) and the DP600Nb30 (inverted blue triangles).

At equilibrium (OE or LENP), the austenite fractions in the micro-alloyed steels are systematically lower than in the DP600 steel. Considering the theoretical LENP austenite fractions, the gap between the DP600 and the micro-alloyed steels increases from 2 % at 720 °C to 10 % at 800 °C. Considering the OE, this gap rises from 3 % at 720 °C up to 13 % at 800 °C.

In addition, in niobium micro-alloyed steel, NbC carbides are formed due to the high affinity

of niobium with carbon. Due to their high dissolution temperature, carbon in NbC carbides is no more available for the studied austenite formation. Consequently, from a thermodynamic point of view, the austenite formation should be studied in a system considering the nominal composition depleted from the carbon and niobium stored in the NbC carbides.

We investigated the precipitation state of niobium in the two studied niobium micro-alloyed grades, using ICP-OES (II.7), by measuring the mass fraction of niobium kept in the NbC carbides, written  $w_{Nb}^{NbC}$ . The mass fraction of carbon in the NbC carbide is then calculated. Considering  $M_x$  the molar mass of the element x, mass fraction of carbon in the NbC carbide is linked to the mass fraction of niobium as follows:

$$w_C^{NbC} = \frac{M_C}{M_{Nb}} \times w_{Nb}^{NbC} \quad (III.4)$$

In both DP600Nb15 CR65 and DP600Nb30 CR65, the amount of niobium in NbC is measured at  $22 \pm 2$  ppm. This represents 16 % of the niobium in the DP600Nb15 and 8 % of the niobium in the DP600Nb30. Removing the NbC of the system, the new niobium content is 0.012 wt% in the DP600Nb15 and 0.026 wt% in the DP600Nb30, considered in solid solution. The carbon mass fraction trapped in NbC carbides is 3 ppm, which represents only 0.3 % of the carbon in the studied steels. Considering the nominal composition of the studied steels, removing the NbC of the system, the austenite fraction at equilibrium (OE or LENP) is shifted by only 1 % by the niobium micro-alloying.

The main difference in the equilibrium is attributed to the difference in measured nominal composition, for carbon in particular. In the following, the austenite fraction at OE and theoretical LENP are plotted only for the reference DP600, to ensure readability of the figures. Yet, the gap presented above should be kept in mind for discussions.

In the following, the results for the DP600 CR65, the DP600Nb15 CR65 and the DP600Nb30 CR65 are plotted using blue diamonds, triangles and inverted triangles respectively.

### III.2.1.2 Description of the cold-rolled samples

As presented in Chapter II, the studied DP600 grade was cold rolled using four ratios: 30 %, 45 %, 60 % and 65 %. In the following, the samples are labeled DP600 CRx, with x the cold-rolling ratio. Once again, the DP600 CR65 studied in the previous sections is used as reference.

In the following, the results for the DP600 CR30, the DP600 CR45, the DP600 CR60 and the DP600 CR65 are plotted using opened blue squares, open blue diamonds, filled blue squares and filled blue diamonds, respectively. The austenite fractions are compared to the expected theoretical LENP and OE fractions, computed with Thermo-Calc, as in previous section.

## III.2.2 Results

### III.2.2.1 Experiments on niobium micro-alloyed grades

In this sub-section, we present the results of the experiments on the niobium micro-alloyed grades, namely the DP600Nb15 CR65 and the DP600Nb30 CR65. The results on the DP600CR65 are reminded for the sake of comparison.

**III.2.2.1.1 Initial microstructure** SEM micrographs of the initial microstructures in the cold-rolled state of our two niobium micro-alloyed steels are shown in Figure III.17 (a and b). The

initial microstructure of the reference DP600 CR65 (Figure III.2) is shown again in Figure III.17 (c) to ease the comparison.

In the cold-rolled state, both micro-alloyed grades contain a deformed ferrite matrix, indicated by white arrows, and show an elongated shape in the cold-rolling direction, as in the DP600 CR65. The deformed ferrite grains are 2.1  $\mu\text{m}$  thick in the DP600Nb15 CR65 and 1.8  $\mu\text{m}$  thick in the DP600Nb30 CR65.

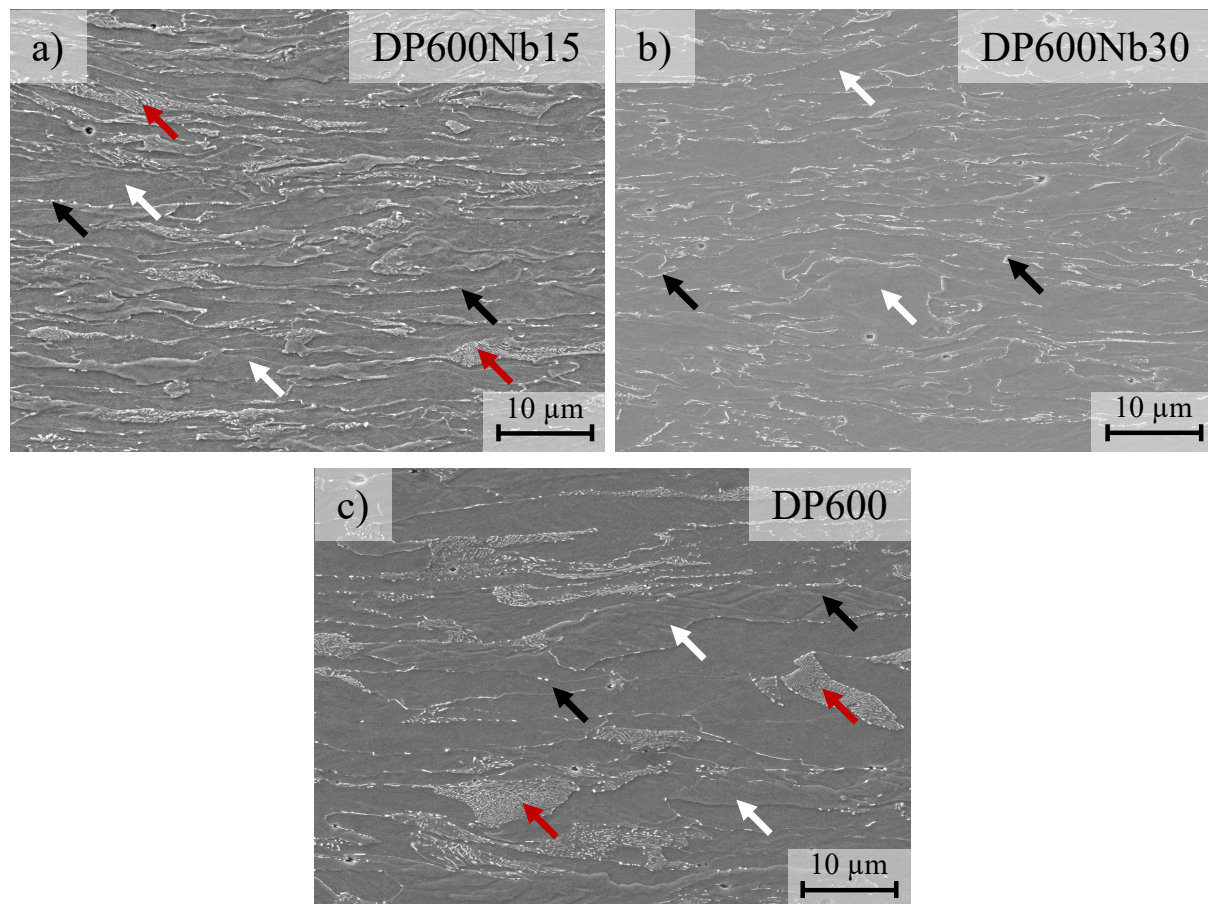


Figure III.17: SEM micrographs of the microstructures of the DP600Nb15 CR65 (a) and the DP600Nb30 CR65 (b) in the cold-rolled state. Cementite particles (either in pearlite or in the matrix) are in white contrast and ferrite in dark contrast.

The initial microstructure of the DP600Nb15 CR65 (Figure III.17 a) is composed of thin (1.5  $\mu\text{m}$ ) elongated pearlite islands (red arrows) and intergranular cementite particles (black arrows). Pearlite islands are typically twice thinner than in the DP600 CR65 (Table III.4). The volume fraction of pearlite and intergranular cementite particles is estimated on binarized optical micrographs following the method detailed in Chapter II. The DP600Nb15 CR65 sample contains  $10.7 \pm 2.3$  % of carbon rich zones, shared as 7.9 % of pearlite and 2.8 % of isolated cementite particles.

In contrast, the initial microstructure of the DP600Nb30 CR65 contains mainly thin cementite films. Pearlite is rarely observed and its mean size 0.6  $\mu\text{m}$  makes it very difficult to identify

Label	Pearlite thickness	Pearlite islands length	Ferrite thickness	$f_{CP}$ (vol.%)	$f_P$ (vol.%)
DP600	2.7 $\mu\text{m}$	17.9 $\mu\text{m}$	2.6 $\mu\text{m}$	2.3	16
DP600Nb15	1.5 $\mu\text{m}$	X	2.1 $\mu\text{m}$	2.8	7.9
DP600Nb30	0.6 $\mu\text{m}$	X	1.8 $\mu\text{m}$	10.7	1.5

Table III.4: Typical mean sizes in the initial microstructures of the studied steels.

as pearlite and not as isolated cementite particles. Using image analysis on optical micrographs, we found  $12.2 \pm 0.8$  % of carbon rich zones, shared as 1.5 % of pearlite and 10.7 % of isolated cementite particles, i.e. the microstructure is mainly composed of isolated cementite particles. The repartition between pearlite and isolated cementite particles is probably strongly biased, as the pearlite is easily misidentified as isolated particles.

The typical sizes are reported in Table III.4.

**III.2.2.1.2 Microstructure at the end of the heating stage** Optical micrographs of the microstructures of our niobium micro-alloyed steels at the end of the heating stage (3 °C/s) are shown in Figure III.18. At 800 °C, the microstructure of the DP600Nb15 CR65 (Figure III.18 a) and the DP600Nb30 CR65 (Figure III.18 b) are very similar. The microstructure of the reference DP600 (Figure III.13 a) is show again in (Figure III.18 c) for comparison. The microstructure of the niobium micro-alloyed steels is characterized by numerous small (1.5  $\mu\text{m}$ ) austenite grains (martensite after quenching), in brown, and ferrite islands, in white, elongated (4  $\mu\text{m}$  thick and 35  $\mu\text{m}$  long) in the cold rolling direction.

The microstructures of our niobium micro-alloyed steels are strongly different from the one of the DP600 CR65 (Figure III.18 c). The microstructure of the micro-alloyed steels is much thinner and conserved the elongated shape of the cold-rolled state, contrary to the microstructure of the DP600 with its larger austenite grains and equiaxed ferrite grains.

These typical sizes are summarized in Table III.5.

Label	Ferrite grain thickness	Ferrite grain length	Austenite grain thickness
DP600	5 $\mu\text{m}$	X	10.4 $\mu\text{m}$
DP600Nb15 and Nb30	4 $\mu\text{m}$	35 $\mu\text{m}$	1.5 $\mu\text{m}$

Table III.5: Typical mean sizes in the microstructures of the studied steels at the end of a heating stage at 3 °C/s.

**III.2.2.1.3 Kinetics of ferrite recrystallization and austenite formation** Recrystallization is followed using the IDST method, detailed in Chapter II. The number of diffraction spots tracked during slow heating (3 °C/s) of the DP600Nb15 CR65 (triangles) and the DP600Nb30 CR65 (inverted triangles) is plotted in Figure III.19 (a). The results for the DP600 CR65 (diamonds) are presented in the previous section (Figure III.12 (a)) but plotted again in Figure III.19 (a).

During the heating stage of the DP600Nb15 CR65 and the DP600Nb30 CR65, the number of diffraction spots stays very low. Less than 200 spots are detected on the diffraction patterns

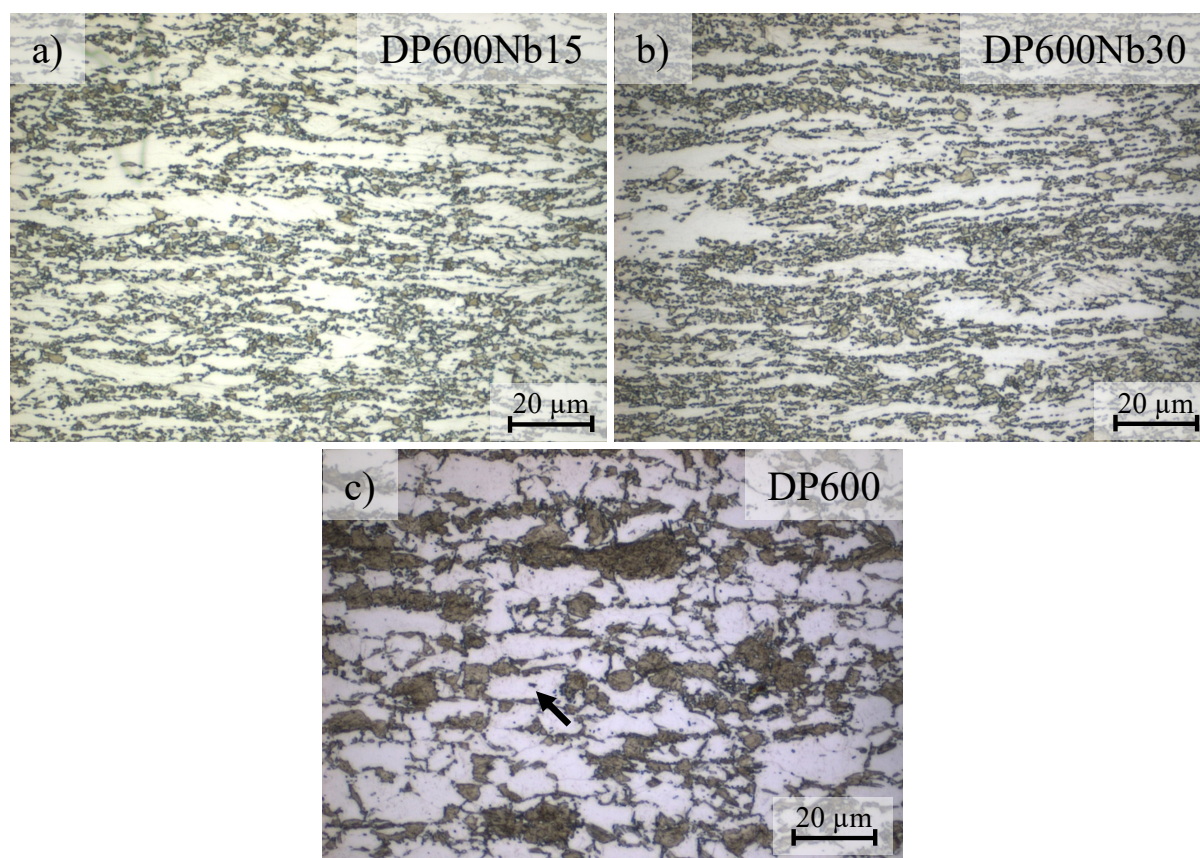


Figure III.18: Optical micrographs of the microstructures of the DP600Nb15 CR65 (a) and the DP600Nb30 CR65 (b) at 800 °C. Martensite (austenite before quenching) is colored in brown by the etchant and ferrite stays in white.

of the micro-alloyed steels, while up to 1700 spots are detected on the diffraction patterns of the DP600 CR65 (Figure III.12 (a)).

Figure III.19 (b) shows the austenite weight fraction in the DP600Nb15 CR65 (triangles) and DP600Nb30 CR65 (inverted triangles) during slow heating (3 °C/s) estimated by Rietveld refinement from in situ HEXRD experiments. The results for the DP600 CR65 (diamonds) are presented in the previous section (Figure III.12 (b)) but plotted again in Figure III.19 (b).

All during the heating stage, the austenite fractions in the DP600Nb15 CR65 (triangles) and DP600Nb30 CR65 (inverted triangles) are superposed. The austenite starts being detected at 720 °C. during the heating stage, the austenite fraction in the niobium micro-alloyed steels increases in three steps. First, the austenite fraction increases in a sluggish phase between 720 °C and 730 °C, staying under 5 %. Then, between 730 °C and 750 °C, the austenite fraction bursts from few percent to 20 %. Finally, the austenite fraction follows very closely the theoretical LENP fraction between 750 °C and 800 °C. In this temperature range, the austenite fraction is lower than the theoretical LENP fraction by only 5 %. From 775 °C to 800 °C, the austenite fraction in the three studied steels is superposed. At the end of the heating stage, the austenite fraction reaches 50 % in all three samples.

Figure III.19 (c) shows the austenite weight fraction in the DP600Nb15 CR65 (triangles) and

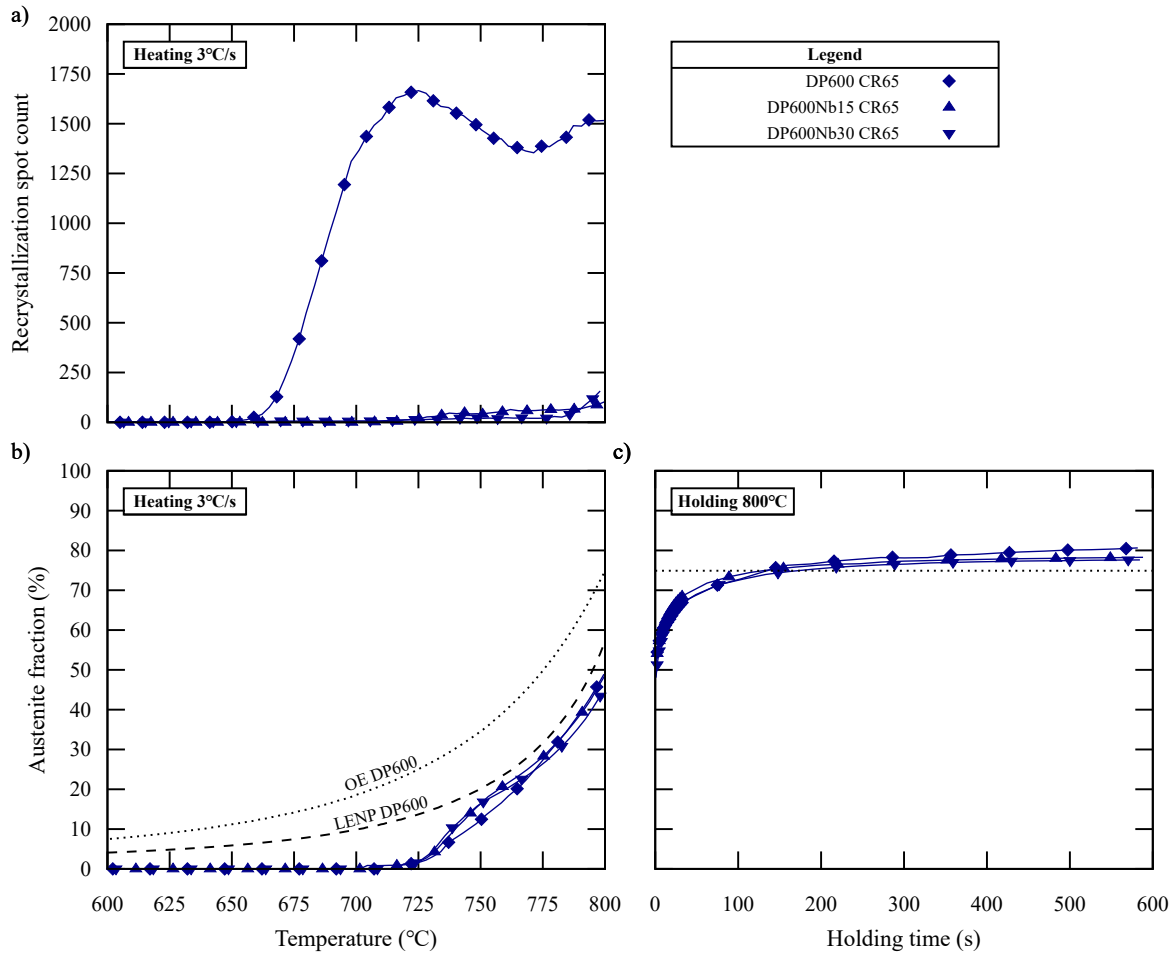


Figure III.19: Recrystallization and austenite formation during the intercritical annealing of the DP600 CR65 (diamonds), the DP600Nb15 CR65 (triangles) and the DP600Nb30 CR65 (inverted triangles) followed by HEXRD. Number of diffraction spots tracked during the heating stage (a). Austenite weight fraction during the heating (b) and isothermal holding (c) stages.

DP600Nb30 CR65 (inverted triangles) during the isothermal holding stage at 800 °C estimated by Rietveld refinement from in situ HEXRD experiments. During this stage, the austenite fractions in the three studied steels are superposed. The austenite fraction increases from 50 % at the beginning of the holding stage up to 80 % after 600 s at 800 °C. The austenite fraction exceeds the austenite fraction at OE.

Due to their respective nominal compositions, the theoretical LEMP and OE austenite fractions are different from one studied steel to another, as shown in Figure III.16. To help rationalize these austenite fractions, Figure III.20 (a) plots the gap between the austenite fraction estimated from HEXRD experiment, plotted in Figure III.19 (b), and the theoretical LEMP austenite fraction during the heating. Figure III.20 (b) plots the austenite fraction estimated from HEXRD experiment, plotted in Figure III.19 (c), and the OE during the isothermal holding. Note that the scale is enlarged for a better readability.

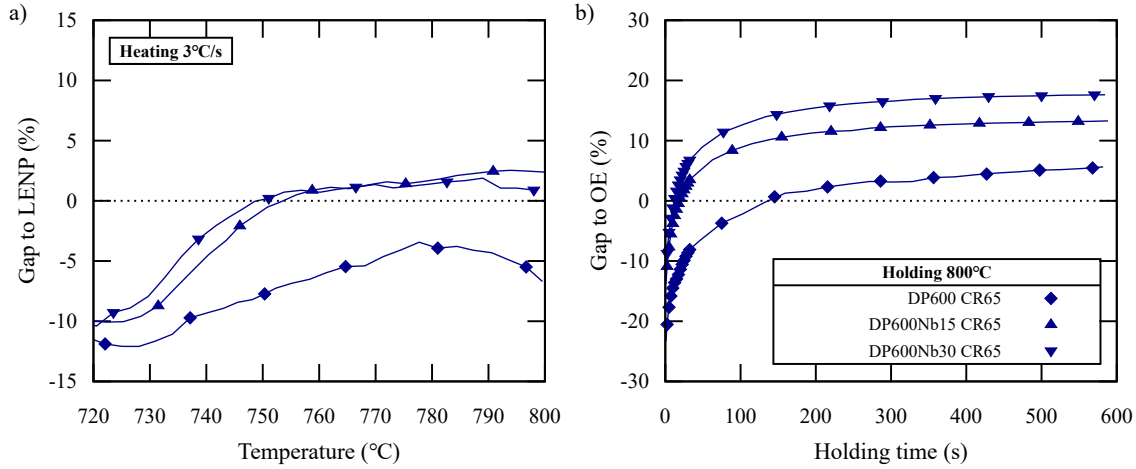


Figure III.20: Gap between the austenite fraction estimated from HEXRD experiment and the OE during the isothermal holding of the DP600 CR65 (diamonds), the DP600Nb15 CR65 (triangles) and the DP600Nb30 CR65 (inverted triangles).

During the heating stage (Figure III.20 (a)), the gap to LERP in the DP600Nb15 CR65 (triangles) and DP600Nb30 CR65 (inverted triangles) follows a similar evolution. Between 720 °C and 740 °C, the gap to LERP is the widest, around 10 %. This gap is similar to the one observed in the DP600 CR65 (around 12 %). Then, the gap to LERP reduces down to 5 % at 780 °C in the DP600 CR65, before slightly increasing up to 7 % at 800 °C. In the niobium micro-alloyed steels, the gap to LERP decreases faster. Above 750 °C, the experimental fractions stay very close to the theoretical LERP fraction.

During the isothermal holding stage (Figure III.20 (b)), the austenite fraction exceeds the OE fraction of the respective steels after 140 s in the DP600 CR65, 20 s in the DP600Nb15 CR65 and 10 s in the DP600Nb30 CR65. The higher the niobium content, the earlier the measured fraction exceeds the OE fraction. At the end of the holding stage, the austenite fraction exceeds the OE fraction by 6 % in the DP600 CR65, 12 % in the DP600Nb15 CR65 and 18 % in the DP600Nb30 CR65. The higher the niobium content, the higher the excess from the OE fraction.

### III.2.2.2 Experiments on the DP600 with various cold-rolling ratios

In this sub-section, we present the results of the experiments carried on the DP600 with four cold-rolling ratios, namely the DP600 CR30, the DP600 CR45, the DP600 CR60 and the DP600 CR65, before discussing the results obtained on micro-alloyed steels. The studied DP600 CR30 and DP600 CR60 are materials taken back from the previous PhD work from [Mor19]. The experiments on these two steels were performed during this previous PhD study but the post-processment was carried out in the present work.

**III.2.2.2.1 Initial microstructure** SEM micrographs of the initial microstructures in the cold-rolled state of our DP600 steels cold-rolled at 45 % (DP600 CR45) and 60 % (DP600 CR60) are shown in Figure III.21. No SEM micrograph of the initial microstructure of the DP600 CR30 was performed during the previous PhD, but a strong similarity is expected with the CR45. The

initial microstructure of the reference DP600 CR65 (Figure III.2) is shown again in Figure III.21 (c) to ease the comparison.

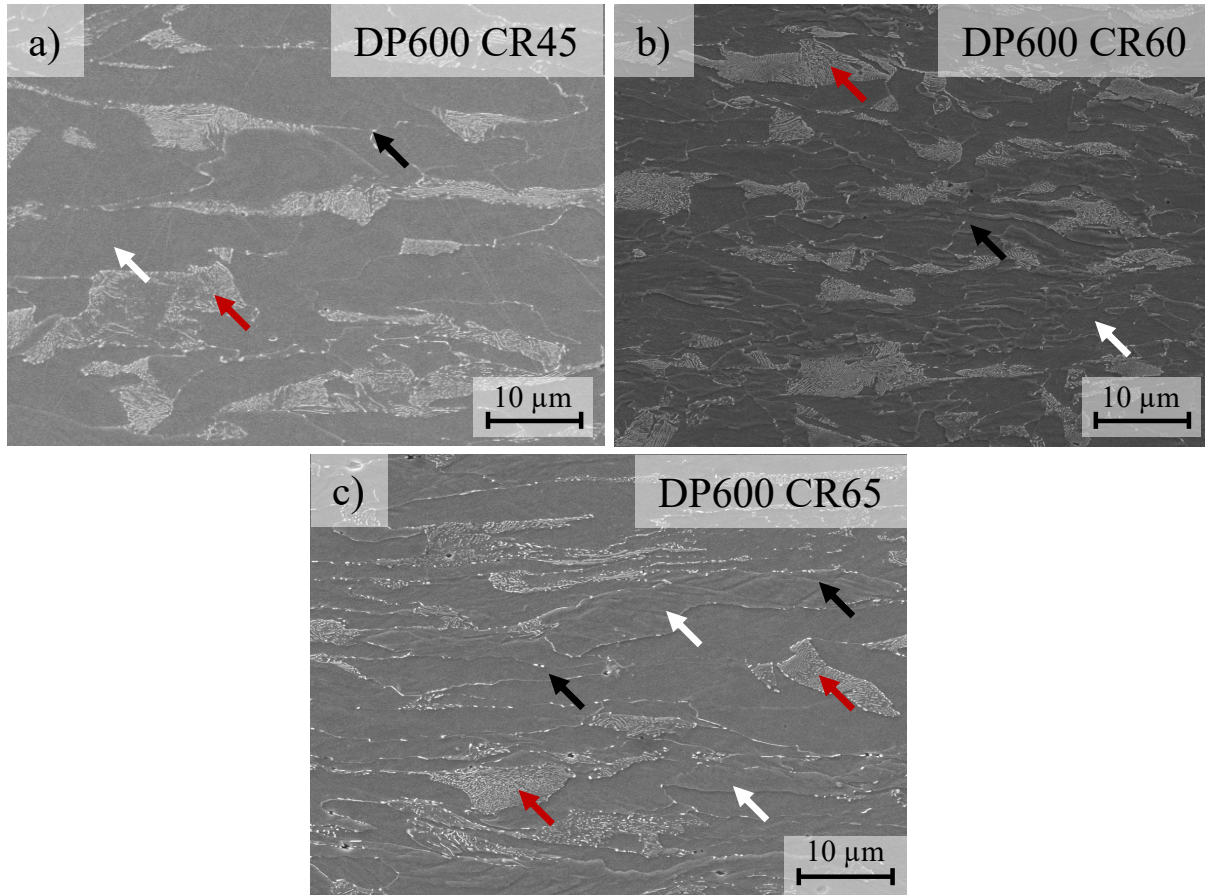


Figure III.21: SEM micrographs of the microstructures of the DP600 CR45 (a), the DP600 CR60 (b) and the DP600 CR65 (c) in the cold-rolled state. Cementite particles (either in pearlite or in the matrix) are in white contrast and ferrite in dark contrast.

In the cold-rolled state, the microstructures of both the DP600 CR45 and the DP600 CR60 contain a deformed ferrite matrix, indicated by white arrows in Figure III.21. The deformed ferrite grains are 7.3  $\mu\text{m}$  thick in the DP600 CR45, while 2.4  $\mu\text{m}$  thick in the DP600 CR60. The initial microstructure is composed of thick pearlite islands elongated in the cold-rolling direction, indicated by red arrows. Their thickness is 4.7  $\mu\text{m}$  in the DP600 CR45 and 2.5  $\mu\text{m}$  in the DP600 CR60. Their length is 22  $\mu\text{m}$  in the DP600 CR45 and 14  $\mu\text{m}$  in the DP600 CR60. These typical sizes are summarized in Table III.6. Inter-granular cementite particles, indicated by black arrows, are observed in the ferrite matrix. They are often in clusters grouping few of them (3 to 5 particles).

The aspect ratio of the pearlite islands (here the relation between their length and their thickness) is 6.6 in the DP600 CR65, from the results presented in the previous section (Figure III.21 c), 5.6 in the DP600 CR60 and 4.7 in the DP600 CR45. The higher the cold-rolling ratio, the more the microstructure is elongated in the cold-rolling direction as expected.

Label	Pearlite thickness	Pearlite islands length	Aspect ratio pearlite	Ferrite thickness
DP600 CR45	4.7 $\mu\text{m}$	22 $\mu\text{m}$	4.7	7.3 $\mu\text{m}$
DP600 CR60	2.5 $\mu\text{m}$	14 $\mu\text{m}$	5.6	2.4 $\mu\text{m}$
DP600 CR65	2.7 $\mu\text{m}$	17.9 $\mu\text{m}$	6.6	2.6 $\mu\text{m}$

Table III.6: Typical mean sizes in the initial microstructures of the studied DP600 depending of the cold-rolling ratio.

**III.2.2.2.2 Microstructure at the end of the heating stage** Optical micrographs of the microstructures of our DP600 steels cold-rolled at 30 % (DP600 CR30) and 60 % (DP600 CR60) at the end of the heating stage (3 °C/s), i.e. at 800 °C, are shown in Figure III.22. The microstructure of the reference DP600 CR65 (Figure III.13 a) is show again in (Figure III.22 c) for comparison.

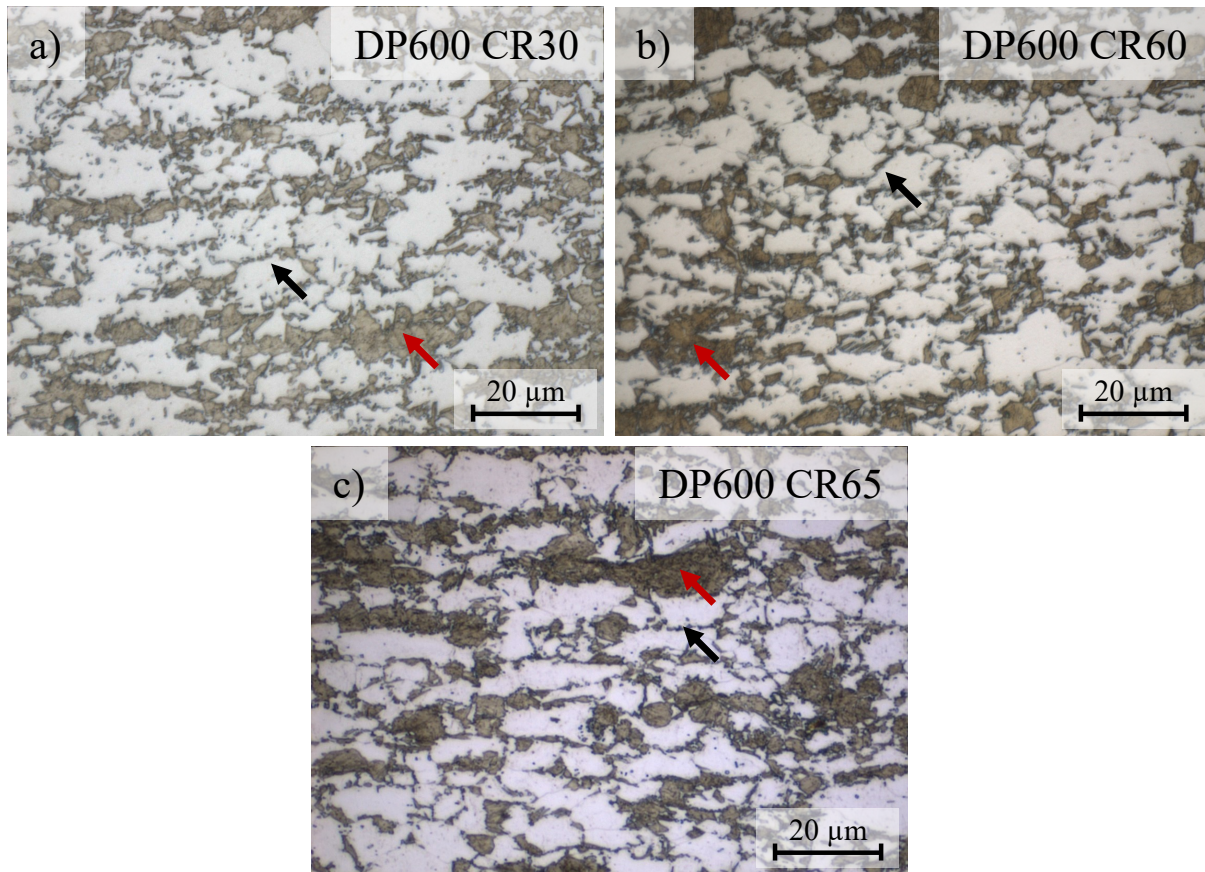


Figure III.22: Optical micrographs of the microstructures of the DP600 CR30 (a) and the DP600 CR60 (b) at 800 °C. Martensite (austenite before quenching) in colored in brown by the etchant and ferrite stays in white. Martensite is either in large islands, indicated by red arrows, or in thin films at ferrite grain boundaries, indicated by black arrows.

At 800 °C, the microstructures of the DP600 CR30 (Figure III.22 a) and the DP600 CR60

(Figure III.22 b) are similar to the one of the DP600 CR65 (Figure III.22 c). The microstructures are characterized by large recrystallized ferrite grains (in white), 7.6  $\mu\text{m}$  in the DP600 CR30, 5.7  $\mu\text{m}$  in the DP600 CR60 and 5.0  $\mu\text{m}$  in the DP600 CR65. The lower the cold-rolling ratio, the larger the recrystallized grains. Austenite (martensite after quenching, in brown) is either in large islands (red arrows) or in thin films at ferrite grain boundaries, indicated by black arrows. Their thickness of the austenite islands is 5.4  $\mu\text{m}$  in the DP600 CR30, 7.2  $\mu\text{m}$  in the DP600 CR60 and 10.4  $\mu\text{m}$  in the DP600 CR65 and their length is about 35.2  $\mu\text{m}$  in the DP600 CR30, 14.8  $\mu\text{m}$  in the DP600 CR60 and 28.3  $\mu\text{m}$  in the DP600 CR65. These sizes are reported in Table III.7.

Label	Ferrite grain thickness	Austenite grain thickness	Austenite grain length	Austenite aspect ratio
DP600 CR30	7.6 $\mu\text{m}$	5.4 $\mu\text{m}$	35.2 $\mu\text{m}$	6.5
DP600 CR60	5.7 $\mu\text{m}$	7.2 $\mu\text{m}$	14.8 $\mu\text{m}$	2.0
DP600 CR65	5.0 $\mu\text{m}$	10.4 $\mu\text{m}$	28.3 $\mu\text{m}$	2.7

Table III.7: Typical mean sizes in the microstructures of the studied DP600 at the end of a heating stage at 3  $^{\circ}\text{C}/\text{s}$  depending on the cold-rolling ratio.

The aspect ratio of the austenite islands is 6.5 in the DP600 CR30, 2.0 in the DP600 CR60 and 2.7 in the DP600 CR65. The lower the cold-rolling ratio, the more the austenite islands are elongated in the cold-rolling direction.

**III.2.2.2.3 Kinetics of ferrite recrystallization and austenite formation** Figure III.23 shows an enlargement of the HEXRD 2D patterns at 760  $^{\circ}\text{C}$  of the DP600 CR30 (a), the DP600 CR45 (b), the DP600 CR60 (c) and the DP600 CR65 (d) during the heating stage (3  $^{\circ}\text{C}/\text{s}$ ). The diffracting phases and planes are indicated on the corresponding diffraction rings. As shown by our study on the DP600 CR65 in the previous section (Figure III.9 and Figure III.10), cementite diffraction 2D patterns cannot be observed due to their very low intensity with the considered scale. At 760  $^{\circ}\text{C}$ , both ferrite and austenite diffract, regardless the cold-rolling ratio (Figure III.23). Numerous bright diffraction spots, indicated by blue arrows, are observed, only on ferrite diffraction rings.

Recrystallization is followed using the IDST method, detailed in Chapter II. The number of diffraction spots tracked during slow heating (3  $^{\circ}\text{C}/\text{s}$ ) of the DP600 CR30 (opened blue squares), the DP600 CR45 (open blue diamonds) and the DP600 CR60 (filled blue squares) are plotted in Figure III.24. The results for the DP600 CR65 (diamonds) are presented in the previous section (Figure III.11) but plotted again in Figure III.24.

During the heating stage, the number of diffraction spots detected follow the same trends in all studied samples. Three steps are observed. First a burst up to a local maximum around 1700 spots. Then, a drop followed by a second increase. The first burst starts at higher temperature for lower heating rates: at 645  $^{\circ}\text{C}$  in the CR65, 660  $^{\circ}\text{C}$  in the CR60 and the CR 45 and 680  $^{\circ}\text{C}$  in the CR30.

Regardless the cold-rolling ratio, only ferrite diffraction patterns show diffraction spots under 760  $^{\circ}\text{C}$ , as shown in Figure III.23. At temperatures lower than 760  $^{\circ}\text{C}$ , the detected spots are only due to recrystallized ferrite grains.

As in the previous section, the first increase in the number of detected diffraction spots (Figure III.24) follows a sigmoidal shape, typical feature of recrystallization kinetics [HH95;

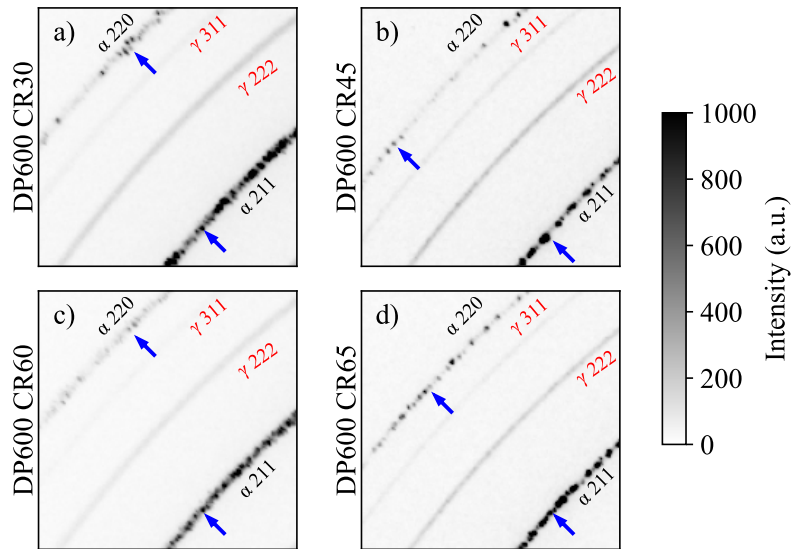


Figure III.23: Partial diffraction patterns at 760 °C of the DP600 CR30 (a), the DP600 CR45 (b), the DP600 CR60 (c) and the DP600 CR65 (d) during the heating stage (3 °C/s). The diffracting phase and planes are indicated on the corresponding diffraction rings. Arrows highlight few diffraction spots on diffraction rings.

Mor+18; OMG08; Rei52] and is attributed to primary recrystallization. The following decrease is attributed to ferrite grain growth, as discussed in Chapter II, and austenite formation, which starts at 725 °C, as shown in Figure III.25 (b). After 760 °C, the final increase in detected diffraction spots is mainly due to diffraction spots appearing also on austenite rings (Figure III.9 (g and i)). After 760 °C, the count of diffraction spots is no more representative of the ferrite recrystallization progress.

From these observations, the ferrite recrystallization kinetics during the heating stage (3 °C/s) of the DP600 CR30 (opened blue squares), the DP600 CR45 (open blue diamonds), the DP600 CR60 (filled blue squares) and for the DP600 CR65 (diamonds) are plotted in Figure III.25 (a). We use the same convention as in the previous section. All recrystallization kinetics show a typical sigmoidal shape, as expected from literature [HH95; Mor+18; OMG08; Rei52], and the beginning of ferrite recrystallization is delayed by 15 °C in the CR60 and the CR 45 and 35 °C in the CR30.

Figure III.25 (b) shows the austenite weight fraction in the DP600 CR30 (opened blue squares), the DP600 CR45 (open blue diamonds), the DP600 CR60 (filled blue squares) and the DP600 CR65 (filled blue diamonds) during slow heating (3 °C/s) estimated by Rietveld refinement from in situ HEXRD experiments.

During the heating stage, the austenite fractions of all the studied samples are superimposed. The austenite starts being detected at 720 °C. Its fraction increases almost monotonously up to 50 % at 800 °C. At first, the austenite fraction is far from the theoretical LENP fraction ( $T < 750$  °C). From 775 °C to 800 °C, the austenite fraction is close to the theoretical LENP fraction (less than 2 % lower).

Figure III.25 (c) shows the austenite weight fraction during the isothermal holding stage at 800 °C. During this stage, the austenite fractions in the DP600 CR60 and DP600 CR65

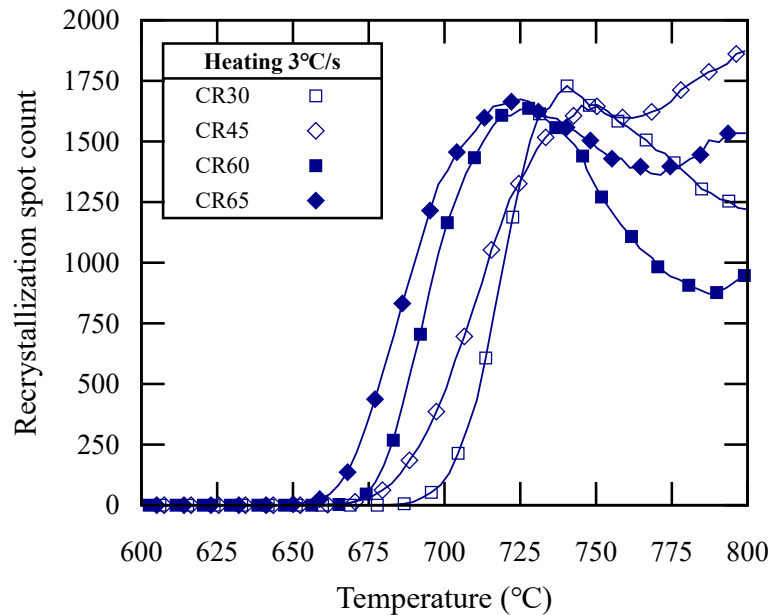


Figure III.24: Number of diffraction spots tracked during the heating stage (3 °C/s) of the intercritical annealing of the DP600 CR30 (opened blue squares), the DP600 CR45 (open blue diamonds), the DP600 CR60 (filled blue squares) and the DP600 CR65 (filled blue diamonds).

samples are superposed. Then, the lower the cold-rolling ratio, the slower the kinetics. during the isothermal holding, the DP600 CR30 sample is 5 % lower than the DP600 CR60 and DP600 CR65. Up to 300 s holding, the DP600 CR45 is 3 % lower than the DP600 CR60 and DP600 CR65. After 300 s, the austenite fraction gap lowers and the austenite fraction in the DP600 CR45 finally reaches the austenite fraction in the DP600 CR60 and the DP600 CR65. At the end of the isothermal holding stage (600 s), the austenite fractions in the DP600 CR45, DP600 CR60 and the DP600 CR65 exceed the OE by 5 %, while the austenite fraction in the DP600 CR30 just reached the OE fraction (75 %). The kinetics tends towards stabilization at the end of the holding stage but still increases very slowly.

### III.2.3 Discussions

#### III.2.3.1 Effect of niobium micro-alloying and cold-rolling on the initial microstructure

The SEM micrographs of the initial microstructures of the niobium micro-alloyed steels in Figure III.17 show much finer microstructures than in the reference DP600 CR65 (Table III.4). The refinement of the microstructure with niobium micro-alloying is a known in literature [Gra08]. During the hot rolling process, niobium partially precipitates in NbC particles, as estimated in the Subsection III.2.1. As obstacles for grain boundaries, grain boundaries are pinned or slowed down. Both niobium in solid solution and NbC particles delay austenite dynamic recrystallization. This provides more ferrite nucleation site and leads to finer ferrite grains.

On the contrary, the SEM micrographs of the initial microstructures of the DP600 steels cold-rolled at 45 % (DP600 CR45) and 60 % (DP600 CR60) in Figure III.21 show coarser

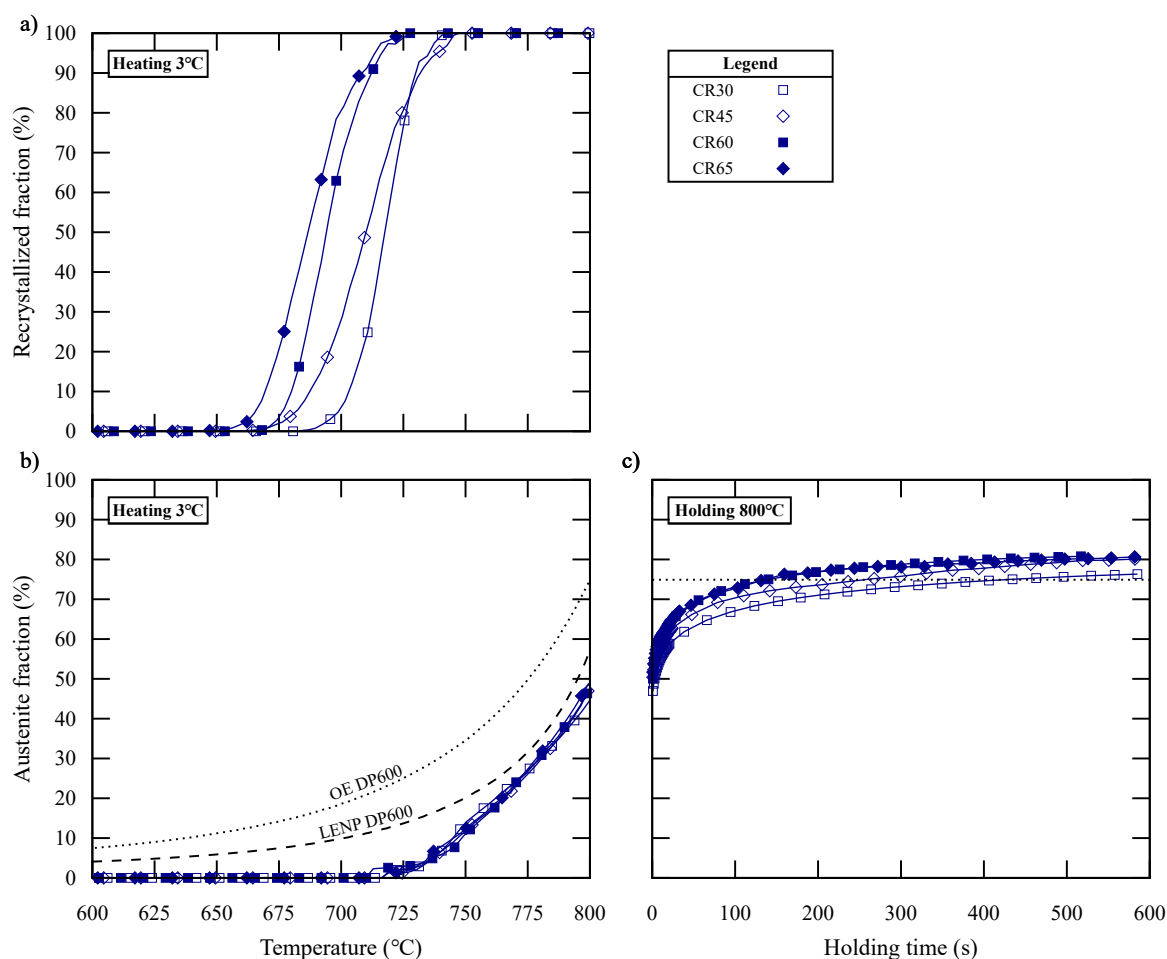


Figure III.25: Recrystallization (a) and austenite formation (b and c) kinetics during the intercritical annealing of the DP600 CR30 (opened blue squares), the DP600 CR45 (open blue diamonds), the DP600 CR60 (filled blue squares) and the DP600 CR65 (filled blue diamonds) followed by HEXRD. Fractions are plotted during the heating stage at 3 °C/s (a and b) and isothermal holding stage (c).

microstructures with lower cold-rolling ratios. As highlighted by their decreasing aspect ratios and expected from literature [HPM04; PÖ20], the pearlite islands are less deformed in the samples with lower cold-rolling ratio. Similarly, the lower the cold-rolling ratio, the thicker the ferrite grains. As it is more deformed in the sample with higher cold-rolling ratio, ferrite is expected to store more energy with a higher dislocation density [HPM04; HH95].

### III.2.3.2 Ferrite recrystallization control

As shown in Figure III.19 (a), very few diffraction spots are detected on ferrite diffraction patterns while heating the niobium micro-alloyed steels. At 800 °C, the ferrite grains keep an elongated shape in the cold-rolling direction, as shown by our optical micrographs in Figure III.18. These results indicate that there is no new recrystallized ferrite grains. The few

diffraction spots detected at temperature under 770 °C are attributed to dislocation cells formed by recovery [HH95; Nes95]. At higher temperature, the diffraction spots are mainly observed on austenite diffraction rings, as in the previous section. As expected [All+20; Son+14; Ver+09], the niobium micro-alloying inhibits completely the ferrite recrystallization in our studied steels, though our slow heating rate is slow enough to enable ferrite recrystallization in the DP600 CR65.

Looking at the effect of cold-rolling, Figure III.25 (a) shows that the beginning of ferrite recrystallization is delayed by 15 °C in the CR60 and the CR45 and 35 °C in the CR30. As expected [HH95; Rei52], lower cold-rolling ratios delay the ferrite recrystallization in our studied DP600. A higher cold-rolling ratio leads to more severe deformation and higher dislocation density. As the elastic energy stored in crystalline defects is the driving force for recrystallization, this latter is promoted by higher cold-rolling ratio. Though our slow heating rate is slow enough to complete ferrite recrystallization before austenite formation in the DP600 CR65, the ferrite matrix is only 80 % in the DP600 CR45 and 50 % in the DP600 CR30 when austenite formation starts at 720 °C. We succeed to induce the overlap of ferrite recrystallization and austenite formation by lowering the cold-rolling ratio.

Figure III.26 summarizes the different temperature ranges of ferrite recrystallization in our experiments. As we used a single heating rate, we successfully decorrelated the delay of ferrite recrystallization and the increase of the heating rate. As shown in Figure III.26, our experiments offer different degrees of overlap between ferrite recrystallization and austenite formation. Now, we can study the effect of ferrite recrystallization on the austenite formation separately from purely thermally activated mechanisms.

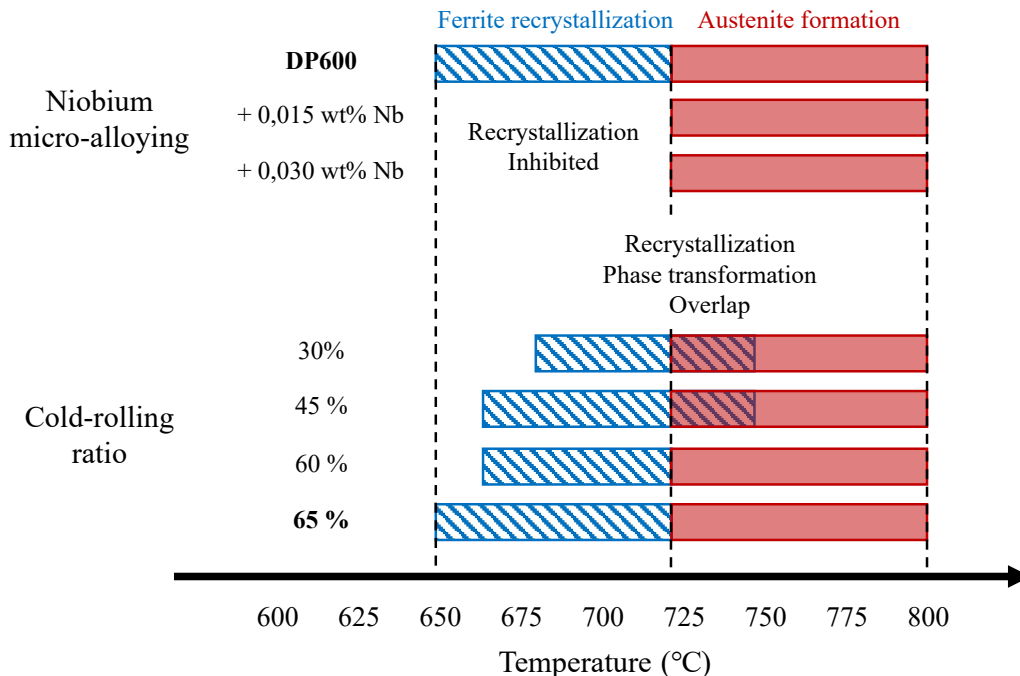


Figure III.26: Schema of the temperature domain overlap between ferrite recrystallization and austenite formation during the heating stage at 3 °C/s.

### III.2.3.3 Austenite morphology strongly affected by ferrite recrystallization

At the end of the heating stage (800 °C), the niobium micro-alloyed samples (Figure III.18) present much thinner microstructures than the reference DP600 CR65 (Figure III.5 (d) and Figure III.13 (a)). As ferrite grains conserve an elongated shape in the cold rolling direction, the whole microstructure of the niobium micro-alloyed samples (Figure III.18) seems elongated. Their microstructure contains ferrite bands, alternating with austenite rich bands, giving the microstructure a banded-like morphology, despite the slow heating rate.

The numerous small austenite grains in the microstructure of the niobium micro-alloyed steels at 800 °C are attributed to the isolated cementite particles. As shown in literature [Bel+19; Chb+14; MGF11; Tei+21; TM18], such cementite particles offer preferential nucleation site for austenite. The initial microstructure of the niobium micro-alloyed steels contains much more isolated cementite particles (Figure III.17) than the reference DP600 CR65, and, consequently, offers much more austenite nucleation sites. The numerous austenite nuclei lead to the numerous small austenite grains observed at 800 °C. On the contrary, the reference DP600 CR65 contains more pearlite islands. These preferential nucleation sites are less numerous. Once austenite has nucleated on pearlite islands, austenite grows until complete transformation of the islands. At 800 °C, the microstructure shows large austenite islands (Figure III.5 (d) and Figure III.13 (a)). These observations highlight the contribution of the isolated cementite particles to the formation of thin austenite structures and support the work of Teixeira et al. [Tei+21], attributing the austenite in thin film at ferrite grain boundaries to the isolated cementite particles.

The elongated shape of the microstructure of the niobium micro-alloyed steels at 800 °C is attributed to the absence of ferrite recrystallization. As discussed previously (III.2.3.2), ferrite recrystallization is inhibited by niobium micro-alloying leaving still deformed ferrite grains at 800 °C, elongated in the cold-rolling direction. In addition, the isolated cementite particles are disposed along deformed ferrite grain boundaries in the initial microstructure. The austenite grains formed from these particles, as discussed above, inherits their layout along the deformed ferrite grain boundaries. These observations speaks once again in favor of Teixeira et al. [Tei+21], highlighting the cooperation of both the isolated cementite particles and the still deformed ferrite grains to create a typical banded morphology.

Our experiments using niobium micro-alloying highlighted well the contribution of the isolated cementite particles and the inhibition of ferrite recrystallization to the formation of elongated microstructure, looking alike banded microstructures. However, one cannot transpose yet such conclusions to fast heating and explain the formation of the banded morphology. The elongated morphology in niobium micro-alloyed steels is strongly linked to the very different initial morphology.

On the contrary, by using the cold-rolling ratio to delay ferrite recrystallization, the initial microstructures of the studied steels contain similar proportion of pearlite islands and isolated cementite particles (III.2.2.2.1).

In the initial state the lower the cold-rolling ratio, the lower the aspect ratio of the pearlite islands, as reported in Table III.6. This trend is completely reversed at 800 °C and the higher aspect ratio for austenite islands is found in the DP600 CR30 (Table III.7), with the lower initial cold-rolling ratio. Despite thin austenite film at ferrite grain boundaries, which is a microstructural feature of the necklace morphology, the high aspect ratio of the austenite islands in the DP600 CR30 gives to the microstructure the elongated aspect expected from banded morphologies, making hybrid the morphology of the microstructure of the DP600 CR30. On the contrary, the microstructures in the DP600 CR60 and in the DP600 CR65 are very similar and

present less elongated morphologies with thin austenite film at ferrite grain boundaries, closer to the typical necklace morphology.

As discussed previously (III.2.3.2), the ferrite recrystallization is delayed in the DP600 CR30 and the matrix is only half recrystallized when austenite formation starts at 720 °C. On the contrary, the ferrite recrystallization is complete in both the DP600 CR60 and the DP600 CR65 when austenite formation starts. As the trend of the elongated shape is reversed between the initial state and at the end of the heating stage, the banded features in the DP600 CR30 at 800 °C cannot be attributed only to the initial microstructure, as in the niobium micro-alloyed steels. With these experiments, we confirm the correlation between the austenite morphology and the ferrite recrystallization.

Finally, a common microstructural trend is observed. Higher niobium or higher cold-rolling ratios leads to thinner ferrite grains both in the initial state (Figure III.2, Figure III.17 and Figure III.21) and at 800 °C (Figure III.13, Figure III.18 and Figure III.22). Though ferrite grains are found typically twice thicker at 800 °C than in the initial state, the trends observed on the thickness of ferrite grains in the initial state is conserved during the heating stage. In the present section, the initial microstructure highly determines the typical ferrite grain size at 800 °C, despite ferrite recrystallization.

#### III.2.3.4 Austenite formation kinetics driven by thermo-kinetics

As discussed previously, using lower cold-rolling ratios and niobium micro-alloying delays or inhibits ferrite recrystallization. Niobium micro-alloying also influences the proportion of pearlite islands and isolated cementite particles in the initial microstructure (Table III.4). Yet, as shown by our austenite formation kinetics obtained from our HEXRD experiments, the austenite formation starts at 720 °C regardless the niobium micro-alloying (Figure III.19 b) or the cold-rolling ratio (Figure III.25 b). While literature [HPM04; Li+13] claims that migrating boundaries during ferrite recrystallization delays austenite nucleation, our experiments using different cold-rolling ratios (Figure III.25 b) show no significant effect of recrystallization state of the ferrite matrix on the starting temperature of the austenite formation. Similarly, the proportion of pearlite islands and isolated cementite particles in the initial microstructure (Table III.4) does not impact the starting temperature of the austenite formation, as shown by our experiments using niobium micro-alloying (Figure III.19 b).

Concerning the experiments using slow or fast heating rates presented in the previous section, we already show in III.1.3.2 that a sole thermo-analysis cannot explain the delayed austenite nucleation using fast heating rate. The discussion above leads us to finally attribute this delay to the sole thermal activation affected by the heating rate.

Then, during the heating stage, the steels with different cold-rolling ratios show the same austenite formation kinetics (Figure III.25 b). During the heating stage, the ferrite recrystallization overlaps the austenite formation between 720 °C and 750 °C in the less cold-rolled steels (DP600 CR30 and DP600 CR45). Thus, our experiments show no impact of non-recrystallized ferrite on the austenite formation kinetics and deny a claim in literature [BVS22; Bel+19; Chb+14; TM18] asserting that the presence of still deformed ferrite during austenite formation enhances the austenite formation with an efficient diffusion network made of dislocations.

In addition, our previous discussion on the initial microstructure highlighted that the higher the cold-rolling ratio, the thinner the initial microstructure. The recrystallization is shown to affect the microstructure during the heating stage. In spite of these microstructural differences, the austenite formation kinetics is identical in the steels with different cold-rolling ratios. During

the heating stage, our study highlights no major effect of the size of the microstructure on the austenite formation kinetics.

During the heating stage, the niobium micro-alloyed steels show a slightly faster austenite formation kinetics between 730 °C and 750 °C than the reference DP600 CR65 (Figure III.19 b and Figure III.20 a). As discussed previously (Figure III.26), the niobium micro-alloying inhibited the ferrite recrystallization. We also highlighted that niobium micro-alloying tends to strongly refine the initial microstructure. However, we just showed that non-recrystallized ferrite does not affect austenite formation kinetics, based on our study using cold-rolling ratio. Finally, the niobium micro-alloyed steels present a higher fraction of isolated cementite particles than the reference DP600 CR65, as discussed previously. As the faster kinetics is observed under 760 °C, we can consider separately the austenite formed from pearlite or isolated cementite particles. Previous thermo-analysis [Cou+23; Mor19; Tei+21] showed different austenite formation kinetics depending on the origin of the austenite (pearlite or isolated cementite particles). In particular, the austenite formation kinetics forming from cementite particles shows similar shape as observed in the niobium micro-alloyed samples. However, the fast austenite formation in these simulations occurs around the PNTT considering the mean composition of the cementite particles. This stage is expected to occur on a larger range of temperature in real system (Figure III.15) due to a distribution of composition (Figure III.4). It is most unlikely that the distributions of cementite particles in the niobium micro-alloyed steels are narrow enough to produce the sudden global austenite fraction increase observed between 730 °C and 750 °C.

After 750 °C in the niobium micro-alloyed steels, the austenite fraction also follows the theoretical LENP fraction, as shown in Figure III.20 a). Though the studied DP600Nb30 CR65 contains twice more niobium in solid solution (0.026 wt%) than the DP600Nb15 CR65 (0.012 wt%), their austenite formation kinetics is superposed during the heating rate. Considering solute-drag effect would slow down the austenite formation kinetics, but our experiments show no such effect. In the DP600 steels, regardless the cold-rolling ratio, the austenite fraction after 760 °C follows the theoretical LENP fraction, as shown in Figure III.25 b). Despite the differences in the microstructures with the initial cold-rolling ratio, as discussed above, the austenite formation kinetics are identical in all the studied steels. Consequently, we highlight no significant influence of the microstructure morphology or the concomitance of ferrite recrystallization and austenite formation on the austenite formation kinetics. Yet, the austenite fraction estimated from our HEXRD experiments is actually few per cents ( $\approx 5\%$ ) under the theoretical LENP fraction. These observations speak in favor of austenite growth under control of carbon diffusion in austenite (LENP mode) during the heating stage, as proposed in III.1.3.1 (Figure III.14).

Finally, during the holding stage, one can first conclude that there is no effect of niobium micro-alloying, as Figure III.19 c) shows similar kinetics. However, as the nominal composition slightly differs from one steel to another, it is more relevant to look at the kinetics with the fraction at OE as reference. The gap to OE fraction, plotted in Figure III.20 b), highlights that the higher the niobium content, the faster the kinetics. At a given time, the austenite fraction is higher, making higher the final exceed of the OE fraction. Looking at the austenite formation in the DP600 steels with different cold-rolling ratios (Figure III.25 c), we show that the lower the cold-rolling ratio, the slower the austenite growth kinetics during the holding stage. As discussed in the previous section, such austenite formation kinetics with an excess compared to OE fraction is typical from austenite growth controlled by substitutional element diffusion, i.e. with Local Equilibrium with Partitioning conditions at the interface (LEP mode) and significant redistribution of substitutional elements.

At first sight, we observed contradictory effects. The study using niobium micro-alloyed

steels seems to link the absence of ferrite recrystallization and faster austenite formation kinetics during the holding stage, as using fast heating rates. On the contrary, the study using lower cold-rolling ratios seems to link the interaction between ferrite recrystallization and austenite formation to slower austenite formation kinetics during the holding stage. According to our knowledge of the literature, this is the first time that such apparent contraction is highlighted.

Beyond the apparent contradiction, our experiments and findings suggest an alternative explanation based on our microstructural observations. We discussed previously the evolution of the microstructure during the heating stage. Higher niobium content and lower cold-rolling ratio present an opposed effect. Higher niobium content (Figure III.18) leads to thinner and more elongated microstructures at 800 °C than in the reference DP600. Though lower cold-rolling ratio (Figure III.22) also leads to more elongated microstructures, the ferrite grains sizes are actually larger at 800 °C than in the reference DP600 CR65. These observations tend to confirm the impact of the typical sizes in the microstructure proposed in III.1.3.5. As discussed previously, the ferrite recrystallization mainly affects the austenite morphology at 800 °C (elongated or equiaxed) rather than their thickness. In the present section, the thickness of the ferrite grains at 800 °C is rather inherited from the initial microstructure.

In other words, the kinetics during the holding stages is controlled by the diffusion distances in the microstructures, which depends on the nucleus distribution during heating. Recrystallization itself does not affect directly the process (as often finished before the holding).

In the light of the discussion above, we finally propose to attribute the faster austenite formation kinetics during the isothermal holding at the end of fast heating to the finer microstructure observed (Figure III.13), as explained in III.1.3.5.

As a conclusion of this chapter, we propose in Figure III.27 a summary of our findings and conclusions on the main mechanisms controlling the austenite formation kinetics during the intercritical annealing in the studied steels.

### **III.2.4 Conclusion on ferrite recrystallization and austenite formation interaction induced by niobium micro-alloying and cold-rolling ratio**

The present section aimed to discuss further the interaction between ferrite recrystallization and austenite formation, as well as its influence on austenite formation kinetics. To do so, we designed careful experiments to decouple the choice of the heating rate and the concomitance of ferrite recrystallization and austenite formation. We used either niobium micro-alloying or cold-rolling ratio to induce the interaction between ferrite recrystallization and austenite formation. A single heating rate (3 °C/s) was used to prevent an impact on thermally-activated mechanisms. This process introduced new difficulties. Changing the nominal composition generates dispersions of chemistry and different initial microstructures. Changing the reduction rate does not completely prevent recrystallization. However, we completed our investigation of the interaction between ferrite recrystallization and phase transformation thanks to the detailed analysis of these experiments.

As in the first section, we performed optical microscopy, SEM and TEM to investigate the evolution of the microstructures of the studied steels after interrupted treatments.

Thanks to our time-resolved ferrite recrystallization kinetics obtained with our new IDST method, we showed that niobium micro-alloying inhibits ferrite recrystallization, while lower cold-rolling ratios delay ferrite recrystallization so that it overlapped the beginning of austenite formation. These new experiments finally answered several questions. Here are our main conclusions:

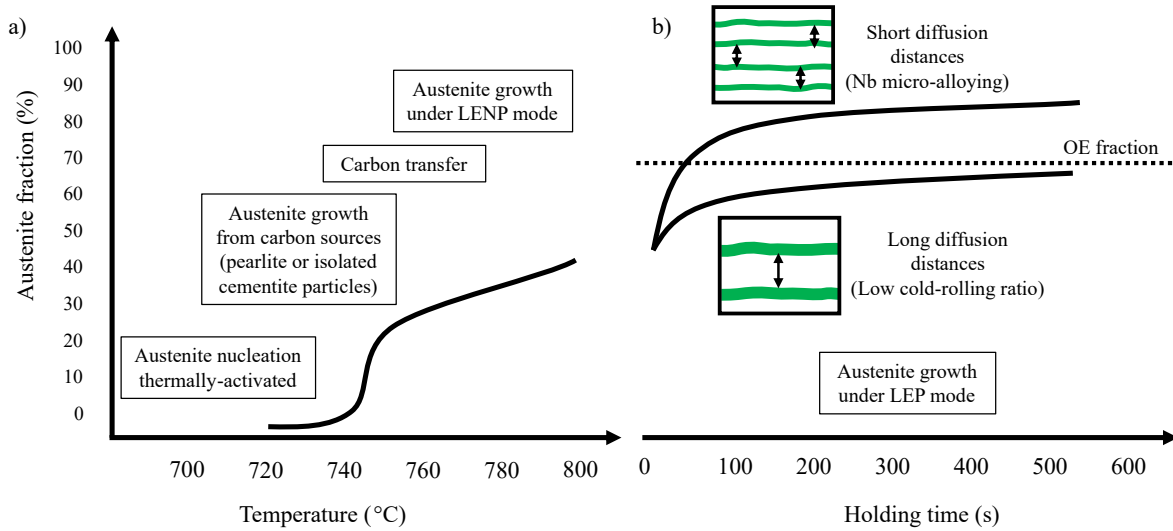


Figure III.27: Mechanisms driving the austenite formation kinetics during the intercritical annealing. (a) During the heating stage, the austenite formation kinetics is mainly driven by thermodynamics. (b) During the isothermal holding stage, the austenite formation kinetics is also driven by thermodynamics but is sensitive in first order by the diffusion distances in the microstructure. These distances depend on the previous heating stage, the nominal composition and the cold-rolling ratio.

- The interaction between ferrite recrystallization and austenite formation strongly affects the microstructure and the austenite morphology. In the niobium micro-alloyed steels, a cooperation between the isolated cementite particles and the inhibition of ferrite recrystallization led to an elongated microstructure at the end of the heating stage, looking alike banded microstructures, supporting the work of Teixeira et al. ([Tei+21]. In the low cold-rolled steels, the microstructure at the end of the heating stage presented elongated shapes expected from typical banded morphologies. This confirmed that the later the ferrite recrystallization, the more banded the austenite morphology at the end of the heating stage. Yet, in the present work, the initial microstructure highly determined the typical ferrite grain size at 800°C, despite ferrite recrystallization.
- The starting temperature of austenite formation is found to be insensitive to the current recrystallization state of the ferrite matrix or to the proportion of pearlite islands and isolated cementite particles in the initial microstructure. We attribute the delayed austenite nucleation using fast heating rate to thermal activation affected by the heating rate.
- The austenite growth kinetics at the beginning of the heating stage is affected by the nature of the carbon sources (pearlite islands or isolated cementite particles). Further investigation on the initial microstructures would be interesting, especially on the enrichment of the isolated cementite particles in the niobium micro-alloyed steels.
- This work confirms that the austenite formation kinetics is led by LEP interface conditions, i.e. by carbon diffusion, during the heating stage, after carbon homogenization in

austenite. The presence of non-recrystallized ferrite, the niobium in solid solution or the size of the microstructure had no significant effect on the austenite formation kinetics.

- During the holding stage, all the obtained austenite formation kinetics showed feature speaking in favor of austenite growth under LEP mode, i.e. with substitutional element redistribution. The niobium micro-alloyed steels, in which ferrite recrystallization is inhibited, the austenite formation kinetics is faster than in the reference DP600 CR65. On the contrary, the low cold-rolled steels, in which ferrite recrystallization is delayed, the austenite formation kinetics is slower than in the reference DP600 CR65. This surprising trend is explained through the size of the microstructure at the end of the heating stage. A finer microstructure offers short diffusion path for substitutional elements, which accelerates the austenite formation under LEP mode during the isothermal holding stage [BVS22; Bel+19; Chb+14; MGF11; Oll+17; TM18]. We finally attribute the faster austenite formation kinetics during the isothermal holding to the finer microstructure observed at the end of fast heating.

### III.3 Conclusions on the interaction between ferrite recrystallization and austenite formation

This chapter investigated the interaction between ferrite recrystallization and austenite formation during the annealing of cold-rolled ferrite-pearlite microstructure for DP steel production.

To do so, we reproduced experiments to study the influence of the heating rate on the studied DP600 CR65 steel during the intercritical annealing. However, in such experiments, the overlap between ferrite recrystallization and austenite formation is led by the heating rate. We revealed a strong interaction between purely thermally activated mechanisms and ferrite recrystallization, blurring their respective impacts, when studying the effect of the heating rate. Then, we used either niobium micro-alloying or cold-rolling ratio to induce the interaction between ferrite recrystallization and austenite formation. Niobium micro-alloying inhibited ferrite recrystallization, while lower cold-rolling ratios delayed ferrite recrystallization so that it overlapped the beginning of austenite formation. A single heating rate (3 °C/s) was used to prevent the impact of a difference in activation of thermally-activated mechanisms.

We performed optical, SEM and TEM micrographs to investigate the microstructure at different scales. The chemical composition of cementite particles was measured by EDXS. The carbon content across the austenite was measured by WDS. Ferrite recrystallization and austenite formation was followed using in situ HEXRD experiments. Time-resolved kinetics were produced using our IDST method, developed during this PhD work, and Rietveld refinement.

The following conclusions are drawn from this experimental work:

- In the studied steels, austenite grows from pearlite islands or isolated cementite particles. Austenite nucleation is found insensitive to the recrystallization state of the ferrite matrix or to the proportion of pearlite islands and isolated cementite particles in the initial microstructure. The delayed austenite nucleation using fast heating rate is attributed to thermal activation affected by the heating rate.
- During slow heating (3 °C/s), austenite growth from these carbon source can be studied separately under 760°C, as proposed by Moreno et al [Mor19; Tei+21]. The austenite growth kinetics is affected by the nature of the carbon sources (pearlite islands or isolated

cementite particles). Both manganese and chromium enrichment of isolated cementite particles was observed during slow heating (3 °C/s). Such enrichment leads to higher PNTT, delaying their fast dissolution stage.

- This work revealed a carbon transfer between austenite grains of both origins after 760°C, making the investigation of austenite growth as a single thermodynamic system more relevant. After carbon homogenization in austenite, the austenite formation kinetics is fully driven by LEP interface conditions, i.e. by carbon diffusion, during the heating stage. The presence of non-recrystallized ferrite, the niobium in solid solution or the thinness of the microstructure had no significant effect on the austenite formation kinetics.
- The interaction between ferrite recrystallization and austenite formation is shown to strongly affect the microstructure and the austenite morphology. The present study supports the work of Teixeira et al. [Tei+21], as shows a cooperation between the isolated cementite particles and the incomplete ferrite recrystallization to produce banded-like microstructures at the end of the heating stage.
- The obtained austenite formation kinetics during the holding stage presents features of austenite growth under LEP mode. This work highlights a major effect the thinness of the microstructure at the end of the heating stage on the austenite formation kinetics during the isothermal holding stage. Shorter diffusion paths for substitutional elements enhance the austenite growth. The faster austenite formation kinetics during the isothermal holding is attributed to the finer microstructure observed at the end of fast heating. This last conclusion is further discussed in the next Chapter IV after a complete numerical thermo-analysis of the austenite formation during the isothermal holding.



---

## Chapter IV

# Thermo-kinetics investigation of austenite formation during intercritical annealing

---

Work it harder, make it better  
Do it faster, makes us stronger  
More than ever, hour after hour  
Work is never over

---

*Harder Better Faster Stronger*  
*Daft Punk*

IV.1 Thermo-kinetic analysis of austenite growth in the quinary Fe-0.1C-1.9Mn-0.2Si-0.2Cr system . . . . .	136
IV.1.1 Simulation strategy and parameters . . . . .	137
IV.1.2 Results . . . . .	139
IV.1.3 Discussions . . . . .	142
IV.1.4 Conclusion on austenite growth . . . . .	144
IV.2 Predictive physically-based model of austenite formation during the holding stage	145
IV.2.1 Hypotheses and notations . . . . .	146
IV.2.2 The equations of the model . . . . .	148
IV.2.3 Validation of the model . . . . .	150
IV.2.4 Effect of the heating rate on the austenite formation kinetics during the isothermal holding stage . . . . .	153
IV.2.5 Conclusions on the austenite formation during the isothermal holding . .	156
IV.3 Conclusions on the thermo-kinetics investigation of austenite formation during intercritical annealing . . . . .	156

One of the objectives of this PhD work required by the industrial partner is to propose a model for the austenite formation kinetics during the intercritical annealing of DP grade steels. The model should be very efficient in term of computation time, as it is expected to drive an industrial production line. The model should be sensitive to the annealing parameters (heating rate and annealing temperature), as well as the chemical composition of the steel. In addition, the model should account for ternary systems at least. Considering up to quinary systems (Fe-C-Mn-Si-Cr) is expected, as the literature review of Chapter I showed its importance for transformation kinetics.

The literature review on the thermo-kinetic analysis of the austenite transformation and the modeling solutions presented and discussed in Chapter I already guide the choice of the final modeling approach and of the modeled mechanisms. The experimental work detailed in Chapter III answered some questions raised by the literature review. In particular, our investigation highlighted no significant effect of the concomitance of the ferrite recrystallization and the austenite formation on the austenite formation kinetics. A carbon transfer between austenite islands between 760 °C and 780 °C was revealed during slow heating (3 °C/s). The austenite growth from the main carbon sources (pearlite bands and isolated cementite particles) can be studied separately under 760 °C, as proposed by Moreno et al [Mor19; Tei+21]. Above this temperature, the identified carbon transfer makes the investigation of austenite growth as a single thermodynamic system more relevant. Our experiments in Chapter III and our numerical work in [Cou+23] support an austenite formation kinetics driven by Local Equilibrium with Negligible Partitioning (LENP) interface conditions, i.e. by carbon diffusion, during the heating stage.

Before attempting to model the austenite formation kinetics, the effect of minor alloying elements (chromium and silicon in the present work) on the austenite growth kinetics is still to be investigated. This final Chapter completes in the first section the thermo-kinetic analysis of the austenite formation during intercritical annealing using DICTRA simulations and considering the full quinary nominal composition of the studied DP600.

Based on our conclusions from Chapter III and the first section of the present chapter, the second section presents our Generalized Wycliffe Model (GWM), which predicts the austenite formation kinetics and the composition profiles in multi-component systems during the isothermal holding.

In Chapter III, we proposed to explain the effect of the heating rate on the austenite formation kinetics during the isothermal holding by considering the thickness of the microstructure at the end of the heating stage. The GWM is finally used to further discuss this hypothesis.

## IV.1 Thermo-kinetic analysis of austenite growth in the quinary Fe-0.1C-1.9Mn-0.2Si-0.2Cr system

The following section aims to complete the thermo-kinetic analysis of the austenite formation in the studied DP600 during intercritical annealing, started in previous studies and already further discussed in Chapter III. This numerical work considers the full quinary nominal composition of the studied DP600 (Fe-0.1C-1.9Mn-0.2Si-0.2Cr), to investigate the influence of the minor alloying elements on the kinetics.

In Chapter III, our experiments revealed a carbon transfer between the austenite from the pearlite bands and the austenite from the isolated cementite particles between 760 °C and 780 °C. In addition, the austenite fraction after this carbon transfer was shown close to the LENP

fraction. After this carbon transfer, the origin of the austenite is no longer relevant for the study of its growth (chemical memory lost but a microstructural memory remains). In the literature review, Subsection I.2.3 details the thermo-kinetics aspects of austenite growth in Fe-C-Mn ternary systems. The same typical thermo-kinetic features, exposed in Chapter I, were highlighted in the simplified ternary Fe-0.1C-1.9Mn, in our previous numerical work published in [Cou+23]. In the following, we consider the same assumptions to initialize the simulation but the full quinary Fe-0.1C-1.9Mn-0.2Si-0.2Cr ( wt%) is investigated. Contrary to the approach proposed by Moreno et al [Mor19; Tei+21], we consider that pearlite is the only carbon source of carbon in the steel. The isolated cementite particles are not considered. As the origin of the austenite is not relevant after 760 °C, this simplification is in agreement with our conclusions from Chapter III. Thanks to this choice, we can easily compare the results to the previous one and highlight the sole effect of the minor substitutional elements (silicon and chromium). The Ortho-Equilibrium (OE), described in detail in Chapter I, is the thermodynamic state to reach in the long term. The austenite fraction computed with Thermo-Calc at OE of the studied DP600 (Fe-0.1C-1.9Mn-0.2Si-0.2Cr) using the simplified ternary Fe-0.1C-1.9Mn, the quaternary Fe-0.1C-1.9Mn-0.2Si, the quaternary Fe-0.1C-1.9Mn-0.2Cr and the full quinary Fe-0.1C-1.9Mn-0.2Si-0.2Cr are reported in Table IV.1.

System	Fe-0.1C-1.9Mn	+0.2Si	+0.2Cr	+0.2Si-0.2Cr
Austenite fraction at OE (vol.%)	87.5	78.1	91.2	80.9

Table IV.1: Austenite fraction at OE at 800 °C of the studied DP600 (Fe-0.1C-1.9Mn-0.2Si-0.2Cr) using the simplified ternary Fe-0.1C-1.9Mn, the quaternary Fe-0.1C-1.9Mn-0.2Si, the quaternary Fe-0.1C-1.9Mn-0.2Cr and the full quinary Fe-0.1C-1.9Mn-0.2Si-0.2Cr

The addition of chromium increases (+ 3.7 %) the austenite fraction at OE, whereas it is strongly lowers by the addition of silicon (− 9.4 %). Though chromium is generally a  $\alpha$ -stabilizer, it tends here to stabilize austenite. As expected, silicon acts as a  $\alpha$ -stabilizer. Combining both behaviors, the austenite fraction at OE in the quinary Fe-0.1C-1.9Mn-0.2Si-0.2Cr is lower (− 6.6 %), but slightly higher than the quaternary Fe-0.1C-1.9Mn-0.2Si.

As  $\gamma$ -stabilizers, manganese and chromium are expected to redistribute in austenite, while silicon, as  $\alpha$ -stabilizer is expected to redistribute in ferrite. Our previous numerical study [Cou+23] and the literature review (I.2.3) already showed that, in the ternary Fe-0.1C-1.9Mn, austenite grows under LENP mode (without manganese partition) during the heating stage and under LEP mode (with manganese partition) during the isothermal holding stage.

The objective is now to know if the minor substitutional elements redistribute during austenite growth and how it affects the growth kinetics. The conclusion from this study will help in the design of our approach to predict the austenite formation kinetics in the following sections.

#### IV.1.1 Simulation strategy and parameters

The simulations were performed using the DICTRA module of the Thermo-Calc software [And+02], presented in details in Chapter II, with the TCFE9 and MOBFE2 databases. The simulations are based on a local field model considering sharp interface and Local Equilibrium (LE) interface conditions. Austenite growth is investigated in our DP600 steel during intercritical annealing at 800 °C, using our reference low heating rate 3 °C/s. As detailed in [Cou+23], the austenite

carbon content is initialized at pearlite carbon content. A prior study on the studied DP600 shows that pearlite formed around 570 °C [Mor19]. Using the Hultgren's extrapolation of  $A_{cm}$  [Hul20], the carbon content of pearlite is estimated at 1.78 at% (0.39 wt%). Ferrite carbon composition in bulk is evaluated with Thermo-Calc, considering the continuity of carbon activity at the interface.

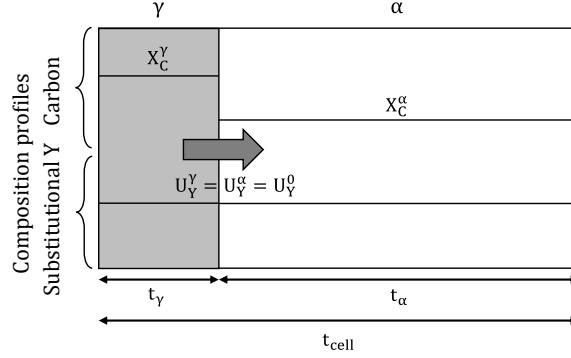


Figure IV.1: Simulation cell for austenite ( $\gamma$ ) planar growth in ferrite ( $\alpha$ ) during annealing at 800 °C for 10 min using a low heating rate (3 °C/s).

Moreno's study [Mor19; Tei+21] shows that initializing the simulation cells with a continuity of manganese u-fraction help the simulations to start and promotes numerical convergence. The manganese, chromium and silicon u-fractions are supposed to be equal and uniform throughout the system and set to the nominal composition, i.e.  $U_Y^\gamma = U_Y^\alpha = U_Y^0$  for each substitutional element Y. Carbon, manganese, chromium and silicon, are considered as homogenized in the austenite in the initial state of our simulations. These assumptions on the initial composition actually initialize the operative tie-line to the LENP one, in agreement with the conclusions from Chapter III. To design the simulation cell, DICTRA offers several options for the geometry (planar, cylindrical and spherical). In their study, Moreno et al [Mor19; Tei+21] used a spherical geometry, considering a sphere of austenite in a shell of ferrite. But, considering the aspect ratio of the pearlite bands, the main carbon sources, the planar geometry seemed more relevant. One could consider an "inverted percolation" geometry, with a shell of austenite around a sphere of ferrite, as the austenite presents a "necklace" morphology using slow heating, as shown in the literature review and in Chapter III. Yet, as we consider up to a quinary system, the simulations were easier to stabilize numerically and faster to run considering a planar geometry. The simulation cell is schematized in Figure IV.1. The growth of austenite ( $\gamma$ ) in the ferrite matrix ( $\alpha$ ) is simulated considering a planar geometry.

The simulation cell size is set to  $t_{cell} = 6 \mu m$ , the half-distance between two pearlite bands in the DP600 CR60 studied in [Mor19; Tei+21]. A carbon balance gives the initial austenite and ferrite volume fractions, as well as the thickness of the austenite,  $t_\gamma$ , and ferrite,  $t_\alpha$ , layers. Key sizes and compositions used in the simulations are reported in Table IV.2.

Meshing nodes are distributed on a unidimensional grid according to a geometrical progression to ensure a finer mesh at the moving interface. Both time and spatial discretization were set to ensure the numerical convergence. Initializing the simulation cells with a continuity of manganese u-fraction or the LE tie-line at interfaces, computed with Thermo-Calc, was found to help the simulations to start and promotes numerical convergence [Mor19; Tei+21].

Simulations in the quaternary systems Fe-0.1C-1.9Mn-0.2Si and Fe-0.1C-1.9Mn-0.2Cr were

System	$X_C^\gamma$	$X_C^\alpha$	$U_{Mn}$	$U_{Si}$	$U_{Cr}$	$t_\gamma$ ( $\mu\text{m}$ )
Fe-0.1C-1.9Mn (from [Cou+23])	1.78	0.0442	1.94			1.42
Fe-0.1C-1.9Mn-0.2Si-0.2Cr (present study)	1.78	0.0485	1.94	0.40	0.20	1.41

Table IV.2: Simulation parameters for each system (compositions in (at%))

also studied as intermediate scenarios, but are not presented in the present manuscript. The "homogenization model" from the DICTRA module was used for the simulation considering the quinary system to ensure its numerical stability. The "homogenization model" uses an implicit finite volume method to increase numerical stability, but generally run slower than the "classical model" (used by default).

### IV.1.2 Results

The austenite fractions computed with DICTRA in the quinary Fe-0.1C-1.9Mn-0.2Si-0.2Cr (in red) are plotted in Figure IV.2 during the heating stage at 3 °C/s (a) and the isothermal holding at 800 °C (b). The austenite fractions computed with DICTRA in the ternary Fe-0.1C-1.9Mn from our previous study [Cou+23] are plotted in black. The expected theoretical LERP and OE fractions are plotted as references. The first one, plotted with dashed lines, is the austenite fraction computed considering LERP interface conditions and no carbon or substitutional element gradient in austenite nor in ferrite. The second one, plotted with dotted lines, is the austenite fraction at OE.

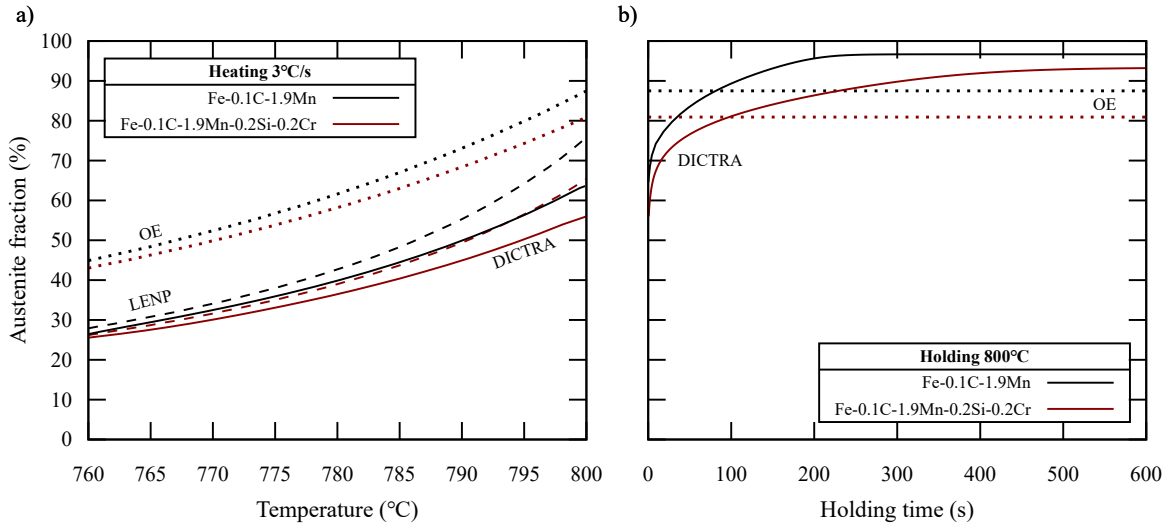


Figure IV.2: Austenite fractions during the slow (3 °C/s) heating stage (a) and the isothermal holding at 800 °C (b) in the ternary Fe-0.1C-1.9Mn (black) and the quinary Fe-0.1C-1.9Mn-0.2Si-0.2Cr (red).

At 760 °C, the simulation cell contains 24 % of austenite. During the heating stage, the

austenite fraction increases with temperature, up to 64 % in the ternary and 56 % in the quinary. The simulated fraction is close to the expected LENP fraction but systematically lower (3 % in average). The gap between simulated fractions and LENP fractions widens as temperature increases, up to 13 % in the ternary and 9 % in the quinary. In the studied temperature range (between 760 °C and 800 °C), the austenite fraction (simulated, expected LENP and OE) in the quinary Fe-0.1C-1.9Mn-0.2Si-0.2Cr is systematically lower than in the ternary Fe-0.1C-1.9Mn (down to 8 % lower at 800 °C).

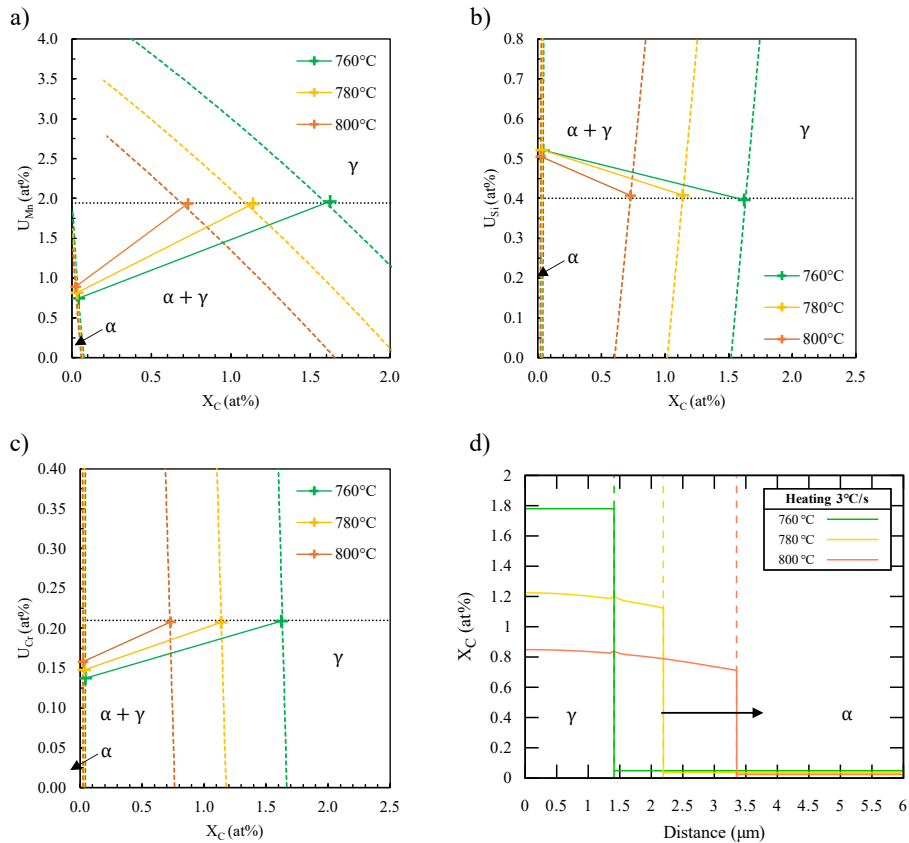


Figure IV.3: Operative tie-lines in pseudo-ternary phase diagram Fe-C-Mn (a), Fe-C-Si (b) and Fe-C-Cr (c) and carbon profiles (d) during the heating stage at 760 °C (green), 780 °C (yellow) and 800 °C (orange) computed in the quinary Fe-0.1C-1.9Mn-0.2Si-0.2Cr. In (a, b and c), the phase diagram boundaries are plotted with dashed lines. The nominal substitutional composition is indicated by a black dotted line. In (d), the position of the interface is indicated by dashed lines.

During the isothermal holding at 800 °C, the austenite fraction keeps increasing in both ternary and quinary systems. In the ternary system, the austenite fraction finally reaches 97 % after 210 s and, then, remains stable. The final fraction overshoots the OE of the simplified ternary (88 %) by 9 %. In the quinary system, the austenite fraction reaches 93 % after 600 s at 800 °C, overshooting the OE fraction (81 %) by 12 %.

2D slices of the quinary phase diagram are plotted in Figure IV.3. The phase diagram is computed with Thermo-Calc. The chosen slices are pseudo-ternary phase diagrams plotted by setting the contents in two of the three substitutional elements to the interface compositions

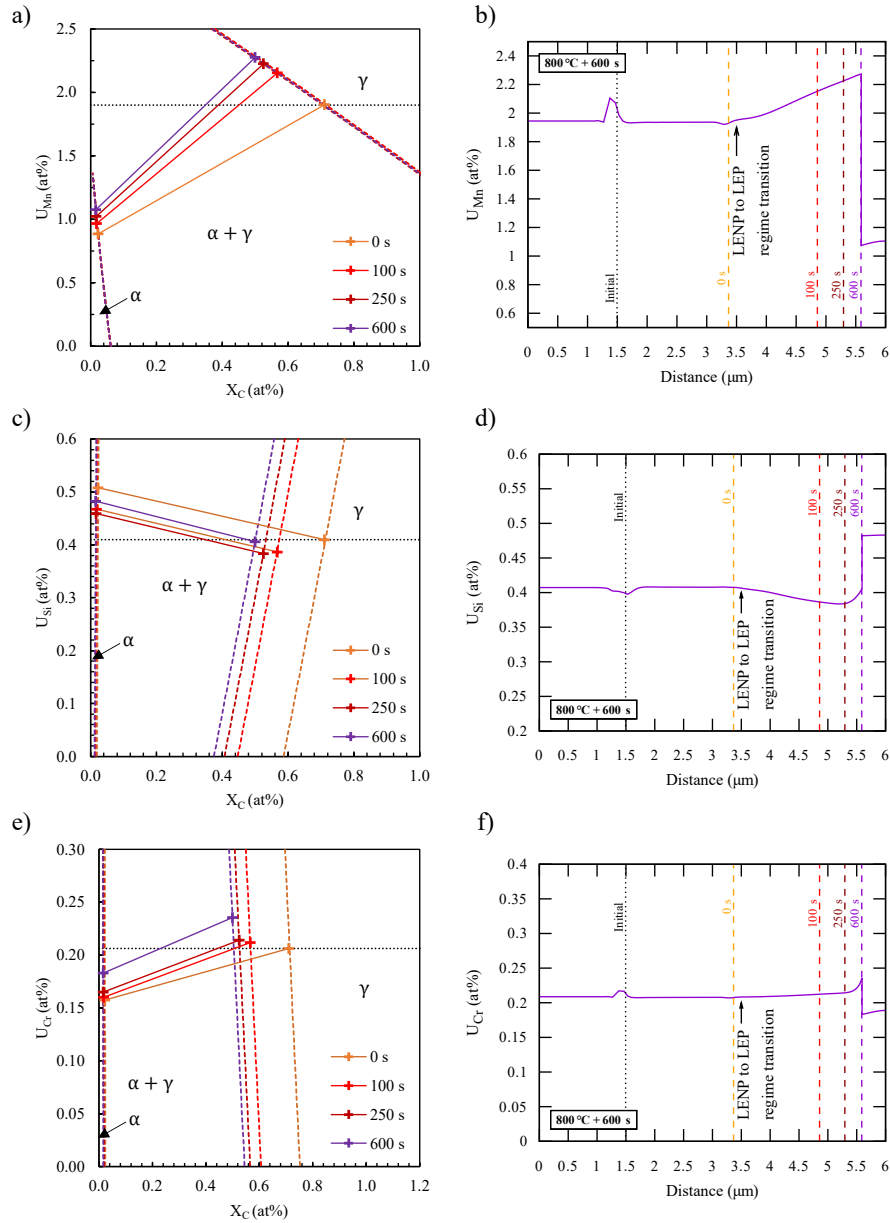


Figure IV.4: Operative tie-lines in pseudo-ternary phase diagram Fe-C-Mn (a), Fe-C-Si (b) and Fe-C-Cr (c) and carbon profiles (d) during the heating stage at 760 °C/sC (green), 780 °C (yellow) and 800 °C (orange) computed in the quinary Fe-0.1C-1.9Mn-0.2Si-0.2Cr. In (a, b and c), the phase diagram boundaries are plotted with dashed lines. The nominal substitutional composition is indicated by a black dotted line. In (d), the position of the interface is indicated by dashed lines.

(results from the simulation). Figure IV.3 (a), (b) and (c) show the pseudo-ternary Fe-C-Mn, Fe-C-Si and Fe-C-Cr respectively. Operative tie-lines (a, b and c) and carbon profiles (d) are plotted at 760 °C (green), 780 °C (yellow) and 800 °C (orange). The plotted operative tie-lines show that substitutional composition in austenite at interface follows the nominal and bulk

ferrite composition (in dotted black line). Figure IV.3 (d) shows a slight carbon gradient in austenite at all the studied temperatures.

Figure IV.4 (a, c, e) show the phase diagrams of pseudo-ternary Fe-C-Mn, Fe-C-Si and Fe-C-Cr. The operative tie-lines are plotted after 0 s (orange), 100 s (red), 250 s (dark red) and 600 s (violet) at 800 °C in the quinary system. Figure IV.4 (b, d, f) show the manganese, silicon and chromium profiles after 600 s (violet). The position of the interface is indicated with dashed lines after 0 s (orange), 100 s (red), 250 s (dark red) and 600 s (violet) at 800 °C.

Figure IV.4 (a, c and e) shows that, the austenite interface compositions in substitutional elements correspond to the nominal and bulk ferrite composition (in black dotted line) at the beginning of the holding stage.

During the holding stage, the austenite interface composition in manganese increases (Figure IV.4 (a)). The manganese u-fraction remains stable from the center of the simulation cell to 3.5  $\mu\text{m}$  (indicated by an arrow). A manganese gradient, from 1.94 at% up to 2.27 at%, is observed from this latter position to the interface position after 600 s at 800 °C (indicated by a violet dashed line). The manganese composition in ferrite is not completely homogeneous. A slight gradient remains in ferrite.

About silicon, Figure IV.4 (c) shows that the austenite interface composition decreases until 250 s holding, before increasing up to the end of the holding stage (600 s). Figure IV.4 (d) shows the silicon composition profile after 600 s holding. The silicon composition is homogeneous in austenite from the center of the simulation cell to 3.5  $\mu\text{m}$  (indicated by an arrow). A depletion of silicon is observed in austenite from this latter position to the interface position after 600 s holding (indicated by a violet dashed line). First, the silicon composition decreases from 0.40 at% to 0.38 at% at 5.26  $\mu\text{m}$ , before increasing up to 0.40 at%. Contrary to manganese, silicon is homogenous in ferrite at the interface composition (0.48 at%). Concerning chromium, Figure IV.4 (e) shows that the austenite interface composition increases slowly at first and faster after 250 s holding. The chromium composition across the simulation cell is plotted after 600 s holding in Figure IV.4 (f). It is stable in austenite from the center of the simulation cell to 3.5  $\mu\text{m}$  (indicated by an arrow). It increases very slowly, from 0.20 at% up to 0.21 at% at 5.26  $\mu\text{m}$ . Then, a sharp increase up to 0.23 at% is observed. In ferrite, a slight gradient remains. The variations of silicon and chromium compositions across the simulation cell lay in a tight range. In particular, experimental measurements would not be precise enough to show such variations.

### IV.1.3 Discussions

The first astonishing result of this numerical study is that considering the minor substitutional elements significantly slows down the austenite formation kinetics (Figure IV.2).

The pseudo-ternary phase diagrams in the quinary Fe-0.1C-1.9Mn-0.2Si-0.2Cr (Figure IV.3) highlight a similar behavior, as observed in the simplified ternary Fe-0.1C-1.9Mn in [Cou+23]. Austenite inherits its substitutional element (manganese, silicon and chromium) compositions from bulk ferrite. The three studied substitutional elements undergo negligible redistribution. As highlighted in the ternary in [Cou+23], the heating rate is too high for carbon to be homogeneously spread in austenite. This carbon gradient in austenite leads to the average 3 % gap observed between expected under theoretical LEMP conditions (LEMP interface conditions and no composition gradient) and the simulated austenite fraction seen in Figure IV.2. This result confirms that the average 5 % gap between the theoretical LEMP fractions and the austenite fractions measured by our HEXRD experiments presented in Chapter III (Figure III.12 in III.1.2.5) can be explained by a slight carbon gradient in austenite.

Despite the gap due to carbon diffusion, the austenite fractions during the heating stage (after the carbon transfer) are very close to the theoretical LENP fraction and can be easily predicted using equilibrium computations tabulated with the temperature.

Concerning the isothermal holding stage, the present study draws similar conclusions as the previous study in the simplified ternary system [Cou+23]. The operative tie-lines in Figure IV.4 a, c and e show that, austenite interface compositions in manganese and chromium increases. Up to 250 s holding, austenite interface composition in silicon decreases. These observations reveal redistribution of all the substitutional elements up to the end of the isothermal holding stage. As found in the ternary system, austenite grows under LEP mode during the isothermal holding stage. Manganese and chromium redistribute in austenite and silicon in ferrite, as expected by our preliminary analysis (Table IV.1).

Manganese, silicon and chromium diffusion coefficients are three orders of magnitude lower in austenite than in ferrite. As in the ternary system, the evolution of the austenite interface composition builds the gradients observed in austenite at the end of the isothermal holdings (Figure IV.4 b, d and f). In the studied range of time, substitutional elements do not have enough time to diffuse and to homogenize in austenite, leading to the fraction overshoot, as in ternary systems [HPM04; Kam+15; Lai+16; Mor19; Oll+17; Wei+13]. Literature reports around  $10^5$  s for final equilibration by manganese diffusion in austenite in ternary systems [Kam+15; Lai+16; Oll+17; Wei+13]. In addition, the substitutional profiles in austenite show the history of the interface compositions in austenite, i.e. the history of the operative tie-lines.

Contrary to the ternary system, at the end of the holding stage, there is still a manganese gradient in ferrite (Figure IV.4 b). Chromium also still shows a gradient in ferrite at the end of the holding stage (Figure IV.4 f). Concerning silicon, the interface composition in austenite first decreases before increasing again after 250 s holding (Figure IV.4 c). Before 250 s, silicon redistributes in ferrite and accumulates close to the interface. A silicon gradient is built in ferrite. After 250 s, the silicon profile in ferrite is flat and at the interface composition, as shown after 600 s in Figure IV.4 d. Ferrite is saturated in silicon. The interface continues to move, driven by manganese and chromium diffusion in ferrite and partitioning in austenite (LEP mode). The decreasing ferrite fraction makes the silicon content increase, both in bulk and at the interface.

Finally, Figure IV.5 compares the austenite fractions during the heating stage at  $3\text{ }^\circ\text{C/s}$  (a) and the isothermal holding stage at  $800\text{ }^\circ\text{C}$  (b) predicted in this work, using the quinary system Fe-0.1C-1.9Mn-0.2Si-0.2Cr (red solid line), with the fraction predicted in the previous numerical work from Moreno et al. [Mor19; Tei+21] (blue solid line), using the simplified ternary Fe-0.1C-1.9Mn and separated subsystems, and the experimental data (in blue diamonds), from the HEXRD experiments from Chapter III (Figure III.12). As already discussed in the literature review, the austenite formation kinetics obtained in [Mor19; Tei+21] using their approach in separated subsystems is far too fast compared to the experimental kinetics.

During the heating stage (Figure IV.5 a), our simulation using a single quinary system above  $780\text{ }^\circ\text{C}$  produces a more realistic kinetics, meaning fractions closer to the experimental data. This result speaks in favor of the austenite growth under LENP mode. It tends to confirm that considering separated subsystems (in red solid line) above  $780\text{ }^\circ\text{C}$  is less accurate than considering the full system.

As the simulated austenite fraction (in red solid line in Figure IV.5 a) stays very close to the theoretical LENP fraction (in red dashed line in Figure IV.5 a), one could easily predict the austenite fraction during the heating stage by a simple balance based only on thermodynamics, in very short time whatever the complexity of the system. Modeling the austenite growth under LENP would produce a kinetics closer to the experiments. In addition, by starting the simulation

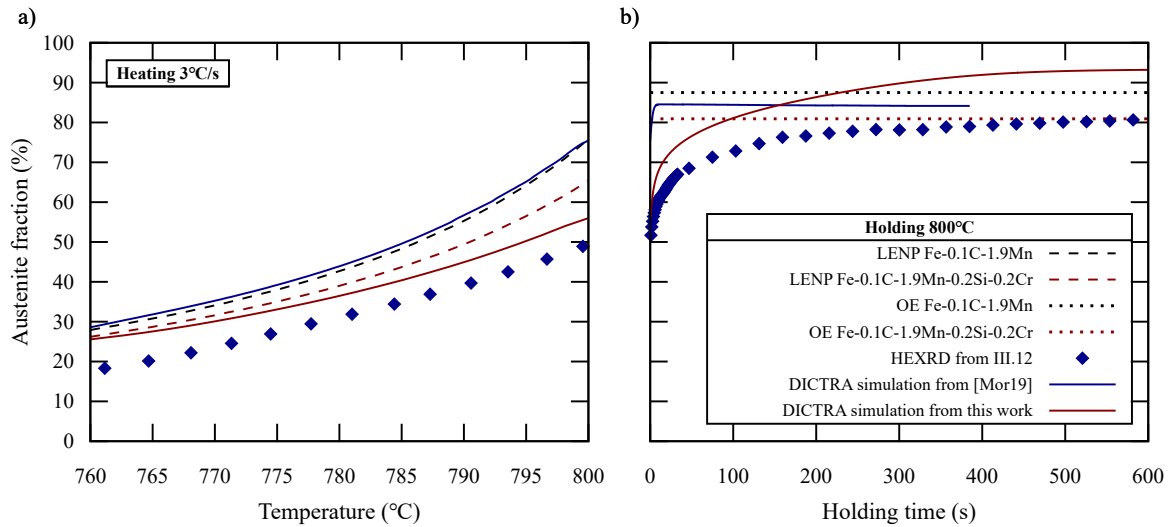


Figure IV.5: Austenite fractions during the heating stage at 3 °C/s (a) and the isothermal holding at 800 °C (b). The austenite fractions predicted in this work, using the quinary system Fe-0.1C-1.9Mn-0.2Si-0.2Cr (in red solid line), is compared with the fraction predicted in the previous numerical work from Moreno et al. [Mor19; Tei+21] (in blue solid line), using the simplified ternary Fe-0.1C-1.9Mn, and the experimental data (in blue diamonds), from the HEXRD experiments from Chapter III (Figure III.12). The LENP and OE fractions of the simplified ternary (in black) and the quinary system Fe-0.1C-1.9Mn-0.2Si-0.2Cr (in red) are indicated by dashed and dotted lines respectively.

at the fraction given by our current approach at 780 °C would avoid the present discontinuity. Wycliffe et al. [WPE81] proposed such a model, presented in Chapter I. As it will be shown in next section, this model can even be adapted to quinary systems and would still require few computation resources.

During the holding stage (Figure IV.5 b), our simulation produces a much slower kinetics and, once again, closer to the experimental fractions. Yet, the final austenite fraction is predicted with more accuracy in [Mor19; Tei+21] than in the present work. We attribute this gap to experimental data to the nominal composition and the cell size used for the present simulation. We used the targeted nominal composition but our studied DP600 is shown to contain less carbon (Table III.1). Then, the cell size is set at 6  $\mu\text{m}$  to compare with previous work [Cou+23], but the next section will highlight the importance of the cell size, representing typical distances between austenite islands in the microstructure, on the austenite formation kinetics (IV.2.4).

#### IV.1.4 Conclusion on austenite growth

This section reports the investigations on the thermo-kinetics of austenite growth in the quinary Fe-0.1C-1.9Mn-0.2Si-0.2Cr. Comparing with the thermo-analysis of the simplified ternary Fe-0.1C-1.9Mn highlights the effect of the minor substitutional elements, silicon and chromium here.

Considering the minor substitutional elements strongly slows down the austenite formation kinetics. The substitutional elements, even minor ones, affect the Local Equilibrium composi-

tions and the redistribution regimes.

During the heating stage, the austenite growth occurs under LENP mode. No substitutional element redistributes and austenite growth is controlled by carbon diffusion in austenite. A gap between the theoretical LENP fraction (LENP interface conditions and no composition gradient) is observed as the heating rate is too high for carbon to homogenize in austenite. This remaining gradient can explain the gap between the experimental data and the theoretical LENP fraction observed during our experimental work, presented in Chapter III (III.1.2.5).

Based on these conclusions, the following section proposes a model for austenite growth during the isothermal holding stage. We used the PNTT distribution presented in III.1.3.2 to predict the austenite fraction formed from cementite particles below 780 °C. Full details are provided in appendix C.

## IV.2 Predictive physically-based model of austenite formation during the holding stage

This section proposes a model for austenite growth during the isothermal holding stage. For industrial application, the model is expected to properly model 100 s of intercritical annealing and to be robust to the annealing temperature, as well as to the chemical composition of the steel. Chapter III and the previous section investigated the mechanisms of austenite formation in a DP600 steel through experiments and DICTRA simulations. Here are our main conclusions:

- Austenite grows under LENP mode up to the end of the heating stage. The austenite fraction at 800 °C is expected to be close to the theoretical LENP fraction.
- The minor alloying elements, chromium and silicon, significantly impact the austenite growth kinetics.
- At the studied annealing temperatures, austenite grows with redistribution of all the substitutional elements (LEP mode).
- The annealing times used in this work are too short to observe significant diffusion of substitutional elements in austenite.

The objectives of the model are to predict the transformation kinetics during this holding stage and the redistribution of substitutional elements (LEP mode) in a quinary system with high numerical stability.

In the present section, we present our model for austenite growth, inspired from the work of Wycliffe [WPE81] in the ternary Fe-C-Mn presented in Chapter I (I.4.2.1). Here, the Wycliffe's model is generalized to multi-constituent systems. In the following, the model is detailed considering the quinary system Fe-0.1C-1.9Mn-0.2Si-0.2Cr, corresponding to the studied DP600.

First, the hypothesis and notations of the model are presented, before detailing the equations of the model. Then, simulations are run and results are compared to DICTRA simulations to validate the model and test its reliability regarding the annealing temperature and the nominal composition of the studied steel.

Finally, our experimental work in Chapter III highlighted a major effect the thickness of the microstructure (spacing of austenite islands) at the end of the heating stage on the austenite formation kinetics during the isothermal holding stage. Shorter diffusion paths for substitutional

elements enhance the austenite growth. We proposed to attribute the faster austenite formation kinetics during the isothermal holding using faster heating rate to the finer microstructure observed at the end of fast heating. This conclusion is further discussed in the last sub-section using our model.

### IV.2.1 Hypotheses and notations

The austenite growth in ferrite during the isothermal holding stage is modeled, inspired from the work of Wycliffe [WPE81], presented in Chapter I (I.4.2.1). The approach is very close to DICTRA simulations, as it consists of a 1D sharp-interface model considering Local Equilibrium (LE) at the interface. The main advantage from the Wycliffe's model is the use of the Zener's approximation [Zen49], i.e. the composition profiles are locally linearized. This considerably reduces the computation time as no space discretization is required.

Figure IV.6 schematizes a typical simulation cell using our generalized Wycliffe's model. Planar geometry is assumed and symmetry conditions are set at the boundaries of the cell. The size of the simulation cell, written  $D$ , represents one half of a typical distance between austenite islands.

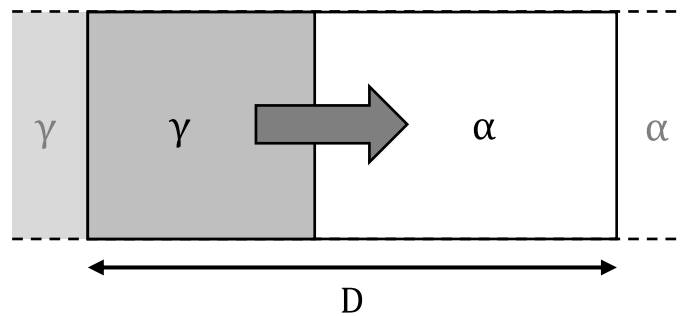


Figure IV.6: Schema of a typical simulation cell in our generalized Wycliffe's model.

As presented in our literature review (I.2.3), the austenite grows under LENP mode at the very beginning of the isothermal holding up to complete carbon homogenization in austenite. This stage is very short in our studied systems (less than 4 s in [Cou+23]). Still, despite a slight carbon gradient in austenite, the austenite fraction at the end of the heating stage is expected to be close to the theoretical LENP fraction. From these conclusions from our previous numerical work, we neglect this first stage. The initial state of the simulation is set with LENP interface conditions and no carbon nor substitutional element gradient is considered across the system (flat profiles). Austenite is assumed to inherit the substitutional  $u$ -fraction of ferrite during growth under LENP mode at the end of the heating stage. A narrow substitutional gradient is imposed in ferrite near the interface to ensure LE at the interface (the so-called spike of LENP mode [Gou+15]). Consequently, the initial austenite fraction in the simulation cell is the theoretical LENP fraction at the considered temperature.

The present work models austenite growth in ferrite under LEP mode, i.e. with substitutional element redistribution. The typical holding time studied in the present work (10 min) is short enough to consider only the redistribution controlled by diffusion of substitutional element in ferrite. In particular, no significant substitutional element diffusion occurs in austenite in the studied time range (IV.1.3). Substitutional element diffusion in austenite is thus neglected in the present model. Due to slower diffusion in austenite (three order of magnitude slower), the

redistribution controlled by diffusion of substitutional element in austenite is only observed after long holding time (around  $10^5$  s) [Kam+15; Lai+16; Oll+17; Wei+13]. The LEP mode produces composition gradient in austenite behind the interface (Figure IV.4). These gradients are assumed linear, following the Wycliffe's approach.

Carbon diffusion is much faster than substitutional element diffusion. We assume no carbon gradient due to carbon diffusion. We also neglect the effect of local substitutional content on carbon activity. Consequently, the carbon profile is always flat in considered phases. As the carbon composition in ferrite is far lower than in austenite (thirty times less), carbon composition in ferrite is neglected in the carbon balance. This simplification introduces a mean relative error on the carbon balance evaluated at only 0.5 at%. Still, carbon in ferrite is calculated at the interface during the computation of the operative tie-line.

In the following, we use molar compositions. The nominal content in element  $y$  is written  $X_y^0$ . With the assumptions stated above, the initial composition in the phase  $\Phi$  is  $X_C^{\Phi 0}$  in carbon and  $X_y^{\Phi 0} = X_y^0 \times (1 - X_C^{\Phi 0}) / (1 - X_C^0)$  in substitutional element  $y$ . The interface compositions in element  $y$  on austenite and ferrite sides are written  $X_y^{\gamma/\alpha}$  and  $X_y^{\alpha/\gamma}$ , respectively.

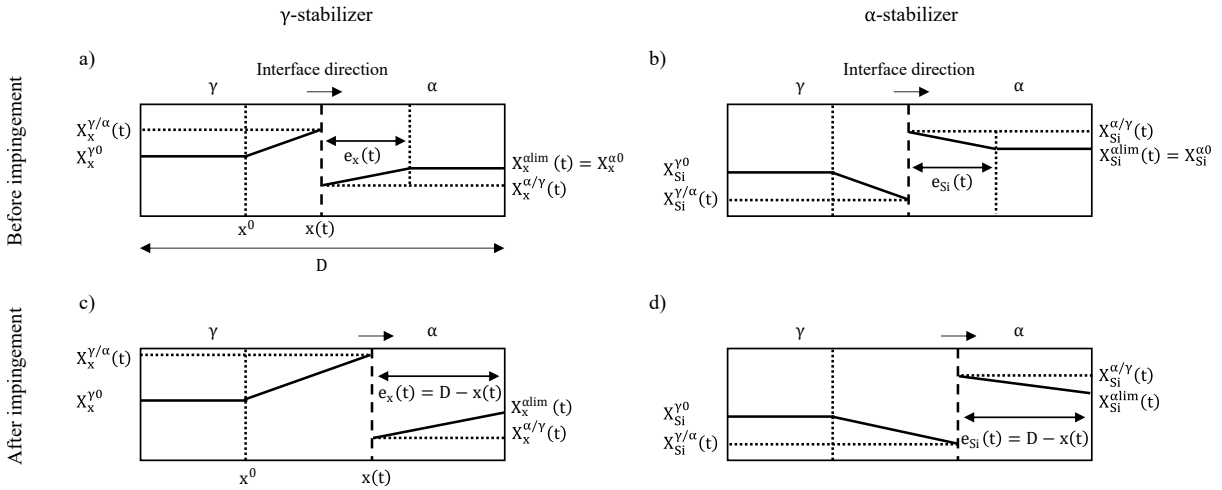


Figure IV.7: Profile of  $\gamma$ -stabilizers (a, c) (manganese and chromium) and the  $\alpha$ -stabilizer (b, d) (silicon) before (a, b) and after (c, d) soft-impingement.

Figure IV.7 represents the profile of (a) a  $\gamma$ -stabilizer (manganese and chromium for instance) and (b) the  $\alpha$ -stabilizer (silicon) before soft-impingement (the gradient in ferrite reached the edge of the simulation cell). The initial interface position is  $x^0$ . At a time  $t$ , the interface position is  $x(t)$ . The width of the area of ferrite affected by redistribution is written  $e_y(t)$  with  $y$  the substitutional element.

When soft-impingement occurs, i.e. when  $e_y(t) = D - x(t)$ , the substitutional composition at the edge of the cell, written  $X_y^{\alpha \text{ lim}}(t)$ , becomes relevant. Figure IV.7 shows the profile of (c) a  $\gamma$ -stabilizer (manganese and chromium here) and (d) the  $\alpha$ -stabilizer (silicon) after soft-impingement. Before soft impingement,  $X_y^{\alpha \text{ lim}}(t)$  is set at  $X_y^{\alpha 0}$ . In the initial state,  $e_y(0) = e_y^0$  is set at 10 nm. This introduces a relative error on the substitutional element balance estimated between 0.01 % and 0.04 %.

### IV.2.2 The equations of the model

Considering the assumptions on carbon (homogeneous in phases and neglected in ferrite), the carbon molar balance in the simulation cell gives:

$$X_C^0 = \frac{x(t)}{D} \times X_C^\gamma(t) \quad (IV.1)$$

A bulk molar balance is written for each substitutional element. Before soft-impingement ( $e_y(t) < D-x(t)$ ), the bulk balance of the substitutional element  $y$  is written:

$$\frac{1}{2}(X_y^{\gamma/\alpha}(t) - X_y^{\gamma 0}) \times (x(t) - x^0) = \frac{1}{2}((X_y^{\alpha 0} - X_y^{\alpha/\gamma}(t)) \times e_y(t) - (X_y^{\alpha 0} - X_y^{\alpha/\gamma}(0)) \times e_y^0) \quad (IV.2)$$

These equations ensure the respect of the balance of each studied element all during the simulation. On the contrary, DICTRA simulations often shows unstable balances. Equation IV.2 gives an expression of  $e_y(t)$  as a function of the operative tie-line and the interface position:

$$e_y(t) = \frac{1}{X_y^{\alpha 0} - X_y^{\alpha/\gamma}(t)} ((X_y^{\gamma/\alpha}(t) - X_y^{\gamma 0}) \times (x(t) - x^0) + (X_y^{\alpha 0} - X_y^{\alpha/\gamma}(0)) \times e_y^0) \quad (IV.3)$$

Before soft-impingement,  $X_y^{\alpha \text{ lim}}(t)$  is set at  $X_y^{\alpha 0}$ . If  $e_y(t)$  is found greater than  $D-x(t)$ ,  $e_y(t)$  is set at  $D-x(t)$  and soft-impingement starts. During soft-impingement, i.e. when  $e_y(t)$  equals  $D-x(t)$ , Equation IV.2 becomes:

$$\begin{aligned} \frac{1}{2}(X_y^{\gamma/\alpha}(t) - X_y^{\gamma 0}) \times (x(t) - x^0) = & (X_y^{\alpha 0} - X_y^{\alpha \text{ lim}}) \times (D - x(t)) + \\ & \frac{1}{2} \left( (X_y^{\alpha \text{ lim}} - X_y^{\alpha/\gamma}(t)) \times (D - x(t)) - (X_y^{\alpha 0} - X_y^{\alpha/\gamma}(0)) \times e_y^0 \right) \end{aligned} \quad (IV.4)$$

and gives the composition at the edge of the cell  $X_y^{\alpha \text{ lim}}$  as a function of the operative tie-line and the interface position:

$$X_y^{\alpha \text{ lim}}(t) = 2X_y^{\alpha 0} - X_y^{\alpha/\gamma}(t) - \frac{1}{D - x(t)} [(X_y^{\gamma/\alpha}(t) - X_y^{\gamma 0}) \times (x(t) - x^0) + (X_y^{\alpha 0} - X_y^{\alpha/\gamma}(0)) \times e_y^0] \quad (IV.5)$$

Soft-impingement stops when  $e_y(t)$  equals  $D-x(t)$  and  $X_y^{\alpha \text{ lim}}(t)$  reaches  $X_y^{\alpha/\gamma}(t)$ . When this condition is reached, the austenite growth controlled by substitutional element diffusion in ferrite ends. Growth controlled by substitutional element diffusion in austenite should takes over [SDM81]. As shown by our DICTRA simulations, this stage is only reached at the very end of our isothermal holding treatment. For this reason, this stage is not modeled for the present study.

Considering the assumption on diffusion in austenite (no substitutional diffusion in austenite), the interface molar balance of the substitutional  $y$  is written:

$$(X_y^{\gamma/\alpha}(t) - X_y^{\alpha/\gamma}(t)) \times \frac{dx}{dt} = D_y^\alpha \frac{X_y^{\alpha \text{ lim}}(t) - X_y^{\alpha/\gamma}(t)}{e_y(t)} \quad (IV.6)$$

Equation IV.7 gives the increment of the interface position as a function of the operative tie-line:

$$dx = dt \times D_y^\alpha \frac{X_y^{olim}(t) - X_y^{\alpha/\gamma}(t)}{e_y(t) \times (X_y^{\gamma/\alpha}(t) - X_y^{\alpha/\gamma}(t))} \quad (IV.7)$$

The quinary phase diagram, computed with Thermo-Calc using the TCFE9 database, is linearized. The linearization describes a hyperplane in the space of compositions. Two row vectors  $A^\gamma(T)$  and  $A^\alpha(T)$ , temperature dependant, constrains linearly the interface composition of austenite and ferrite as follows:

$$A^\gamma(T) \times \begin{pmatrix} 1 \\ X_C^{\gamma/\alpha}(t) \\ X_{Mn}^{\gamma/\alpha}(t) \\ X_{Si}^{\gamma/\alpha}(t) \\ X_{Cr}^{\gamma/\alpha}(t) \end{pmatrix} = 0 \text{ and } A^\alpha(T) \times \begin{pmatrix} 1 \\ X_C^{\alpha/\gamma}(t) \\ X_{Mn}^{\alpha/\gamma}(t) \\ X_{Si}^{\alpha/\gamma}(t) \\ X_{Cr}^{\alpha/\gamma}(t) \end{pmatrix} = 0 \quad (IV.8)$$

In their work, Wycliffe [WPE81] proposed to describe the tie-lines using a proportionality coefficient linking manganese interface compositions. We propose to extend this idea to the composition vectors as follows:

$$\begin{pmatrix} X_C^{\alpha/\gamma}(t) \\ X_{Mn}^{\alpha/\gamma}(t) \\ X_{Si}^{\alpha/\gamma}(t) \\ X_{Cr}^{\alpha/\gamma}(t) \end{pmatrix} = k(T) \times \begin{pmatrix} X_C^{\gamma/\alpha}(t) \\ X_{Mn}^{\gamma/\alpha}(t) \\ X_{Si}^{\gamma/\alpha}(t) \\ X_{Cr}^{\gamma/\alpha}(t) \end{pmatrix} \quad (IV.9)$$

With  $k(T)$  is a square matrix of dimension 4, temperature dependent. The coefficients of the matrix  $k(T)$  were fitted on Thermo-Calc data, using the python library sklearn. This hypothesis considerably simplifies the description of the tie-lines and predicts with a great accuracy the interface composition in ferrite, knowing the one in austenite. The  $R^2$  scores on  $X_C^{\alpha/\gamma}$ ,  $X_{Mn}^{\alpha/\gamma}$ ,  $X_{Si}^{\alpha/\gamma}$  and  $X_{Cr}^{\alpha/\gamma}$  are 0.9991, 0.9995, 0.9971 and 0.9985 respectively. Because of its low magnitude, carbon composition in ferrite at the interface  $X_C^{\alpha/\gamma}$  is very sensitive to the quality of the fit. Though, the relative mean error was evaluated at 0.8 % on the studied composition range. The quality of the prediction validates the linear hypothesis.

The system of equation is solved explicitly step by step. At a time  $t$ , the new interface position  $x(t)$  is obtained by the addition of the position increment  $dx(t-dt)$  to the previous interface position  $x(t-dt)$ . The new austenite carbon content is computed using the carbon balance (Equation IV.1).

The tie-line is computed such that, the increment in interface position computed with the balance at interface (Equation IV.7) is equal regardless the considered substitutional, i.e.  $dx_{Mn} = dx_{Si} = dx_{Cr}$ . On the 2D-space  $(X_{Si}^{\gamma/\alpha}, X_{Cr}^{\gamma/\alpha})$ ,  $X_{Mn}^{\gamma/\alpha}$  is computed using the phase diagram (Equation IV.9).  $e_y(t)$  or  $X_y^{\alpha\ lim}(t)$  is given by Equation IV.3 or Equation IV.5 respectively. The increments in interface position  $dx_x$  are obtained with Equation IV.7. The zero set of the function  $|dx_{Mn} - dx_{Si}| + |dx_{Si} - dx_{Cr}| + |dx_{Mn} - dx_{Cr}|$  gives the operative tie-line.

### IV.2.3 Validation of the model

The reliability of the model regarding the time increment, the cell size (i.e. the typical sizes in the microstructures), the annealing temperature and the steel nominal composition is tested. Several simulations were run and changing one of these parameters. The austenite fraction computed with the Generalized Wycliffe Model (GWM) (in solid lines) are plotted in Figure IV.8 and compared with DICTRA simulations (in dotted lines) using the same initial state.

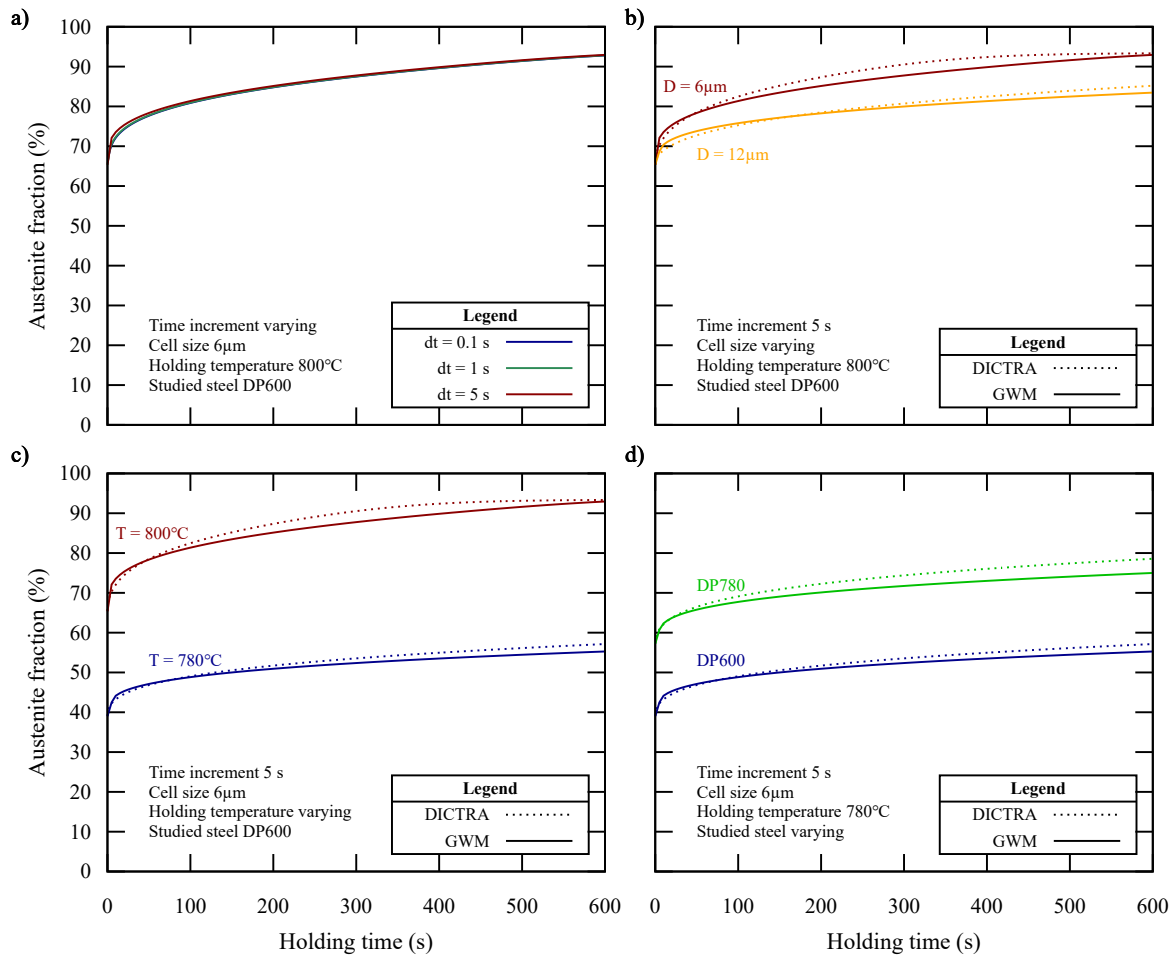


Figure IV.8: Austenite fraction during isothermal holding. The fractions computed with the Generalized Wycliffe's Model (GWM in solid lines) are compared to the ones computed with DICTRA simulations (in dotted lines). The reliability of the GWM regarding the increment time (a), the cell size (b), the holding temperature (c) and the nominal composition of the steel (d) is tested.

Figure IV.8 a) shows the austenite fractions during the holding stage at 800  $^{\circ}\text{C}$  for 600 s in a Fe-0.1C-1.9Mn-0.2Si-0.2Cr (nominal composition of our DP600) computed with the GWM. The cell size is set at the mean half distance between pearlite bands in the DP600 CR60 studied by Moreno et al. [Mor19], estimated at 6  $\mu\text{m}$ , so that we can compare the results of the GWM with our previous investigation using DICTRA simulations (Figure IV.2) and [Cou+23;

Mor19; Tei+21]. Three time increments  $dt$  are used to study the reliability of the model to this numerical parameter: 0.1 s in blue, 1 s in green and 5 s in red. Regardless the time increment used, the computed austenite fractions are superposed. This observation ensures the stability of the results, even when using a large time increment (5 s). This makes possible a faster computation of the final austenite fraction.

In the following, all computations with the GWM are run using a time increment set at 5 s.

Figure IV.8 b) plots the austenite fraction during the holding stage at 800 °C for 600 s in a Fe-0.1C-1.9Mn-0.2Si-0.2Cr (nominal composition of our DP600) computed with the GWM. The cell size is set at 6  $\mu\text{m}$  as in Section IV.1 and [Cou+23; Mor19; Tei+21] (in red) or 12  $\mu\text{m}$  (in orange). The GWM produces austenite fractions very close to the ones computed with DICTRA. In addition, the results show that longer cell sizes lead to a slower austenite formation kinetics. This is due to longer diffusion path and austenite growth in LEP mode. In larger simulation cells, substitutional elements need more time to diffuse in phases and to redistribute. As the cell size represents the typical size in the microstructure, this result show that our GWM catches the trend reported in literature: a finer microstructure accelerates the austenite formation under LEP mode during the isothermal holding stage [BVS22; Bel+19; Chb+14; MGF11; Oll+17; TM18].

To continue our verifications on the GWM, we set the simulation cell at 6  $\mu\text{m}$ .

Figure IV.8 c) shows the austenite fraction during the holding stage at 780 °C (in blue) and 800 °C (in red) for 600 s in a Fe-0.1C-1.9Mn-0.2Si-0.2Cr (nominal composition of our DP600) computed with the GWM. The results at 800 °C are the same as plotted in red in Figure IV.8 b). The fractions computed with our GWM are still in agreement with results from DICTRA simulations. The computed austenite fractions are globally lower at 780 °C than at 800 °C, as expected in the intercritical temperature range. The GWM is reliable regarding the annealing temperature.

Lastly, we set the annealing temperature at 780 °C and study the annealing in a DP600 (in blue), the same as in Figure IV.8 c), and in a Fe-0.15C-1.9Mn-0.2Si-0.2Cr (nominal composition of an industrial DP780 steel), plotted in green. Once again, the fractions obtained with the GWM and DICTRA are very close. The austenite fractions are globally higher in the DP780, as expected from a steel with a higher carbon content.

Figure IV.9 shows the carbon (a), manganese (b), silicon (c) and chromium (d) profiles after 100 s at 800 °C in the DP600 ( $D = 6 \mu\text{m}$  and  $dt = 5 \text{ s}$ , in red in Figure IV.8 b) and c)) computed with our GWM (in red) and with DICTRA (in black). The interface position in the initial state is indicated by a black dotted line. The interface positions after 100 s are indicated by dashed lines.

For industrial application, the GWM was expected to properly model 100 s of intercritical annealing. After 100 s, the interface position predicted by the GWM is slightly behind the interface position predicted by DICTRA (1 % of austenite less in Figure IV.8). The profile of all elements computed with the DICTRA simulation are well reproduced by the GWM. The profiles show manganese and chromium redistribution in austenite, as well as silicon redistribution in ferrite. The carbon profile predicted by DICTRA is flat and not significantly affected by the local composition in substitutional elements, as the carbon content across the austenite is in a 0.004 at% range. The carbon content in austenite predicted by our GWM is 0.57 at%, only 0.02 at% higher than the one predicted by DICTRA. The substitutional element gradients in austenite and in ferrite predicted by the GWM are in very good agreement with the DICTRA simulation, despite the more parabolic shapes of profiles in ferrite computed with DICTRA. These observations validate the assumption of linear profiles.

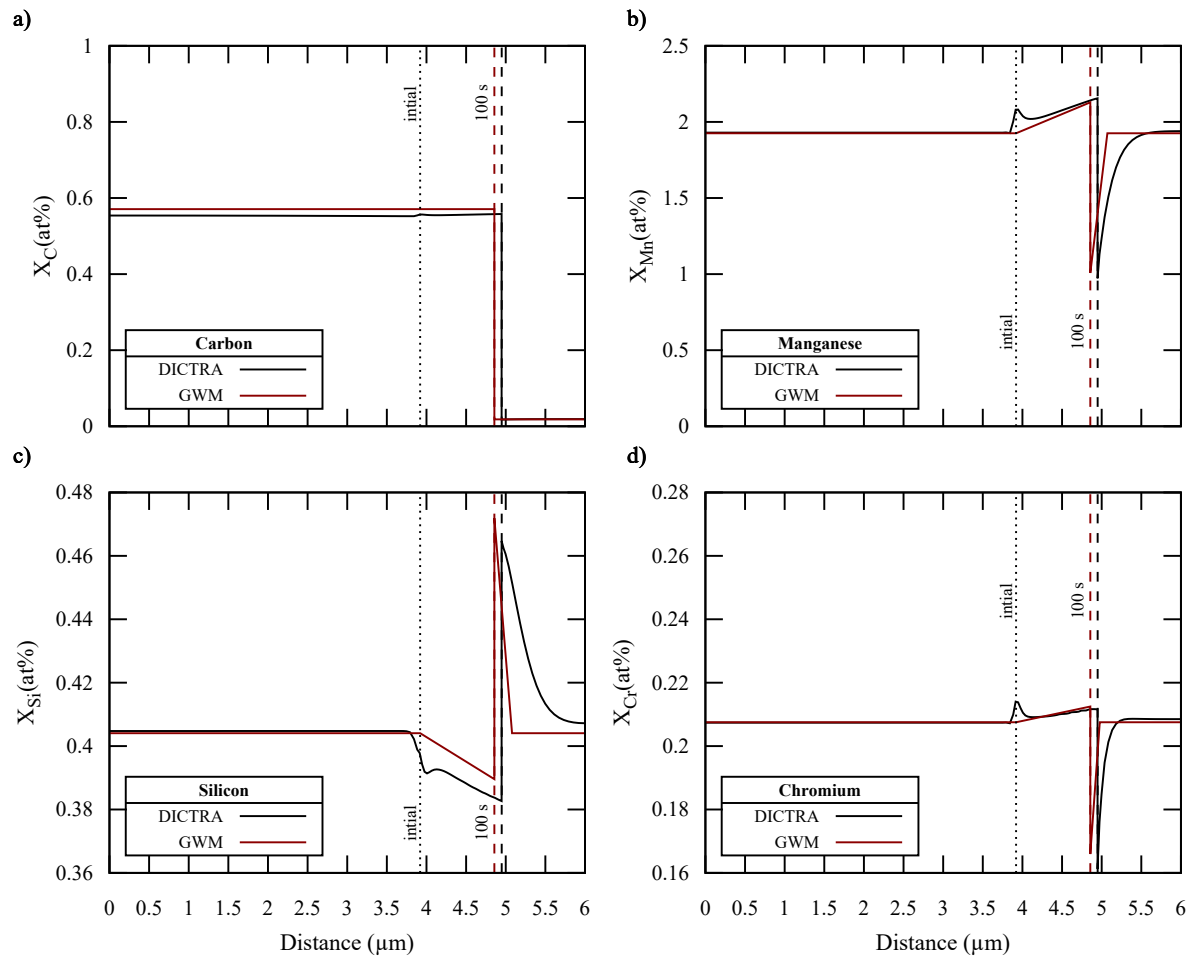


Figure IV.9: Carbon (a), manganese (b), silicon (c) and chromium (d) profiles after 100 s at 800 °C, computed with our model (red) and with DICTRA (black).

The model reaches the industrial expectations. Our numerical investigation in Section IV.1 show gradient profiles of substitutional elements in austenite after 250 s (Figure IV.4) that would not be described by a single line as accurately as after 100 s holding (Figure IV.9). To overcome this limitation, one could implement the diffusion of substitutional element as done in ferrite.

All profiles predicted by DICTRA show an instability around the initial interface position. This is due to numerical instabilities at the very beginning of the DICTRA simulations. The profiles predicted by our model present no such numerical artefact. Thus, the GWM not only compute faster the austenite fractions and element profiles during the intercritical annealing but is also more numerically stable, which is of great importance to drive an industrial production line.

Thus, we developed, implemented and validated an original extended version of the model proposed by Wycliffe in [WPE81]. Our Generalized Wycliffe's Model accounts for multi-constituent systems Fe-C systems with  $n$  substitutional elements ( $n \geq 1$ ). Our GWM is reliable regarding the annealing temperature, as well as to the chemical composition of the steel, as expected

by the industrial partner. This 1D sharp-interface model is shown to have a high numerical stability and short computation times, as necessary for the industrial application. The model catches the effect of the typical size of the microstructure and its stability regarding the time increment ensures short computation time. The GWM is shown to be an efficient alternative to DICTRA simulations, as it reproduces with great accuracy the results of DICTRA simulations (both austenite fractions and composition profiles).

#### IV.2.4 Effect of the heating rate on the austenite formation kinetics during the isothermal holding stage

Both our literature review (Figure I.27) [BVS22; Bel+19; Chb+14; HPM04; Li+13; MGF11; Mor19; Tei+21; TM18] and our experimental study in Chapter III (Figure III.12 in III.1.2.5) shows that faster heating leads to a faster austenite formation kinetics and a higher overshoot from OE, i.e. the fraction of austenite temporarily exceeds the OE fraction, during the isothermal holding. No clear consensus is reached among the authors to explain the trend observed.

Though, from our experimental investigation in Chapter III (III.2), we finally proposed to attribute the faster austenite formation kinetics during the isothermal holding to the finer microstructure observed at the end of fast heating (III.13). Shorter diffusion paths for substitutional elements enhance the austenite growth (III.27). The present sub-section further discusses this hypothesis.

The size of the simulation cell  $D$  in our implementation of the GWM represents one half of the typical distance between austenite islands. To highlight the importance of the microstructure size, we first perform a parametrical study to highlight the effect of the microstructure size on the austenite formation kinetics. Our GWM, detailed and validated previously in this section, makes possible fast computation of austenite formation kinetics during isothermal holding using a large range of investigation for the cell sizes  $D$ . Then, we compare experimental kinetics presented in Chapter III (Figure III.12) with simulation results to support our hypothesis.

The present study investigates the austenite formation in the DP600 studied in Chapter III during an isothermal holding at 800 °C. As we will finally compare the simulation results to the experimental data, we consider the measured nominal composition of the steel (Table III.1). According to our implementation of the GWM, the simulations are initialized with theoretical LENP conditions. The theoretical LENP fraction and carbon content in austenite and ferrite, computed with Thermo-Calc at 800 °C, are reported in Table IV.3.

$f_{\gamma}^{\text{LENP}}(800\text{ °C})$	$X_C^{\gamma^0}$ ( at%)	$X_C^{\alpha^0}$ ( at%)
55 %	0.749	0.0242

Table IV.3: Theoretical LENP fraction and carbon content in austenite and ferrite, computed with Thermo-Calc at 800 °C

Figure IV.10 shows the austenite formation kinetics resulting from 42 simulations performed using cell sizes  $D$  between 0.5  $\mu\text{m}$  and 25  $\mu\text{m}$  with a step of 0.5  $\mu\text{m}$ . The OE fraction (75 %) is indicated by a black dotted line. The shorter the cell size, the faster the austenite growth kinetics. For cell size thinner than 3.5  $\mu\text{m}$ , the austenite fraction increases from 55 % (initial LENP fraction) up to 90 %. Then, the austenite fraction remains stable. As already shown in Figure IV.8 (b), the short diffusion paths accelerate the kinetics and soft-impingement occur before the end of the simulation. As the substitutional element diffusion in austenite is not implemented in our GWM, the transformation stops. Though the holding time is very short

for significant diffusion in austenite, the short diffusion distances may enhance the diffusion in austenite. Substitutional diffusion in austenite would make the austenite fraction decrease down to the OE fraction.

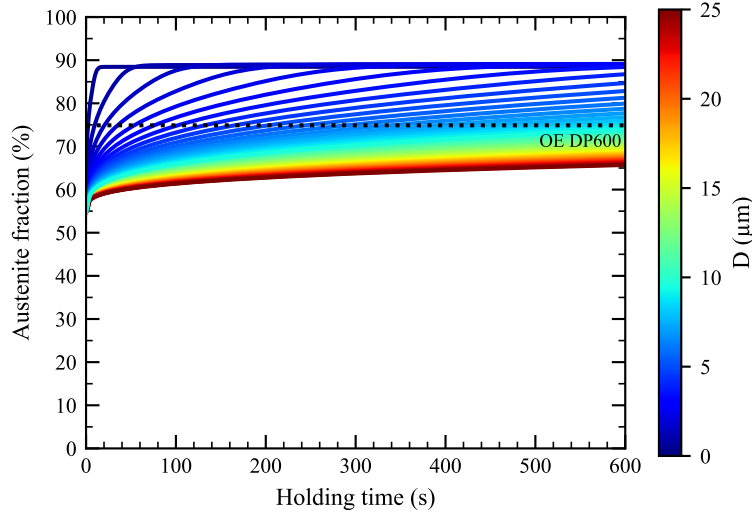


Figure IV.10: Austenite fraction during an isothermal holding at 800 °C in the studied DP600 computed with our GWM using cell sizes  $D$  between 0.5  $\mu\text{m}$  and 25  $\mu\text{m}$  with a step of 0.5  $\mu\text{m}$ . The OE fraction is indicated by a black dotted line.

For cell sizes larger than 3.5  $\mu\text{m}$ , the austenite fraction increases all during the isothermal holding. After 600 s, the austenite fraction keeps increasing and the longer the cell size, the lower the austenite fraction. Longer simulation cell means slower kinetics. Yet, the austenite should reach the same maximum fraction (90 %) as using sizes thinner than 3.5  $\mu\text{m}$ , only after longer holding times than 600 s. The different final austenite fractions are explained by the different growth kinetics stopped at 600 s. This result supports a discussion in Chapter III (III.1.3.5).

This parametrical study shows that the cell size greatly impacts the austenite formation kinetics and the austenite fraction at the end of the holding stage, making the typical microstructural size a crucial parameter controlling the kinetics.

Our microstructural investigation in Chapter III (Figure III.13) showed that the microstructure at the end of the heating stage is thinner using faster heating rate. The mean distance between austenite islands is found to be 11  $\mu\text{m}$  after slow heating (3 °C/s) and 8  $\mu\text{m}$  after fast heating (30 °C/s) (III.1.2.6). We simulate the austenite growth during an isothermal holding at 800 °C using the half of the mean distances between austenite islands as cell sizes. The cell size and initial position of the interface (Figure IV.7) are reported in Table IV.4.

Previous heating rate	$D$ ( $\mu\text{m}$ )	$x^0 = f_{\gamma}^{\text{LENP}}(800\text{ °C}) \times D$ ( $\mu\text{m}$ )
3 °C/s	5.5	3.02
30 °C/s	4.0	2.19

Table IV.4: Cell size and initial position of the interface for simulation of austenite growth after slow (3 °C/s) and fast (30 °C/s) heating.

Figure IV.11 shows the austenite fraction during an isothermal holding at 800 °C after slow (3 °C/s in blue) or fast (30 °C/s in green) heating in our DP600 computed with our GWM (solid lines). The simulated fractions are compared with experimental data (filled diamonds) obtained from HEXRD experiments (Figure III.12)

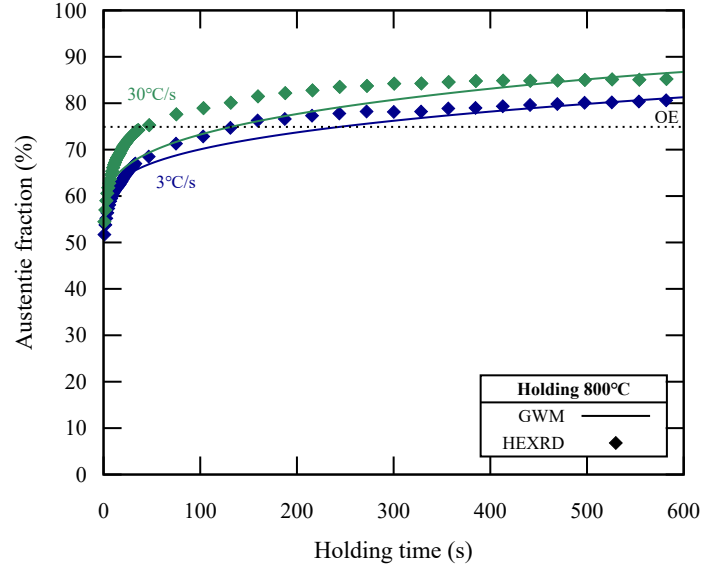


Figure IV.11: Austenite fraction during the isothermal holding at 800 °C after slow (3 °C/s in blue) or fast (30 °C/s in green) heating of our DP600 computed with our GWM (solid lines) compared with experimental data (filled diamonds) obtained from HEXRD experiments (Figure III.12).

The simulated austenite starts at 55 %, the theoretical LEP fraction of the system at 800 °C. Then, the simulated fractions increase up to 81 % after slow heating ( $D = 5.5 \mu\text{m}$  in blue) and 87 % after fast heating ( $D = 4 \mu\text{m}$  in green). The simulated austenite formation kinetics is faster after fast heating 30 °C/s, as the simulation cell is thinner than after slow heating. The simulated fractions (solid lines) describe the experimental fractions (diamonds) with excellent accuracy after 400 s holding. In particular, our simulations reproduce very well the final fraction and the exceed of OE fraction. The prediction of the austenite formation kinetics is less accurate at the beginning of the holding stage ( $t < 300$  s). Yet, the maximum difference between the simulations and the experiments is only 6 %, despite the simplifying assumptions of the GWM.

Contrary to the previous numerical work by Moreno et al. [Mor19; Tei+21] (Figure I.34), our simulations not only reproduce the gap of final austenite fraction at the end of the holding stage depending on the previous heating stage but also reproduces with fairly good accuracy the full kinetics and the absolute values of the fractions. These results speak in favor of our hypothesis proposed in the previous Chapter III. According to our experimental investigation, supported by the present numerical study, the austenite formation kinetics during the holding stage is fully driven by LEP mode, controlled by diffusion in ferrite, and the effect of the heating rate during the isothermal holding comes from the finer microstructure at the end of the heating stage using faster heating rate.

### IV.2.5 Conclusions on the austenite formation during the isothermal holding

This section proposed a 1D sharp-interface model of the austenite growth during the isothermal holding stage. An original extended version of the model proposed by Wycliffe et al. in [WPE81], accounting for multi-constituent systems, was developed, implemented and validated. Our Generalized Wycliffe Model (GWM) meets the expectations of the industrial partner, as it is reliable regarding the annealing temperature, as well as to the chemical composition of the steel. The GWM also have a higher numerical stability and shorter computation times compared to similar numerical solutions (DICTRA).

Using our newly developed numerical tool, we further investigated the impact of the microstructural size on the austenite formation kinetics.

This parametrical study highlighted an important sensitivity of the austenite growth kinetics to the typical microstructural size. Our simulations using mean distances between austenite islands, taken from our experimental investigation in Chapter III, reproduced with accuracy the experimental austenite formation kinetics during the isothermal holding after both slow (3 °C/s) and fast (30 °C/s) heating, contrary to previous work [Mor19; Tei+21]. These results speak in favor of our hypothesis stating that the austenite formation kinetics during the holding stage is fully driven by LEP mode, controlled by diffusion in ferrite, and the effect of the heating rate during the isothermal holding comes from the finer microstructure at the end of the heating stage using faster heating rate.

## IV.3 Conclusions on the thermo-kinetics investigation of austenite formation during intercritical annealing

This final chapter aimed to propose a numerical solution to predict the austenite fraction evolutions during the intercritical annealing of DP steels for industrial applications. To do so, we referred to the literature review and our experimental investigation from Chapter III to account for the relevant metallurgical mechanisms.

First, we investigated the effect of minor alloying elements (chromium and silicon in the present work) using DICTRA simulations to better understand the austenite formation kinetics during the intercritical annealing after the carbon transfer reveal in Chapter III. The minor substitutional elements are shown to strongly slow down the austenite formation kinetics. During the heating stage, the austenite grows under LENP mode, with no redistribution of the substitutional element, controlled by carbon diffusion in austenite. After the carbon transfer (above 780 °C), the austenite fraction can be predicted using the theoretical LENP fraction. During the holding stage, the austenite grows mainly under LEP mode, controlled by diffusion in ferrite.

Finally, we developed an original extended version of the model proposed by Wycliffe et al. in [WPE81], accounting for multi-constituent systems. This 1D sharp-interface model of the austenite growth during the isothermal holding stage, which simplifies the composition profiles by linearization, is reliable regarding the effect of annealing temperature, of the chemical composition of the steel and of the size of the simulation cell (and hence the representative sizes inside the represented microstructure). It has also a higher numerical stability and shorter computation times compared to similar numerical solutions (DICTRA).

Using our newly developed numerical tool, we highlighted that the spacing between austenite islands at the end of the heating stage is a crucial parameter, controlling the austenite formation kinetics during the isothermal holding stage. Using mean distances between austenite islands, we

reproduced with accuracy the experimental austenite formation kinetics during the isothermal holding after both slow (3 °C/s) and fast (30 °C/s) heating, contrary to previous work [Mor19; Tei+21].

This final numerical investigation leads us to think that the austenite formation kinetics during the holding stage is fully driven by LEP mode, controlled by diffusion in ferrite, and the effect of the heating rate during the isothermal holding comes from the finer microstructure at the end of the heating stage using faster heating rate.



---

# Main conclusions and possible future investigations

---

À partir de maintenant  
j'commence mon ascension  
J'ai plus peur du vide, d'affronter  
la spirale sans fond  
Donc j'arrête d'arrêter,  
j'abandonne l'abandon  
Si j dois finir une seule chose c'est  
cette \*\*\* d'chanson

---

*Inachevés  
Casseurs Flowters*

The present PhD work provides a new insight on the austenite formation mechanisms along the intercritical annealing of flat cold-rolled low carbon steels and its possible interactions with recrystallization. The knowledge, data and developed models will contribute to the Steel Industry 4.0 and help the digital transition of this sector with the implementation of virtual twins.

Even if the obtained results and the discussions on the metallurgical mechanisms are applicable to many steels, this work focused on the heating phase of the intercritical annealing of the production of Dual-Phase steels (Ferrite-Martensite) used mainly for car manufacturing. They are flat, cold-rolled steels of very high diffusion and used for their high strength and good stamping capacity. The challenges of the industrial partner of the project lie more in the improvement of production methods and their deployment than in the search for better performance of these products, already industrial-grade and marketed widely in the world.

To this end, we first developed an original method based on in situ High Energy X-Ray Diffraction (HEXRD) experiments on synchrotron beamlines to simultaneously investigate ferrite recrystallization and austenite formation in a single experiment with a high time resolution during an intercritical annealing treatment. Chapter II presented in detail this method called Isolated Diffraction Spot Tracking (IDST), inspired from 3DXRD and the RPC method set up in the previous work of Moreno [Mor19; Mor+18]. Our IDST method is based on the detection and tracking of diffraction spots of high intensity, observed on 2D diffraction patterns, originating from newly recrystallized grains. Ferrite recrystallization was successfully monitored in model cold-rolled ultra-low carbon ferritic steels during heat treatments. More conventional methods

(Vickers micro-hardness measurements, post-treatment of SEM/EBSD observations) were used to interpret and calibrate our new approach. But, contrary to these *ex situ* methods, the IDST method offers an excellent time resolution.

The IDST method was used in Chapter III to study the concomitance of ferrite recrystallization and austenite formation during the intercritical annealing of cold-rolled ferrite-pearlite microstructure for DP steel production. We first reproduced the effect of the heating rate observed in the literature on our reference steel grade used to produce DP600 products. As expected, the heating rate impacted the concomitance of the ferrite recrystallization and the austenite formation, the morphology of austenite and the kinetics of the austenite formation. The microstructures were investigated at different scales by optical microscopy, SEM and TEM. The chemical composition of cementite particles was measured by EDXS and the carbon content across the austenite by WDS.

To challenge the conclusions drawn in literature on the effect of the heating rate and how it controls the formation kinetics and the morphogenesis of austenite, we then proposed additional and original “decoupling” experiments. Niobium micro-alloying was used to inhibit ferrite recrystallization, while lower cold-rolling ratios were used to delay ferrite recrystallization. By doing so, we manage to control the concomitance of ferrite recrystallization and austenite formation, while keeping our “slow” reference heating rate (3 °C/s). Thus, we prevented the impact of a difference in activation of thermally-activated mechanisms and studied the possible interactions between ferrite recrystallization and austenite formation.

A practical objective of this PhD work was to develop a CPU-efficient model for the austenite formation kinetics along the intercritical annealing, accounting for multi-constituent systems (quinary systems in the present work). In Chapter IV, we first investigated the effect of minor alloying elements (chromium and silicon) using DICTRA simulations to better understand the austenite formation kinetics along the intercritical annealing. Using this numerical study and the experimental work from Chapter III, we developed an original extended version of the model proposed by Wycliffe in [WPE81], accounting for multi-constituent systems. This 1D local field sharp-interface model of the austenite growth computes the austenite fractions and the composition profiles, simplified by linearization, during an isothermal holding in the intercritical temperature range. We used DICTRA simulations to validate our Generalized Wycliffe Model (GWM) that was shown to be reliable regarding the effect of annealing temperature, of the chemical composition of the steel and of the size of the simulation cell (representing the typical sizes of the microstructure). It has also a higher numerical stability and shorter computation times than similar numerical solutions using the reference software. This newly developed numerical tool was then used to further discuss our hypothesis proposed at the end of Chapter III to explain the effect of the heating rate on the austenite formation kinetics.

Here are the main scientific conclusions of the present PhD work:

- During the heating stage:
  - In the studied conditions, austenite originates from pearlite islands or cementite particles isolated in the ferrite matrix. The studied steels thus have two types of nucleation and growth sites of austenite. This distinction, introduced by Li et al. [Li+13] and studied in [Cou+23; Mor19; Tei+21], is still rarely made in the literature but is crucial to understand the inheritance effects highlighted in this thesis.
  - Under slow heating (3 °C/s), austenite growth from these carbon sources should be studied separately under 760 °C, as proposed in [Mor19; Tei+21]. The austenite

growth kinetics is affected by the nature of the carbon sources (pearlite islands or isolated cementite particles). Especially, both manganese and chromium enrichment of isolated cementite particles was observed during slow heating (3 °C/s), which shifts the Partition to Non-partition Transition Temperature (PNTT) to higher temperatures and, thus, delay the fast dissolution stage of the particles.

- This work revealed a carbon transfer between austenite grains of both origins above 760 °C leading to a homogeneous carbon distribution in austenite. This new result is key to understanding the transformation kinetics as the austenite growth can be studied as a single thermodynamic system. We clearly show that the austenite formation kinetics is fully driven by LEP interface conditions, i.e. by carbon diffusion, along the heating stage.
  - In our HEXRD experiments, faster heating rate, higher niobium content and lower cold-rolling ratios delayed the ferrite recrystallization making it concomitant with the austenite formation. Some authors [BVS22; Bel+19; Chb+14; TM18] in literature claim that the presence of deformed ferrite with high dislocation density or recovered ferrite with dislocation sub-structures accelerates diffusion and consequently, austenite formation. Our HEXRD experiments clearly showed that not only the presence of non-recrystallized ferrite, but also niobium in solid solution and the size of the microstructure had no significant effect on the austenite formation kinetics. This result has a practical consequence in terms of modeling: beyond the critical temperature of 760 °C, the transformation kinetics can be calculated by a simple balance based only on thermodynamics, in a very short time independently of the complexity of the system for any heating rate.
  - As already widely shown in the literature [BVS22; Bel+19; Chb+14; HPM04; Li+13; MGF11; Mor19; Tei+21; TM18], our experiments confirm that the concomitance of ferrite recrystallization and austenite formation strongly affects the microstructure and the austenite morphology. The present study supports the work of Teixeira et al. [Tei+21] and shows that the banded-like microstructure is produced by interactions between the isolated cementite particles and the on-going ferrite recrystallization.
- During the holding stage:
    - The austenite formation kinetics is fully driven by LEP mode, i.e. by the diffusion of substitutional elements in ferrite (considering our holding time).
    - Taking into account the minor substitutional elements (chromium and silicon) strongly slows down the austenite formation kinetics and affects the final austenite fraction. This result is important from a practical point of view, because even in very small quantities, alloying elements can control the transformation kinetics of austenite by their diffusion.
    - The size of the microstructure at the end of the heating stage strongly affects the austenite formation kinetics. Spacing between austenite islands at the end of the heating stage is shown to be a crucial parameter, controlling the austenite formation kinetics during the isothermal holding stage. Using mean distances between austenite islands, we reproduced with accuracy the experimental austenite formation kinetics during the isothermal holding after both slow (3 °C/s) and fast (30 °C/s) heating, contrary to previous work [Mor19; Tei+21]. We propose to attribute the effect of the

heating rate during the isothermal holding to the finer microstructure at the end of the heating stage with a faster heating rate. Shorter diffusion paths for substitutional elements enhance the austenite growth.

- Our study therefore highlights that there is a hidden coupled effect between the initial microstructure (obtained by hot- and cold-rolling) and the heating conditions on the transformation kinetics, through the distances between nucleation and growth sites of austenite. Through this inheritance effect, we manage to explain the observed, sometimes contradictory, tendencies on transformation kinetics.

After this PhD work and considering the main conclusions cited above, here are several propositions for future investigations:

- First of all, though we proved the relevance of our IDST method, further work can greatly improve its potential. It seems now crucial to implement a systematic separation of diffraction rings from different phases, so that the recrystallization can be safely monitored in multi-phased alloys. Along its development, the IDST method also presented the opportunity to monitor a large number of individual recrystallized grain growths, by systematically and individually studying the detected recrystallization spots. This aspect needs further development on the systematical study of the spots and validation by comparison with other more conventional methods.
- Concerning the investigation on the possible interactions between ferrite recrystallization and austenite formation, a large number of HEXRD experiments were conducted along this PhD work and several experimental data are still not analyzed. In particular, we planned experiments in which we force recrystallization before austenite formation during the annealing of our studied steels, even though the parameters (niobium micro-alloying, cold-rolling, heating rate) foster a concomitance. We conclude that the microstructure sizes drive the austenite formation kinetics during the isothermal holding stage. Thus, a particular care should be given to the characterization of the evolution of the microstructure along the heating stage.
- Finally, this work proposed a model for the austenite formation during the isothermal holding. A model is still to be implemented for the austenite formation during the heating stage. Further investigations are needed to this end:
  - The sole consideration of the PNTT was shown to be too restrictive to capture the effect of the heating rate on the kinetics of austenite formation on the cementite particles isolated in the ferrite matrix. A deeper experimental investigation could consider a larger number of cementite particles and also account for their size.
  - Further investigation on the pearlite to austenite transformation is clearly required. Experimental characterization of the pearlite islands and their transformation kinetics is required. Only then, a proper model, such as the one proposed by Caballero et al. [CCdA01], could be implemented.
  - Our GWM model accurately predicts the austenite formation kinetics from the typical sizes in the microstructure at the end of the heating stage. But these sizes were determined only experimentally in the present work. The implementation of a model for austenite growth during the heating stage able to predict these typical sizes at

the end of the heating stage is now of major importance to complete our modeling approach.

- This work revealed a carbon transfer between austenite grains, which deeply impacts our thermo-kinetics considerations. This transfer could be further characterized. In particular, its trigger and the preferential diffusion mode (in ferrite or in austenite) are still to be determined. Its existence in other conditions (during fast heating or starting from another initial microstructure) is to be verified experimentally. A complete numerical investigation could be of great help on this question.



---

# References

---

- [Aar75] Hubert I Aaronson. *Lectures on the Theory of Phase Transformations*. Metallurgical Society of AIME, 1975 (cit. on p. 49).
- [Age+19] European Environment Agency et al. *Monitoring CO<sub>2</sub> Emissions from Passenger Cars and Vans in 2017*. Publications Office, 2019. DOI: doi/10.2800/74986 (cit. on pp. xix, 1).
- [AA96] T. Akbay and C. Atkinson. “The Influence of Diffusion of Carbon in Ferrite as Well as in Austenite on a Model of Reaustenitization from Ferrite/Cementite Mixtures in Fe-C Steels”. In: *Journal of Materials Science* 31.9 (May 1996), pp. 2221–2226. ISSN: 0022-2461, 1573-4803. DOI: 10.1007/BF01152931 (cit. on p. 49).
- [ARA94] T. Akbay, R.C. Reed, and C. Atkinson. “Modelling Reaustenitisation from Ferrite/Cementite Mixtures in Fe-C Steels”. In: *Acta Metallurgica et Materialia* 42.4 (Apr. 1994), pp. 1469–1480. ISSN: 09567151. DOI: 10.1016/0956-7151(94)90165-1 (cit. on p. 49).
- [AB08] S. Allain and O. Bouaziz. “Microstructure Based Modeling for the Mechanical Behavior of Ferrite-Pearlite Steels Suitable to Capture Isotropic and Kinematic Hardening”. In: *Materials Science and Engineering: A* 496.1-2 (Nov. 2008), pp. 329–336. ISSN: 09215093. DOI: 10.1016/j.msea.2008.06.009 (cit. on p. 5).
- [All+15] S. Y. P. Allain et al. “Towards the Microstructure Design of DP Steels: A Generic Size-Sensitive Mean-Field Mechanical Model”. In: *Materials Science and Engineering: A* 637 (June 2015), pp. 222–234. ISSN: 0921-5093. DOI: 10.1016/j.msea.2015.04.017 (cit. on pp. xix, xx, 1–3, 87).
- [All+20] Sébastien Y.P. Allain et al. “A Physics-Based Mean-Field Model for Ferrite Recovery and Recrystallization”. In: *Metals* 10.5 (May 11, 2020), p. 622. ISSN: 2075-4701. DOI: 10.3390/met10050622 (cit. on pp. xxv, 5, 12, 39, 87, 126).
- [And+02] J-O Andersson et al. “Thermo-Calc & DICTRA, Computational Tools for Materials Science”. In: *Calphad* 26.2 (June 1, 2002), pp. 273–312. ISSN: 0364-5916. DOI: 10.1016/S0364-5916(02)00037-8 (cit. on pp. 84, 137).
- [Arc] ArcelorMittal. *Global Automotive & Mobility Solutions*. URL: <https://automotive.arcelormittal.com/home> (cit. on p. 2).

- [Ash+15] Giannis Ashiotis et al. “The Fast Azimuthal Integration Python Library: *pyFAI*”. In: *Journal of Applied Crystallography* 48.2 (Apr. 1, 2015), pp. 510–519. ISSN: 1600-5767. DOI: 10.1107/S1600576715004306 (cit. on p. 74).
- [Avr39] Melvin Avrami. “Kinetics of Phase Change. I General Theory”. In: *The Journal of chemical physics* 7.12 (1939), pp. 1103–1112 (cit. on p. 48).
- [Aya+12] Abdelhak Ayad et al. “Grain Orientation Spread Values in IF Steels after Plastic Deformation and Recrystallization”. In: *Materials Science Forum*. Vol. 702. Trans Tech Publ, 2012, pp. 269–272 (cit. on p. 16).
- [AM10] Hamid Azizi-Alizamini and Matthias Militzer. “Phase Field Modelling of Austenite Formation from Ultrafine Ferrite–Carbide Aggregates in Fe–C”. In: *International Journal of Materials Research* 101.4 (Apr. 1, 2010), pp. 534–541. ISSN: 2195-8556, 1862-5282. DOI: 10.3139/146.110307 (cit. on pp. 52, 53).
- [BVS22] Bharath Bandi, Joost Van Krevel, and Prakash Srirangam. “Interaction Between Ferrite Recrystallization and Austenite Formation in Dual-Phase Steel Manufacture”. In: *Metallurgical and Materials Transactions A* 53.4 (Apr. 2022), pp. 1379–1393. ISSN: 1073-5623, 1543-1940. DOI: 10.1007/s11661-022-06597-2 (cit. on pp. xix, xxviii, 3, 24, 35, 37, 39–45, 93, 109, 110, 128, 132, 151, 153, 161).
- [Bel+19] Marion Bellavoine et al. “Ferrite Recrystallization and Austenite Formation during Annealing of Cold-Rolled Advanced High-Strength Steels: In Situ Synchrotron X-ray Diffraction and Modeling”. In: *Materials Characterization* 154 (Aug. 2019), pp. 20–30. ISSN: 10445803. DOI: 10.1016/j.matchar.2019.05.020 (cit. on pp. xx, xxviii, 3, 23, 24, 35, 37–40, 42–45, 93, 103, 109, 110, 127, 128, 132, 151, 153, 161).
- [Bha16] H.K.D.H. Bhadeshia. “Some Difficulties in the Theory of Diffusion-Controlled Growth in Substitutionally Alloyed Steels”. In: *Current Opinion in Solid State and Materials Science* 20.6 (Dec. 2016), pp. 396–400. ISSN: 13590286. DOI: 10.1016/j.cossms.2016.07.004 (cit. on p. 28).
- [Bor+00] Annika Borgenstam et al. “DICTRA, a Tool for Simulation of Diffusional Transformations in Alloys”. In: *Journal of Phase Equilibria* 21.3 (May 1, 2000), pp. 269–280. ISSN: 1054-9714. DOI: 10.1361/105497100770340057 (cit. on p. 83).
- [BMS10] C. Bos, M.G. Meozzi, and J. Sietsma. “A Microstructure Model for Recrystallisation and Phase Transformation during the Dual-Phase Steel Annealing Cycle”. In: *Computational Materials Science* 48.3 (May 2010), pp. 692–699. ISSN: 09270256. DOI: 10.1016/j.commatsci.2010.03.010 (cit. on p. 52).
- [BS07] C. Bos and J. Sietsma. “A Mixed-Mode Model for Partitioning Phase Transformations”. In: *Scripta Materialia* 57.12 (Dec. 2007), pp. 1085–1088. ISSN: 13596462. DOI: 10.1016/j.scriptamat.2007.08.030 (cit. on p. 51).
- [BS09] C. Bos and J. Sietsma. “Application of the Maximum Driving Force Concept for Solid-State Partitioning Phase Transformations in Multi-Component Systems”. In: *Acta Materialia* 57.1 (Jan. 2009), pp. 136–144. ISSN: 13596454. DOI: 10.1016/j.actamat.2008.08.060 (cit. on p. 51).

- [CCdA01] F. G. Caballero, C. Capdevila, and C. García de Andrés. “Influence of Pearlite Morphology and Heating Rate on the Kinetics of Continuously Heated Austenite Formation in a Eutectoid Steel”. In: *Metallurgical and Materials Transactions A* 32.6 (June 2001), pp. 1283–1291. ISSN: 1073-5623, 1543-1940. DOI: 10.1007/s11661-001-0218-3 (cit. on pp. 47, 162, 191).
- [Cah56] John W Cahn. “Transformation Kinetics during Continuous Cooling”. In: *Acta Metallurgica* 4.6 (Nov. 1956), pp. 572–575. ISSN: 00016160. DOI: 10.1016/0001-6160(56)90158-4 (cit. on p. 191).
- [Chb+14] A. Chbihi et al. “Interactions between Ferrite Recrystallization and Austenite Formation in High-Strength Steels”. In: *Journal of Materials Science* 49.10 (May 2014), pp. 3608–3621. ISSN: 0022-2461, 1573-4803. DOI: 10.1007/s10853-014-8029-2 (cit. on pp. xx, xxiii, xxviii, 3, 4, 24, 35, 37–40, 42–45, 93, 103, 106, 109, 110, 127, 128, 132, 151, 153, 161).
- [Chr02] John Christian. *The Theory of Transformations in Metals and Alloys*. Newnes, 2002 (cit. on pp. 51, 71).
- [Coa72] D. E. Coates. “Diffusion-Controlled Precipitate Growth in Ternary Systems I”. In: *Metallurgical Transactions* 3.5 (May 1972), pp. 1203–1212. ISSN: 0360-2133, 1543-1916. DOI: 10.1007/BF02642453 (cit. on p. 26).
- [Coa73a] D. E. Coates. “Diffusion Controlled Precipitate Growth in Ternary Systems: II”. In: *Metallurgical Transactions* 4.4 (Apr. 1973), pp. 1077–1086. ISSN: 0360-2133, 1543-1916. DOI: 10.1007/BF02645611 (cit. on p. 28).
- [Coa73b] D. E. Coates. “Diffusional Growth Limitation and Hardenability”. In: *Metallurgical Transactions* 4.10 (Oct. 1973), pp. 2313–2325. ISSN: 0360-2133, 1543-1916. DOI: 10.1007/BF02669370 (cit. on pp. 26, 28).
- [Cou+21] Clélia Couchet et al. “Recovery of Severely Deformed Ferrite Studied by in Situ High Energy X-ray Diffraction”. In: *Materials Characterization* 179 (Sept. 1, 2021), p. 111378. ISSN: 1044-5803. DOI: 10.1016/j.matchar.2021.111378 (cit. on pp. xx, 4, 10, 15, 17, 18, 108).
- [Cou+23] Clélia Couchet et al. “Numerical Investigations of Phase Transformations Controlled by Interface Thermodynamic Conditions during Intercritical Annealing of Steels”. In: *Metals* 13.7 (7 July 2023), p. 1288. ISSN: 2075-4701. DOI: 10.3390/met13071288 (cit. on pp. xxi, xxii, xxviii, 5, 32, 33, 35–37, 39, 47, 93, 105, 106, 108, 109, 129, 136, 137, 139, 142–144, 146, 150, 151, 160, 185–187, 190).
- [Dar42] LS Darken. “Diffusion in Metal Accompanied by Phase Change”. In: *Metals Technology* 9.5 (1942), pp. 1–13 (cit. on p. 83).
- [Dar49] LS Darken. “Diffusion of Carbon in Austenite with a Discontinuity in Composition”. In: *Trans. AIME*. 180 (1949), pp. 430–438 (cit. on p. 83).
- [DFS92] Sabine Denis, D Farias, and A Simon. “Mathematical Model Coupling Phase Transformations and Temperature Evolutions in Steels”. In: *ISIJ international* 32.3 (1992), pp. 316–325 (cit. on p. 48).
- [Doh+97] R D Doherty et al. “Current Issues in Recrystallization: A Review”. In: *Materials Science and Engineering A* (1997), p. 56 (cit. on pp. 9–11, 14, 15, 64, 108).

- [Eno+18] M. Enomoto et al. “Partition and Non-Partition Transition of Austenite Growth from a Ferrite and Cementite Mixture in Hypo- and Hypereutectoid Fe-C-Mn Alloys”. In: *Calphad* 61 (June 2018), pp. 116–125. ISSN: 03645916. DOI: 10.1016/j.calphad.2018.03.002 (cit. on pp. 30–32, 34, 49).
- [Esi+14] VA Esin et al. “In Situ Synchrotron X-ray Diffraction and Dilatometric Study of Austenite Formation in a Multi-Component Steel: Influence of Initial Microstructure and Heating Rate”. In: *Acta materialia* 80 (Nov. 2014), pp. 118, 131. ISSN: 1359-6454 (cit. on p. 75).
- [ECP] S Estay, Li Chengji, and G R Purdy. “Carbide Dissolution and Austenite Growth in the Intercritical Annealing of Fe–C–Mn Dual Phase Steels”. In: (), p. 10 (cit. on p. 26).
- [Fon15] Nina Fonstein. *Advanced High Strength Sheet Steels*. Springer, 2015 (cit. on p. 83).
- [FKM04] T. Furuhashi, K. Kobayashi, and T. Maki. “Control of Cementite Precipitation in Lath Martensite by Rapid Heating and Tempering”. In: *ISIJ International* 44.11 (2004), pp. 1937–1944. ISSN: 0915-1559. DOI: 10.2355/isijinternational.44.1937 (cit. on p. 16).
- [GD81] C. I. Garcia and A. J. Deardo. “Formation of Austenite in 1.5 Pct Mn Steels”. In: *Metallurgical Transactions A* 12.3 (Mar. 1981), pp. 521–530. ISSN: 0360-2133, 1543-1940. DOI: 10.1007/BF02648551 (cit. on p. 24).
- [Gen+20] Xiaoxiao Geng et al. “Modeling of CCT Diagrams for Tool Steels Using Different Machine Learning Techniques”. In: *Computational Materials Science* 171 (Jan. 2020), p. 109235. ISSN: 09270256. DOI: 10.1016/j.commatsci.2019.109235 (cit. on pp. 53, 54).
- [GMD12] M. Gouné, P. Maugis, and J. Drillet. “A Criterion for the Change from Fast to Slow Regime of Cementite Dissolution in Fe–C–Mn Steels”. In: *Journal of Materials Science & Technology* 28.8 (Aug. 2012), pp. 728–736. ISSN: 10050302. DOI: 10.1016/S1005-0302(12)60122-4 (cit. on pp. 31, 32).
- [Gou+15] M. Gouné et al. “Overview of the Current Issues in Austenite to Ferrite Transformation and the Role of Migrating Interfaces Therein for Low Alloyed Steels”. In: *Materials Science and Engineering: R: Reports* 92 (June 2015), pp. 1–38. ISSN: 0927796X. DOI: 10.1016/j.mser.2015.03.001 (cit. on pp. 26, 27, 49, 51, 146).
- [Gra08] Granbom. “Effects of Process Parameters Prior to Annealing on the Formability of Two Cold Rolled Dual Phase Steels”. In: *steel research international* 79.4 (2008), pp. 297–305 (cit. on p. 124).
- [HBB20] Thawin Hart-Rawung, Johannes Buhl, and Markus Bambach. “A Fast Approach for Optimization of Hot Stamping Based on Machine Learning of Phase Transformation Kinetics”. In: *Procedia Manufacturing* 47 (2020), pp. 707–712. ISSN: 23519789. DOI: 10.1016/j.promfg.2020.04.218 (cit. on pp. 53, 54).
- [Hil71] M Hillert. “Diffusion Controlled Growth of Lamellar Eutectics and Eutectoids in Binary and Ternary Systems”. In: *Acta Metallurgica* 19.8 (Aug. 1971), pp. 769–778. ISSN: 00016160. DOI: 10.1016/0001-6160(71)90133-7 (cit. on pp. 34, 35).

- [HS76] Mats Hillert and Bo Sundman. “A Treatment of the Solute Drag on Moving Grain Boundaries and Phase Interfaces in Binary Alloys”. In: *Acta Metallurgica* 24.8 (Aug. 1976), pp. 731–743. ISSN: 00016160. DOI: 10.1016/0001-6160(76)90108-5 (cit. on p. 51).
- [HPM04] J. Huang, W. J. Poole, and M. Militzer. “Austenite Formation during Intercritical Annealing”. In: *Metallurgical and Materials Transactions A* 35.11 (Nov. 2004), pp. 3363–3375. ISSN: 1073-5623, 1543-1940. DOI: 10.1007/s11661-004-0173-x (cit. on pp. xx, 3, 4, 24, 25, 30, 35, 37–40, 42, 43, 45, 48, 66, 93, 109, 125, 128, 143, 153, 161).
- [Hul20] Axel Hultgren. *A Metallographic Study on Tungsten Steels*. J. Wiley, 1920 (cit. on pp. 24, 90, 96, 138).
- [Hul47] Axel Hultgren. “Isothermal Transformation of Austenite”. In: *Transactions of the American Society for Metals* 39 (1947), pp. 915–1005 (cit. on pp. 26, 28).
- [Hul53] Axel Hultgren. *Isothermal Transformation of Austenite and Partitioning of Alloying Elements in Low Alloy Steels*. Almqvist och Wiksell, 1953 (cit. on p. 26).
- [HH95] F. J. Humphreys and M. Hatherly. *Recrystallization and Related Annealing Phenomena*. 1st ed. Oxford, OX, UK ; Tarrytown, N.Y., U.S.A: Pergamon, 1995. ISBN: 978-0-08-041884-1 (cit. on pp. xx, xxv, 4, 9–18, 39, 64, 71, 80, 81, 87, 99, 100, 108, 122, 123, 125, 126).
- [Hum97] F.J. Humphreys. “A Unified Theory of Recovery, Recrystallization and Grain Growth, Based on the Stability and Growth of Cellular Microstructures—I. The Basic Model”. In: *Acta Materialia* 45.10 (Oct. 1997), pp. 4231–4240. ISSN: 1359-6454. DOI: 10.1016/S1359-6454(97)00070-0 (cit. on pp. 10, 14, 15, 64).
- [Hum99] F.J. Humphreys. “A New Analysis of Recovery, Recrystallisation, and Grain Growth”. In: *Materials Science and Technology* 15.1 (Jan. 1999), pp. 37–44. ISSN: 0267-0836, 1743-2847. DOI: 10.1179/026708399773002791 (cit. on pp. 9, 16).
- [JM39] William Johnson and Robert Mehl. “Reaction Kinetics in Processes of Nucleation and Growth”. In: *Trans. Metall. Soc. AIME* 135 (1939), pp. 416–442 (cit. on p. 48).
- [Kam+15] H. Kamoutsi et al. “Kinetics of Solute Partitioning During Intercritical Annealing of a Medium-Mn Steel”. In: *Metallurgical and Materials Transactions A* 46.11 (Nov. 2015), pp. 4841–4846. ISSN: 1073-5623, 1543-1940. DOI: 10.1007/s11661-015-3118-7 (cit. on pp. 29, 30, 109, 143, 147).
- [KLH11] Jun-Yun Kang, Hu-Chul Lee, and Seong Ho Han. “Effect of Al and Mo on the Textures and Microstructures of Dual Phase Steels”. In: *Materials Science and Engineering: A* 530 (Dec. 2011), pp. 183–190. ISSN: 09215093. DOI: 10.1016/j.msea.2011.09.071 (cit. on p. 22).
- [Kho+11] A. Khorsand Zak et al. “X-Ray Analysis of ZnO Nanoparticles by Williamson–Hall and Size–Strain Plot Methods”. In: *Solid State Sciences* 13.1 (Jan. 2011), pp. 251–256. ISSN: 12932558. DOI: 10.1016/j.solidstatesciences.2010.11.024 (cit. on p. 18).
- [Kol37] AN Kolmogorov. “A Statistical Theory of Metal Crystallization”. In: *Acad. Nauk USSR, Ser. Math.*, 3 355 (1937) (cit. on p. 48).

- [KSvdZ97] Gerben P. Krielaart, Jilt Sietsma, and Sybrand van der Zwaag. “Ferrite Formation in Fe-C Alloys during Austenite Decomposition under Non-Equilibrium Interface Conditions”. In: *Materials Science and Engineering: A* 237.2 (Sept. 1997), pp. 216–223. ISSN: 09215093. DOI: 10.1016/S0921-5093(97)00365-1 (cit. on p. 51).
- [KPM13] M. Kulakov, W. J. Poole, and M. Militzer. “The Effect of the Initial Microstructure on Recrystallization and Austenite Formation in a DP600 Steel”. In: *Metallurgical and Materials Transactions A* 44.8 (Aug. 2013), pp. 3564–3576. ISSN: 1073-5623, 1543-1940. DOI: 10.1007/s11661-013-1721-z (cit. on pp. 24, 48, 190, 191).
- [KPM14] Mykola Kulakov, Warren J. Poole, and Matthias Militzer. “A Microstructure Evolution Model for Intercritical Annealing of a Low-carbon Dual-phase Steel”. In: *ISIJ International* 54.11 (2014), pp. 2627–2636. ISSN: 0915-1559, 1347-5460. DOI: 10.2355/isijinternational.54.2627 (cit. on pp. 48, 190).
- [Kwo+10] Ohjoon Kwon et al. “New trends in advanced high strength steel developments for automotive application”. In: *Materials Science Forum*. Vol. 638. Trans Tech Publ. 2010, pp. 136–141 (cit. on p. 2).
- [Lai+16] Qingquan Lai et al. “Mechanism of Austenite Formation from Spheroidized Microstructure in an Intermediate Fe-0.1C-3.5Mn Steel”. In: *Metallurgical and Materials Transactions A* 47.7 (July 2016), pp. 3375–3386. ISSN: 1073-5623, 1543-1940. DOI: 10.1007/s11661-016-3547-y (cit. on pp. xxi, 4, 5, 30–35, 46, 47, 50, 109, 143, 147).
- [Lau+03] E.M Lauridsen et al. “Recrystallization Kinetics of Individual Bulk Grains in 90% Cold-Rolled Aluminium”. In: *Acta Materialia* 51.15 (Sept. 2003), pp. 4423–4435. ISSN: 13596454. DOI: 10.1016/S1359-6454(03)00278-7 (cit. on pp. 11, 12, 19, 20, 76, 81).
- [Lau+06] E.M. Lauridsen et al. “Non-Destructive Characterization of Recrystallization Kinetics Using Three-Dimensional X-ray Diffraction Microscopy”. In: *Scripta Materialia* 55.1 (July 2006), pp. 51–56. ISSN: 13596462. DOI: 10.1016/j.scriptamat.2006.02.028 (cit. on pp. 11, 12, 19, 20, 76, 81).
- [Lau01] Erik Mejdal Lauridsen. “The 3D X-Ray Diffraction Microscope and Its Application to the Study of Recrystallization Kinetics”. PhD thesis. 2001 (cit. on pp. 19, 20).
- [LTH90] J -W Lee, SW Thompson, and PR Howell. “Microstructural Development in Non-Oriented Lamination Steels: Part 2 Isothermal Transformation Studies”. In: *Journal of materials science* 25 (1990), pp. 1699–1710 (cit. on p. 23).
- [Lee+93] JW Lee et al. “The Interaction between Proeutectoid Ferrite and Austenite during the Isothermal Transformation of Two Low-Carbon Steels—a New Model for the Decomposition of Austenite”. In: *Journal of materials science* 28 (1993), pp. 4571–4577 (cit. on p. 23).
- [Li+13] Pei Li et al. “Effect of Heating Rate on Ferrite Recrystallization and Austenite Formation of Cold-Roll Dual Phase Steel”. In: *Journal of Alloys and Compounds* 578 (Nov. 2013), pp. 320–327. ISSN: 09258388. DOI: 10.1016/j.jallcom.2013.05.226 (cit. on pp. xx, 3, 4, 24, 25, 35, 37, 39, 40, 42–45, 48, 93, 109, 128, 153, 160, 161).

- [LFZ19] Shenglong Liang, Fateh Fazeli, and Hatem S. Zurob. “Effects of Solutes and Temperature on High-Temperature Deformation and Subsequent Recovery in Hot-Rolled Low Alloy Steels”. In: *Materials Science and Engineering: A* 765 (Sept. 2019), p. 138324. ISSN: 09215093. DOI: 10.1016/j.msea.2019.138324 (cit. on pp. 71, 82).
- [Liu97] Zi-Kui Liu. “The Transformation Phenomenon in Fe-Mo-C Alloys: A Solute Drag Approach”. In: *Metallurgical and Materials Transactions A* 28 (1997), pp. 1625–1631 (cit. on p. 51).
- [Liu+91] Zi-Kui Liu et al. “An Experimental and Theoretical Study of Cementite Dissolution in an Fe-Cr-C Alloy”. In: *Metallurgical Transactions A* 22.8 (Aug. 1991), pp. 1745–1752. ISSN: 0360-2133, 1543-1940. DOI: 10.1007/BF02646498 (cit. on pp. 30, 50).
- [Liu+16] Zhenyu Liu et al. “Microstructural Characterization and Recrystallization Kinetics Modeling of Annealing Cold-Rolled Vanadium Microalloyed HSLA Steels”. In: *Journal of Alloys and Compounds* 679 (Sept. 15, 2016), pp. 293–301. ISSN: 0925-8388. DOI: 10.1016/j.jallcom.2016.04.057 (cit. on p. 15).
- [Mad+13] L. Madej et al. “Multi Scale Cellular Automata and Finite Element Based Model for Cold Deformation and Annealing of a Ferritic–Pearlitic Microstructure”. In: *Computational Materials Science* 77 (Sept. 2013), pp. 172–181. ISSN: 09270256. DOI: 10.1016/j.commatsci.2013.04.020 (cit. on p. 52).
- [Mar+20] Arthur Marceaux dit Clément et al. “Effects of Cementite Size and Chemistry on the Kinetics of Austenite Formation during Heating of a High-Formability Steel”. In: *Computational Materials Science* 182 (Sept. 1, 2020), p. 109786. ISSN: 0927-0256. DOI: 10.1016/j.commatsci.2020.109786 (cit. on pp. 30, 35, 47, 50, 106, 107).
- [MAG04] A Martínez-de-Guerenu, F Arizti, and I Gutiérrez. “Recovery during Annealing in a Cold Rolled Low Carbon Steel. Part II: Modelling the Kinetics”. In: *Acta Materialia* 52.12 (July 2004), pp. 3665–3670. ISSN: 13596454. DOI: 10.1016/j.actamat.2004.04.020 (cit. on pp. 15–18).
- [Mar+04] A Martínez-de-Guerenu et al. “Recovery during Annealing in a Cold Rolled Low Carbon Steel. Part I: Kinetics and Microstructural Characterization”. In: *Acta Materialia* 52.12 (July 2004), pp. 3657–3664. ISSN: 13596454. DOI: 10.1016/j.actamat.2004.04.019 (cit. on pp. 9, 10, 15).
- [Mat20] Alexandre Mathevon. “Characterization and modelling of microstructural evolutions and mechanical properties during the thermal treatments of Dual-Phase steels”. In: (2020) (cit. on pp. 53, 54).
- [Mat+12] David K Matlock et al. “Recent developments in advanced high strength sheet steels for automotive applications: an overview”. In: *Jestech* 15.1 (2012), pp. 1–12 (cit. on p. 2).
- [MBS15] M.G. Mecozzi, C. Bos, and J. Sietsma. “A Mixed-Mode Model for the Ferrite-to-Austenite Transformation in a Ferrite/Pearlite Microstructure”. In: *Acta Materialia* 88 (Apr. 2015), pp. 302–313. ISSN: 13596454. DOI: 10.1016/j.actamat.2015.01.058 (cit. on p. 51).

- [Miy+10] G. Miyamoto et al. “Effects of Mn, Si and Cr Addition on Reverse Transformation at 1073K from Spheroidized Cementite Structure in Fe–0.6 Mass% C Alloy”. In: *Acta Materialia* 58.13 (Aug. 2010), pp. 4492–4502. ISSN: 13596454. DOI: 10.1016/j.actamat.2010.04.045 (cit. on pp. 30, 31, 34, 35, 42, 47, 93, 105, 106).
- [MGF11] R. R. Mohanty, O. A. Girina, and N. M. Fonstein. “Effect of Heating Rate on the Austenite Formation in Low-Carbon High-Strength Steels Annealed in the Inter-critical Region”. In: *Metallurgical and Materials Transactions A* 42.12 (Dec. 1, 2011), pp. 3680–3690. ISSN: 1543-1940. DOI: 10.1007/s11661-011-0753-5 (cit. on pp. xx, xxviii, 3, 23, 24, 37, 39, 40, 42–45, 93, 109, 110, 127, 132, 151, 153, 161).
- [Mor19] Marc Moreno. “Metallurgical Mechanisms and Their Interactions during the Annealing of Cold-Rolled Ferrite-Pearlite Steels : Characterization and Modeling”. PhD thesis. Université de Lorraine, June 18, 2019. URL: <https://hal.univ-lorraine.fr/tel-02349113> (cit. on pp. xxi–xxiii, xxv, xxix, 4, 5, 20, 30, 32, 35–40, 42, 43, 45–47, 55, 61, 63, 73, 76, 83, 87, 88, 90, 91, 93, 95, 96, 103–106, 108–111, 119, 129, 132, 136–138, 143, 144, 150, 151, 153, 155–157, 159–161, 186, 187, 190–194).
- [Mor+18] Marc Moreno et al. “Real-Time Investigation of Recovery, Recrystallization and Austenite Transformation during Annealing of a Cold-Rolled Steel Using High Energy X-ray Diffraction (HEXRD)”. In: *Metals* 9.1 (Dec. 2018), p. 8. ISSN: 2075-4701. DOI: 10.3390/met9010008 (cit. on pp. xxi, 11, 16, 18, 20–22, 54, 64, 76, 81, 83, 99, 100, 108, 123, 159).
- [Mor+19] Marc Moreno et al. “Evolution of Cementite Composition along the Processing of Cold-Rolled and Annealed Dual-Phase Steels”. In: *Materialia* 6 (June 2019), p. 100179. ISSN: 25891529. DOI: 10.1016/j.mtla.2018.100179 (cit. on pp. 91–93).
- [MH96] K. Mukunthan and E. B. Hawbolt. “Modeling Recovery and Recrystallization Kinetics in Cold-Rolled Ti-Nb Stabilized Interstitial-Free Steel”. In: *Metallurgical and Materials Transactions A* 27.11 (Nov. 1996), pp. 3410–3423. ISSN: 1073-5623, 1543-1940. DOI: 10.1007/BF02595434 (cit. on p. 18).
- [Nak04] James Thomas Nakos. *Uncertainty Analysis of Thermocouple Measurements Used in Normal and Abnormal Thermal Environment Experiments at Sandia’s Radiant Heat Facility and Lurance Canyon Burn Site*. SAND2004-1023. Sandia National Laboratories (SNL), Albuquerque, NM, and Livermore, CA (United States), Apr. 1, 2004. DOI: 10.2172/918777 (cit. on pp. 61, 75).
- [Nan+19] Tarun Nanda et al. “Third generation of advanced high-strength steels: Processing routes and properties”. In: *Proceedings of the Institution of Mechanical Engineers, Part L: Journal of Materials: Design and Applications* 233.2 (2019), pp. 209–238 (cit. on p. 2).
- [Nes95] E. Nes. “Recovery Revisited”. In: *Acta Metallurgica et Materialia* 43.6 (June 1995), pp. 2189–2207. ISSN: 0956-7151. DOI: 10.1016/0956-7151(94)00409-9 (cit. on pp. xx, 4, 10, 126).

- [Oll+17] M. Ollat et al. “Modeling of the Recrystallization and Austenite Formation Overlapping in Cold-Rolled Dual-Phase Steels During Intercritical Treatments”. In: *Metallurgical and Materials Transactions A* 48.10 (Oct. 2017), pp. 4486–4499. ISSN: 1073-5623, 1543-1940. DOI: 10.1007/s11661-017-4231-6 (cit. on pp. xxviii, 26, 30, 31, 35, 47–51, 66, 132, 143, 147, 151, 190, 191).
- [Oll17] Mélanie Ollat. “Characterization and Modeling of Microstructural Evolutions during the Thermal Treatment of Cold-Rolled Dual-Phase Steels”. PhD thesis. 2017 (cit. on pp. 109, 110).
- [Oll+18] Mélanie Ollat et al. “Mixed-Mode Model for Ferrite-to-Austenite Phase Transformation in Dual-Phase Steel”. In: *Computational Materials Science* 149 (June 15, 2018), pp. 282–290. ISSN: 0927-0256. DOI: 10.1016/j.commatsci.2018.02.052 (cit. on pp. 51, 52).
- [OMG08] M. Oyarzábal, A. Martínez-de-Guerenu, and I. Gutiérrez. “Effect of Stored Energy and Recovery on the Overall Recrystallization Kinetics of a Cold Rolled Low Carbon Steel”. In: *Materials Science and Engineering: A* 485.1-2 (June 2008), pp. 200–209. ISSN: 09215093. DOI: 10.1016/j.msea.2007.07.077 (cit. on pp. 9, 11, 12, 15, 18, 71, 81, 99, 100, 123).
- [Per+10] N. Peranio et al. “Microstructure and Texture Evolution in Dual-Phase Steels: Competition between Recovery, Recrystallization, and Phase Transformation”. In: *Materials Science and Engineering: A* 527.16-17 (June 2010), pp. 4161–4168. ISSN: 09215093. DOI: 10.1016/j.msea.2010.03.028 (cit. on p. 22).
- [Peš+03] J. Pešička et al. “The Evolution of Dislocation Density during Heat Treatment and Creep of Tempered Martensite Ferritic Steels”. In: *Acta Materialia* 51.16 (Sept. 2003), pp. 4847–4862. ISSN: 13596454. DOI: 10.1016/S1359-6454(03)00324-0 (cit. on p. 18).
- [Pou+11] S.O. Poulsen et al. “In Situ Measurements of Growth Rates and Grain-Averaged Activation Energies of Individual Grains during Recrystallization of 50% Cold-Rolled Aluminium”. In: *Scripta Materialia* 64.11 (June 2011), pp. 1003–1006. ISSN: 13596462. DOI: 10.1016/j.scriptamat.2011.01.046 (cit. on pp. 11, 12, 19, 20, 76, 81, 108).
- [Pow79] M. J. Powell. “Site Percolation in Randomly Packed Spheres”. In: *Physical Review B* 20.10 (Nov. 15, 1979), pp. 4194–4198. ISSN: 0163-1829. DOI: 10.1103/PhysRevB.20.4194 (cit. on p. 105).
- [PÖ20] Okan Poyraz and Bilgehan Ögel. “Recrystallization, Grain Growth and Austenite Formation in Cold Rolled Steels during Intercritical Annealing”. In: *Journal of Materials Research and Technology* 9.5 (Sept. 2020), pp. 11263–11277. ISSN: 22387854. DOI: 10.1016/j.jmrt.2020.08.015 (cit. on p. 125).
- [PWK64] GR Purdy, DH Weichert, and JS Kirkaldy. “Growth of Proeutectoid Ferrite in Ternary Iron-Carbon-Manganese Austenites”. In: *Transactions of the Metallurgical Society of AIME* 230.5 (1964), p. 1025 (cit. on p. 26).
- [Pus+15] Irina Pushkareva et al. “Relationship between Microstructure, Mechanical Properties and Damage Mechanisms in High Martensite Fraction Dual Phase Steels”. In: *ISIJ International* 55.10 (2015), pp. 2237–2246. ISSN: 0915-1559, 1347-5460. DOI: 10.2355/isijinternational.ISIJINT-2015-186 (cit. on pp. xix, xx, 1, 3, 5, 87).

- [Rad15] Krzysztof Radwański. “Application of FEG-SEM and EBSD Methods for the Analysis of the Restoration Processes Occurring During Continuous Annealing of Dual-Phase Steel Strips”. In: *steel research international* 86.11 (Nov. 2015), pp. 1379–1390. ISSN: 16113683. DOI: 10.1002/srin.201400361 (cit. on pp. 15, 16, 64).
- [Ray85] R. K. Ray. “Deformation and Recrystallization Textures in a Dual-Phase Steel”. In: *Journal of Materials Science Letters* 4.1 (Jan. 1985), pp. 67–70. ISSN: 0261-8028, 1573-4811. DOI: 10.1007/BF00719899 (cit. on p. 22).
- [Rei52] Stanley F. Reiter. “Recrystallization Kinetics of Low Carbon Steel”. In: *JOM* 4.9 (Sept. 1952), pp. 972–979. ISSN: 1047-4838, 1543-1851. DOI: 10.1007/BF03397755 (cit. on pp. xxv, 11, 14, 81, 87, 99, 100, 108, 123, 126).
- [RGU04] G. Ribárik, J. Gubicza, and T. Ungár. “Correlation between Strength and Microstructure of Ball-Milled Al–Mg Alloys Determined by X-ray Diffraction”. In: *Materials Science and Engineering: A* 387–389 (Dec. 2004), pp. 343–347. ISSN: 09215093. DOI: 10.1016/j.msea.2004.01.089 (cit. on p. 18).
- [RU10] Gábor Ribárik and Tamás Ungár. “Characterization of the Microstructure in Random and Textured Polycrystals and Single Crystals by Diffraction Line Profile Analysis”. In: *Materials Science and Engineering: A* 528.1 (Nov. 2010), pp. 112–121. ISSN: 09215093. DOI: 10.1016/j.msea.2010.08.059 (cit. on p. 18).
- [Rie69] H. M. Rietveld. “A Profile Refinement Method for Nuclear and Magnetic Structures”. In: *Journal of Applied Crystallography* 2.2 (June 2, 1969), pp. 65–71. ISSN: 00218898. DOI: 10.1107/S0021889869006558 (cit. on p. 74).
- [Rod93] Juan Rodríguez-Carvajal. “Recent Advances in Magnetic Structure Determination by Neutron Powder Diffraction”. In: *Physica B: Condensed Matter* 192.1-2 (Oct. 1993), pp. 55–69. ISSN: 09214526. DOI: 10.1016/0921-4526(93)90108-I (cit. on p. 74).
- [RGF83] A. Roósz, Z. Gácsi, and E.G. Fuchs. “Isothermal Formation of Austenite in Eutectoid Plain Carbon Steel”. In: *Acta Metallurgica* 31.4 (Apr. 1983), pp. 509–517. ISSN: 00016160. DOI: 10.1016/0001-6160(83)90039-1 (cit. on p. 47).
- [Rud+11] J. Rudnizki et al. “Phase-Field Modeling of Austenite Formation from a Ferrite plus Pearlite Microstructure during Annealing of Cold-Rolled Dual-Phase Steel”. In: *Metallurgical and Materials Transactions A* 42.8 (Aug. 2011), pp. 2516–2525. ISSN: 1073-5623, 1543-1940. DOI: 10.1007/s11661-011-0626-y (cit. on pp. 45, 52, 53).
- [Sal+15] N. Sallel et al. “In Situ Characterization of Microstructural Instabilities: Recovery, Recrystallization and Abnormal Growth in Nanoreinforced Steel Powder”. In: *Acta Materialia* 87 (Apr. 2015), pp. 377–389. ISSN: 13596454. DOI: 10.1016/j.actamat.2014.11.051 (cit. on p. 18).
- [Sco+17] C. P. Scott et al. “Structure-Properties Relationship of Ultra-Fine Grained V-microalloyed Dual Phase Steels”. In: *Materials Science and Engineering: A* 703 (Aug. 4, 2017), pp. 293–303. ISSN: 0921-5093. DOI: 10.1016/j.msea.2017.07.051 (cit. on pp. xix, xx, 1, 3, 87).
- [SvdZ04] Jilt Sietsma and Sybrand van der Zwaag. “A Concise Model for Mixed-Mode Phase Transformations in the Solid State”. In: *Acta Materialia* 52.14 (Aug. 2004), pp. 4143–4152. ISSN: 13596454. DOI: 10.1016/j.actamat.2004.05.027 (cit. on p. 51).

- [Sla18] Meriem Ben Haj Slama. “Étude Multi-Échelle et in Situ Des Évolutions Microstructurales En Conditions Isothermes d’aciers Bainitiques En Lattes”. PhD thesis. Université de Lorraine, 2018 (cit. on p. 15).
- [Smi+04] Ali Smith et al. “Recovery Processes in the Ferrite Phase in C-Mn Steel”. In: *ISIJ International* 44.7 (2004), pp. 1188–1194. ISSN: 0915-1559. DOI: 10.2355/isijinternational.44.1188 (cit. on p. 16).
- [Son+14] Rongjie Song et al. “Effects of Nb on Microstructural Evolution and Mechanical Properties of Low-Carbon Cold-Rolled Dual-Phase Steels”. In: *Metallography, Microstructure, and Analysis* 3.3 (June 1, 2014), pp. 174–184. ISSN: 2192-9270. DOI: 10.1007/s13632-014-0133-9 (cit. on pp. xxv, 12, 39, 87, 126).
- [SDM81] G. R. Speich, V. A. Demarest, and R. L. Miller. “Formation of Austenite During Intercritical Annealing of Dual-Phase Steels”. In: *Metallurgical and Materials Transactions A* 12.8 (Aug. 1981), pp. 1419–1428. ISSN: 1073-5623, 1543-1940. DOI: 10.1007/BF02643686 (cit. on pp. xxi, 5, 26, 28–30, 46, 49, 109, 148).
- [ST94] G. Sundararajan and Y. Tirupataiah. “The Hardness-Flow Stress Correlation in Metallic Materials”. In: *Bulletin of Materials Science* 17.6 (Nov. 1, 1994), pp. 747–770. ISSN: 0973-7669. DOI: 10.1007/BF02757555 (cit. on p. 17).
- [Sun] B Sundman. “SGTE (Scientific Group Thermodata Europe) Solution Database of Jan. 1994”. In: *Div. of Computational thermodynamics* () (cit. on p. 84).
- [Swa64] M. L. Swanson. “LOW-TEMPERATURE RECOVERY OF DEFORMED ALUMINUM”. In: *Canadian Journal of Physics* 42.10 (Oct. 1964), pp. 1890–1901. ISSN: 0008-4204, 1208-6045. DOI: 10.1139/p64-178 (cit. on p. 18).
- [TMT18] Setsuo Takaki, Takuro Masumura, and Toshihiro Tsuchiyama. “Proposal of Simplified Modified Williamson-Hall Equation”. In: *ISIJ International* 58.12 (Dec. 2018), pp. 2354–2356. ISSN: 0915-1559, 1347-5460. DOI: 10.2355/isijinternational.ISIJINT-2018-517 (cit. on p. 18).
- [TMT19] Setsuo Takaki, Takuro Masumura, and Toshihiro Tsuchiyama. “Dislocation Characterization by the Direct-fitting/Modified Williamson-Hall (DF/mWH) Method in Cold Worked Ferritic Steel”. In: *ISIJ International* 59.3 (Mar. 2019), pp. 567–572. ISSN: 0915-1559, 1347-5460. DOI: 10.2355/isijinternational.ISIJINT-2018-623 (cit. on p. 18).
- [Tei+21] J. Teixeira et al. “Intercritical Annealing of Cold-Rolled Ferrite-Pearlite Steel: Microstructure Evolutions and Phase Transformation Kinetics”. In: *Acta Materialia* 212 (June 2021), p. 116920. ISSN: 13596454. DOI: 10.1016/j.actamat.2021.116920 (cit. on pp. xx–xxiii, xxv, xxvi, xxix, 3, 5, 24, 26, 29–31, 34–40, 42–47, 50, 55, 83, 87, 93, 95, 96, 103–106, 108–111, 127, 129, 131–133, 136–138, 143, 144, 151, 153, 155–157, 160, 161, 185–187, 190, 194).
- [TM18] Larrin S. Thomas and David K. Matlock. “Formation of Banded Microstructures with Rapid Intercritical Annealing of Cold-Rolled Sheet Steel”. In: *Metallurgical and Materials Transactions A* 49.10 (Oct. 1, 2018), pp. 4456–4473. ISSN: 1543-1940. DOI: 10.1007/s11661-018-4742-9 (cit. on pp. xx, xxviii, 3, 24, 35, 37, 39, 40, 42–45, 93, 109, 110, 127, 128, 132, 151, 153, 161).
- [TK87] Yong Lai Tian and R Wayne Kraft. “Mechanisms of Pearlite Spheroidization”. In: *Metallurgical transactions A* 18 (1987), pp. 1403–1414 (cit. on pp. xxi, 4, 93).

- [Ung04] T Ungár. “Microstructural Parameters from X-ray Diffraction Peak Broadening”. In: *Scripta Materialia* 51.8 (Oct. 2004), pp. 777–781. ISSN: 13596462. DOI: 10.1016/j.scriptamat.2004.05.007 (cit. on p. 18).
- [UB96] T. Ungár and A. Borbély. “The Effect of Dislocation Contrast on X-ray Line Broadening: A New Approach to Line Profile Analysis”. In: *Applied Physics Letters* 69.21 (Nov. 1996), pp. 3173–3175. ISSN: 0003-6951, 1077-3118. DOI: 10.1063/1.117951 (cit. on p. 18).
- [Ung+99] T. Ungár et al. “The Contrast Factors of Dislocations in Cubic Crystals: The Dislocation Model of Strain Anisotropy in Practice”. In: *Journal of Applied Crystallography* 32.5 (Oct. 1999), pp. 992–1002. ISSN: 0021-8898. DOI: 10.1107/S0021889899009334 (cit. on p. 18).
- [Ung+14] Tamás Ungár et al. “Slip Systems and Dislocation Densities in Individual Grains of Polycrystalline Aggregates of Plastically Deformed CoTi and CoZr Alloys”. In: *Acta Materialia* 71 (June 2014), pp. 264–282. ISSN: 13596454. DOI: 10.1016/j.actamat.2014.03.024 (cit. on p. 18).
- [VR90] R.A. Vandermeer and B.B. Rath. “Interface Migration during Recrystallization: The Role of Recovery and Stored Energy Gradients”. In: *Metallurgical Transactions A* 21.4 (1990), pp. 1143–1149 (cit. on p. 14).
- [Vat+96] H.E. Vatne et al. “Modelling Recrystallization after Hot Deformation of Aluminium”. In: *Acta Materialia* 44.11 (Nov. 1996), pp. 4463–4473. ISSN: 13596454. DOI: 10.1016/1359-6454(96)00078-X (cit. on pp. 14, 64).
- [VBG98] M. Verdier, Y. Brechet, and P. Guyot. “Recovery of AlMg Alloys: Flow Stress and Strain-Hardening Properties”. In: *Acta Materialia* 47.1 (Dec. 1998), pp. 127–134. ISSN: 13596454. DOI: 10.1016/S1359-6454(98)00350-4 (cit. on pp. 10, 16, 18).
- [Ver+09] Stephanie Vervynckt et al. “Austenite Recrystallization–Precipitation Interaction in Niobium Microalloyed Steels”. In: *ISIJ International* 49.6 (2009), pp. 911–920. ISSN: 0915-1559, 1347-5460. DOI: 10.2355/isijinternational.49.911 (cit. on pp. xxv, 12, 13, 17, 39, 87, 126).
- [Wei+13] R. Wei et al. “Growth of Austenite from As-Quenched Martensite during Intercritical Annealing in an Fe–0.1C–3Mn–1.5Si Alloy”. In: *Acta Materialia* 61.2 (Jan. 2013), pp. 697–707. ISSN: 13596454. DOI: 10.1016/j.actamat.2012.10.019 (cit. on pp. 26, 29, 30, 50, 109, 143, 147).
- [WH53] G.K Williamson and W.H Hall. “X-Ray Line Broadening from Filed Aluminium and Wolfram”. In: *Acta Metallurgica* 1.1 (Jan. 1953), pp. 22–31. ISSN: 00016160. DOI: 10.1016/0001-6160(53)90006-6 (cit. on p. 18).
- [Wu+20] Y.X. Wu et al. “The Effect of Alloying Elements on Cementite Coarsening during Martensite Tempering”. In: *Acta Materialia* 183 (Jan. 2020), pp. 418–437. ISSN: 13596454. DOI: 10.1016/j.actamat.2019.11.040 (cit. on pp. 30, 34, 35, 39, 42, 47, 50, 93, 105).
- [WPE81] P A Wycliffe, G R Purdy, and J D Embury. “Growth of Austenite in the Intercritical Annealing of Fe-C-Mn Dual Phase Steels”. In: (1981), p. 12 (cit. on pp. xxii, xxix, 26, 49, 50, 54, 55, 110, 144–146, 149, 152, 156, 160, 194).

- [Xia+13] Yuan Xia et al. “Effects of Alloying Elements on the Kinetics of Austenitization from Pearlite in Fe–C–M Alloys”. In: *Philosophical Magazine* 93.9 (Mar. 2013), pp. 1095–1109. ISSN: 1478-6435, 1478-6443. DOI: 10.1080/14786435.2012.744484 (cit. on p. 31).
- [Yan+85] D. Z. Yang et al. “The Formation of Austenite at Low Intercritical Annealing Temperatures in a Normalized 0.08C-1.45Mn-0.21Si Steel”. In: *Metallurgical Transactions A* 16.8 (Aug. 1985), pp. 1523–1526. ISSN: 0360-2133, 1543-1940. DOI: 10.1007/BF02658685 (cit. on p. 40).
- [Zen49] Clarence Zener. “Theory of Growth of Spherical Precipitates from Solid Solution”. In: *Journal of Applied Physics* 20.10 (1949), p. 950. ISSN: 0021-8979. DOI: 10.1063/1.1698258 (cit. on pp. 49, 146).
- [Zha+13] Guo-Hong Zhang et al. “Effects of Mn, Si and Cr Addition on the Dissolution and Coarsening of Pearlitic Cementite during Intercritical Austenitization in Fe-1mass%C Alloy”. In: *Materials Characterization* 81 (July 2013), pp. 56–67. ISSN: 10445803. DOI: 10.1016/j.matchar.2013.04.007 (cit. on p. 35).
- [Zha+14] H. Zhang et al. “New Insights into the Austenitization Process of Low-Alloyed Hypereutectoid Steels: Nucleation Analysis of Strain-Induced Austenite Formation”. In: *Acta Materialia* 80 (Nov. 2014), pp. 296–308. ISSN: 13596454. DOI: 10.1016/j.actamat.2014.07.073 (cit. on p. 16).
- [ZR13] Chengwu Zheng and Dierk Raabe. “Interaction between Recrystallization and Phase Transformation during Intercritical Annealing in a Cold-Rolled Dual-Phase Steel: A Cellular Automaton Model”. In: *Acta Materialia* 61.14 (Aug. 2013), pp. 5504–5517. ISSN: 13596454. DOI: 10.1016/j.actamat.2013.05.040 (cit. on pp. 9, 52).
- [ZM15] Benqiang Zhu and Matthias Militzer. “Phase-Field Modeling for Intercritical Annealing of a Dual-Phase Steel”. In: *Metallurgical and Materials Transactions A* 46.3 (Mar. 2015), pp. 1073–1084. ISSN: 1073-5623, 1543-1940. DOI: 10.1007/s11661-014-2698-y (cit. on pp. 41, 42, 44, 45, 47, 52, 53).
- [ZBD06] H Zurob, Y Brechet, and J Dunlop. “Quantitative Criterion for Recrystallization Nucleation in Single-Phase Alloys: Prediction of Critical Strains and Incubation Times”. In: *Acta Materialia* 54.15 (Sept. 2006), pp. 3983–3990. ISSN: 13596454. DOI: 10.1016/j.actamat.2006.04.028 (cit. on pp. 14, 64).



---

## Appendix A

# Ferrite recrystallization followed by SEM/EBSD

---

This appendix shows the SEM/EBSD maps carried out to follow ferrite recrystallization in the Mn05 CR65 and the MN20 CR65, presented in II.1 during annealing at 650 °C.

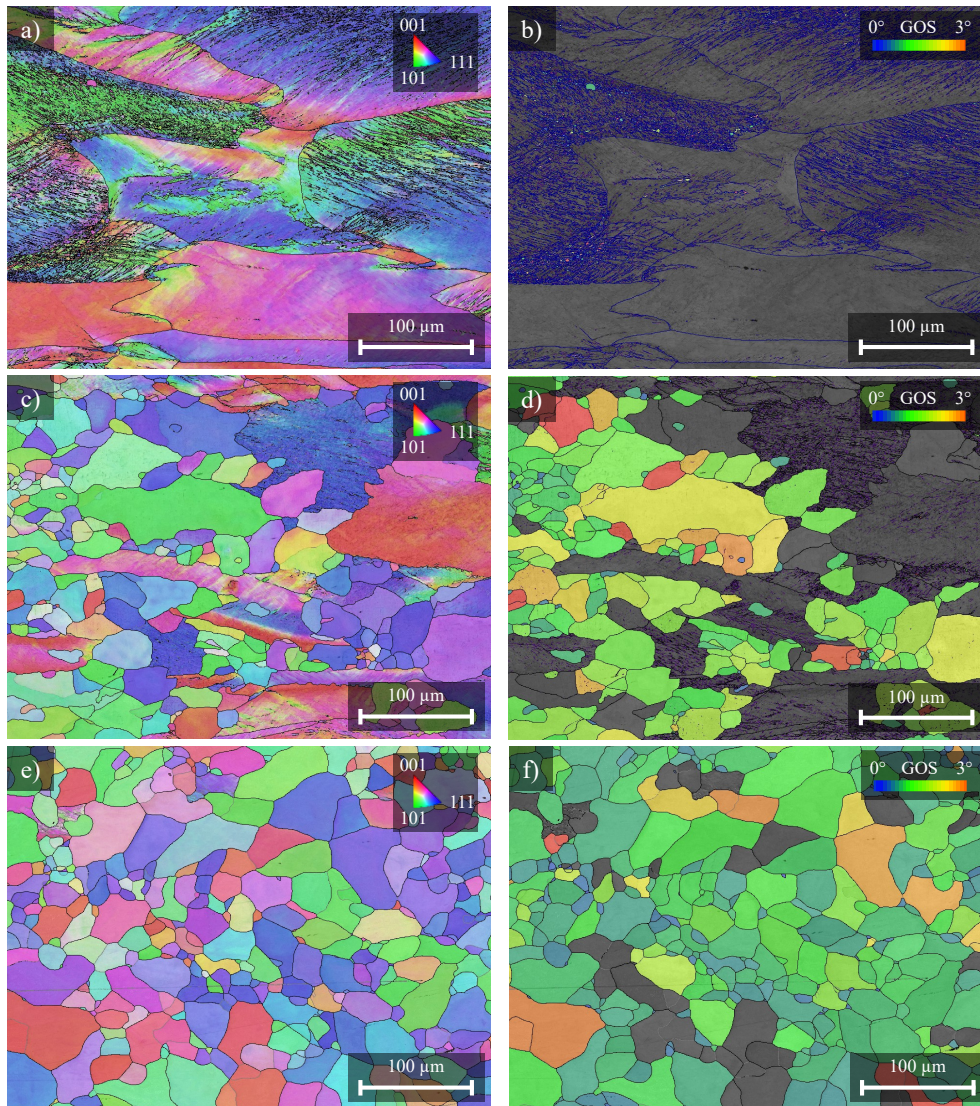


Figure A.1: IPF maps (a, c, e) and GOS maps (b, d, f) (magnification x 300) of the Mn05 CR65 steel after 0 s (a and b), 15 s (c and d) and 50 s (e and f) at 650 °C. (b), (d) and (f) highlight grains with a GOS lower than 3 °.

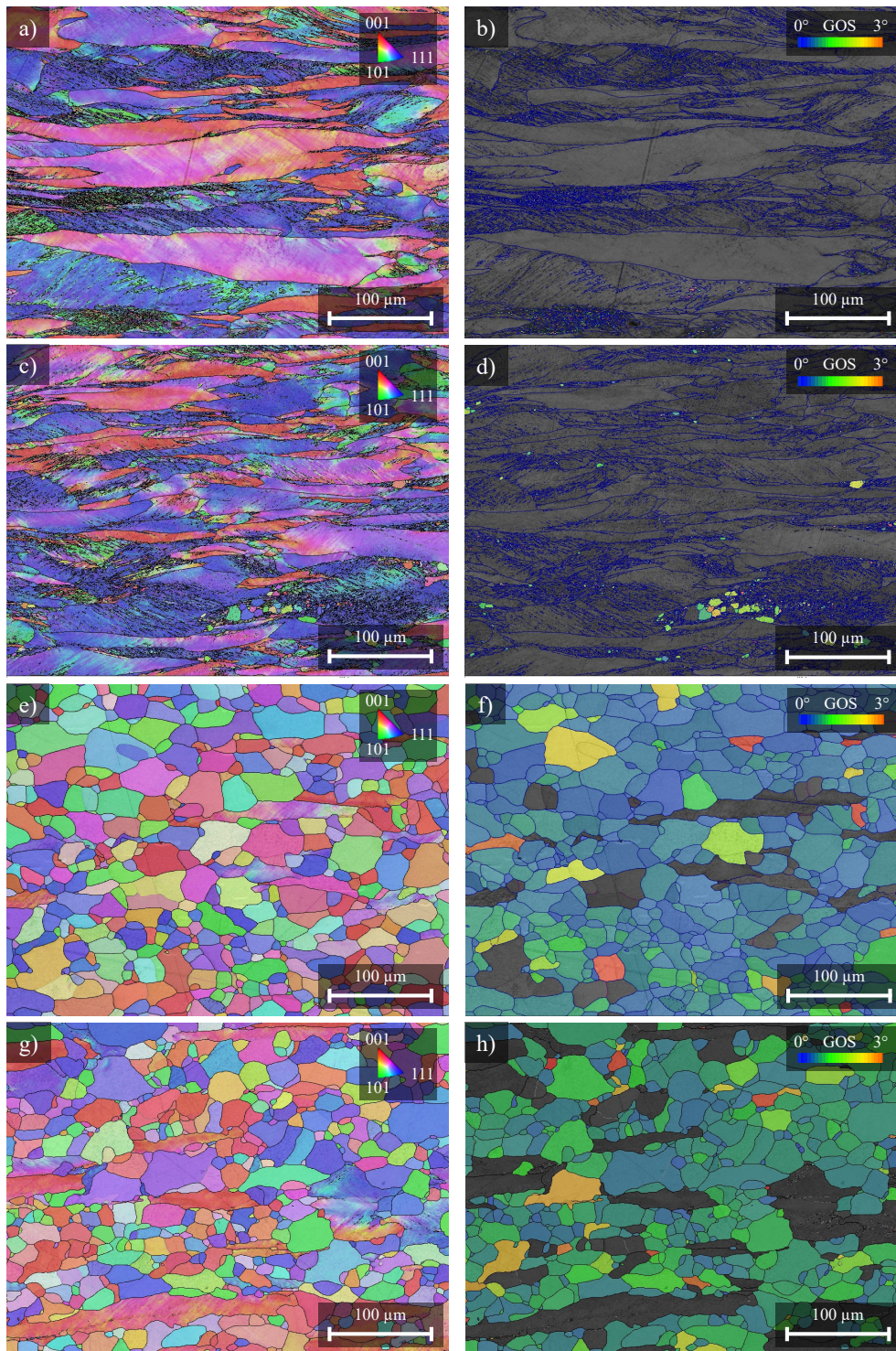


Figure A.2: IPF maps (a, c, e, g) and GOS maps (b, d, f, h) (magnification  $\times 300$ ) of the Mn20 CR65 steel after 0 s (a and b), 25 s (c and d), 300 s (e and f) and 400 s (g and h) at 650 °C. (b), (d), (f) and (h) highlight grains with a GOS lower than 3 °.



---

## Appendix B

# Repeatability of HEXRD experiments

---

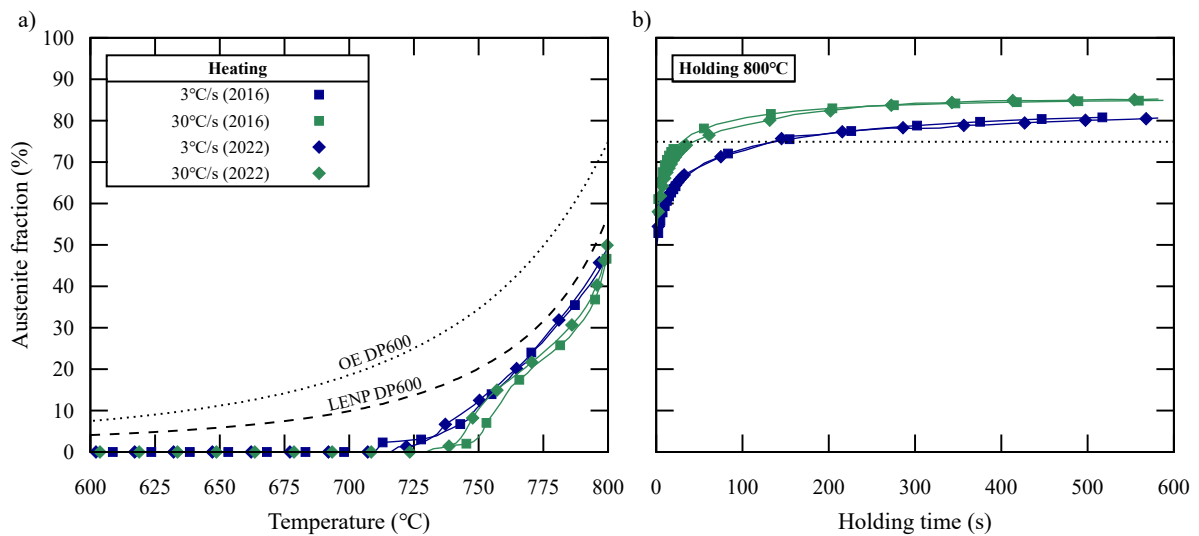


Figure B.1: Austenite formation kinetics during the intercritical annealing of the DP600 CR65 at 3 °C/s (blue) and 30 °C/s (green), during the heating (a) and isothermal holding (b) stages, followed by HEXRD (Rietveld post-treatments respectively). The experiments were performed in 2016 (in squares) and in 2022 (in diamonds) on the PETRA III – P07 synchrotron beamline at DESY facilities.



---

## Appendix C

# Physically-based prediction of the austenite fraction during heating stage

---

This section proposes an approach to predict the austenite fraction along the heating stage of the studied DP600. The mechanisms of austenite formation were studied through experiments in Chapter III and numerical simulations in the previous section and previous published works [Cou+23; Tei+21]. Here is the strategy developed in the section from the conclusions drawn. Figure C.1 schematizes our strategy.

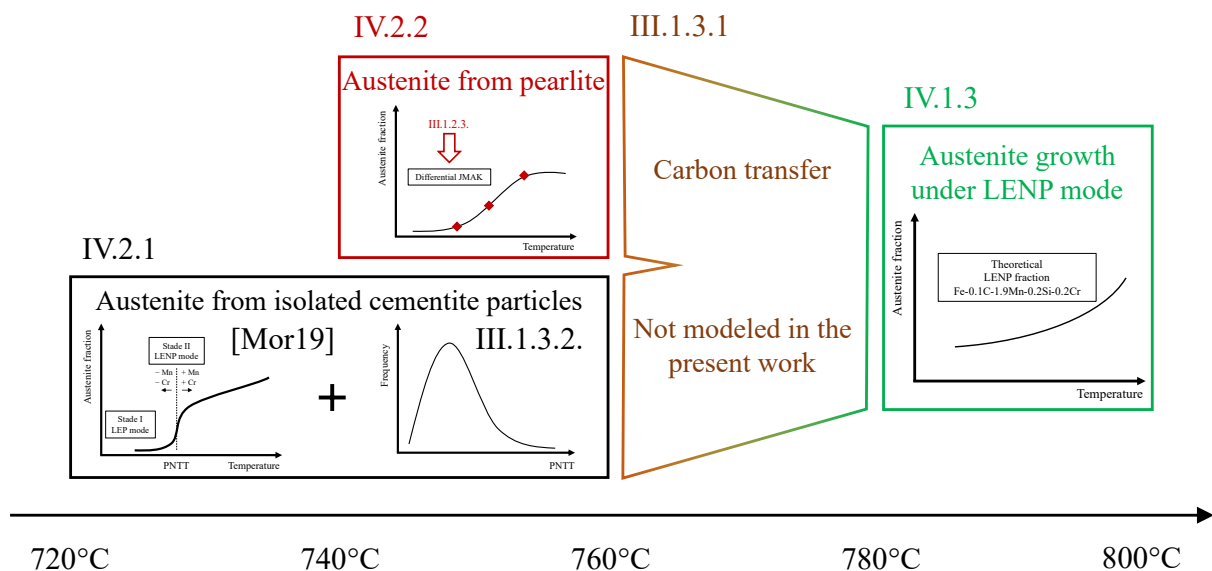


Figure C.1: Diagram of the approach to predict the austenite formation kinetics along the heating stage.

Chapter III supports an approach considering the austenite growth from the isolated cemen-

tite particles and from the pearlite islands separately up to 760 °C. Then, a carbon transfer was revealed between both growing austenites between 760 °C and 780 °C, making such separation irrelevant. This carbon transfer and the evolution of the austenite fraction during this stage are not modeled in the present work. The approach in separated subsystems is maintained up to 780 °C, at the end of the carbon transfer. At temperature above 780 °C, the thermo-kinetic analysis from Section IV.1 in addition to the discussion in Chapter III shows that the austenite grows under LENP mode and that its fraction is close to the theoretical LENP fraction (LENP interface conditions, no carbon or substitutional element gradient in austenite nor in ferrite) considering the full quinary system Fe-0.1C-1.9Mn-0.2Si-0.2Cr.

The next sub-sections detail of the proposed modeling strategy.

The first sub-section shows the method used to predict the austenite fraction formed from the isolated cementite particles. We use the conclusions from previous work [Cou+23; Mor19] on the austenite formation kinetics from an isolated cementite particle, associated with the experimental data presented in Chapter III.

Then, the prediction of the austenite fraction formed from the pearlite bands is based on the microstructural observations and austenite fraction estimation from Chapter III. A differential JMAK is fitted on these experimental data.

Finally, in the last sub-section, we present the global kinetics predicted with our simplified approach.

Below 780 °C, the studied DP600 is separated in two closed subsystems. One subsystem contains the cementite particles and the ferrite matrix (CP&M). The other contains the pearlite islands (P). The carbon contained in each subsystem is given by a carbon balance:

$$\underbrace{w_C^0}_{0.1 \text{ wt\%}} = f_{CP\&M} \times w_C^{CP\&M} + f_P \times \underbrace{w_C^P}_{0.39 \text{ wt\%}} \quad (\text{C.1})$$

with  $f_P = 16 \%$  is the fraction of pearlite in the studied DP600 and  $w_C^P = 0.39 \text{ wt\%}$  (1.78 at%) is its carbon content (III.1.1). The subsystem CP&M occupies a fraction  $f_{CP\&M} = 1 - f_P$  of the full system. The carbon balance gives its carbon nominal content  $w_C^{CP\&M} = 0.045 \text{ wt\%}$  (0.21 at%). The u-fraction of substitutional elements is assumed uniform in the whole system, thus, equal in each subsystem.

This division is inspired from [Mor19; Tei+21]) but is very different. Their division was designed to last up to the end of the heating stage. The growth of austenite after complete transformation of the pearlite or after the complete dissolution of the cementite particles should be possible, making the separation in subsystems a tricky step in their study. In the present study, the analysis in subsystem is stopped when the subsystems at 780 °C, when all cementite particles are dissolved and pearlite is transformed.

## C.1 Austenite fraction from cementite particles isolated in the ferrite matrix (CP&M subsystem)

Our previous work [Cou+23; Mor19; Tei+21] and the discussions in Chapter III and the previous section support that austenite formation from an isolated cementite particle is a purely diffusion-controlled phase transformation. It starts under LEP mode (Stage I). When the temperature reaches the PNTT, austenite growth fast under LENP mode (Stage II). After complete dissolution of the particle, austenite continues its growth. The growth mode (LEP or LENP) is determined by the heating rate and the diffusion distances.

These studies especially reveal that temperature is the main thermodynamic variable leading the austenite formation, through the PNTT and the LENP fraction. Thus, in the present study, diffusion is not modeled.

We propose an approach based on thermodynamic parameters only. This saves numerical resources, as no time or space discretization is needed, contrary to most of the modeling solution presented in Chapter I.

The following hypothesis result from this choice:

The austenite fraction formed during stage I is neglected. During this stage, manganese diffusion highly limits the austenite growth. In our previous DICTRA simulations [Cou+23; Mor19; Tei+21], this stage produces only 5 % of austenite.

The stage II starts at the PNTT of the studied cementite particle. In [Cou+23; Mor19; Tei+21], carbon diffusion delays the starting temperature of stage II by only few degrees (5 °C maximum)

Fast dissolution of the cementite particle in stage II is instantaneous. In [Cou+23; Mor19; Tei+21], stage II occurs in a 1 °C range during slow heating and 4 °C during fast heating.

The austenite fraction along stage III follows the theoretical LENP fraction, written  $f_{\gamma}^{\text{LENP}}(T)$  at the temperature T (weighted by the fraction of carbon contained by the particle). This assumption is further discussed in the following.

### C.1.1 Validation of the approach

To discuss further these hypotheses, we first compute the austenite fraction formed considering an average composition of cementite particle and we compare the results to the DICTRA simulation presented in [Cou+23]. As the simulation in [Cou+23] is performed in the DP600 considering the simplified ternary Fe-0.1C-1.9Mn ( wt%), the computation of the theoretical LENP fraction only considers the simplified ternary too. The cementite particles are assumed enriched along slow heating (3 °C/s). Their average manganese content and radius are estimated at 8.8 at% and 110 nm respectively. Note that the radius is only relevant for the full DICTRA simulation. The PNTT of the considered cementite particles is 731 °C.

Figure C.2 shows the austenite fraction calculated with the proposed approach in red and with DICTRA during slow heating (3 °C/s) in black. Our approach (in red) predicts no austenite under the PNTT, in respect with the first assumption. Under the PNTT, the DICTRA simulation (in black) predicts only 2 % of austenite. This difference during the stage I is considered acceptable. At the PNTT, the austenite fraction predicted by our approach (in red) shows a discontinuity. It increases instantaneously from zero to the current theoretical LENP fraction according to the second and third assumptions. In the DICTRA simulation (in black), stage II is slightly shifted by 5 °C. Finally, above the PNTT, the austenite fraction predicted by our approach is the theoretical LENP fraction, according to the last assumption. But the DICTRA simulation shows a larger austenite fraction, as it predicts growth under LEP mode. The gap between our prediction and the DICTRA simulation increases with the temperature. The DICTRA simulation shows + 4 % at 760 °C and + 7 % at 780 °C higher than our prediction with the simplified schema. Under 760 °C, the difference between DICTRA and our prediction is acceptable. Then, the temperature range between 760 °C and 780 °C is outside the scope of our assumptions. In this temperature range, the carbon transfer between austenite from the isolated cementite particles and from pearlite should be modeled.

The computation using our approach is almost instantaneous as it simply consists in the evaluation of a thermodynamic condition (under or above the PNTT). The second assumption

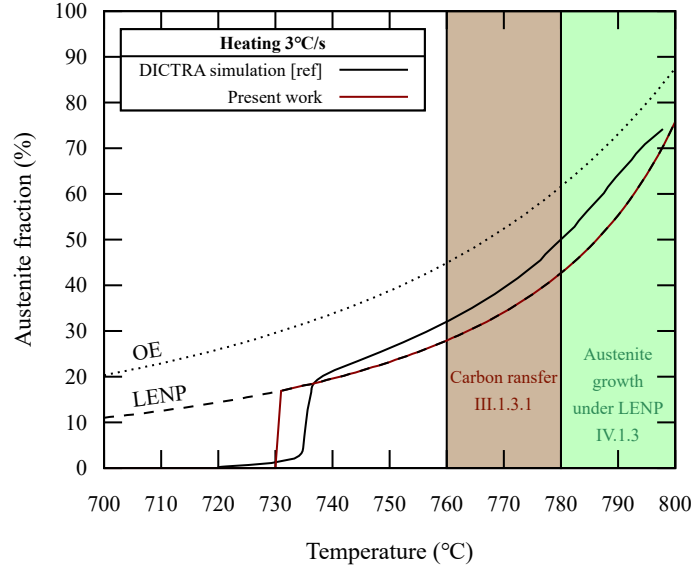


Figure C.2: Austenite fractions computed with the approach proposed in the present work (in red) and with DICTRA during slow heating at 3 °C/s (in black). The theoretical LENP and OE fractions are plotted with a dashed line and a dotted line respectively considering the simplified ternary composition Fe-0.045C-1.9Mn (%wt) of the subsystem CP&M.

makes the model sensitive to the composition of the cementite particle, which shifts the beginning of stage II.

### C.1.2 Computation of the austenite fraction formed from a distribution of cementite particles

As the computation is very fast and is sensitive to the PNTT, we can use it to simulate optionally the austenite formation from cementite particles in the subsystem (CP&M), considering the distribution of compositions presented in Chapter III (III.1.2.2). This calculation is based on an experimental knowledge. If the mean composition of carbide is known, the mean PNTT can be used as above.

The full quinary composition of the studied subsystem (CP&M) Fe-0.045C-1.9Mn-0.2Si-0.2Cr (wt%), as Chapter III highlighted its impact on the PNTT and the previous section shows a lower theoretical LENP fraction than considering the simplified ternary. The theoretical LENP fractions are computed with Thermo-Calc, using the TCFE9 database.

The fraction of cementite particle having a PNTT between  $T$  and  $T + dT$  is written  $f_{PNTT}(T)$ . The fraction of cementite particle already dissolved at a given temperature  $T$ , i.e. whose PNTT is lower than  $T$ , is given by the integral  $\frac{1}{T-T_s} \int_{T_s}^T f_{PNTT}(T) dT$ . Finally, the austenite fraction formed from cementite particles at a temperature  $T$  is given by the formula:

$$f_{\gamma}^{CP}(T) = f_{\gamma}^{LENP}(T) \times \frac{1}{T - T_s} \int_{T_s}^T f_{PNTT}(T) dT \quad (C.2)$$

Figure C.3 shows the results of our approach accounting for the distribution of compositions of the isolated cementite particles, presented in Chapter III (III.1.2.2). The prediction of the

austenite fraction is plotted in solid lines considering the distribution of composition of the non-enriched cementite particles (in green) and the enriched cementite particles (in blue). As the subsystem (CP&M) represents 84 % of the full system,  $f_{\gamma}^{CP}(T)$  is multiplied by 0.84 to obtain the austenite fraction in the full system. The predicted fractions are compared to the austenite fraction obtained by optical micrography (black open diamonds). The theoretical LENP (in black dashed line) and OE (in black dotted line) fraction of the subsystem (CP&M) Fe-0.045C-1.9Mn-0.2Si-0.2Cr (wt%) are plotted as references.

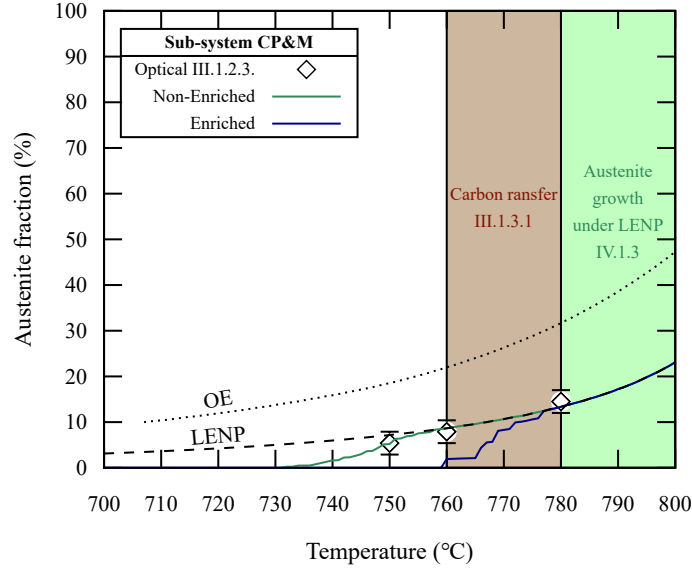


Figure C.3: Austenite fractions predicted with our approach accounting for the distribution of compositions of the isolated cementite particles, enriched (blue) along slow heating or not (green), presented in Chapter III (III.1.2.2). The predicted fractions are compared to the austenite fraction obtained by optical micrography (black open diamonds). The theoretical LENP (in black dashed line) and OE (in black dotted line) fraction of the subsystem (CP&M) Fe-0.045C-1.9Mn-0.2Si-0.2Cr (wt%) are plotted as references.

The austenite fractions computed using the distribution of non-enriched cementite particles (in green) starts increasing at 730 °C and reaches the theoretical LENP fraction around 755 °C. Using the distribution of the enriched cementite particles (in blue), the beginning of austenite formation is shifted 30 °C higher, as it starts at 760 °C and the theoretical LENP fraction is reached at 780 °C. These temperature ranges correspond to the range of PNTT plotted in III.15 (b).

The austenite fractions computed using the distribution of the non-enriched particles reproduce with accuracy the austenite fractions obtained by optical metallography (less than 3 % error). On the contrary, considering the enriched cementite particles (in blue) make the computed fractions widens the gap from experimental fractions.

At 750 °C, the experimental fraction indicates 5 %. Considering our first assumption (neglecting the austenite fraction formed in stage I), this is in the error range of our approach in the early stage of the phase transformation. The last assumption (Stage III forms a theoretical LENP fraction of austenite) also introduces an error. Though, it is more likely to impact the

kinetics later in the heating stage. These cumulated errors can explain the discrepancy between the experimental fractions and the fractions predicted with our simplified approach. Neglecting the growth of austenite with manganese redistribution (in stage I and III) seems a too sharp assumption. Modeling austenite growth with manganese redistribution could be of great interest in the future to improve the current prediction.

In addition, the distributions of cementite particle composition used to compute the PNTT are obtained from EDXS measurements presented in Chapter III (Figure III.4). The distribution of composition of non-enriched cementite particles is obtained from the analysis of 22 cementite particles. On the contrary, only 9 cementite particles were analyzed to produce the distribution of composition of enriched cementite particles. The lower predictive capacity of our approach using this latter distribution may be due to low statistics.

The present study focused on predicting the austenite fraction formed in the subsystem (CP&M), containing the ferrite matrix and the cementite particles. Contrary to previous work [Cou+23; Mor19; Tei+21] using mean values in DICTRA simulations, this part shows it is possible to consider the distributions of cementite particle composition. The proposed approach offers a very fast computation of the austenite fractions from cementite particle and accounts easily for a distribution of composition of the cementite particles.

## C.2 Austenite fraction from the pearlite (P subsystem)

Previous studies [Mor19; Tei+21]) on the pearlite to austenite transformation show that the spheroidized cementite particles in pearlite dissolves under LEP mode, thanks to very short diffusion paths. Consequently, the previous approach would not suit to predict the austenite fraction formed from pearlite bands under 780 °C.

Along this PhD work on the mechanisms of austenite formation, we have mainly focused on the experimental characterization and modeling of the austenite formation from cementite particles and along the isothermal holding stage. In the end, few experimental data were available on pearlite. But we still needed to predict the austenite fraction formed from pearlite with reasonable precision to complete the study of austenite formation along the heating stage. We chose an empirical approach and we predict the austenite fraction formed in the subsystem (P), containing the pearlite, using the differential form of the JMAK model [KPM14; KPM13; Oll+17]. This empirical approach is an efficient option, as its implementation is quick and easy, but the parameters must be fitted on experimental data (as the ones presented in Chapter III (III.1.2.3)).

The austenite fraction in the subsystem (P) is written  $Y$  in the following. The austenite fraction  $Y$  is linked to the fraction  $f_\gamma^P$  in the full system of austenite formed in pearlite islands as  $Y \frac{f_\gamma^P}{f_P}$ , with  $f_P = 16$  % the initial pearlite fraction in the full system. The increment in transformed fraction is given by the formula:

$$\frac{dY}{dt} = (nb(t))^n t^{n-1} (1 - Y(t)) \quad (\text{C.3})$$

The Avrami exponent  $n$  is constant with temperature. The rate constant  $b$  (in s<sup>-1</sup>) is a function of temperature  $T$  as follows:

$$b(T) = b_0 \exp\left(\frac{-Q}{RT}\right) \quad (\text{C.4})$$

with  $b_0$  a constant (in  $s^{-1}$ ),  $Q$  the activation energy of the transformation (in J/mol) and  $R$  the gas constant ( $8.314 \text{ J.K}^{-1}.\text{mol}^{-1}$ ). As working with temperature  $T$  rather than time  $t$ , the variable  $t$  is changed to  $\frac{T-T_s}{h}$ .  $T_s$  is the temperature, which the transformation starts at, and  $h$  is the heating rate.

The austenite fraction formed along the transformation of pearlite is estimated using an additivity rule [Cah56; KPM13; Oll+17].

In Chapter III, the subsystem (P) was experimentally investigated only using our slow heating rate ( $3 \text{ }^\circ\text{C/s}$ ). The estimation of the constant  $b_0$  and the activation energy  $Q$  is not possible with our current data. To overpass this lack of data, we consider  $b$  constant with temperature. The starting temperature is set at  $730 \text{ }^\circ\text{C}$  from the observations in the study of Moreno et al. [Mor19]. As the subsystem (P) is 16 % of the full system,  $Y$  is multiplied by 0.16 to obtain the austenite fraction  $f_\gamma^P$  in the full system. Figure C.4 shows the fraction  $f_\gamma^P$  in the full system of austenite formed in pearlite islands during the heating stage at  $3 \text{ }^\circ\text{C/s}$ . The austenite fraction is reproduced the differential JMAK (in black line) is compared to the experimental fraction, presented in Chapter III (in red filled diamonds). The austenite fraction increases from  $730 \text{ }^\circ\text{C}$  up to  $12.5 \text{ }%$  at  $780 \text{ }^\circ\text{C}$ .

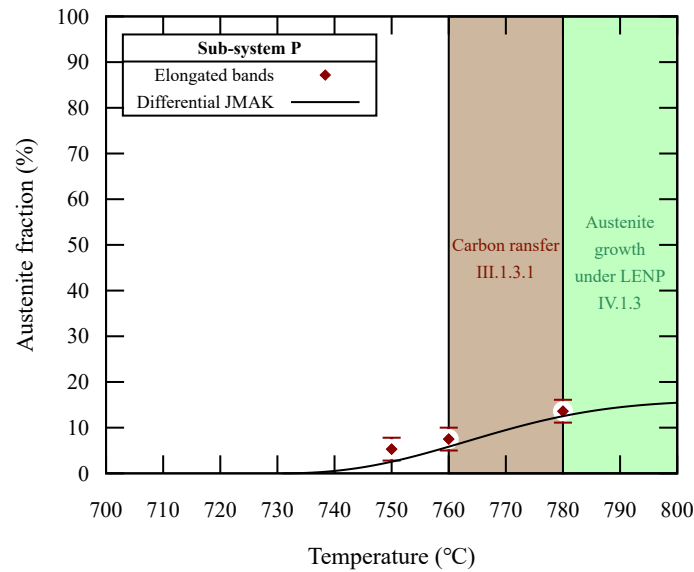


Figure C.4: Austenite fraction computed with the differential JMAK (in black line) formed from pearlite in the full system during the heating stage ( $3 \text{ }^\circ\text{C/s}$ ). The computed fractions are compared with the experimental fractions presented in Chapter III (in red filled diamonds).

A deeper investigation on the pearlite to austenite transformation is clearly required. Further experimental characterization of the pearlite islands and their transformation kinetics is required. Only then, a proper model, such as the one proposed by Caballero et al. [CCdA01], could be implemented.

### C.3 Global kinetics

The two previous sub-sections detailed our approach to predict the austenite fractions along the heating stage, under 780 °C, using two closed subsystems, (CP&M) containing the ferrite matrix and the cementite particles and (P) containing the pearlite islands.

As the subsystems constitute only a fraction of the full system (84 % and 16 % respectively), the simulated austenite fractions were weighted by the size of the subsystems. Under 780 °C, the global austenite fraction is obtained by the addition of the austenite fraction formed in the two subsystems.

Figure C.5 plots the global austenite fraction along the heating stage. Under 780 °C, we predict the austenite fractions accounting for the distribution of compositions of the isolated cementite particles enriched (in blue solid line) along slow heating or not (in green solid line), as presented in Chapter III (Figure III.4). Above 780 °C, the austenite fraction (in black solid line) is assumed equal to the theoretical LENP fraction considering the nominal composition of the studied DP600, as supported by the discussion in Chapter III and in the previous section.

The austenite fractions predicted with our strategy are compared to the kinetics obtained by Moreno et al. [Mor19] (in red solid line) in their thermo-kinetics analysis with subsystems using DICTRA simulations (considering the diffusion). Experimental data are also plotted as references: the austenite fraction obtained by optical micrography (in blue open diamonds) and the austenite fraction obtained from HEXRD experiments (in blue filled diamonds), presented in Chapter III (Figure III.12). The theoretical LENP and OE fractions of the studied DP600 (measured nominal composition from Table III.1) are plotted using black dashed line and black dotted line respectively.

The austenite fraction predicted with our approach in separated subsystems starts increasing at 730 °C up to 26 % at 780 °C (blue and green solid lines), regardless the considered distribution of cementite composition. Using the distribution of composition of the enriched cementite particles (in blue solid line) makes lower the predicted global austenite fraction, as it shifts their PNTT to higher temperature.

Our HEXRD experiments (presented in Chapter III in Figure III.12) and previous SEM investigation [Mor19] highlights that austenite nucleates between 710 °C and 720 °C, first on cementite particles. Regardless the distribution used, our prediction hardly catches the very beginning of the austenite formation, due to the limitations of our approach already discussed in III.1.3.2. In particular, the austenite fraction predicted by Moreno et al. [Mor19] using DICTRA simulations (in red solid line) reproduces with greater accuracy the HEXRD data (in blue filled diamonds) between 720 °C and 747 °C. In this temperature range, their simulations show that austenite mainly comes from the dissolution of the cementite particles under LEP mode. Thus, considering Stage I of austenite growth from cementite particles would be necessary to accurately predict the austenite fraction at the very beginning of the austenite formation.

Between 730 °C and 780 °C, the predicted austenite fraction using the distribution of composition of the non-enriched cementite particles offers a fair good description of the experimental data. This is due to the better description of the fraction of austenite formed from cementite particle, as shown in C.3. Yet, as presented in Chapter III, the studied enriched particles were enriched along slow heating stage at 3 °C/s. On the contrary, the non-enriched particles are assumed to represent the state of the particles along faster heating (30 °C/s for instance). As anticipated in the discussion in III.1.3.2, the austenite fraction from the enriched cementite particles increases at higher temperature that from the non-enriched particles, which is in contradiction with the HEXRD data presented in Figure III.12. To catch the effect of the heating

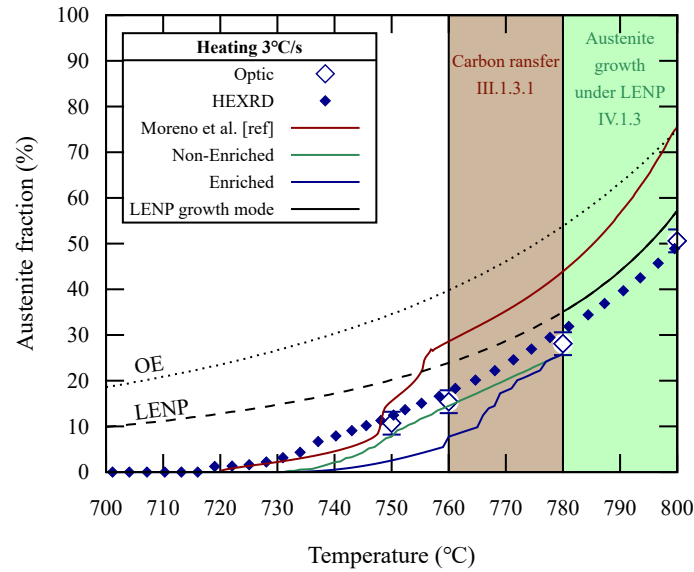


Figure C.5: Global austenite fraction during the heating stage (3 °C/s). Our prediction of the austenite fraction under 780 °C uses the approach with the subsystems (CP&M) and (P). The prediction accounts for the distribution of compositions of the isolated cementite particles, enriched (blue) during slow heating or not (green), as presented in Chapter III (Figure III.4). Above 780 °C, the global austenite fraction (in black) is supposed to follow the theoretical LENP fraction considering the full quinary composition of the studied DP600. The predicted fractions are compared to the fraction predicted by Moreno et al. [Mor19] using their DICTRA simulations and the experimental fraction obtained from the HEXRD experiments (in blue filled diamonds – Figure III.12) and from optical observations (in blue open diamonds – Figure III.6). The theoretical LENP (in black dashed line) and OE (in black dotted line) fraction of the DP600 (measured nominal composition – Table III.1) are plotted as references.

rate, accounting for the enrichment of the cementite particle may be not enough. Considering a nucleation flux may be necessary.

Despite the limitations discussed above, working with distributions of PNTT instead of a single value (the mean compositions) produces smoother increase of the austenite fractions along the heating stage compared to formation kinetics obtained from the thermo-kinetics approach of Moreno et al. [Mor19] (in red solid line).

At 780 °C, all the studied cementite particles are considered dissolved and our differential JMAK computation predicts that pearlite is almost completely transformed. The global austenite fraction is very close to the experimental data.

Above 780 °C, the predicted austenite fraction (in black solid line), which is assumed to be the theoretical LENP fraction of the full system, is much closer to the experimental data than the fraction predicted by Moreno et al. [Mor19] (in red solid line). This result speaks in favor of the austenite growth under LENP mode. It tends to confirm that considering separated subsystems (in red solid line) above 780 °C is less accurate than considering the full system.

Changing from the approach in subsystems to the theoretical LENP fraction at 780 °C introduces a discontinuity in the predicted austenite fraction (+ 13 %). Modeling the austenite

growth under LENP would produce a kinetics closer to the experiments. In addition, by starting the simulation at the fraction given by our current approach at 780 °C would avoid the present discontinuity. Wycliffe et al. [WPE81] proposed such a model, presented in Chapter I (I.4). As it will be shown in next section, this model can even be adapted to quinary systems and would still require few computation resources.

Despite the limitations presented here, the presented approach to predict the austenite fraction along the heating stage is precise for the industrial application.

## C.4 Conclusions on the prediction of austenite fraction along the heating stage

In this section, we proposed a computationally-efficient approach to predict the austenite fraction along the heating stage (a simplified model based only on purely thermodynamic calculations with diffusion and empirical inputs).

Based on our experimental investigation in Chapter III, our simulation work in the previous section and previous numerical work [Mor19; Tei+21]), simplifying hypotheses were assumed.

Under 780 °C, the system must be divided in two closed subsystems. The austenite fraction formed from cementite particles is computed using four assumptions. Austenite growth in LEP mode (stage I) is neglected. Fast austenite growth under LENP (Stage II) occurs instantaneously at the PNTT of the cementite particles. After complete dissolution of the particle (Stage III), the austenite fraction follows the theoretical LENP fraction. The distribution of cementite particle compositions could be considered optionally but for the moment our first results are difficult to apprehend.

A differential JMAK is fitted on these experimental data to predict the austenite fraction formed from pearlite.

Above 780 °C, the approach in separated subsystems is abandoned, to account for the carbon transfer revealed in Chapter III. Then, the full system is assumed to produce the theoretical LENP austenite fraction considering the quinary composition of the studied DP600.

These hypotheses make the computation of the austenite fractions is almost instantaneous, as no discretization of time or space is needed. The computation mainly relies on thermodynamic equilibrium calculations.

The predicted austenite fractions follow with fairly good accuracy the experimental data. In particular, considering a distribution of PNTT for the cementite particles helps smooth the austenite fractions compared to previous work based on DICTRA simulations. Our hypothesis above 780 °C also produces austenite fractions closer to the experimental data. These results tend to validate our assumptions and the computation of the austenite fraction is believed fast and precise enough to drive an industrial production line in real-time, as expected.

Though, few experimental data were available for the present PhD work. It would be interesting to investigate deeper the pearlite subsystem, to ensure the reliability of the approach regarding the heating rate. The global prediction also hardly catches the very beginning of the austenite formation, while the previous work based on DICTRA simulations reproduces it with great accuracy. Neglecting stage I of austenite formation from cementite particles is probably a too sharp assumption. Finally, to ensure the continuity of the model at 780 °C, a model for austenite growth under LENP mode could be implemented. Wycliffe et al. [WPE81] proposed such a model, which can even be adapted to quinary systems (see IV.2).





# New insights in understanding the interaction between recrystallization and phase transformation during intercritical annealing in DP steels

The formation of microstructures is a crucial step for steelmakers. In the case of DP steels, used for automotive construction, this formation takes place during intercritical annealing after cold-rolling. During this thermal treatment, after the heating step, the microstructure is made of recrystallized ferrite and austenite. During cooling, the austenite partially transforms into ferrite and then into martensite to reach the expected final ferrite/martensite microstructure. The austenitization step is therefore crucial for the manufacturers of these steels, to control the final phase fractions and sizes and, consequently, their mechanical properties. Numerous studies show that the heating rate controls the transformation kinetics and the morphology of the austenite ("necklace" or "banded"), but the underlying mechanisms remains a bone of contention. The overlap between ferrite recrystallization and austenite formation is often made responsible for these effects, through different mechanisms.

Using recent advances in in situ experiments on synchrotron beamlines, this PhD proposes a new insight in the understanding of the interactions between ferrite recrystallization and austenite formation and develops a predictive model for the austenite formation kinetics.

The main experimental development of this thesis is a new coupled time-resolved analysis technique, based on in situ High-Energy X-Ray Diffraction to track recrystallization and phase transformations during the annealing phase, including at high heating speeds. Our new method, called Isolated Diffraction Spot Tracking (IDST), is first validated to study recrystallization on model ferritic steels. These in situ measurements are supplemented by observations of microstructures after interrupted treatments in microscopy (optical, Scanning Electron Microscopy and Transmission Electron Microscopy), and from local chemistry measurements (Energy-Dispersive X-ray Spectroscopy and Wavelength Dispersion Spectroscopy)

We first reproduce experiments to study the influence of the heating rate on the studied steel during the intercritical annealing. In such experiments, the overlap between ferrite recrystallization and austenite formation is governed by the heating rate. To go further, we designed experiments to decorrelate the effect of the heating rate and this overlap. During these, the heating rate is fixed to maintain the same conditions for thermo-activated mechanisms, but the niobium microalloying and lower cold-rolling ratio are used to delay ferrite recrystallization. These experiments show unambiguously that austenite transformation kinetics is not controlled by the recrystallization, but by the sole thermodynamic condition of interfaces and maybe by the diffusion distance in the microstructures.

Finally, we propose a detailed thermo-kinetics analysis of the mechanisms of austenite formation during the intercritical annealing based on DICTRA/Thermo-Calc simulations and on our experimental work. The effect of minor alloying elements on the austenite growth kinetics is investigated. This work finally proposes new predictive models for austenite formation during the intercritical annealing.

This PhD work finally shows no significant effect of the concomitance of the two studied mechanisms on the austenite formation kinetics along the heating stage. We demonstrate that the austenite formation kinetics is diffusion-controlled. The difference in austenite formation kinetics along the holding stage is explained by microstructural considerations, affecting the diffusion distances.

**Key words:** Dual-Phase steel, recrystallization, phase transformation, High Energy X-Ray Diffraction (HEXRD), thermo-kinetics

# Nouvelles perspectives dans la compréhension de l'interaction entre la recristallisation et la transformation de phase lors du recuit intercritique dans les aciers DP

La formation des microstructures est cruciale pour la sidérurgie. Pour les aciers Dual Phase (DP), utilisés dans l'automobile, celle-ci a lieu lors du recuit intercritique après le laminage à froid. Après la chauffe, la microstructure est composée de ferrite et d'austénite recristallisées. Lors du refroidissement, l'austénite se transforme partiellement en ferrite puis en martensite pour atteindre la microstructure ferrite/martensite finale. L'austénitisation est cruciale pour contrôler les fractions et tailles de phase finales et donc leurs propriétés mécaniques. De nombreuses études montrent que la vitesse de chauffe contrôle la cinétique de transformation et la morphologie de l'austénite ("collier" ou "bande"). Ces effets sont souvent attribués au chevauchement entre la recristallisation de la ferrite et la formation de l'austénite, mais les mécanismes sous-jacents restent controversés.

En utilisant les progrès récents dans les expériences in situ sur les lignes de faisceaux synchrotron, ce travail de doctorat vise à proposer une nouvelle compréhension des interactions entre la recristallisation de la ferrite et la formation de l'austénite et à développer un modèle prédictif pour la cinétique de formation de l'austénite.

Le développement expérimental principal de cette thèse est une nouvelle technique d'analyse basée sur la diffraction des rayons X de haute énergie pour suivre in situ la recristallisation et les transformations de phase pendant la phase de recuit, y compris à des vitesses de chauffe élevées. Notre nouvelle méthode, appelée Isolated Diffraction Spot Tracking (IDST), est d'abord validée pour étudier la recristallisation sur des aciers ferritiques modèles. Ces mesures in situ sont complétées par des observations des microstructures après traitements interrompus en microscopie (optique, microscopie électronique à balayage et à transmission), et par des mesures de chimie locale (spectroscopie de rayons X à dispersion d'énergie et de dispersion en longueur d'onde).

Nous reproduisons d'abord des expériences pour étudier l'influence de la vitesse de chauffe sur l'acier étudié pendant le recuit intercritique. Dans celles-ci, le chevauchement entre la recristallisation de la ferrite et la formation de l'austénite est régi par la vitesse de chauffe. Ensuite, nous avons conçu des expériences pour décorrélérer l'effet de la vitesse de chauffe et ce chevauchement. La vitesse de chauffe est fixée pour maintenir les mêmes conditions pour les mécanismes thermo-activés, mais le micro-alliage au niobium et le taux de laminage à froid plus faible retardent la recristallisation de la ferrite. Ces expériences montrent que la cinétique de transformation de l'austénite n'est pas contrôlée par la recristallisation, mais par la seule condition thermodynamique de l'interface de transformation et peut-être par la distance de diffusion dans les microstructures. Enfin, une analyse thermocinétique détaillée des mécanismes de formation de l'austénite au cours du recuit intercritique est proposée sur la base de simulations DICTRA/Thermo-Calc et de notre travail expérimental. L'effet des éléments d'alliage mineurs sur la cinétique de croissance de l'austénite est étudié et un modèle prédictif pour la formation de l'austénite pendant le recuit intercritique est développé. Finalement, ce travail montre l'absence d'effet significatif de la concomitance des mécanismes étudiés sur la cinétique de formation de l'austénite au cours de la chauffe. Nous montrons que la cinétique de formation de l'austénite est contrôlée par la diffusion. La différence de cinétique de formation de l'austénite au cours de la phase de maintien est expliquée par des considérations microstructurales, affectant les distances de diffusion.

**Mots clés :** Acier Dual-Phase, recristallisation, transformation de phase, High Energy X-Ray Diffraction (HEXRD), thermocinétique